THESIS FOR THE DEGREE OF DOCTOR OF PHILOSOPHY

Multilevel three-phase dual active bridge dc-dc converters

Babak AlikhanzadehAlamdari

Department of Electrical Engineering
Chalmers University of Technology
Gothenburg, Sweden, 2023

Multilevel three-phase dual active bridge dc-dc converters

Babak AlikhanzadehAlamdari

ISBN 978-91-7905-831-9
Doktorsavhandlingar vid Chalmers tekniska högskola.
Ny serie 5297
ISSN 0346-718X
This thesis has been prepared using LaTeX.

Department of Electrical Engineering
Chalmers University of Technology
SE-412 96 Gothenburg, Sweden
Phone: +46 (0)31 772 1000
www.chalmers.se

Printed by Chalmers Digital Printing
Gothenburg, Sweden, April 2023

Abstract

The collection and transmission of power from offshore wind turbines using dc have advantages over the ac system. One of the enabling technologies for deploying dc collection is the dc-dc converter that boosts the dc output from the turbine to the medium voltage direct current level of the collection grid. This dc-dc converter should be able to transfer nominal power of at least 15 MW, boost the voltage from a few kilovolts to tens of kilovolts, have high power density and efficiency. The dual active bridge (DAB) converter concept is a suitable candidate for this application. It comprises two active inverters and an intermediate transformer which provides galvanic isolation and voltage matching between the low voltage and medium voltage systems. Its soft-switching capabilities allow an increase in the switching frequency without deteriorating the efficiency of the converter. Therefore, the size of passive components can be reduced to achieve high power densities.

Using partial power processing DAB converters for this application has been studied extensively in the literature, while this document considers bulk power transmission using multilevel converter topologies focusing on three-phase topologies. Different aspects of the converters are studied in detail, including; desired leakage inductance of the transformer; capacitive energy storage requirement of the converters; the lifetime of semiconductors; the effect of winding configurations; the flux waveforms inside the transformer core; the transformer's core losses; the soft-switching boundaries; and harmonic and partial load performance. Mathematical models are developed for different studies and verified by simulations or measurements.

Several converter topologies and winding configurations are studied. As an example, it is shown that a three-phase DAB with YΔ winding configuration, controlled transition bridge converter, and the quasi-two-level modulation is the best choice for this application. A modulation strategy is proposed to improve the partial load performance. A loss split calculation showed that the semiconductor losses decreased by 94 % and 81 % at 5 % and 10 % of the nominal power, respectively compared to the quasi-two-level modulation.

Keywords: Dual active bridge, medium frequency transformer, multilevel converters, three-phase system, high power-density systems, high-voltage power converters, soft-switching converters, dc collector network, transformer winding connection, harmonic analysis, core loss modeling, capacitor sizing.

List of Publications

This thesis is based on the following publications:

[I] **Babak Khanzadeh**, Torbjörn Thiringer, "Closed-Form ZVS Boundaries for Three-Phase M-level-to-N-level DAB Converters with Different Winding Configurations". Published in *IEEE Transactions on Power Electronics*, pp. 1–16, 2023 , doi: 10.1109/TPEL.2023.3260682.

[II] **Babak Khanzadeh**, Torbjörn Thiringer, Yuriy V. Serdyuk, "Loss Reduction at Partial Loads of Multi-Level DAB Converters Using Adjusted Switching Patterns". Submitted to *IEEE Transactions*, 2023, (under review).

[III] **Babak Khanzadeh**, Torbjörn Thiringer, Mohammad Kharezy, "Multilevel Dual Active Bridge Leakage Inductance Selection for Various DC-link Voltage Spans". Published in *Energies*, vol. 16, no. 2, 2023, issn: 1996-1073, doi: 10.3390/en16020859.

[IV] **Babak Khanzadeh**, Yuhei Okazaki, Torbjörn Thiringer, "Capacitor and Switch Size Comparisons on High-Power Medium-Voltage dc–dc Converters With Three-Phase Medium-Frequency Transformer". Published in *IEEE Journal of Emerging and Selected Topics in Power Electronics*, vol. 9, no. 3, pp. 3331-3338, June 2021, doi: 10.1109/JESTPE.2020.2999726.

[V] **Babak Khanzadeh**, Torbjörn Thiringer, Yuriy Serdyuk, "Analysis and Improvement of Harmonic Content in Multi-level Three-phase DAB Converters with Different Transformer Windings Connections". *in Proceedings of International Power Electronics Conference (IPEC-Himeji 2022- ECCE Asia)*, 2022, pp. 2653-2658, doi: 10.23919/IPEC-Himeji2022-ECCE53331.2022.9807076.

[VI] **Babak Khanzadeh**, Yuriy Serdyuk, Torbjörn Thiringer, "Evaluation of Core Losses in Transformers for Three-phase Multi-level DAB Converters". *in Proceedings of 24th European Conference on Power Electronics and Applications (EPE'22 ECCE Europe)*, 2022, pp. 1-11.

[VII] **Babak Khanzadeh**, Torbjörn Thiringer, Yuhei Okazaki, "Capacitor Size Comparison on High-Power dc-dc Converters with Different Transformer

Winding Configurations on the ac-link". *in Proceedings of 22nd European Conference on Power Electronics and Applications (EPE'20 ECCE Europe)*, 2020, pp. P.1-P.7, doi: 10.23919/EPE20ECCEEurope43536.2020.9215924.

[VIII] **Babak Khanzadeh**, Chengjun Tang, Torbjörn Thiringer, "A Study on the Lifetime of Q2L-MMC-DAB's Switches for Wind Turbine Applications". *in Proceedings of fifteenth International Conference on Ecological Vehicles and Renewable Energies (EVER)*, 2020, pp. 1-6, doi: 10.1109/EVER48776.2020.9243073.

[IX] **Babak Khanzadeh**, Torbjörn Thiringer, Mohammad Kharezy, "Optimum Leakage Inductance Determination for a Q2L-Operating MMC-DAB with Different Transformer Winding Configurations". *in Proceedings of 20th International Symposium on Power Electronics (Ee)*, 2019, pp. 1-6, doi: 10.1109/PEE.2019.8923224.

Other publications by the author, not included in this thesis, are:

[X] **Babak Khanzadeh**, Amin Bahmani, Torbjörn Thiringer, "Efficiency investigation of 2L-DAB and ML-DAB for high-power PV applications". *In Proceedings of Thirteenth International Conference on Ecological Vehicles and Renewable Energies (EVER)*, 2018, pp. 1-6, doi: 10.1109/EVER.2018.8362340.

Acknowledgments

First, I would like to thank my main supervisor and examiner Prof. Torbjörn Thiringer and my co-supervisor Prof. Yuriy Serdyuk for their patient guidance and supervision.

Thanks to Dr. Amin Bahmani, Dr. Yuhei Okazaki, and Dr. Alireza Nami for their guidance in the initial phases of the project. I want to thank Robert Karlsson, Mohammad Kharezy, Dr. Zeyang Geng, Dr. Douglas Jutsell Nilsson, and Dr. Thomas Hammarström for their suggestions or assistance during laboratory tests. I would also like to thank Chengjun Tang for cooperating on a few projects.

I am also grateful to my family members and friends for their support and encouragement. Also, I want to thank my colleagues at the electric power engineering division for the open work environment and interesting discussions.

The financial support from Swedish Energy Agency (Energimyndigheten) is gratefully acknowledged.

Acronyms

2LC	two-level converter
ac	alternating current
CTB	controlled transition bridge
DAB	dual active bridge
dc	direct current
FEM	finite element method
HV	high voltage
HVAC	high voltage alternating current
HVDC	high voltage direct current
IGBT	insulated-gate bipolar transistor
IGSE	improved generalized Steinmetz equation
IPOS	input-parallel output-series
LV	low voltage
LVDC	low voltage direct current
MFT	medium frequency transformer
MMC	modular multilevel converter
MOSFET	metal–oxide–semiconductor field-effect transistor
MTAC	modular transition arm converter
MV	medium voltage
MVAC	medium voltage alternating current
MVDC	medium voltage direct current

N2G	neutral-to-ground
NPC	neutral-point-clamped
P2G	phase-to-ground
P2N	phase-to-neutral
P2P	phase-to-phase
PWM	pulse width modulation
Q2L	quasi-two-level
RMS	root mean square
RMSPE	root mean squared percentage error
SiC	silicon carbide
SPS	single-phase-shift
TAC	transition arm converter
THD	total harmonic distortion
TUF	transformer utilization factor
ZCS	zero current switching
ZVS	zero voltage switching

Mathematical symbols

Symbols

1ϕ	Single-phase system
3ϕ	Three-phase system
A	Cross-section of MFT's core
α	Steinmetz coefficients of core material
α	$\alpha \in \{0, \pm 2\pi/3\}$ is the phase shift in three-phase waveforms
B	Magnetic flux density
β	Steinmetz coefficients of core material
$C_{\mathrm{dc}}^{\pm}$	Positive (or negative) dc-link capacitance
C_{sm}	Submodule capacitance
$C_{\mathrm{sm}k}$	The kth submodule capacitance
D	Ratio of primary dc-link voltage to secondary dc-link voltage
D_j^{all}	DC ratio where all switches of the primary (or secondary) converter looses ZVS; where $j \in \{\mathrm{p}, \mathrm{s}\}$
D_j^{first}	DC ratio where the first switch from the primary (or secondary) converter looses ZVS; where $j \in \{\mathrm{p}, \mathrm{s}\}$
$D_j^{\sim}$	Approximate dc ratio where the first switch from the primary (or secondary) bridge loose ZVS; where $j \in \{\mathrm{p}, \mathrm{s}\}$
$D_{k_{\mathrm{p}}\mathrm{p}}^{\pm}$	DC ratio where a switch of the primary converter looses ZVS which is responsible for the k_{p}th transition event of the positive (+) or negative (-) half cycle in the P2G voltage waveform
$D_{k_{\mathrm{s}}\mathrm{s}}^{\pm}$	DC ratio where a switch of the secondary converter looses ZVS which is responsible for the k_{s}th transition event of the positive (+) or negative (-) half cycle in the P2G voltage waveform

D_{sw}	Accumulated damage of switches under a single run of a given mission profile
δ_{θ_k}	Kronecker delta function [see (A.1)]
E_{a}	Activation energy (SKiM63 model)
E_{cl}	Capacitive energy storage capacity of chain-link
E_{dc}	Capacitive energy storage capacity of dc-link
E_{tot}	Total capacitive energy storage capacity of converter
f_{sw}	Switching frequency of converter
φ	Phase shift between primary phase voltage and primary-referred secondary phase voltage of MFT
$\Phi_{\mathrm{L}}(\omega t)$	Total instantaneous magnetic flux in limbs of MFT
G_{L_σ}	Coefficient used to calculate the optimum L_σ [see (5.14)]
H	Harmonic order of waveforms
$h_1(\omega t)$	Piecewise linear periodic function [see (A.2)]
$h_2(\omega t)$	Piecewise linear periodic function [see (A.8)]
$i^{\pm}_{C_{\mathrm{dc}}}(\omega t)$	DC-link's positive or negative pole capacitor current
$i_{C_{\mathrm{sm}k}}(\omega t)$	The kth submodule capacitor's current
$i^{\pm}_{\mathrm{dc}}(\omega t)$	Positive pole or negative pole dc-link currents
$i_{\phi x}(\omega t)$	Phase current of phase x of MFT, where $x \in$ {A,a,B,b,C,c}
$i_{\mathrm{L}x}(\omega t)$	Line current of phase x of MFT, where $x \in$ {A,a,B,b,C,c}
$i^{\pm}_{\Sigma}(\omega t)$	Positive (or negative) pole current flowing from (or to) the dc-link to (or from) converter arms
$i_x(\omega t)$	Phase current of converter flowing from the converter to the ac-link, where $x \in$ {A,a,B,b,C,c}
$i^{\pm}_x(\omega t)$	Upper (+) arm or lower arm (−) current of converter, where $x \in$ {A,a,B,b,C,c}

$i_x^0(\omega t)$	Clamping arm current of NPC, CTB, and T-type converters, where $x \in \{\text{A,a,B,b,C,c}\}$
k	Steinmetz coefficient of core material
K_B	The Boltzmann constant
k_σ	Ratio representing the distribution of leakage inductance between the primary and secondary windings [see (8.2)]
L_m	Magnetizing branch inductance of MFT
L_σ	Total series leakage inductance of MFT
M	Number of voltage steps (from zero to peak) in a Q2L P2G voltage waveform
$\mathbb{N}$	The set of all natural numbers
N_cl	Number of chain-links of converter
N_f	Expected number of cycles to failure (SKiM63 model)
N_p	Number of turns of the primary winding of MFT
N_s	Number of turns of the secondary winding of MFT
N_sm	Number of submodules per arm of MMC, TAC, and MTAC converters (per leg of CTB converter)
$\mathcal{O}_\text{d}$	Operation domain of converter [see Figure 5.2]
ω	Angular switching frequency of converter
$P_{3\phi}$	3ϕ active power of converter
$P_{3\phi}(\omega t)$	3ϕ instantaneous power of converter
$\overline{P_\text{v}}$	Average power loss per unit volume of a magnetic material
$Q^{\pm}_{C_\text{dc}}(\omega t)$	Converter dc-link capacitors' instantaneous charge
$\overline{Q^{\pm}_{C_\text{dc}}}$	Average value of dc-link capacitors' instantaneous charge
$Q_{C_{\text{sm}k}}(\omega t)$	The kth submodule capacitor's instantaneous charge
R_ac	Series ac resistance of MFT

R_{m}	Magnetizing branch resistance of MFT
$\mathbb{R}^{+}$	The set of all positive real numbers
S_{f}	Safety margin of the blocking voltage of semiconductors
ψ	Duration of each step in a Q2L P2G voltage waveform
$\Psi\left(\omega t\right)$	Flux linkage of a coil
σ_{dc}	Deviations in the dc-link voltage of converter from the center of $\mathcal{O}_{\mathrm{d}}$ [see Figure 5.2]
$\sigma_{\mathrm{dc}}^{\pm}$	Percentage of deviation in the dc-link voltage of converter from its nominal value in the positive or negative direction
σ_{sm}	Percentage of deviation in submodule capacitor voltage from its nominal value
T	Fundamental period of waveforms
t_{d}	Dead time of switch
t_{on}	Load pulse duration (SKiM63 model)
τ	Transition time from one dc-rail to another
$\tau_{\%}$	Percentages of τ per fundamental period ($\tau_{\%} \triangleq \tau f_{\mathrm{sw}} \times 100\,\%$)
θ_k	kth-step phase shift in Q2L waveforms
T_{j}	Junction temperature of semiconductor
T_{jm}	Mean junction temperature of semiconductor
U	Submodule voltage in multilevel converters
u_{Hj}	Function used in modeling of Q2L waveforms where $j \in \{\mathrm{p}, \mathrm{s}\}$ [see (4.20)]
$U_{j\mathrm{m}}$	The center of $\mathcal{O}_{\mathrm{d}}$ [see Figure 5.2] where $j \in \{\mathrm{p}, \mathrm{s}\}$
V_{dc}	DC-link voltage (pole-to-pole) of converter
$v_{\mathrm{NG}}\left(\omega t\right)$	Primary side N2G voltage
$v_{\mathrm{ng}}\left(\omega t\right)$	Secondary side N2G voltage

$v_{\mathrm{p}}(\omega t)$	MFT's primary winding voltage waveform
$v_{\mathrm{s}}(\omega t)$	MFT's secondary winding voltage waveform
V_{sw}	Voltage across semiconductor
$v_{x\mathrm{G}}\,(\omega t)$	Primary side P2G voltage where $x \in \{\mathrm{A,B,C}\}$
$v_{x\mathrm{g}}\,(\omega t)$	Secondary side P2G voltage where $x \in \{\mathrm{a,b,c}\}$
$v_{x\mathrm{N}}\,(\omega t)$	Primary side P2N voltage where $x \in \{\mathrm{A,B,C}\}$
$v_{x\mathrm{n}}\,(\omega t)$	Secondary side P2N voltage where $x \in \{\mathrm{a,b,c}\}$
$v_{xy}\,(\omega t)$	Primary side P2P voltage where $xy \in \{\mathrm{AB,BC,CA}\}$
$v_{xy}\,(\omega t)$	Secondary side P2P voltage where $xy \in \{\mathrm{ab,bc,ca}\}$
χ_{Q2L}	Design factor used to estimated the core losses of an MFT excited with Q2L voltage waveforms
$\mathbb{Z}$	The set of all integer numbers
Z_H	Series impedance of MFT for the Hth harmonic [see (5.5)]

Superscripts

Δ,Y	Used for different winding connections; their permutations are used for transformer configurations
calc	The value is obtained from calculation
conv	For conv $\in$ {2LC, NPC, T-type, TAC, MTAC, CTB}, the respective converter's parameter
meas	The value is obtained from measurements
nom	Nominal value of the parameter
pu	Per-unit value of the parameter
p	Used for primary-side-referred secondary bridge parameters
rated	Rated value of component

RMS	RMS value of the parameter
sim	The value is obtained from simulation
s	Used for secondary-side referred primary bridge parameters

Subscripts

$1\phi, 3\phi$	Used to distinguish between 1ϕ and 3ϕ systems parameters
A, B, C	Used for primary side phase parameters
a, b, c	Used for secondary side phase parameters
aux	Submodules auxiliary switch's parameters
conv	For conv $\in$ {2LC, NPC, T-type, TAC, MTAC, CTB}, the respective converter's parameter
H	Hth harmonic component of the parameter where $H \in \mathbb{N}$
main	Submodules main switch's parameters
max	Maximum value of the parameter
min	Minimum value of the parameter
non-opt	Non-optimum value of the parameter
opt	Optimum value of the parameter
p, s	Used to distinguish between primary and secondary bridge parameters
ϕ, L	Used to distinguish between phase and line parameters
RMS	RMS value of the parameter
sw$k$	The kth switch parameter

Contents

Part I

Overview

CHAPTER 1

Introduction

1.1 Background

A glimpse into an offshore wind farms database reveals that nearly 80 GW of offshore wind farms are operational or under construction, and more than 830 GW of offshore wind farm projects are planned or approved [1]. The same figures, four years earlier, were 30 GW and 180 GW, respectively [2]. The figures show a more than four times increase in less than four years.

To maximize the power capture and minimize the visual impacts, it is preferred to increase the distance of the farms from the shores. For distances longer than 80 km, the transmission of power with high voltage direct current (HVDC) is economically advantageous compared to high voltage alternating current (HVAC) systems [3], [4]. Moreover, the conduction losses can be decreased by using direct current (dc) instead of alternating current (ac) due to the elimination of reactive power flow and the skin effect.

Figure 1.1 shows a schematic of a classic offshore wind farm with medium voltage alternating current (MVAC) collection grid. The power is collected from the wind turbines using an MVAC collection grid to a central offshore platform. Then the current is rectified and transmitted to the mainland using

HVDC power cables.

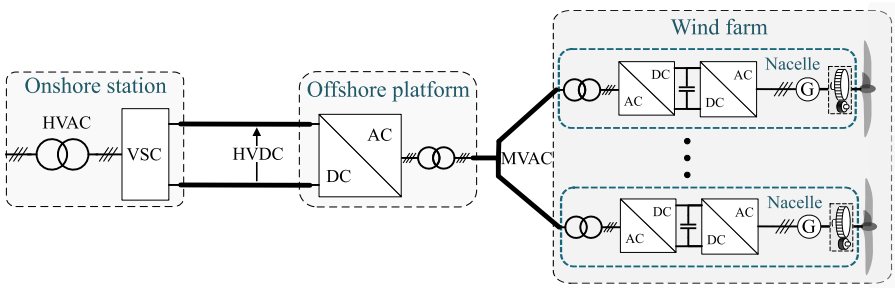

Figure 1.1: Offshore wind farm with MVAC collection grid.

The collection of power from the wind turbines in the form of dc also has several advantages over the ac collection [3]–[5]. Figure 1.2 shows a schematic of an offshore wind farm with an MVDC collection grid. As can be seen, dc-dc converters are needed to boost up the voltage from the low voltage direct current (LVDC) level of the turbines to the MVDC level of the MV grid. Due to the high transformation ratio of these dc-dc converters [6], galvanic isolation between the MVDC and LVDC links is required.

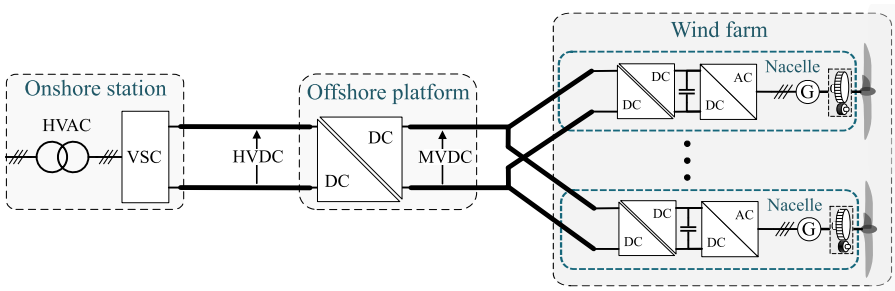

Figure 1.2: Offshore wind farm with MVDC collection grid.

The DAB converter concept, proposed in [7], is a suitable candidate for this application due to its inherent galvanic isolation feature and the possibility of achieving an arbitrary transformation ratio. Figure 1.3 shows the schematic of a DAB converter. Two active bridges invert the dc-links voltages into alternating voltages, and the intermediate transformer provides galvanic

isolation and voltage matching between the primary side and the secondary side [7]. The power flow is controlled by adjusting the phase shift between the ac-link voltage waveforms. The frequency of the ac-link waveforms can

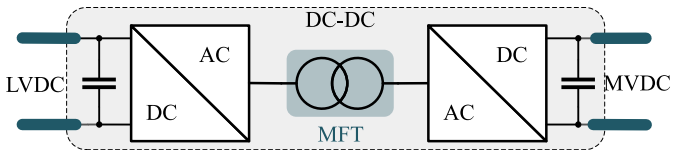

Figure 1.3: Schematic of a DAB dc-dc converter.

be increased to several kHz to reduce the transformer's size and weight [8]. The former heavy 50 Hz transformer, along with the ac-dc converter inside the nacelle (shown in Figure 1.1) will now be replaced with a dc-dc converter and a lightweight MFT. Therefore, potentially the bearing capacity of the turbine structure can be reduced.

As shown in Figure 1.3, the DAB is composed of three main components—two inverters and a transformer. This allows for selecting from a large variety of options for each component [9]. The ac-link can have a single-phase, 1ϕ, or multi-phase configurations. The single-phase and three-phase, 3ϕ, ac-links configurations are the most common for DAB converters. However, the 3ϕ-DAB is preferred over the single-phase variant for high power applications [10], [11], due to smaller dc-link filters. A 3ϕ ac-link provides extra degrees of freedom (e.g., winding configurations), which can be used for performance improvement of the converter.

For the MVDC collection grid of offshore windfarms different voltage levels spanning from 30 kV up to 50 kV are considered in the literature [5], [12]–[17]. The conventional 3ϕ-DAB is composed of two two-level converters (2LCs) and is unsuitable for these voltage levels. Parallel and series connections of DAB converter blocks can be used to overcome the voltage issue. Figure 1.4 shows the schematic of a input-parallel output-series (IPOS) DAB converter, which is used extensively in the literature to solve this issue.

Even though the IPOS-DAB solves the voltage limitation of the conventional DAB, its power density is debatable. The insulation of the MFT should be rated to handle the dc offset introduced by the series connection on the MVDC link. This means that most transformers should be overdesigned to have full modularity. Moreover, considering connection requirements in high

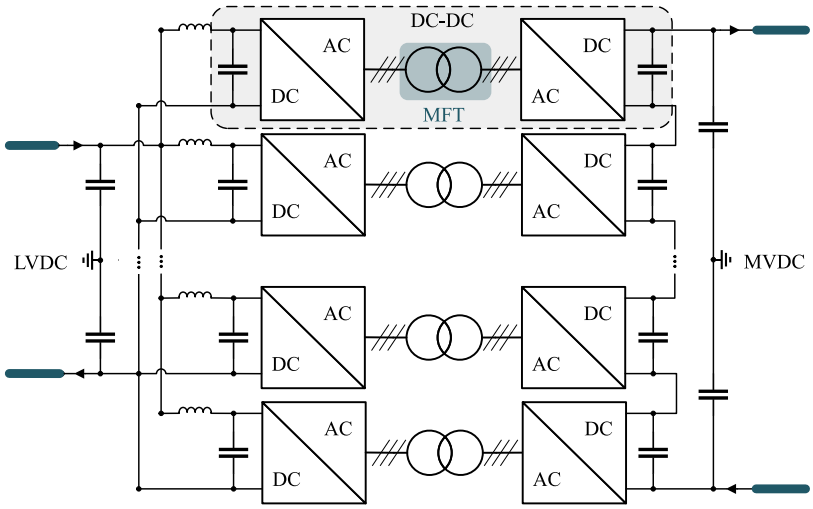

Figure 1.4: Schematic of a IPOS DAB dc-dc converter.

voltage levels and excessive interconnection points of this converter, poses questions on the final power density of the converter.

Multilevel inverter topologies can be used instead of the two-level inverter to solve the voltage limitation issue of the conventional DAB. Then a single bulky MFT can process the full power instead of several partial power processing units (IPOS topology). Several multilevel topologies are proposed in the literature, which can be used to form a DAB converter [6], [10], [18]. Each converter has its own benefits and drawbacks, and selecting a suitable topology becomes important.

1.2 Aim

The aim of this thesis is to evaluate the performance of multilevel 3ϕ DAB converters for wind turbine applications from different aspects. Also, a target is to select suitable converter topologies and components, modulation strategies, and winding configurations.

1.3 Identified research gaps

The following gaps are identified for selecting a suitable converter topology.

[I] Non-proper selection of the leakage inductance of the MFT may result in extremely large reactive currents through the converter due to small deviations in the dc-link voltages [19]–[21]. Therefore, it is important in multilevel converters design, as the submodule capacitors should be overrated to handle excessive currents. It also is crucial in applications where conduction losses are the main loss component and variable dc-link voltages are required. Missing in the available literature is the identification of the value of this leakage inductance for multilevel 3ϕ DAB converters.

[II] Besides the MFT, capacitors are other passive components that affect the power density and cost of the converter. Especially in multilevel converters where each submodule requires a capacitive storage unit. The higher this requirement, the lower the power density of the converter and the higher the costs. Q2L modulation was introduced for multilevel converters in [22], with the aim of reducing the capacitor requirement and improving the power density. In [23], the cell capacitance design and comparison for multilevel converters with the Q2L modulation were presented. However, the dc-link capacitors were not considered, and only the YY winding configuration was studied. Missing in the available literature is the energy storage requirement quantification and comparison for multilevel DAB converters, including both dc-link and submodule capacitors, and the effects of winding configurations.

[III] One of the advantages of the Q2L modulation is the possibility of using smaller devices for the auxiliary switches compared to the main switches [23]. This feature is discussed and investigated for a Q2L-operating MMC-based DAB in [22], [24]. However, the thermal stresses on the switches are not quantified.

[IV] One of the essential characteristics of a 3ϕ-DAB dc-dc converter is its inherent ZVS capability during the turn-ON of the switches. It is essential to identify the ZVS operation range of the converter to ensure soft-switching at different load levels. The soft-switching boundaries of 3ϕ two-level and multilevel DAB converters are studied in the literature

[7], [24]–[27]. However, available literature has focused on combinations of specific converter topologies with certain winding configurations. The effects of having a different number of levels or transition times for the bridges have not been studied in detail. Furthermore, the effects of winding configurations on the ZVS operation of the multilevel converters are not considered.

[V] A few papers have studied different aspects of 3ϕ multilevel DAB converters with Q2L modulation [22], [24], [28], [29]. However, the effects of the modulation strategy on the transformer core losses are not investigated. To estimate these losses, different methods can be used [30], [31]. If research focuses on transformer design, finite element method (FEM) can be used for detailed and accurate iron loss analysis. However, for research focusing on the power electronics aspects, FEM analysis is time inefficient. A closed-form formulation of transformer core losses is missing in the available literature for the multilevel DAB converters, which allows for a quick estimate of the losses with high accuracy.

[VI] Since the ac-link waveforms of DAB are non-sinusoidal, the transformer is subjected to harmonics of the fundamental frequency. The higher the harmonic content of the voltages and the currents, the higher the losses in the transformer. Thus, it is crucial to study the harmonic performance of the converter. Studies considering the effects of the transformer winding connections on the harmonic performance of multilevel DAB converters are scarce. One such study is done in [24], where the focus has been on the harmonic content of the phase voltages of a multilevel 3ϕ-YY-DAB. However, neither the ΔY connection of the windings nor the harmonic content of the phase currents is considered in the study.

[VII] It has been shown in [25], [32] that the 3ϕ-ΔY-DAB has poor efficiency and low transformer utilization in partial loads. This makes the 3ϕ-ΔY-DAB unattractive for applications with recurrent operation at these points unless the partial load performance could be improved. On the other hand, the small capacitor requirement of the 3ϕ-ΔY-DAB converter is an advantage for high power density applications. This provides an incentive to improve its partial load performance and reduce losses. In [33], the authors have tried to improve the performance of a

three-level ΔY-DAB. However, the proposed control method results in complicated switching patterns, has low accuracy in the partial loads, and has a large no-load current flow in the ac-link, resulting in poor efficiencies. Missing in the available literature is a proposal for utilizing the benefits of the 3ϕ-ΔY-DAB, while also tackling the problem with high reactive current at low loads.

1.4 Contributions

The following are the main contributions of the present Ph.D. thesis.

[I] Analytical expressions for calculating the desired leakage inductance value of the 3ϕ MFT are derived, and their accuracy is evaluated [see chapter 5 or paper III (11.3) and paper IX (11.9)].

[II] The capacitor requirements of selected converter topologies are quantified, considering not only the submodule capacitors of the converters but also the dc-link capacitors. It is also shown that the winding configuration of the MFT has a dramatic effect on this requirement. Finally, the combination of winding configuration and converter topology, which results in the minimum installed energy storage, is identified [see chapter 6 or paper IV (11.4) and paper VII (11.7)].

[III] The impact of the Q2L modulation on the lifetime of the semiconductors of an MMC-based DAB converter is quantified and analyzed [see chapter 6 or paper VIII (11.8)].

[IV] A set of closed-form generalized ZVS boundaries for 3ϕ M-level-to-N-level DAB converters are derived. The derived expressions are independent of the topologies of the bridges and can be used for different converter topologies, including but not limited to 2LC, three-level NPC converter, T-type converter, TAC, MMC, and CTB converter. The effect of different winding configurations of the MFT is also considered in the study. This includes YY, YΔ, and ΔΔ winding configurations. The impact of the number of levels in the bridges, the transition times, the dead times, and the winding configurations on the ZVS conditions are quantified. Additionally, easy-to-implement simplified ZVS boundaries

are provided, and the effects of different parameters on the simplification results are quantified. The derived models are validated with the experimental results [see chapter 7 or paper I (11.1)].

[V] Closed-form expressions are derived for estimating the core losses of a 3ϕ MFT excited with multilevel converters. The impact of different winding configurations and the converter parameters on the estimated losses are quantified. Also, analytical expressions are derived to estimate the flux waveform inside the transformer core. Experimental results show a perfect match with the derived expressions [see chapter 8 or paper VI (11.6)].

[VI] The harmonic content of the phase voltages and currents of a 3ϕ multilevel DAB converter is analyzed for different power levels and two winding configurations. A control method is proposed to improve the harmonic performance of the ΔY-connected DAB converter at partial loads [see chapter 9 or paper V (11.5)].

[VII] Two control strategies have been proposed to minimize the RMS current and improve the partial load performance of the 3ϕ-ΔY converter. The performance improvement is achieved by introducing a zero-level voltage on the Y-side of the converter and (or) reducing the Δ-side dc-link voltage. The proposed strategies are validated with measurements [see chapter 9 or paper II (11.2)].

CHAPTER 2

Converters Topologies and Modulation

2.1 Introduction

3ϕ DAB converters with multilevel bridges are suitable candidates for high-power, medium- and high-voltage applications. Different aspects should be considered in the design and topology selection process to ensure high power density and efficiency for these converters. Multiple multilevel converters are studied throughout this thesis. Moreover, because of having a 3ϕ ac-link, different winding configurations are considered for the MFT. This chapter provides theoretical bases for different converter topologies.

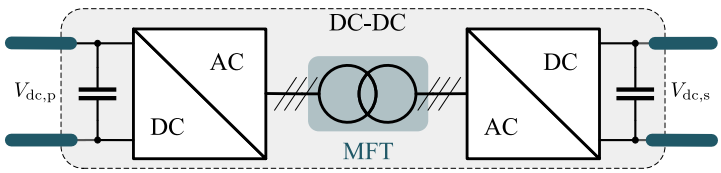

Figure 2.1: Schematic of a 3ϕ-DAB dc-dc converter.

Figure 2.1 shows the schematic of a 3ϕ-DAB converter. Two active bridges

invert the dc-links voltages into alternating voltages, and the intermediate MFT provides galvanic isolation and voltage matching between the primary side, and the secondary side [7]. The power flow is controlled by adjusting the phase shift, φ, between the ac-link voltage waveforms.

2.2 Conventions

The following conventions will be used hereafter:

(i) The nodes of the primary converter are identified by capital letters **A**, **B**, **C**, **N**, and **G**. Likewise, the secondary bridge nodes are denoted by lowercase letters **a**, **b**, **c**, **n**, and **g**. In general, capital letters are used for derivations that are independent of the converter sides.

(ii) The subscripts **p** and **s** are used to distinguish between the parameters of the primary bridge and the secondary bridge, respectively.

(iii) The subscripts ϕ and L are used to distinguish between the phase and line parameters, respectively.

(iv) The superscript **p** is used for the primary-side-referred secondary bridge parameters. Similarly, the superscript **s** is used for the secondary-side-referred primary bridge parameters.

(v) The superscripts Δ and Y and their permutations are used for different winding connections and transformer configurations.

(vi) The superscript **nom** is used for nominal values of the parameters.

(vii) Single- and three-phase systems are denoted by 1ϕ and 3ϕ, respectively.

(viii) The 1ϕ converters are tagged with 1ϕ-(primary bridge topology)-(secondary bridge topology)-DAB (e.g., 1ϕ-MMC-2LC-DAB).

(ix) The 3ϕ converters are tagged with 3ϕ-(primary winding connections, secondary winding connections)-(primary bridge topology)-(secondary bridge topology)-DAB (e.g., 3ϕ-YΔ-MMC-2LC-DAB).

(x) To refer to general cases, the respective parts are removed from the names of converters. (e.g., 3ϕ-MMC-2LC-DAB refers to a 3ϕ MMC-2LC-DAB converter with any winding configuration. Or 3ϕ-YΔ-DAB refers to a 3ϕ DAB with arbitrary converters and YΔ windings.)

Throughout this thesis, it is assumed that the ac-link is a balanced 3ϕ system to simplify the analysis—unless otherwise specified. Thus, it is sufficient to analyze phase A.

2.3 Windings configuration

The terminals of MFT's windings can be connected differently [34]. In this thesis, only YY, YΔ, ΔY, and ΔΔ configurations are considered. Figure 2.2 shows these configurations and related conventions used hereafter. In this

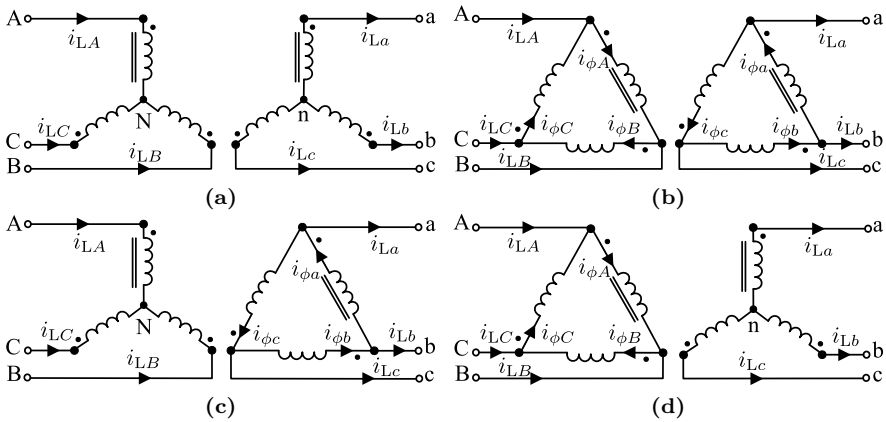

Figure 2.2: Different winding configurations of the MFT. **(a)** The YY configuration. **(b)** The ΔΔ configuration. **(c)** The YΔ configuration. **(d)** The ΔY configuration.

thesis, only phase displacement groups one (YY0, ΔΔ0), three (YΔ1, ΔY1) and four (YΔ11, ΔY11) are studied [34]. To avoid complicated notations and the involvement of clock-face numbers in the equations, the phase displacement introduced by the windings is compensated by the φ. The power is assumed to flow from the primary to the secondary side. Therefore, φ is limited between 0° and 90°; where $\varphi = 0°$ results in zero active power for all winding configurations. In this way, the studies become independent of the phase displacement groups. Therefore, notations YY, YΔ, ΔY, and ΔΔ will be used without clock-face numbers.

2.4 Inverter topologies and modulation

Similar to different winding configurations, different converter topologies can be used to form the DAB converter of Figure 2.1. Figure 2.3 and Figure 2.4

show some of these converter topologies that are studied in this thesis.

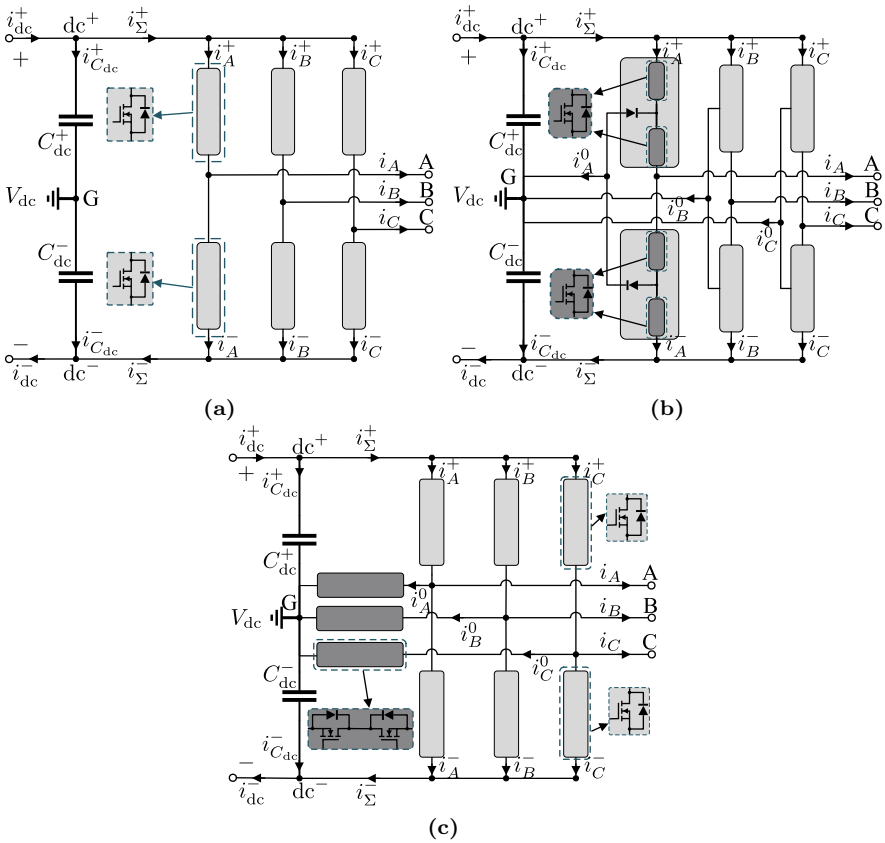

Figure 2.3: Two- and three-level converters. **(a)** 2LC. **(b)** NPC converter. **(c)** T-type converter.

The P2G voltages of a $(2M+1)$-level converter are depicted in Figure 2.5. These waveforms are used as the basis to generalize the analysis for different converters and modulation techniques. By adjusting the parameters of these waveforms, the P2G voltages of each converter of Figure 2.3 and Figure 2.4 can be obtained.

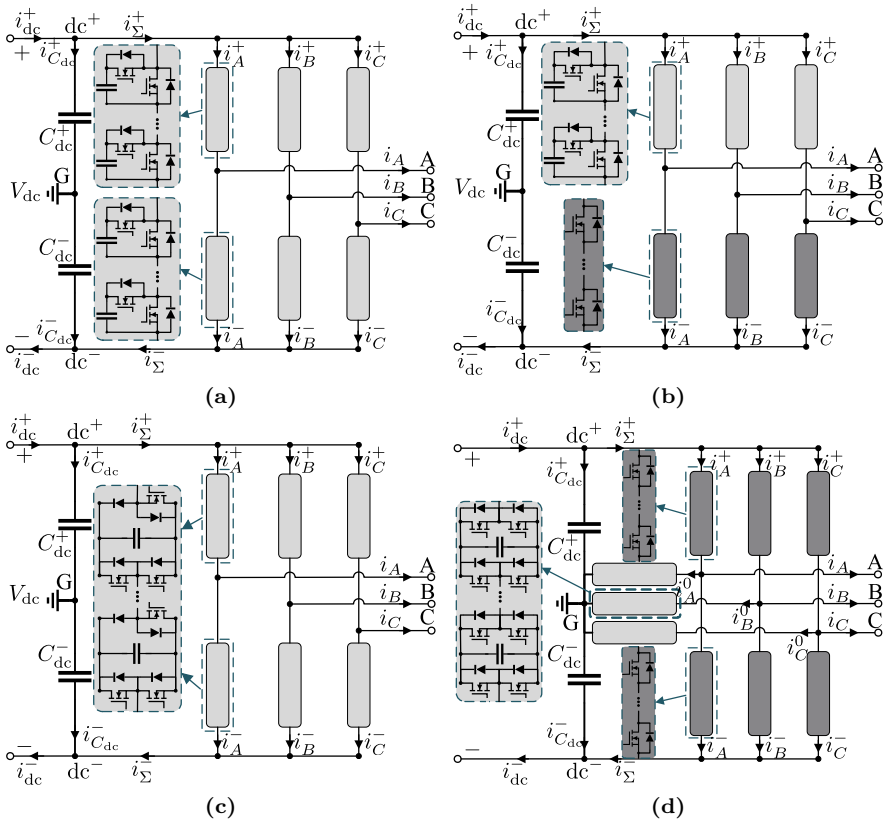

Figure 2.4: Multilevel converters **(a)** MMC. **(b)** TAC. **(c)** MTAC. **(d)** CTB converter.

Two-level converter (2LC)

Figure 2.3a shows the topology of a 2LC. Each arm can be formed by a series of switches to block the dc-link voltage. The resultant DAB converter using 2LCs as building blocks is the conventional DAB, introduced in [7]. Single-phase-shift (SPS) control is used here to modulate the converter. The upper and the lower arms of each leg are operated with a duty cycle of 50 %, and the gate signals of the legs are phase-shifted with 120°. The power can be transferred from the primary side to the secondary side by delaying the gate

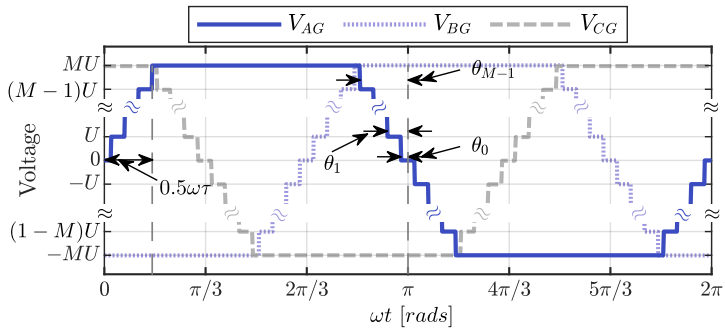

Figure 2.5: The P2G voltages of a 3ϕ $(2M+1)$-level converter; where $\omega = 2\pi f_{\text{sw}}$ and f_{sw} is the switching frequency of the converter, M is the number of steps starting from zero in the positive direction in the waveform, θ_k is the kth-step phase shift (where $k \in \{0, ..., M-1\}$), U is the amplitude of each step and τ is the transition time.

signals of the secondary bridge by φ radians with respect to the primary bridge. Detailed analysis and description of SPS modulation can be found in [7], [35]. Figure 2.5 will represent waveforms of a SPS-modulated 2LC if $M = 1$, $\theta_0 = 0$, and $U \equiv 0.5V_{\text{dc}}$ (where V_{dc} is the dc-link voltage).

Neutral-point-clamped (NPC) and T-type converters

In these converters, the switches of the upper and lower arms operate with a duty cycle of less than 50 %. The clamping switches are used to introduce a zero voltage level on the terminals of the converter. In this thesis, only the three-level NPC is studied. More information on operating principles of three and multilevel 1ϕ-NPC-DAB can be found in [36], [37]. A good source for 3ϕ-YY-NPC-DAB and 3ϕ-YY-T-type-DAB converters is [26]. With $M = 1$ and $\theta_0 \in \left(0, \frac{\pi}{2}\right)$, Figure 2.5 will illustrate the waveforms of an NPC or a T-type converter. Similar to the 2LC, $U \equiv 0.5V_{\text{dc}}$.

Quasi-two-level (Q2L) modulation

In the conventional DAB, the transition between the positive and negative dc-rails takes place instantly. Instant switching of high voltages is not desirable for the insulation system of the MFT. The Q2L operation of multilevel DAB

converters was introduced in [22], [24]. In this modulation method, chain-links of submodules are used to perform a smooth transition between the positive and negative dc-rails. In this way, the electrical stress over the MFT's insulation can be controlled. Compared to the sinusoidal modulation, the Q2L modulation of multilevel converters also reduces the size of the submodules capacitors and required semiconductor chip area [22], [24]. Therefore, the power density of the converter can be improved.

In this thesis, the Q2L is used to refer to a staircase P2G voltage waveform where the times spent on each intermediate voltage level (dwell times) are kept constant. As a result, one can define ψ as

$$2\theta_0 \equiv \psi \triangleq \frac{\omega\tau}{2M-1} \tag{2.1a}$$

$$\theta_k = (k+0.5)\,\psi \quad \forall k \in \{0, ..., M-1\} \tag{2.1b}$$

where $\omega = 2\pi f_{\text{sw}}$ and f_{sw} is the switching frequency of the converter, M is the number of steps starting from zero in the positive direction in the waveform, θ_k is the kth-step phase shift (where $k \in \{0, ..., M-1\}$), U is the amplitude of each step and τ is the transition time. As shown in Figure 2.5, it takes τ seconds to transit from one dc-rail to the other. Every ψ/ω seconds, a new submodule is inserted or bypassed to form the stair-shaped waveforms. The slope of the waveforms can be altered by controlling ψ. The minimum value of ψ is limited by the switching capability of the switches, and $\mathrm{d}v/\mathrm{d}t$ stress on the insulation of the MFT [24]. Its maximum determines the capacitor requirement of the submodules [24], [28], [29].

Modular multilevel converter (MMC)

Figure 2.4a depicts the configuration of an MMC with half-bridge submodules. Complementary switching is used here to modulate the converter. Both arms are used to perform the transition. During the transition time, the upper and the lower arms share the current between themselves. When the transition is over, the arm with the cells switching to OFF-mode clamps the ac terminal to the respective dc-rail. The other arm's capacitors are kept inserted, and their charges get balanced at the instant of clamping to the dc-rail [22], [24]. So, each arm is balanced once per fundamental cycle. For an MMC, $M \equiv 0.5N_{\text{sm}}$, where N_{sm} is the number of half-bridge submodules per arm of the converter.

According to this definition, the number of submodules should be an even number. Additionally, U is the nominal voltage of the submodules and can be related to the dc-link voltage as $UN_{\mathrm{sm}} = V_{\mathrm{dc}}$.

Transition arm converter (TAC)

The TAC—shown in Figure 2.4b—was proposed in [38] to reduce the number of submodules required for an MMC and potentially decrease the physical footprint of the converter. This is achieved by replacing one of the chain-links of each leg with a series connection of switches. Its operation is similar to an MMC; however, only the arms with submodules conduct the current during the transition periods. Similar to an MMC, the capacitors' voltages of each chain-link are balanced once per fundamental cycle. For TAC converters $M \equiv 0.5N_{\mathrm{sm}}$, where N_{sm} is the number of half-bridge submodules per arm of the converter. According to this definition, the number of submodules should be an even number. Additionally, U is the nominal voltage of the submodules and is related to the dc-link voltage as $UN_{\mathrm{sm}} = V_{\mathrm{dc}}$.

Modular transition arm converter (MTAC)

The MTAC was proposed in [23] to eliminate complications with the series connection of switches and to introduce modularity in the design of the TAC. Figure 2.4c shows the schematic of the converter and its submodules. One switch and one half-bridge submodule are series-connected to form a new submodule topology. The new submodules are evenly distributed between the upper and the lower arms. For the positive half-cycle of the voltage, the upper arm conducts the phase current, and for the rest of the period, the lower arm takes over the current. When the voltage approaches zero, there is an overlap period where the commutation between the arms takes place, and the capacitors of both arms get balanced. Therefore, the capacitors of each arm are balanced twice per fundamental cycle. For the MTAC, $M \equiv N_{\mathrm{sm}}$, where N_{sm} is the number of MTAC submodules per arm of the converter. In addition, U is the nominal voltage of each submodule, and it is related to the dc-link voltage as $UN_{\mathrm{sm}} = 0.5V_{\mathrm{dc}}$.

Controlled transition bridge (CTB) converters

The CTB—proposed in [39], [40]—is another high-voltage topology that can be used to form trapezoidal waveforms on the ac-link. It is a combination of a two-level inverter and full-bridge chain-links, as depicted in Figure 2.4d. The chain-links form the voltage waveforms during the transition periods and only conduct the currents in these intervals. The two-level inverter arms clamp the ac-link to the dc-poles for the rest of the period. The capacitor voltages of each chain-link are balanced twice per fundamental cycle when they clamp to one of the dc-rails. For the CTB converter $M \equiv N_{\mathrm{sm}}$, where N_{sm} is the number of full-bridge submodules per leg of the converter. In addition, U is the nominal voltage of each submodule, and it is related to the dc-link voltage as $UN_{\mathrm{sm}} = 0.5V_{\mathrm{dc}}$.

CHAPTER 3

Study Case Setup

3.1 Introduction

The main aim of this thesis is to examine the design and evaluate the performance of multilevel DAB converters for wind turbine applications from different aspects. A combination of theoretical analysis, computer simulations, and experimental validations are used throughout the thesis to reach this goal. An overview of the theoretical models is provided here. Also, simulation models and experimental setups used for verification are discussed in this chapter. Detailed theoretical modeling of different parts and analysis of the results is done in the respective sections.

3.2 Theoretical modeling

As mentioned in Chapter 1, this thesis has mainly focused on bulk power transfer using multilevel converters with Q2L modulation. Because of the complexity of the ac-link voltage and current waveforms, Fourier series decomposition is used as the main modeling tool. Models of these waveforms

are developed for arbitrary modulation and different winding configurations in Chapter 4. Consequently, studies depending on the ac-link waveforms are also done using the Fourier series. The parametric modeling used in the theory development phase makes the results independent of the system ratings.

Nominal point selection

The first step in the design is to select the nominal operating point of the converter. This point depends mainly on the phase shift between the bridges and the leakage inductance of the transformer. The former is the main degree of freedom to control power flow, and the latter shapes the ac-link current waveforms. Therefore, the selection of these two parameters goes hand in hand. In Chapter 5, the selection and optimization of these two parameters are discussed. The leakage inductance is selected to minimize the RMS current for a given variation in the dc-link voltage. Subsequently, the phase shift is selected to transfer the nominal power of the converter.

MFT electrical modeling

For simplicity, the transformer is modeled using the series leakage inductance for all the studies focusing on the converter. The leakage inductance is selected using the method described in Chapter 5 for all the subsequent studies. The transformer's turn ratio is selected to equal the ratio of the amplitudes of the first harmonics of the primary and the secondary winding voltages. This is to minimize the reactive power flow of the fundamental component.

Submodule and dc-link capacitor modeling

Different converter topologies for the primary and the secondary bridges are compared together from a capacitor requirements point of view in Chapter 6. The lower the capacitor requirement, the higher the power density. The aim is to select converter topologies with the lowest capacitor requirements for further studies. The submodule and dc-link capacitors are modeled with an ideal capacitor for these studies. They are designed to limit voltage variations in a predefined range. Firstly, the waveforms of the currents are used to calculate the charge variations. Then, the capacitance is selected to limit the voltage variations. The effect of winding configurations is considered using the respective configurations' current waveforms.

Semiconductor and lifetime modeling

To complement the capacitor studies, the converters are also compared from the total installed switch power point of view. The installed switch power is calculated using the RMS current of the switch and its voltage rating. In this stage, the semiconductors are modeled with ideal switches. In a later stage, the lifetime of semiconductors is studied and compared.

The semiconductors are modeled in two decoupled electrical and thermal domains for the lifetime study. In the electrical domain, they are modeled with ideal switches, and in the thermal domain, with a power source and a fourth-order Foster thermal network connected to a heatsink. The parameters of these models are extracted from the datasheets of semiconductors. The currents and voltages of the switches are obtained from the electrical domain, and the total losses are calculated and fed to the thermal network. Only conduction and switching losses are considered in the loss modeling. The junction temperature profile is outputted from the thermal model and is fed into the SKiM63 lifetime model [41] to estimate the lifetime of the semiconductors.

Soft-switching modeling

It is essential to identify and analyze the soft-switching of the converter at different load levels. The soft-switching boundaries are studied for combinations of different converter topologies, winding configurations, and converter parameters to identify the effects of different choices.

Derivation of soft-switching boundaries for a 3ϕ-ML-NL-DAB is done in Chapter 7. A current-based method is used to derive the turn-ON ZVS boundaries. According to this method, the switch will turn ON with zero voltage if the antiparallel diode conducts the current during the switching event [7]. The phase currents of the converters in Fourier series form are used to determine the boundaries. The results are transformed into a closed-form equation using a special series as discussed in Chapter 7. For these calculations, the output capacitance of the switches and the switching transients are neglected, while the effects of dead time are considered. Therefore, the obtained models describe the minimum requirement for the converter to achieve turn-ON ZVS.

Harmonic analysis

It is desirable to have low harmonic content in the waveforms of voltages and currents from a loss point of view. Using the models developed for the waveforms in Chapter 4, the harmonic content of the voltage and current waveforms are analyzed at different load levels for different winding configurations in Chapter 9. A control strategy is proposed to eliminate the low-order current harmonics for the ΔY winding configuration.

MFT modeling for loss split analysis

Transformer's core loss is one of the major loss components in the partial loads. Therefore, it should be modeled and analyzed during the design process. Equations are derived in Chapter 8 using the improved generalized Steinmetz equation (IGSE) method to estimate the core losses inside the transformer core excited with multilevel converter waveforms. The derivations assume that the flux is homogeneously distributed in the core cross-section. Also, it is assumed that the flux waveform inside the core depends on either the primary or secondary winding voltage waveforms.

3.3 Base verification

The largest offshore wind turbine currently available has a capacity of 15 MW. This thesis is aiming for a full-scale converter with a capacity of 20 MW, a LVDC rated voltage of 5 kV, and an MVDC rated voltage of 50 kV. Mathematical modeling of such a converter is not an issue. However, extensive simulation and comparison of different converter topologies pose some difficulties. As an example, an MMC converter with half-bridge submodules rated for 50 kV dc-link and 1.7 kV switches requires; 94 switches and 47 capacitors per arm; and in a total of 564 switches and 282 capacitors. Simulating such a converter is time and resource inefficient.

For the studies performed in this thesis, the simulated converter can be downscaled without the loss of generality of the conclusions. Different downscaled ratings are used for different studies depending on the nature of the model. Four main parameters of the converter are the nominal power, $P_{3\phi}^{\text{nom}}$, the switching frequency, f_{sw}, and the primary and the secondary nominal dc-link voltages, $V_{\text{dc,p}}^{\text{nom}}$ and $V_{\text{dc,s}}^{\text{nom}}$. Table 3.1 summarizes these parameters for

different studies. Detailed ratings of each model are provided in the respective chapter. The developed theories are validated with a down-scaled prototype.

Table 3.1: Main specifications of the simulated dc-dc converters

Study topic	Chapter	$V_{\mathrm{dc,p}}^{\mathrm{nom}}$	$V_{\mathrm{dc,s}}^{\mathrm{nom}}$	$P_{3\phi}^{\mathrm{nom}}$	f_{sw}
Leakage inductance	5	5 kV	5 kV	2 MW	5 kHz
Capacitor requirement	6	5 kV	5 kV	2 MW	$[1, 20]$ kHz
Semiconductor Lifetime	6	5 kV	5 kV	2 MW	5 kHz
Soft-switching	7	5 kV	5 kV	-	5 kHz
MFT core loss	8	5 kV	5 kV	2 MW	5 kHz
Harmonic content	9	5 kV	50 kV	10 MW	5 kHz
ΔY-DAB performance	9	1 kV	5 kV	2 MW	5 kHz

3.4 Simulation models

MATLAB and PLECS are the main simulation tools used throughout this thesis. Three types of models are developed for converters. These include

- scripts that emulate the converters' response.
- scripts based on developed theory to model the converter.
- PLECS models of the converters.

Simulations of capacitor requirement and semiconductor lifetime studies are time-demanding. Therefore, scripts that emulate the converters' behavior are developed for these studies. Steady-state waveforms of the ac-links are used as the starting point, and currents and voltages at different branches are back calculated. Then the charge variations of the capacitors are calculated using the current waveforms, and capacitors are designed to limit these variations

in a predefined range. A balancing algorithm is also implemented to handle the submodule capacitor voltage balancing.

For the lifetime study, the semiconductors are modeled using lookup tables—a similar implementation to PLECS models. The semiconductor losses are calculated using these lookup tables and are fed into a thermal network model of the switches. These models are implemented using discrete difference equations. The junction temperatures of the switches are obtained from these models and fed back to the loss calculation block to model the transient thermal behavior of the semiconductors.

Certain studies like harmonic content analysis or leakage inductance calculations directly depend on the waveforms of the currents and voltages. For these studies, the equations developed in Chapter 4 are coded as MATLAB scripts and used to analyze the converter performance.

PLECS models of the converters are used to validate all of the developed models and theories. Even the script-based models are first validated with PLECS models and then used for analysis and design. For pure simulations (not code generation), the converter and controller are both implemented using the Simulink PLECS blockset. The transformer is modeled in both the electrical and magnetic domains of PLECS. A respective model is used based on the study type. Similarly, the semiconductors are modeled in both the electrical and thermal domains of PLECS. A digital controller is used to control the active power flow, generate the references, and perform the capacitor balancing (in the case of multilevel converters).

3.5 Experimental system

An experimental setup is prepared to validate the developed theories. Figure 3.1 shows an overview of the whole system. The prototype is downscaled 3ϕ DAB with a 2LC converter on one side and a CTB converter with two submodules per leg on the other. The dc-links are fed from two bidirectional dc power supplies, and the converters are interconnected with a re-configurable MFT. The circuit diagram of the prototype is shown in Figure 3.2.

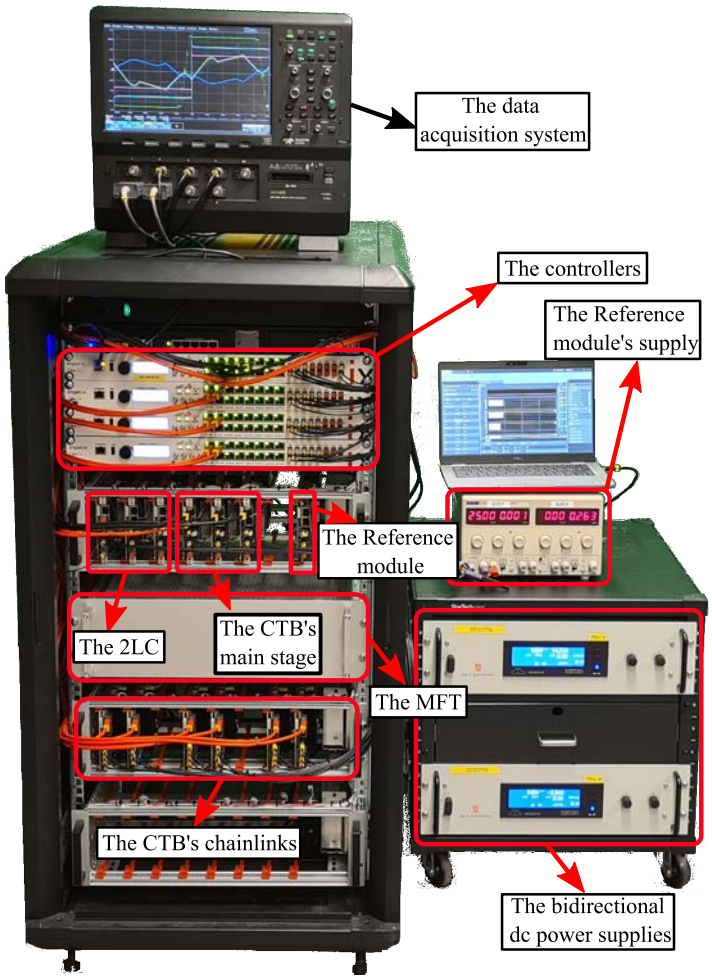

Figure 3.1: The down-scaled prototype used for the theory validation.

Components and ratings

The converter is set up using components with different ratings. The 3ϕ MFT is assembled from three custom-made 1ϕ transformers. The power electronics stage comprises three sets of half-bridge and full-bridge submodules,

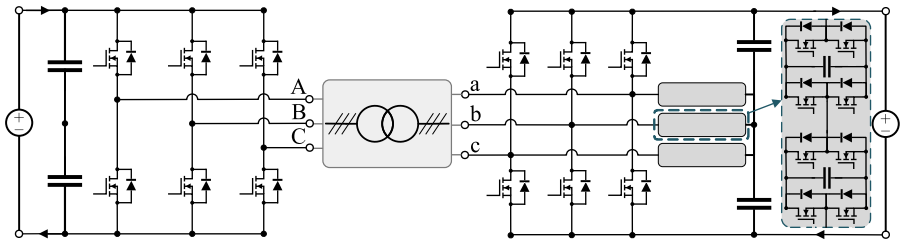

Figure 3.2: The circuit diagram of the down-scaled prototype.

PEB8038, PEH2015, and PEB8024, from Imperix power electronics. These modules are interconnected to build the topology shown in Figure 3.2. The dc-links of the converter are fed from two bidirectional SM1500-CP-30 dc power supplies through precharge circuits. The converter and power supplies are controlled using four B-Box controllers from Imperix power electronics. More information about these components is summarized in the following sections.

Bidirectional dc power supplies

Two bidirectional SM1500-CP-30 dc power supplies from Delta Elektronika form the primary and secondary dc-links [42] [see Figure 3.1]. These power supplies can provide up to 15 kW of power at 1.5 kV with ±30 A. Whenever either of the limits is reached, these operate with constant power, voltage, or current depending on the limiting variable. The outputs of the power supplies are connected to the converters using precharge circuits and are controlled remotely with a PC using the TCP/IP protocol.

Precharge circuits

Precharge circuits are used to avoid large inrush currents during the initial charging and final discharging of dc-links' and submodules' capacitors. The input from the dc power supply is fed to Imperix current and voltage sensors first. These signals are used for control purposes. A power resistor connects the output of the current sensor to the converter during the charging and discharging stages. After these stages are finished, the resistor is bypassed using a contactor and a relay.

Two-level converters

Generally, a 3ϕ 2LC converter is formed using three half-bridge legs. Both the 2LC converter and the two-level stage of the CTB converter are made using three PEB8038 half-bridge submodules from Imperix power electronics [43]. The dc-links of three PEB8038 submodules are parallel connected together and are fed from the precharge circuit. The ac-links are directly connected to the terminals of the MFT. Onboard voltage and current sensors feedback the dc-link voltage and the ac-link current to the controller for control and monitoring purposes.

These submodules are rated for a dc-link voltage of 800 V, maximum continuous leg current of 38 A at 20 kHz switching frequency, and maximum pulsed leg current of 80 A. The gate signals are delivered by fiber optics from a controller, and a minimum dead time of 500 ns are considered.

CTB converter

As mentioned, the two-level stages of the CTB converter are built from PEB8038 half-bridge submodules. The chain-links are made using PEH2015 full-bridge submodules from Imperix power electronics [44]. Only two submodules are used per leg of the converter due to the limitation of available pulse width modulation (PWM) signals. The dc-link voltages are measured using onboard voltage sensors and are fed back to the controller for capacitor balancing.

These submodules are rated for a dc-link voltage of 200 V, maximum continuous leg current of 15 A at 10 kHz switching frequency, and maximum pulsed leg current of 56 A. The gate signals are delivered by fiber optics from a controller, and a minimum dead time of 400 ns are considered.

Reference module

A reference submodule is used to keep track of different measurements, record exact switching instances, and trigger the data acquisition system consistently. A PEB8024 silicon carbide (SiC) half-bridge submodule from Imperix power electronics is used as the reference module [45]. The dc-link of this submodule is fed with 25 V isolated dc power supply, and the ac-link is left open. A minimum dead time of 150 ns is considered for the module. Since the submodule is not feeding any load, the rising edge of the ac terminal to the midpoint of the dc-link can be used to identify the exact turn-ON instant of the modules'

switches.

Medium frequency transformer

Figure 3.3 shows the MFT used in the prototype. As can be seen, three 1ϕ transformers with ring cores are used inside the box to form the 3ϕ MFT. The transformers are designed for 25 kHz fundamental frequency. The cores are made of Vitroperm500F—a nanocrystalline material from Vacuumschmelze [46]. The LV and high voltage (HV) windings have 15 and 30 turns, respectively. Moreover, the HV-side is rated for 700 V dc-link voltage and 50 A RMS current.

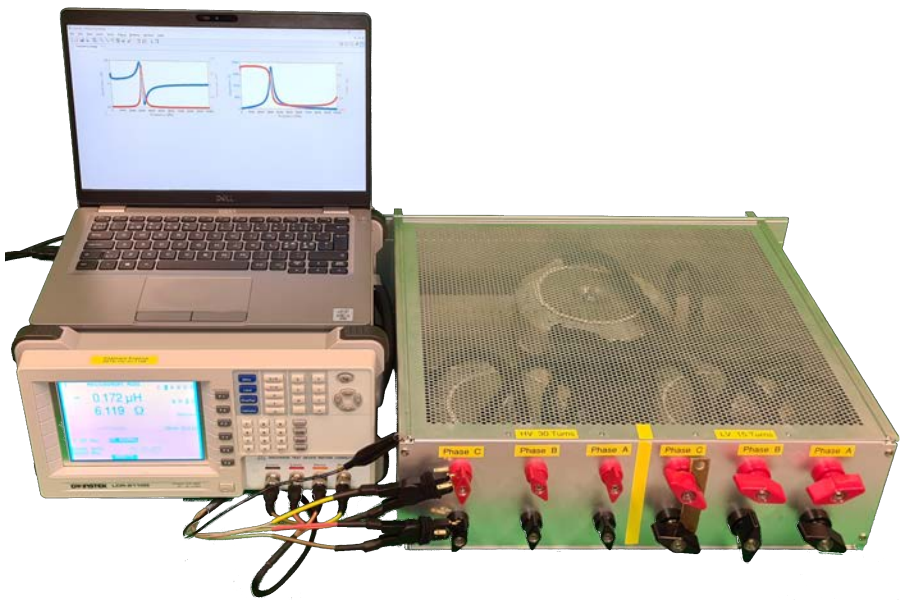

Figure 3.3: Impedance measurement setup of MFT.

As shown in Figure 3.3, a GW Instek 8110G LCR meter is used to characterize the transformers. The terminals of LV windings are short-circuited one at a time, and the impedance is measured from the HV side. Assuming that the magnetizing impedance is infinite, the resulting impedance is the sum of total leakage inductance and series ac resistance. Figure 3.4a shows the results of these measurements. As can be seen, the leakage inductance of phase

A is lower than the other two phases. This is compensated later with external inductors. The impedance of the magnetizing branch is also measured for

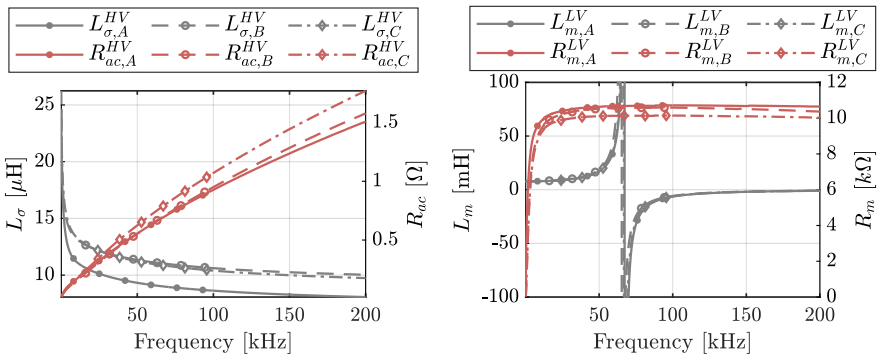

Figure 3.4: Impedance measurements of the MFT shown in Figure 3.3. **(a)** Measured on the HV-side with the LV-side short-circuited. **(b)** Measured on the LV-side with open circuit HV-side.

modeling purposes. This test is done by measuring on the LV side and leaving the HV side terminals open. Figure 3.4b shows the results of these tests.

External inductors

The MFTs are designed for 25 kHz fundamental frequency. With this switching frequency, the dead time of submodules becomes comparable with the fundamental period. For the CTB stage, the sum of all dead times for the three phases amounts to 24 % of the fundamental period. To avoid distortion of the waveforms, the switching frequency is reduced by five times. This means the reactance will be five times lower, and the current will be approximately five times higher (in the worst case) for a given phase shift between the converters. A set of external inductors are used in series with the MFTs to extend the phase shift range of the converter and limit the current peak. Depending on the study, a different set of inductors are used. The inductors are designed using Ferrite cores with air gaps to avoid saturation and have low core losses.

Converter control and modulation

Four B-Box controllers from Imperix power electronics [47] are used to control the converter. The controllers are daisy-chained, with one master and three slaves. The master controller itself is supervised at a higher level using a PC. The PC sends the reference values to the master controller and gets feedback on the system status for monitoring. Voltage and current feedback from different circuit parts are collected using RJ45 cables to these controllers. The control algorithm runs on the master unit, and the PWM duty cycles and phase shifts are propagated to the slaves. These electrical signals are converted into optical and transmitted to the submodules to control the gate drivers.

The basic control algorithm consists of an active power controller, a capacitor balancing algorithm for the CTB converter, and a state machine to observe and control the converter. Different extra control blocks are added depending on the nature of the study. The capacitor balancing algorithm is always active, ensuring that the submodules of the CTB converter are balanced. The state machine controls the start-up, shut-down and operating stages. Moreover, several layers of protection are implemented to ensure proper operation.

Start-up stage

The activation command is sent from the PC to the master controller. The state machine steps to the pre-charging stage and transmits the reference dc-links voltages to the PC. The PC controls the dc power supplies and slowly increases the dc-link voltages. When the steady state is reached, the precharge resistors are bypassed, and the converter is ready to operate.

Shut-down stage

The deactivation command is sent from the PC to the master controller. The state machine steps to the shut-down stage. The power reference slowly reduces to zero. Afterward, the precharge resistors are inserted into the circuit, and the dc power supplies slowly reduce their output. The converter shuts down after all the capacitors are discharged.

Measuring system

Two sets of measuring systems are used. One for controlling the converter and the other for data acquisition. For the former, the onboard voltage and current sensors of Imperix submodules are used along with a set of external current and voltage sensors from the same company. For the data acquisition, a set of differential voltage and clamp-on current probes are used.

Current sensors

The currents are measured with AP015 current probes from Teledyne Lecroy [48]. These probes can measure both dc signals up to ±30 A, and ac signals up to ±50 A. The probes have a high bandwidth 50 MHz and a sensitivity between 10 mA/div and 20 A/div.

Voltage sensors

Different differential probes are used to measure voltages. These include

- AP031 700 V, 25 MHz high-voltage differential probe [49].
- TA043 700 V, 100 MHz differential oscilloscope probe [50].
- TT-SI 9101 700 V, 100 MHz active differential probe [51].

Data acquisition unit

An MDA805 500 MHz 12-bit 8-channel motor drive analyzer from Teledyne Lecroy is used as the data acquisition unit. For all the measurements, the system is triggered on the rising edge of the reference modules' ac-link voltage. This ensures that the reference point is independent of the converter load level. Moreover, the switching instants can be easily identified. The signals are sampled with 2.5 GS/s without pre-filtering. In the post-processing phase, a moving average window filter is used to filter high-frequency noise from the measured signals.

The data is collected from the MDA805, Imperix control system, and the internal measurement units of the dc power supplies for post-processing. These measurements are automated. The PC sends the reference values to the converter and the dc power supplies. After a steady state is reached, the data

acquisition unit activates. Each channel is scaled to fit the full screen to reduce noise and increase accuracy. Afterward, a single trigger is used to acquire data from all the channels.

CHAPTER 4

Converters Modeling

This chapter provides theoretical bases and mathematical models for the analysis of the converters discussed in Chapter 2. The models developed here will be used in all subsequent chapters. Refer to Chapter 2 for the conventions.

4.1 Voltage waveforms

Voltages of M-level-to-N-level DAB converters (ML-NL-DAB) with different winding configurations are modeled in this section.

Phase-to-ground voltage waveforms

To simplify the later studies, the waveforms will be represented with Fourier series. The Fourier series of a square wave with amplitude U, a phase offset of α, and $4\theta_k$ zero level, $v_{k\mathrm{G}}(\omega t)$, can be derived as

$$v_{k\mathrm{G}}(\omega t) = \sum_{H=1}^{\infty} \left(\frac{4U}{H\pi} \sin(H(\omega t + \alpha)) \cos(H\theta_k) \right) \tag{4.1}$$

where $H \in \{2h-1 | h \in \mathbb{N}\}$ is the harmonic order. A staircase waveform with M levels can be represented by a linear summation of M square waves, where each square wave has $4\theta_k$ (where $k \in \{0, ..., M-1\}$) duration of zero level voltage. Therefore, the P2G voltages of Figure. 2.5, $v_{x\mathrm{G}}$, can be expressed in the form of the Fourier series as

$$v_{x\mathrm{G}}(\omega t) = \sum_{H=1}^{\infty} \sum_{k=0}^{M-1} \left(\frac{4U}{H\pi} \sin(H(\omega t + \alpha)) \cos(H\theta_k) \right) \tag{4.2}$$

where $H \in \{2h-1 | h \in \mathbb{N}\}$ is the harmonic order, $\alpha \in \{0, -2\pi/3, 2\pi/3\}$ is the phase offset of each phase, and $(x, \alpha) \in \{(A, 0), (B, -2\pi/3), (C, 2\pi/3)\}$.

In some multilevel converters (i.e., MMC and TAC with five submodules per arm), the amplitude of the first step (for $\theta_0 = 0$) is half of the others. To take this into account for these converters M should be redefined as $M \equiv \lceil 0.5 N_{\mathrm{sm}} \rceil$. Also, (2.1b) should be modified to $\theta_k = k\psi$, where $k \in \{0, ..., M-1\}$. Finally, (4.2) should be modified to

$$v_{x\mathrm{G}}(\omega t) = \sum_{H=1}^{\infty} \sum_{k=0}^{M-1} \left(\frac{4U(1 - 0.5\delta_{\theta_k})}{H\pi} \sin(H(\omega t + \alpha)) \cos(H\theta_k) \right) \tag{4.3}$$

where δ_{θ_k} is Kronecker delta defined in (A.1). This case will be disregarded from the derived equations hereafter. Whenever it is necessary, U can be replaced with $U(1 - 0.5\delta_{\theta_k})$ in the equations to consider this case.

Phase-to-neutral voltage waveforms

If the converter is connected to a star-connected balanced impedance and the midpoint of the star connection (neutral) is not grounded, then the N2G voltage, v_{NG}, can be calculated as

$$v_{\mathrm{NG}}(\omega t) = \frac{v_{A\mathrm{G}}(\omega t) + v_{B\mathrm{G}}(\omega t) + v_{C\mathrm{G}}(\omega t)}{3}. \tag{4.4}$$

Subsequently, the P2N voltage of phase x, $v_{x\mathrm{N}}$, where $x \in \{\mathrm{A,B,C}\}$, can be calculated from $v_{x\mathrm{N}}(\omega t) = v_{x\mathrm{G}}(\omega t) - v_{\mathrm{NG}}(\omega t)$ as

$$v_{x\mathrm{N}}(\omega t) = \sum_{H=1}^{\infty} \sum_{k=0}^{M-1} \left(\frac{4U}{H\pi} \sin(H(\omega t + \alpha)) \cos(H\theta_k) \right) \tag{4.5}$$

where $H \in \{2h-1 | h \in \mathbb{N},\ 3 \nmid 2h-1\}$ and $(x, \alpha) \in \{(A,0),(B,-2\pi/3),(C,2\pi/3)\}$. Equation (4.5) can be written in a closed-form using (A.8) as

$$v_{x\mathrm{N}}(\omega t) = \frac{2U}{\pi} \sum_{k=0}^{M-1} \left(h_2(\omega t + \alpha + \theta_k) + h_2(\omega t + \alpha - \theta_k)\right) \tag{4.6}$$

For certain studies, it is necessary to expand (4.6). Due to the quarter-wave symmetry of (4.6) for $\alpha = 0$, it is enough to expand it only for a quarter of the fundamental cycle, which results in

$$v_{x\mathrm{N}}(\omega t) = \frac{U}{3} \begin{cases} 0 & 0 \le \omega t + \alpha \le \theta_0 \\ 2k & \begin{cases} \theta_{k-1} \le \omega t + \alpha \le \theta_k, \\ \forall k \in \{1, ..., M-1\} \end{cases} \\ 2M & \theta_{M-1} \le \omega t + \alpha \le \frac{\pi}{3} - \theta_{M-1} \\ 2M + k & \begin{cases} \frac{\pi}{3} - \theta_{M-k} \le \omega t + \alpha \le \frac{\pi}{3} - \theta_{M-k-1}, \\ \forall k \in \{1, ..., M-1\} \end{cases} \\ 3M & \frac{\pi}{3} - \theta_0 \le \omega t + \alpha \le \frac{\pi}{3} + \theta_0 \\ 3M + k & \begin{cases} \frac{\pi}{3} + \theta_{k-1} \le \omega t + \alpha \le \frac{\pi}{3} + \theta_k, \\ \forall k \in \{1, ..., M-1\} \end{cases} \\ 4M & \frac{\pi}{3} + \theta_{M-1} \le \omega t + \alpha \le \frac{\pi}{2} \end{cases} \tag{4.7}$$

where $(x, \alpha) \in \{(A,0),(B,-2\pi/3),(C,2\pi/3)\}$.

Phase-to-phase voltage waveforms

The P2P voltages can be calculated using P2G voltages as

$$v_{xy}(\omega t) = \sum_{H=1}^{\infty} \sum_{k=0}^{M-1} \left(\frac{8U}{H\pi} \cos\Big(H(\omega t + \alpha - \frac{\pi}{3})\Big) \sin\left(\frac{H\pi}{3}\right) \cos(H\theta_k) \right) \tag{4.8}$$

where $H \in \{2h-1 | h \in \mathbb{N},\ 3 \nmid 2h-1\}$ and $(xy, \alpha) \in \{(AB,0),(BC,-2\pi/3),(CA,2\pi/3)\}$. The P2P voltages can also be expressed in piecewise linear form using (4.8) and (A.8) as

$$v_{xy}(\omega t) = \frac{2U}{\pi} \sum_{k=0}^{M-1} \Big(h_2(\omega t + \alpha + \theta_k) - h_2(\omega t + \alpha + \theta_k - \frac{2\pi}{3}) + h_2(\omega t + \alpha - \theta_k) - h_2(\omega t + \alpha - \theta_k - \frac{2\pi}{3}) \Big) \tag{4.9}$$

where $(xy, \alpha) \in \{(AB, 0), (BC, -2\pi/3), (CA, 2\pi/3)\}$. Due to the quarter-wave symmetry of (4.9) along $\omega t = -\pi/6$ for $\alpha = 0$, it is enough to expand the equation only for a quarter of the fundamental cycle, which results in

$$v_{xy}(\omega t) = U \begin{cases} 0 & -\frac{\pi}{6} \leq \omega t + \alpha \leq -\theta_{M-1} \\ k & \begin{cases} -\theta_{M-k} \leq \omega t + \alpha \leq -\theta_{M-k-1}, \\ \forall k \in \{1, ..., M-1\} \end{cases} \\ M & -\theta_0 \leq \omega t + \alpha \leq \theta_0 \\ M+k & \begin{cases} \theta_{k-1} \leq \omega t + \alpha \leq \theta_k, \\ \forall k \in \{1, ..., M-1\} \end{cases} \\ 2M & \theta_{M-1} \leq \omega t + \alpha \leq \frac{\pi}{3} \end{cases} \tag{4.10}$$

where $(xy, \alpha) \in \{(AB, 0), (BC, -2\pi/3), (CA, 2\pi/3)\}$.

4.2 Current waveforms

For different winding configurations, the MFT is modeled with the series leakage inductance either on the primary side, L_σ^{p}, or on the secondary side, L_σ^{s}.

YY-connected DAB

The phase currents of the 3ϕ-YY-DAB can be calculated as

$$i_{\mathrm{L}A}^{\mathrm{YY}}(\omega t) \equiv i_{\phi A}^{\mathrm{YY}}(\omega t) = \frac{v_{AN}(\omega t) - v_{an}^{\mathrm{p}}(\omega t - \varphi)}{j\omega L_\sigma^{\mathrm{p}}} \tag{4.11a}$$

$$i_{\mathrm{L}a}^{\mathrm{YY}}(\omega t) \equiv i_{\phi a}^{\mathrm{YY}}(\omega t) = \frac{N_{\mathrm{p}}}{N_{\mathrm{s}}} i_{\phi A}^{\mathrm{YY}}(\omega t) \tag{4.11b}$$

where $\varphi \in [0, \pi/2]$ and N_j, $j \in \{\mathrm{p}, \mathrm{s}\}$ is the number of winding turns. The primary line currents can be calculated using (4.5), and (4.11a) as

$$\begin{aligned} i_{\mathrm{L}x}^{\mathrm{YY}} = &\sum_{H=1}^{\infty} \sum_{k=0}^{M_{\mathrm{s}}-1} \left(\frac{4U_{\mathrm{s}} N_{\mathrm{p}} \cos(H\theta_k)}{N_{\mathrm{s}} H^2 \pi \omega L_{\sigma}^{\mathrm{p}}} \cos(H(\omega t + \alpha - \varphi)) \right) \\ &- \sum_{H=1}^{\infty} \sum_{k=0}^{M_{\mathrm{p}}-1} \left(\frac{4U_{\mathrm{p}} \cos(H\theta_k)}{H^2 \pi \omega L_{\sigma}^{\mathrm{p}}} \cos(H(\omega t + \alpha)) \right) \end{aligned} \tag{4.12}$$

where $H \in \{2h-1 | h \in \mathbb{N},\ 3 \nmid 2h-1\}$, $(x, \alpha) \in \{(A, 0), (B, -2\pi/3), (C, 2\pi/3)\}$.

YΔ-connected DAB

The phase currents of the 3ϕ-YΔ-DAB can be calculated as

$$i_{\mathrm{L}A}^{\mathrm{Y}\Delta}(\omega t) \equiv i_{\phi A}^{\mathrm{Y}\Delta}(\omega t) = \frac{v_{AN}(\omega t) - v_{ab}^{\mathrm{p}}(\omega t - \varphi)}{j\omega L_{\sigma}^{\mathrm{p}}} \tag{4.13a}$$

$$i_{\phi a}^{\mathrm{Y}\Delta}(\omega t) = \frac{N_{\mathrm{p}}}{N_{\mathrm{s}}} i_{\phi A}^{\mathrm{Y}\Delta}(\omega t) \tag{4.13b}$$

$$\begin{aligned} i_{\mathrm{L}a}^{\mathrm{Y}\Delta}(\omega t) &= i_{\phi a}^{\mathrm{Y}\Delta}(\omega t) - i_{\phi c}^{\mathrm{Y}\Delta}(\omega t) \\ &= \frac{N_{\mathrm{p}}}{N_{\mathrm{s}}} \left(i_{\mathrm{L}A}^{\mathrm{Y}\Delta}(\omega t) - i_{\mathrm{L}A}^{\mathrm{Y}\Delta}(\omega t + 2\pi/3) \right) \end{aligned} \tag{4.13c}$$

where $\varphi \in [0, \pi/2]$. The open form of primary line currents can be calculated using (4.5), (4.8), and (4.13a) as

$$\begin{aligned} i_{\mathrm{L}x}^{\mathrm{Y}\Delta} = &\sum_{H=1}^{\infty} \sum_{k=0}^{M_{\mathrm{s}}-1} \left(\frac{4U_{\mathrm{s}} N_{\mathrm{p}} \cos(H\theta_k)}{N_{\mathrm{s}} H^2 \pi \omega L_{\sigma}^{\mathrm{p}}} \cos\left(H(\omega t + \alpha - \varphi - \frac{\pi}{6}) \right) \right) \\ &- \sum_{H=1}^{\infty} \sum_{k=0}^{M_{\mathrm{s}}-1} \left(\frac{4U_{\mathrm{s}} N_{\mathrm{p}} \cos(H\theta_k)}{N_{\mathrm{s}} H^2 \pi \omega L_{\sigma}^{\mathrm{p}}} \cos\left(H(\omega t + \alpha - \varphi - \frac{5\pi}{6}) \right) \right) \\ &- \sum_{H=1}^{\infty} \sum_{k=0}^{M_{\mathrm{p}}-1} \left(\frac{4U_{\mathrm{p}} \cos(H\theta_k)}{H^2 \pi \omega L_{\sigma}^{\mathrm{p}}} \cos(H(\omega t + \alpha)) \right) \end{aligned} \tag{4.14}$$

where $H \in \{2h-1 | h \in \mathbb{N},\ 3 \nmid 2h-1\}$,$(x, \alpha) \in \{(A, 0), (B, -2\pi/3), (C, 2\pi/3)\}$. Similarly, the open form of secondary line currents can be calculated as

$$\begin{aligned} i_{\mathrm{L}x}^{\mathrm{Y}\Delta} = & \sum_{H=1}^{\infty} \sum_{k=0}^{M_{\mathrm{s}}-1} \left(\frac{12U_{\mathrm{s}} \cos(H\theta_k)}{H^2 \pi \omega L_{\sigma}^{\mathrm{s}}} \cos\Big(H(\omega t + \alpha - \varphi - \frac{\pi}{6})\Big) \right) \\ & - \sum_{H=1}^{\infty} \sum_{k=0}^{M_{\mathrm{p}}-1} \left(\frac{4U_{\mathrm{p}} N_{\mathrm{s}} \cos(H\theta_k)}{N_{\mathrm{p}} H^2 \pi \omega L_{\sigma}^{\mathrm{s}}} \cos(H(\omega t + \alpha)) \right) \\ & + \sum_{H=1}^{\infty} \sum_{k=0}^{M_{\mathrm{p}}-1} \left(\frac{4U_{\mathrm{p}} N_{\mathrm{s}} \cos(H\theta_k)}{N_{\mathrm{p}} H^2 \pi \omega L_{\sigma}^{\mathrm{s}}} \cos\Big(H(\omega t + \alpha + \frac{2\pi}{3})\Big) \right) \end{aligned} \tag{4.15}$$

where $H \in \{2h-1 | h \in \mathbb{N},\ 3 \nmid 2h-1\}$, $(x, \alpha) \in \{(a, 0), (b, -2\pi/3), (c, 2\pi/3)\}$.

ΔY-connected DAB

The phase currents of the 3ϕ-ΔY-DAB can be calculated as

$$i_{\mathrm{L}a}^{\Delta\mathrm{Y}}(\omega t) \equiv i_{\phi a}^{\Delta\mathrm{Y}}(\omega t) = \frac{v_{AB}^{\mathrm{s}}(\omega t) - v_{an}(\omega t - \varphi)}{j\omega L_{\sigma}^{\mathrm{s}}} \tag{4.16a}$$

$$i_{\phi A}^{\Delta\mathrm{Y}}(\omega t) = \frac{N_{\mathrm{s}}}{N_{\mathrm{p}}} i_{\phi a}^{\Delta\mathrm{Y}}(\omega t) \tag{4.16b}$$

$$\begin{aligned} i_{\mathrm{L}A}^{\Delta\mathrm{Y}}(\omega t) &= i_{\phi A}^{\Delta\mathrm{Y}}(\omega t) - i_{\phi C}^{\Delta\mathrm{Y}}(\omega t) \\ &= \frac{N_{\mathrm{s}}}{N_{\mathrm{p}}} \left(i_{\mathrm{L}a}^{\Delta\mathrm{Y}}(\omega t) - i_{\mathrm{L}a}^{\Delta\mathrm{Y}}(\omega t + 2\pi/3) \right) \end{aligned} \tag{4.16c}$$

where $\varphi \in [0, \pi/2]$ is the phase shift between the secondary-side-referred primary side phase voltage (v_{AB}^{s}) and the secondary side phase voltage of the MFT. The open form of secondary line currents can be calculated using (4.5), (4.8), and (4.16a) as

$$\begin{aligned} i_{\mathrm{L}x}^{\Delta\mathrm{Y}} = & \sum_{H=1}^{\infty} \sum_{k=0}^{M_{\mathrm{s}}-1} \left(\frac{4U_{\mathrm{s}} \cos(H\theta_k)}{H^2 \pi \omega L_{\sigma}^{\mathrm{s}}} \cos\Big(H(\omega t + \alpha - \varphi + \frac{\pi}{6})\Big) \right) \\ & - \sum_{H=1}^{\infty} \sum_{k=0}^{M_{\mathrm{p}}-1} \left(\frac{4U_{\mathrm{p}} N_{\mathrm{s}} \cos(H\theta_k)}{N_{\mathrm{p}} H^2 \pi \omega L_{\sigma}^{\mathrm{s}}} \cos(H(\omega t + \alpha)) \right) \end{aligned}$$

$$+\sum_{H=1}^{\infty}\sum_{k=0}^{M_\mathrm{p}-1}\left(\frac{4U_\mathrm{p}N_\mathrm{s}\cos(H\theta_k)}{N_\mathrm{p}H^2\pi\omega L_\sigma^\mathrm{s}}\cos\Big(H(\omega t+\alpha-\frac{2\pi}{3})\Big)\right) \tag{4.17}$$

where $H\in\{2h-1|h\in\mathbb{N},\ 3\nmid 2h-1\}$, $(x,\alpha)\in\{(a,0),(b,-2\pi/3),(c,2\pi/3)\}$. Similarly, the open form of primary line currents can be calculated

$$\begin{aligned}i_{\mathrm{L}x}^{\Delta\mathrm{Y}} =&\sum_{H=1}^{\infty}\sum_{k=0}^{M_\mathrm{s}-1}\left(\frac{4N_\mathrm{p}U_\mathrm{s}\cos(H\theta_k)}{N_\mathrm{s}H^2\pi\omega L_\sigma^\mathrm{p}}\cos\Big(H(\omega t+\alpha-\varphi+\frac{\pi}{6})\Big)\right)\\ &-\sum_{H=1}^{\infty}\sum_{k=0}^{M_\mathrm{s}-1}\left(\frac{4N_\mathrm{p}U_\mathrm{s}\cos(H\theta_k)}{N_\mathrm{s}H^2\pi\omega L_\sigma^\mathrm{p}}\cos\Big(H(\omega t+\alpha-\varphi+\frac{5\pi}{6})\Big)\right)\\ &-\sum_{H=1}^{\infty}\sum_{k=0}^{M_\mathrm{p}-1}\left(\frac{12U_\mathrm{p}\cos(H\theta_k)}{H^2\pi\omega L_\sigma^\mathrm{p}}\cos(H(\omega t+\alpha))\right)\end{aligned} \tag{4.18}$$

where $H\in\{2h-1|h\in\mathbb{N},\ 3\nmid 2h-1\}$, $(x,\alpha)\in\{(A,0),(B,-2\pi/3),(C,2\pi/3)\}$.

4.3 RMS value of the currents

The RMS of current $i(\omega t)$ can be calculated as

$$I_\mathrm{RMS}=\sqrt{\frac{1}{2\pi}\int_0^{2\pi}\left(i(\omega t)\right)^2\mathrm{d}\omega t}. \tag{4.19}$$

Let's define $u_{H\mathrm{p}}$ and $u_{H\mathrm{s}}$ as

$$u_{Hj}=\sum_{k=0}^{M_j-1}\left(U_j\cos(H\theta_k)\right),\qquad \forall j\in\{\mathrm{p},\mathrm{s}\}. \tag{4.20}$$

Applying (4.19) on (4.12), (4.14), and (4.18) results in

$$I_{\phi\mathrm{p,RMS}}^{\mathrm{YY}}=\frac{\sqrt{8}}{\pi\omega L_\sigma^\mathrm{p}}\times\sqrt{\sum_{H=1}^{\infty}\frac{\left(u_{H\mathrm{p}}\right)^2+\left(\frac{N_\mathrm{p}u_{H\mathrm{s}}}{N_\mathrm{s}}\right)^2-\frac{2N_\mathrm{p}u_{H\mathrm{p}}u_{H\mathrm{s}}}{N_\mathrm{s}}\cos(H\varphi)}{H^4}} \tag{4.21a}$$

$$I_{\phi\mathrm{p,RMS}}^{\mathrm{Y}\Delta} = \frac{\sqrt{8}}{\pi\omega L_{\sigma}^{\mathrm{p}}} \times \sqrt{\sum_{H=1}^{\infty} \frac{\left(u_{H\mathrm{p}}\right)^2 + 3\left(\frac{N_{\mathrm{p}} u_{H\mathrm{s}}}{N_{\mathrm{s}}}\right)^2 - \frac{4N_{\mathrm{p}} u_{H\mathrm{p}} u_{H\mathrm{s}}}{N_{\mathrm{s}}}\gamma_H(\varphi)}{H^4}} \tag{4.21b}$$

$$I_{\phi\mathrm{s,RMS}}^{\Delta\mathrm{Y}} = \frac{\sqrt{8}}{\pi\omega L_{\sigma}^{\mathrm{s}}} \times \sqrt{\sum_{H=1}^{\infty} \frac{\left(u_{H\mathrm{s}}\right)^2 + 3\left(\frac{N_{\mathrm{s}} u_{H\mathrm{p}}}{N_{\mathrm{p}}}\right)^2 - \frac{4N_{\mathrm{s}} u_{H\mathrm{p}} u_{H\mathrm{s}}}{N_{\mathrm{p}}}\gamma_H(\varphi)}{H^4}} \tag{4.21c}$$

where $H \in \{2h-1 | h \in \mathbb{N},\ 3 \nmid 2h-1\}$, and $\gamma_H(\varphi)$ is defined as

$$\gamma_H(\varphi) \triangleq \sin\left(\frac{H\pi}{3}\right) \sin\left(\frac{H\pi}{2}\right) \cos(H\varphi). \tag{4.22}$$

4.4 Instantaneous and average active power

The 3ϕ instantaneous power can be calculated from instantaneous phase voltages and phase currents as [52]

$$P_{3\phi}(\omega t) = \sum_{x\in\{A,B,C\}} v_{\phi x}(\omega t)\, i_{\phi x}(\omega t). \tag{4.23}$$

Using Fryze's approach, the active power for a 3ϕ balanced system can be calculated as

$$P_{3\phi} = \frac{1}{2\pi}\int_0^{2\pi} P_{3\phi}(\omega t)\,\mathrm{d}\omega t = \frac{3}{2\pi}\int_0^{2\pi} v_{\phi x}(\omega t)\, i_{\phi x}(\omega t)\,\mathrm{d}\omega t. \tag{4.24}$$

Therefore, the active power for DABs can be calculated from (4.24) as

$$P_{3\phi}^{\mathrm{YY}} = \frac{3}{2\pi}\int_0^{2\pi} v_{AN}(\omega t)\, i_{\phi A}^{\mathrm{YY}}(\omega t)\,\mathrm{d}\omega t \tag{4.25a}$$

$$P_{3\phi}^{\mathrm{Y}\Delta} = \frac{3}{2\pi}\int_0^{2\pi} v_{AN}(\omega t)\, i_{\phi A}^{\mathrm{Y}\Delta}(\omega t)\,\mathrm{d}\omega t \tag{4.25b}$$

$$P_{3\phi}^{\Delta\mathrm{Y}} = \frac{3}{2\pi}\int_0^{2\pi} v_{an}(\omega t)\, i_{\phi a}^{\Delta\mathrm{Y}}(\omega t)\,\mathrm{d}\omega t. \tag{4.25c}$$

Substituting the currents and voltages from (4.5), (4.12), (4.14), and (4.17) and calculating the integrals results in

$$P_{3\phi}^{\mathrm{YY}} = \frac{24N_{\mathrm{p}}}{N_{\mathrm{s}}\pi^2\omega L_{\sigma}^{\mathrm{p}}} \sum_{H=1}^{\infty} \frac{u_{H\mathrm{p}} u_{H\mathrm{s}} \sin(H\varphi)}{H^3} \tag{4.26a}$$

$$P_{3\phi}^{\mathrm{Y\Delta}} = \frac{48N_{\mathrm{p}}}{N_{\mathrm{s}}\pi^2\omega L_{\sigma}^{\mathrm{p}}} \sum_{H=1}^{\infty} \frac{u_{H\mathrm{p}} u_{H\mathrm{s}} \sin\left(\frac{H\pi}{3}\right) \sin\left(\frac{H\pi}{2}\right) \sin(H\varphi)}{H^3} \tag{4.26b}$$

$$P_{3\phi}^{\Delta\mathrm{Y}} = \frac{48N_{\mathrm{s}}}{N_{\mathrm{p}}\pi^2\omega L_{\sigma}^{\mathrm{s}}} \sum_{H=1}^{\infty} \frac{u_{H\mathrm{p}} u_{H\mathrm{s}} \sin\left(\frac{H\pi}{3}\right) \sin\left(\frac{H\pi}{2}\right) \sin(H\varphi)}{H^3}. \tag{4.26c}$$

A $\Delta\Delta$ windings connection can be modeled electrically with a YY connection. If $L_{\sigma}^{\Delta\Delta}$ is the leakage inductance of a $\Delta\Delta$ connected MFT, by applying Δ-Y transformation the equivalent YY MFT is obtained if $L_{\sigma}^{\mathrm{YY}} \equiv L_{\sigma}^{\Delta\Delta}/3$. Replacing this value in (4.12), (4.21a), and (4.26a) will give the line current, RMS current and active power of the $\Delta\Delta$-DAB.

CHAPTER 5

Desired Leakage Inductance Identification

This chapter is based on the following articles

[I] **B. Khanzadeh**, T. Thiringer, M.Kharezy, "Multilevel Dual Active Bridge Leakage Inductance Selection for Various DC-Link Voltage Spans," Published in *Energies*, vol. 16, no. 2, 2023, issn: 1996-1073.

[II] **B. Khanzadeh**, T. Thiringer, and M. Kharezy, "Optimum leakage inductance determination for a Q2L-operating MMC-DAB with different transformer winding configurations," in Proceedings of *20th International Symposium on Power Electronics (Ee)*, 2019, pp. 1–6.

5.1 Introduction

Two important factors in the design of a DAB converter are power density and efficiency. The power density can be improved drastically by reducing the size of passive components like the transformer and capacitors (in the case of a multilevel converter). The MFT is not an off-the-shelf product and should be designed for the specific application to have high power density and efficiency. The design optimization of the MFT can be combined with the converter

design [53] or performed stand-alone with the specifications imposed from the converter side [17], [54]–[61].

The MFT's leakage inductance directly impacts the current waveforms, the power factor, and the converter's performance [7]. Therefore, it can be considered to be a design requirement for the MFT optimization [17], [19], [20], [54]–[63]. The value of desired leakage inductance is used as an input for the optimization of an MFT in [17], [54]–[59]. Its value is selected such that all of the switches achieve turn-ON ZVS at the nominal power of the converter for a given deviation from the nominal dc-link voltages [17], [56]. This method is suitable for applications where the switching losses make up a substantial part of the converter's losses.

If the leakage inductance is selected inappropriately, a small deviation in the dc-link voltages will give huge reactive currents through the converter [19]–[21]. This is important in designing multilevel converters, as the submodule capacitors must be oversized to handle excessive currents. It also is crucial in applications where conduction losses are the main loss component and variable dc-link voltages are required.

In [64], leakage inductance optimization of a 1ϕ conventional DAB is studied for vehicular applications. The phase shift between the two bridges, the leakage inductance, and the dc conversion ratio are swept to find an optimum value of the leakage inductance that minimizes the RMS current. A similar approach is taken in [65] to select the optimum leakage inductance of a 3ϕ multilevel DAB for wind turbine applications. [64], [65] uses a brute-force optimization method, which is computationally demanding and time-consuming.

A leakage inductance optimization methodology is presented in [21] for a 3ϕ conventional DAB and utility applications. It uses the analytical power and current expressions of the 3ϕ DAB with a numerical solver to find the optimum value. Even though the method used in [21] gives the optimum leakage inductance value faster than the brute-force method used in [64], [65], it does not provide a holistic view of the dependency of the leakage inductance on the design parameters. Moreover, if the topologies of the inverters are altered, the method should be adapted to the new topology.

An interesting approach is taken in [19] for a 1ϕ DAB. A closed-form expression is derived for the desired leakage inductance, which results in minimum RMS current for a given variation in the dc-link voltage. This is the fastest method possible which also gives a holistic view of the dependency of the

leakage inductance on the converter parameters. Optimized designs with this method can be found in [62], [63]. Nevertheless, [19] only considers a variation in one of the dc-link voltages and can not be used for applications where both dc-link voltages are variable.

Missing in the available literature is a closed-form equation that provides satisfactory results for the desired leakage inductance of a 3ϕ MFT which results in minimum RMS current for arbitrary variations in both dc-link voltages. Closed-form expressions are derived for the optimum leakage inductance of two- or multilevel 3ϕ-DAB dc-dc converters. Moreover, the accuracy of the solution is evaluated, and the impact of voltage spans on the RMS currents and the leakage inductance is studied. Additionally, the effect of neglecting the ac resistance of the MFT on the optimization results are quantified.

5.2 Formulating leakage inductance optimization

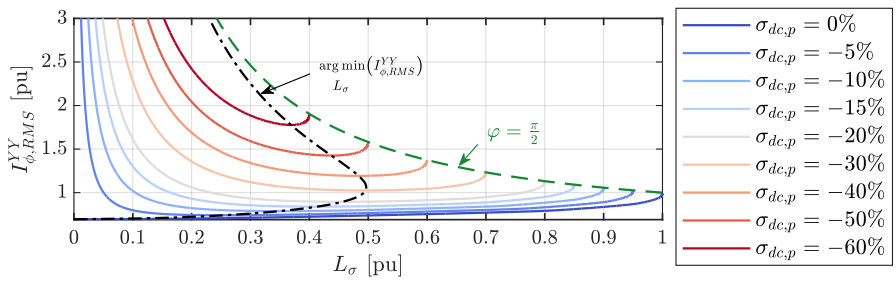

Figure 5.1: Dependency of the RMS value of the phase currents on the leakage inductance for different percentages of deviation in the primary side nominal dc-link voltage, $\sigma_{\mathrm{dc,p}}$, with constant active power.

Figure 5.1 depicts the dependency of the RMS currents of a 3ϕ-YY-DAB, $I^{\mathrm{YY}}_{\phi,\mathrm{RMS}}$, on the leakage inductance for different percentages of deviation from the primary nominal dc-link voltage, $\sigma_{\mathrm{dc,p}}$, while the active power is kept constant at its nominal value. As can be seen, for the operation with fixed dc-link voltage ($\sigma_{\mathrm{dc,p}} = 0\,\%$), the smaller the value of L_σ, the lower the value of $I^{\mathrm{YY}}_{\phi,\mathrm{RMS}}$. Moreover, for any $L_\sigma \in (0, 0.6)\,\mathrm{pu}$, the converter can transfer the nominal power without a large increase in the RMS value of the current. However, for the slightest deviation in the dc-link voltage, huge currents are

required to transfer the nominal power if L_σ is below 0.1 pu. Similarly, if L_σ is too large (e.g., larger than 0.6 pu for $\sigma_{\mathrm{dc,p}} < -40\,\%$), the converter must be derated as the maximum phase shift will be the limiting factor.

For the case shown in Figure 5.1, L_σ can be easily selected because deviations exist only on one of the dc-links. As an example, if a deviation of a maximum of 30 % is expected on the primary side dc-link voltage, the selection of $L_\sigma = 0.5$ pu will ensure that the currents will be kept below 1 pu (as shown in Figure 5.1). Finding an optimum L_σ becomes more complicated for the cases where deviations higher and lower than the nominal dc-link voltage exists on both sides. Therefore, it is necessary to formulate an optimization problem to find the optimum leakage inductance value.

A σ percent deviation in the dc-link voltage of a converter from its nominal value will scale the P2G waveforms of Figure 2.5 by σ percent with respect to their nominal value. Therefore, U will be scaled by σ percent. Let's assume the converter's primary and secondary side voltages have variations in a range of $U_{\mathrm{p}}^{\mathrm{nom}}[(1-\sigma_{\mathrm{dc,p}}^{-}),\ (1+\sigma_{\mathrm{dc,p}}^{+})]$ and $U_{\mathrm{s}}^{\mathrm{nom}}[(1-\sigma_{\mathrm{dc,s}}^{-}),\ (1+\sigma_{\mathrm{dc,s}}^{+})]$, respectively; where $U_{\mathrm{p}}^{\mathrm{nom}}$ and $U_{\mathrm{s}}^{\mathrm{nom}}$ are the nominal values of U_{p} and U_{s}; $\sigma_{\mathrm{dc},j}^{\pm}$, $j \in \{\mathrm{p,s}\}$ are the percentages of deviation in the respective dc-link voltage. Figure 5.2

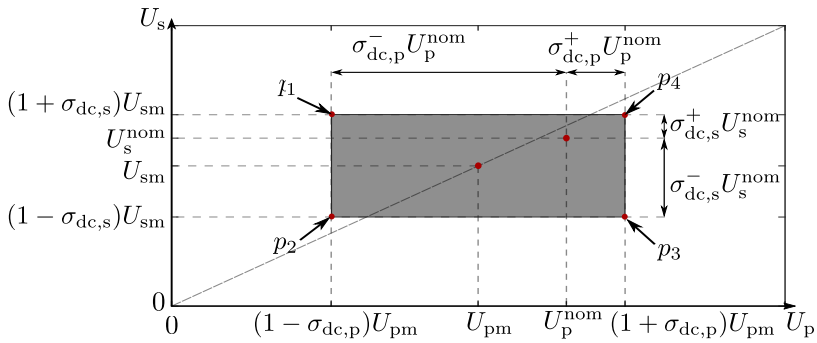

Figure 5.2: The operation region of the converter.

illustrates the operation domain of the converter with the gray-shaded area. This rectangular domain, $\mathcal{O}_{\mathrm{d}}$, can be formulated as

$$\left|\frac{U_{\mathrm{p}}-U_{\mathrm{pm}}}{\sigma_{\mathrm{dc,p}}U_{\mathrm{pm}}}+\frac{U_{\mathrm{s}}-U_{\mathrm{sm}}}{\sigma_{\mathrm{dc,s}}U_{\mathrm{sm}}}\right|+\left|\frac{U_{\mathrm{p}}-U_{\mathrm{pm}}}{\sigma_{\mathrm{dc,p}}U_{\mathrm{pm}}}-\frac{U_{\mathrm{s}}-U_{\mathrm{sm}}}{\sigma_{\mathrm{dc,s}}U_{\mathrm{sm}}}\right|\leq 2. \tag{5.1}$$

where $(U_{\mathrm{pm}}, U_{\mathrm{sm}})$ is the center of the rectangular domain, and $\sigma_{\mathrm{dc,p}}$ and $\sigma_{\mathrm{dc,s}}$ are the deviations from the center given as

$$U_{\mathrm{pm}} = \frac{U_{\mathrm{p}}^{\mathrm{nom}}}{2}\left(2 + \sigma_{\mathrm{dc,p}}^{+} - \sigma_{\mathrm{dc,p}}^{-}\right) \qquad \sigma_{\mathrm{dc,p}} = \frac{\sigma_{\mathrm{dc,p}}^{+} + \sigma_{\mathrm{dc,p}}^{-}}{2 + \sigma_{\mathrm{dc,p}}^{+} - \sigma_{\mathrm{dc,p}}^{-}} \tag{5.2a}$$

$$U_{\mathrm{sm}} = \frac{U_{\mathrm{s}}^{\mathrm{nom}}}{2}\left(2 + \sigma_{\mathrm{dc,s}}^{+} - \sigma_{\mathrm{dc,s}}^{-}\right) \qquad \sigma_{\mathrm{dc,s}} = \frac{\sigma_{\mathrm{dc,s}}^{+} + \sigma_{\mathrm{dc,s}}^{-}}{2 + \sigma_{\mathrm{dc,s}}^{+} - \sigma_{\mathrm{dc,s}}^{-}} \tag{5.2b}$$

The aim is to find the leakage inductance value that minimizes the RMS currents, $I_{\phi,\mathrm{RMS}}$, in $\mathcal{O}_{\mathrm{d}}$ while transferring the nominal power of the converter, $P_{3\phi}^{\mathrm{nom}}$. Therefore, an optimization can be formulated as

$$\begin{aligned} &\arg\min_{L_\sigma \in \mathbb{R}^+} \left(\max_{U_{\mathrm{p}}, U_{\mathrm{s}}} \left(I_{\phi,\mathrm{RMS}} \right) \right) \\ &\text{subject to: } (U_{\mathrm{p}}, U_{\mathrm{s}}) \in \mathcal{O}_{\mathrm{d}}, \\ &\qquad P_{3\phi} = P_{3\phi}^{\mathrm{nom}}. \end{aligned} \tag{5.3}$$

Active power and ac-link currents

The phase A current of a YY-DAB, $i_{\mathrm{L}A}^{\mathrm{YY}}(\omega t)$, can be calculated as

$$\begin{aligned} i_{\mathrm{L}A}^{\mathrm{YY}}(\omega t) = &\sum_{H=1}^{\infty} \frac{4 u_{H\mathrm{p}}}{\pi H \left| Z_H^{\mathrm{p}} \right|} \sin\left(H\omega t - \angle Z_H^{\mathrm{p}} \right) \\ &- \sum_{H=1}^{\infty} \frac{4 N_{\mathrm{p}} u_{H\mathrm{s}}}{\pi N_{\mathrm{s}} H \left| Z_H^{\mathrm{p}} \right|} \sin\left(H(\omega t - \varphi) - \angle Z_H^{\mathrm{p}} \right) \end{aligned} \tag{5.4}$$

where $H \in \{2h-1 | h \in \mathbb{N},\ 3 \nmid 2h-1\}$, Z_H^{p} is the series impedance of the MFT. Moreover,

$$\begin{aligned} \left| Z_H^{\mathrm{p}} \right| &= \sqrt{\left(R_{\mathrm{ac}}^{\mathrm{p}} \right)^2 + \left(H\omega L_\sigma^{\mathrm{p}} \right)^2} \\ \angle Z_H^{\mathrm{p}} &= \tan^{-1}\left(H\omega L_\sigma^{\mathrm{p}} / R_{\mathrm{ac}}^{\mathrm{p}} \right) \end{aligned} \tag{5.5}$$

where L_σ^{p} and $R_{\mathrm{ac}}^{\mathrm{p}}$ are the primary-side-referred leakage inductance and ac resistance of the transformer, respectively. The RMS of the current in (5.4)

can be calculated as

$$I^{\mathrm{YY}}_{\phi\mathrm{p,RMS}} = \sqrt{8\sum_{H=1}^{\infty}\frac{u^2_{H\mathrm{p}} + \left(\frac{N_\mathrm{p}u_{H\mathrm{s}}}{N_\mathrm{s}}\right)^2 - \frac{2N_\mathrm{p}u_{H\mathrm{p}}u_{H\mathrm{s}}}{N_\mathrm{s}}\cos(H\varphi)}{\pi^2 H^2 \left|Z^\mathrm{p}_H\right|^2}} \tag{5.6}$$

and the active power of the converter, $P^{\mathrm{YY}}_{3\phi}$, can be calculated as

$$P^{\mathrm{YY}}_{3\phi} = \sum_{H=1}^{\infty}\frac{24u_{H\mathrm{p}}}{\pi^2 H^2 \left|Z^\mathrm{p}_H\right|}\left(u_{H\mathrm{p}}\cos(\angle Z^\mathrm{p}_H) - \frac{N_\mathrm{p}u_{H\mathrm{s}}}{N_\mathrm{s}}\cos(H\varphi + \angle Z^\mathrm{p}_H)\right). \tag{5.7}$$

Neglecting the ac resistance

The leakage inductance and the ac resistance are measured on two shell-type MFT prototypes, one with Nanocrystalline (MFT_1) and the other with Ferrite (MFT_2) cores. The MFTs are rated for 50 kW, 5 kHz, and 1 kV to 3 kV. More information on the design methodology of MFTs can be found in [8], [56]. The leakage inductance and the ac resistance are measured from the secondary side while the primary side is short-circuited, as shown in Figure 5.3. The measurements are performed in the frequency range of 1 kHz to 40 kHz using an Agilent E4980A RLC meter.

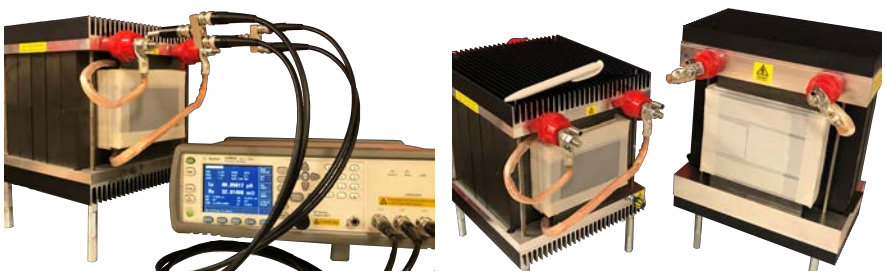

(a) **(b)**

Figure 5.3: Test setup for measuring the leakage inductance and the ac resistance. **(a)** Test setup. **(b)** MFTs.

The ratio of the leakage reactance to the ac resistance is calculated from

the measured leakage inductance and ac resistance and is shown in Figure 5.4. For the fundamental component and operation with 5 kHz, the ratio is 43 and 51 for MFT_1 and MFT_2, respectively. The ratio is above 80 for transformers and the 3^{rd}, 5^{th} and 7^{th} harmonics.

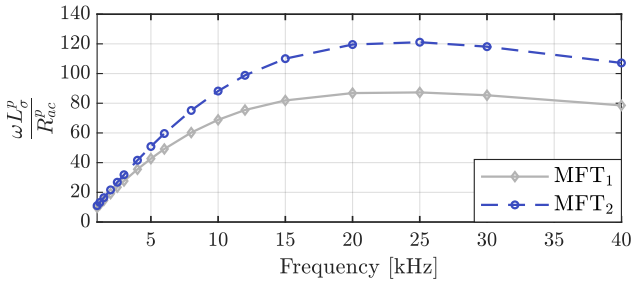

Figure 5.4: The ratio of the leakage reactance to the ac resistance from impedance measurements on the two MFTs.

Figure 5.5 shows the dependency of $\sin(\angle Z_H^{\mathrm{p}})$ and $\cos(\angle Z_H^{\mathrm{p}})$ on the ratio of $\omega L_\sigma^{\mathrm{p}}$ to $R_{\mathrm{ac}}^{\mathrm{p}}$. With an increase in $\omega L_\sigma^{\mathrm{p}}/R_{\mathrm{ac}}^{\mathrm{p}}$, the value of $\sin(\angle Z_H^{\mathrm{p}})$ quickly approaches unity. The rate of decrease of $\cos(\angle Z_H^{\mathrm{p}})$ is much lower compared with $\sin(\angle Z_H^{\mathrm{p}})$, and for $\omega L_\sigma^{\mathrm{p}}/R_{\mathrm{ac}}^{\mathrm{p}} \geq 50$ it can be approximated to be zero. Therefore, the series impedance of the MFT can be approximated with the leakage inductance.

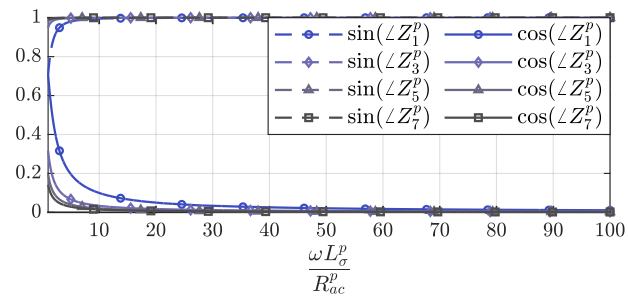

Figure 5.5: Dependencies of $\sin(\angle Z_H^{\mathrm{p}})$ and $\cos(\angle Z_H^{\mathrm{p}})$ on the ratio of $\omega L_\sigma^{\mathrm{p}}$ to $R_{\mathrm{ac}}^{\mathrm{p}}$.

As shown, the MFT's impedance can be approximated with the leakage inductance assuming $\omega L_\sigma^{\mathrm{p}}/R_{\mathrm{ac}}^{\mathrm{p}} \geq 50$. With this assumption (5.6) and (5.7)

simplify to (4.21a) and (4.26a). With the same reasoning, the active power and RMS currents of the YΔ-DAB and ΔY-DAB can be modeled with (4.21b), (4.26b), (4.21c) and (4.26c). By defining $L_\sigma^{\mathrm{p},\Delta\Delta} \triangleq 3L_\sigma^{\mathrm{p},\mathrm{YY}}$ and applying the Y-Δ transformation to the equivalent circuit of the ΔΔ-connected MFT, one can get the same equivalent circuit as the YY-connected MFT. Consequently, (4.21a) and (4.26a) can also be used to model a ΔΔ-DAB. Therefore, ΔΔ-DAB is not analyzed hereafter.

5.3 Numerical solution of the optimization

For each winding configuration, the leakage inductance can be written as a function of active power using (4.26a), (4.26b), or (4.26c). Then (5.3) can be solved numerically by sweeping U_p, U_s, and φ inside their boundaries resulting in a 3D space of operational points. As shown in Figure 5.6, operational points with equal L_σ form iso-surfaces inside this 3D space.

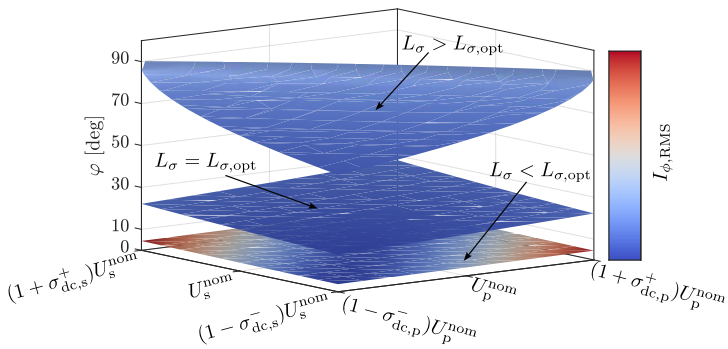

Figure 5.6: The 3D space of $\{U_\mathrm{p}, U_\mathrm{s}, \varphi\}$ with iso-surfaces of L_σ.

The optimum value of the leakage inductance will be the value that, for the available range of φ, ensures the coverage of the whole $U_\mathrm{p}, U_\mathrm{s}$ plane; and simultaneously minimizes the RMS current. As an example, in Figure 5.6, a value of leakage inductance higher than the optimum value does not cover the whole $U_\mathrm{p}, U_\mathrm{s}$ range. In the same figure, the values both higher and lower than the optimum value result in high currents compared to the operation with the optimum leakage inductance, especially in the corners.

5.4 Analytical solution of the optimization

The numerical method is computationally demanding and time-consuming. Moreover, it does not provide a holistic view of the dependency of the leakage inductance on the design parameters. It is desired to have a closed-form equation for the optimum leakage inductance.

First harmonic approximation

Solving (5.3) analytically becomes impossible if all of the harmonics are considered. However, first harmonic approximation can be used since the RMS currents (4.21) and active powers (4.26) are inversely proportional to H^4 and H^3, respectively. Applying the first harmonic approximation and substituting φ from the power equation into the RMS current equation results in

$$I_{1\phi\mathrm{p,RMS}}^{\mathrm{YY}} = \sqrt{8}\frac{\sqrt{u_{1\mathrm{p}}^2 + \left(\frac{N_\mathrm{p} u_{1\mathrm{s}}}{N_\mathrm{s}}\right)^2 - \sqrt{\left(\frac{2N_\mathrm{p} u_{1\mathrm{p}} u_{1\mathrm{s}}}{N_\mathrm{s}}\right)^2 - \left(\frac{\pi^2 \omega L_\sigma^\mathrm{p} P_{3\phi}^\mathrm{nom}}{12}\right)^2}}}{\pi\omega L_\sigma^\mathrm{p}} \tag{5.8a}$$

$$I_{1\phi\mathrm{p,RMS}}^{\mathrm{Y\Delta}} = \sqrt{8}\frac{\sqrt{u_{1\mathrm{p}}^2 + \left(\frac{\sqrt{3}N_\mathrm{p} u_{1\mathrm{s}}}{N_\mathrm{s}}\right)^2 - \sqrt{\left(\frac{2\sqrt{3}N_\mathrm{p} u_{1\mathrm{p}} u_{1\mathrm{s}}}{N_\mathrm{s}}\right)^2 - \left(\frac{\pi^2 \omega L_\sigma^\mathrm{p} P_{3\phi}^\mathrm{nom}}{12}\right)^2}}}{\pi\omega L_\sigma^\mathrm{p}} \tag{5.8b}$$

$$I_{1\phi\mathrm{s,RMS}}^{\Delta\mathrm{Y}} = \sqrt{8}\frac{\sqrt{u_{1\mathrm{s}}^2 + \left(\frac{\sqrt{3}N_\mathrm{s} u_{1\mathrm{p}}}{N_\mathrm{p}}\right)^2 - \sqrt{\left(\frac{2\sqrt{3}N_\mathrm{s} u_{1\mathrm{s}} u_{1\mathrm{p}}}{N_\mathrm{p}}\right)^2 - \left(\frac{\pi^2 \omega L_\sigma^\mathrm{s} P_{3\phi}^\mathrm{nom}}{12}\right)^2}}}{\pi\omega L_\sigma^\mathrm{s}} \tag{5.8c}$$

Therefore, (5.3) can be simplified as

$$\begin{aligned} &\underset{L_\sigma^\mathrm{p} \in \mathbb{R}^+}{\arg\min} \left(\max_{U_\mathrm{p}, U_\mathrm{s}} \left(I_{1\phi\mathrm{p,RMS}} \right) \right) \\ &\text{subject to: } (U_\mathrm{p}, U_\mathrm{s}) \in \mathcal{O}_\mathrm{d}. \end{aligned} \tag{5.9}$$

Solving the optimization problem

Solving the optimization problem will be discussed only for the YY case.

Solving the inner optimization

Problem (5.9) contains the sub-problem $\max_{U_\mathrm{p},U_\mathrm{s}} (I_{1\phi\mathrm{p,RMS}})$, which should be solved first. If all of the local extrema of $I_{1\phi\mathrm{p,RMS}}$ are identified, the global maximum should be among these local extrema. Since the set $\mathcal{O}_\mathrm{d}$ is a convex set and $I_{1\phi\mathrm{p,RMS}}$ is a continuously differentiable function, the potential local maxima of $I_{1\phi\mathrm{p,RMS}}$ are the stationary points of the function. It will be shown here that all of the points in set $\mathcal{O}_\mathrm{d}$ except p_i where $i \in \{1,2,3,4\}$ are either non-stationary or, if they are stationary points, they are not the global maximum [see Figure 5.1]. A point in $\mathcal{O}_\mathrm{d}$—excluding its vertices and edges—is stationary if $\nabla I_{1\phi\mathrm{p,RMS}} = 0$, where

$$\nabla I_{1\phi\mathrm{p,RMS}} = \left(\frac{\partial I_{1\phi\mathrm{p,RMS}}}{\partial U_\mathrm{p}}, \ \frac{\partial I_{1\phi\mathrm{p,RMS}}}{\partial U_\mathrm{s}} \right)^\mathsf{T}. \tag{5.10}$$

Solving $\nabla I_{1\phi\mathrm{p,RMS}} = 0$ results in $\pi^2 \omega L_\sigma^\mathrm{p} P_{3\phi}^\mathrm{nom} = 0$, which is an invalid expression. Therefore, $I_{1\phi\mathrm{p,RMS}}$ has no stationary point inside $\mathcal{O}_\mathrm{d}$. For the edges, a point is stationary if the gradient is perpendicular to the edge and pointing outwards from $\mathcal{O}_\mathrm{d}$. For the edges parallel with the U_s-axis, this means

$$\frac{\partial I_{1\phi\mathrm{p,RMS}}}{\partial U_\mathrm{s}} = 0 \Rightarrow U_\mathrm{1s} = \sqrt{U_\mathrm{1p}^2 + \left(\frac{\pi^2 \omega L_\sigma^\mathrm{p} P_{3\phi}^\mathrm{nom}}{24 U_\mathrm{1p}} \right)^2} \Longrightarrow \frac{\partial I_{1\phi\mathrm{p,RMS}}}{\partial U_\mathrm{p}} < 0. \tag{5.11}$$

This means that there are no stationary points on the edge connecting vertices p_3 and p_4, whereas for a given L_σ^p, there is a single stationary point on the edge connecting vertices p_1 and p_2. For a given L_σ^p, comparing the value of the current on p_2 with the value of the current on this stationary point reveals that the current value in point p_2 is higher irrespective of the L_σ^p value. Therefore, there are no stationary points with the potential of being the global maximum on the edges parallel to the U_s-axis. With a similar approach, it can be shown that there are no stationary points with the potential of being the global maximum on the edges parallel to the U_p-axis. Finally, the only points with the potential to be the global maximum are the points p_i where $i \in \{1,2,3,4\}$.

Solving the outer optimization

It is shown that the potential extrema of $I_{1\phi\mathrm{p,RMS}}$ subject to constraint (5.1) are points p_i where $i \in \{1, 2, 3, 4\}$ [see Figure 5.2]. Therefore, the value of L_σ^{p} that minimizes the maximum value of $I_{1\phi\mathrm{p,RMS}}$ on points p_i is the solution to the problem (5.9). For clarification, Figure 5.7 shows the phase currents of the MFT on the points p_i as a function of the leakage inductance. The green curve is the maximum of the currents on the operation domain (shown in Figure 5.2). The value of L_σ^{p} that minimizes this curve will ensure that the phase currents in the whole operation domain will be kept to their minimum possible values. To solve (5.9), the intersections of the currents at the points p_i and p_j where $\{i, j\} \in \{1, 2, 3, 4\}$ and $i \neq j$ are identified. Subsequently, an analytical expression is derived at each identified interval. The total number of intersections is equal to the number of 2-combinations of $\{p_1, p_2, p_3, p_4\}$ which is six.

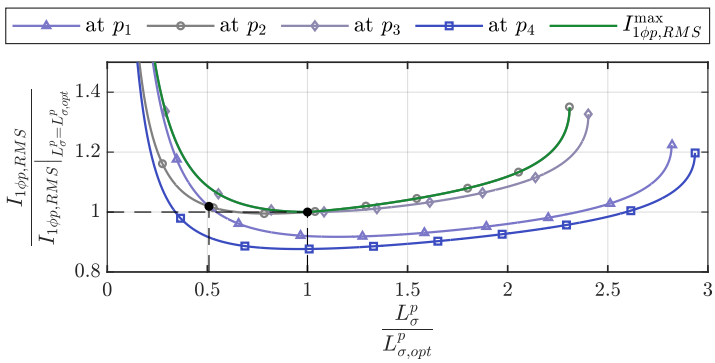

Figure 5.7: $I_{1\phi\mathrm{p,RMS}}$ on the points p_i, $i \in \{1, 2, 3, 4\}$ and their maximum value.

To get a comprehensible analytical expression for the leakage inductance, it is assumed that $u_{1\mathrm{pm}} \approx u_{1\mathrm{sm}}$ where $u_{1\mathrm{pm}}$ and $u_{1\mathrm{sm}}$ are defined as

$$u_{1\mathrm{pm}} \overset{\text{(4.20)}}{\triangleq} \sum_{k=0}^{M_{\mathrm{p}}-1} \left(U_{\mathrm{pm}} \cos(H\theta_k)\right) \tag{5.12a}$$

$$u_{1\mathrm{sm}}^{\mathrm{p}} \overset{\text{(4.20)}}{\triangleq} \frac{N_{\mathrm{p}}}{N_{\mathrm{s}}} \sum_{k=0}^{M_{\mathrm{s}}-1} \left(U_{\mathrm{sm}} \cos(H\theta_k)\right) \tag{5.12b}$$

Solving either $I_{1\phi\mathrm{p,RMS}}\big|_{p_1} = I_{1\phi\mathrm{p,RMS}}\big|_{p_4}$ or $I_{1\phi\mathrm{p,RMS}}\big|_{p_3} = I_{1\phi\mathrm{p,RMS}}\big|_{p_4}$ results in an invalid expression; meaning that there is no real-valued L_σ^{p} satisfying these equations. Similarly, solving $I_{1\phi\mathrm{p,RMS}}\big|_{p_2} = I_{1\phi\mathrm{p,RMS}}\big|_{p_4}$ will result in $L_\sigma^{\mathrm{p}} = 0$. This means that there is no $L_\sigma^{\mathrm{p}} \in \mathbb{R}^+$ where the currents in the points $\{p_1, p_2, p_3\}$ intersect with the current in the point p_4. These can also be seen in Figure 5.7 where there is no intersection of currents for these points. Likewise, $I_{1\phi\mathrm{p,RMS}}\big|_{p_1} = I_{1\phi\mathrm{p,RMS}}\big|_{p_3}$ results in unacceptable solution. On the other hand, there exists $L_\sigma^{\mathrm{p}} \in \mathbb{R}^+$ such that $I_{1\phi\mathrm{p,RMS}}\big|_{p_1} = I_{1\phi\mathrm{p,RMS}}\big|_{p_2}$ or $I_{1\phi\mathrm{p,RMS}}\big|_{p_3} = I_{1\phi\mathrm{p,RMS}}\big|_{p_2}$. $L_{\sigma,\mathrm{opt}}^{\mathrm{p}}$ is calculated by solving these two equations and identifying the regions where each solution is valid.

Closed-from solution

If $u_{1\mathrm{pm}} \approx u_{1\mathrm{sm}}^{\mathrm{p}}$ for the YY; or $u_{1\mathrm{pm}} \approx \sqrt{3}u_{1\mathrm{sm}}^{\mathrm{p}}$ for the YΔ; or $\sqrt{3}u_{1\mathrm{pm}} \approx u_{1\mathrm{sm}}^{\mathrm{p}}$ for the ΔY, then the solution of (5.9) is given as

$$L_{\sigma,\mathrm{opt}}^{\mathrm{p}} = \frac{24u_{1\mathrm{pm}}^2}{\pi^2\omega P_{3\phi}^{\mathrm{nom}}} \times G_{L_\sigma} \tag{5.13}$$

where G_{L_σ} is a gain and is defined as

$$G_{L_\sigma} = \begin{cases} \sqrt{\sigma_{\mathrm{dc,s}}}\sqrt{2-\sigma_{\mathrm{dc,s}}}\sqrt{1-2\sigma_{\mathrm{dc,s}}+\sigma_{\mathrm{dc,s}}^2-\sigma_{\mathrm{dc,p}}^2} & \forall\,(\sigma_{\mathrm{dc,p}},\sigma_{\mathrm{dc,s}}) \in \mathcal{I} \\ \sqrt{\sigma_{\mathrm{dc,p}}}\sqrt{2-\sigma_{\mathrm{dc,p}}}\sqrt{1-2\sigma_{\mathrm{dc,p}}+\sigma_{\mathrm{dc,p}}^2-\sigma_{\mathrm{dc,s}}^2} & \forall\,(\sigma_{\mathrm{dc,p}},\sigma_{\mathrm{dc,s}}) \in \mathcal{J} \end{cases} \tag{5.14}$$

and the subsets $\mathcal{I}$ and $\mathcal{J}$ are defined as

$$\mathcal{I}=\{(\sigma_{\mathrm{dc,p}},\sigma_{\mathrm{dc,s}})|0\leq\sigma_{\mathrm{dc,p}},\ \ \sigma_{\mathrm{dc,p}}\leq\sigma_{\mathrm{dc,s}},\ \ \sigma_{\mathrm{dc,p}}+\sigma_{\mathrm{dc,s}}\leq 1,\ \ \sigma_{\mathrm{dc,s}}+\sqrt{\sigma_{\mathrm{dc,p}}}\leq 1\} \tag{5.15a}$$

$$\mathcal{J}=\{(\sigma_{\mathrm{dc,p}},\sigma_{\mathrm{dc,s}})|0\leq\sigma_{\mathrm{dc,s}},\ \ \sigma_{\mathrm{dc,s}}\leq\sigma_{\mathrm{dc,p}},\ \ \sigma_{\mathrm{dc,p}}+\sigma_{\mathrm{dc,s}}\leq 1,\ \ \sigma_{\mathrm{dc,p}}+\sqrt{\sigma_{\mathrm{dc,s}}}\leq 1\}. \tag{5.15b}$$

Figure 5.8a illustrates the value of G_{L_σ} as a function of $\sigma_{\mathrm{dc,p}}$ and $\sigma_{\mathrm{dc,s}}$. The sets $\mathcal{I}$ and $\mathcal{J}$ are depicted with green and orange dashed lines, respectively. There is symmetry in the value of G_{L_σ} along the identity line ($\sigma_{\mathrm{dc,p}} = \sigma_{\mathrm{dc,s}}$). A zoomed version of Figure 5.8a is depicted in Figure 5.8b. In this region, the iso-lines are almost parallel with the axes, meaning that G_{L_σ} and consequently $L_{\sigma,\mathrm{opt}}^{\mathrm{p}}$ depend mainly on $\max(\sigma_{\mathrm{dc,p}},\ \sigma_{\mathrm{dc,s}})$.

The switching losses also affect the converter's efficiency for applications

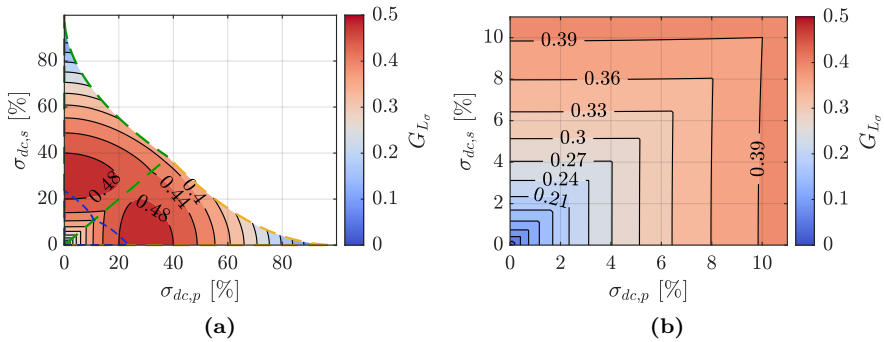

Figure 5.8: Visualization of G_{L_σ} given in (5.14). The triangle with green dashed lines corresponds to the set $\mathcal{I}$ given in (5.15a), and the one with orange dashed lines corresponds to the set $\mathcal{J}$ given in (5.15b). **(a)** For $\sigma_{\mathrm{dc,p}} \leq 100\,\%$ and $\sigma_{\mathrm{dc,s}} \leq 100\,\%$. **(b)** For $\sigma_{\mathrm{dc,p}} \leq 11\,\%$ and $\sigma_{\mathrm{dc,s}} \leq 11\,\%$.

with a high switching frequency. The dashed blue lines in Figure 5.8a show the boundaries of the soft-switching region. For the voltage deviations inside this region, the selection of the leakage inductance from (5.13) also ensures the soft-switching in the whole $\mathcal{O}_{\mathrm{d}}$. As shown in [24], the soft-switching range drifts toward large phase shifts with an increase in the transition time. Therefore, the region marked with the dashed-blue line will shrink for non-zero transition time values and eventually disappear.

Finally, for clarification, Figure 5.9 shows a flowchart of the optimum leakage inductance calculation process.

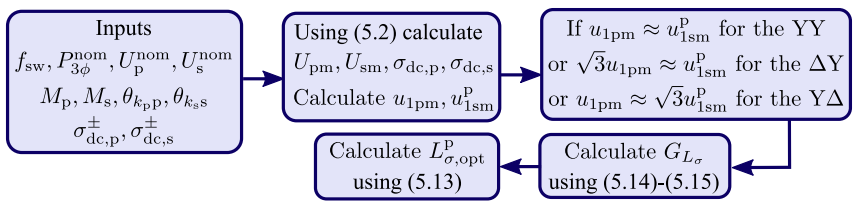

Figure 5.9: Optimum leakage inductance calculation flowchart.

Sensitivity analysis

The presence of harmonics transmitting active power will affect the value of $L^{\mathrm{p}}_{\sigma,\mathrm{opt}}$. It is essential to investigate the sensitivity of the current to changes in the leakage inductance value to validate the relations derived earlier. The deviation in the $L^{\mathrm{p}}_{\sigma,\mathrm{opt}}$ value, $\delta_{L^{\mathrm{p}}_{\sigma,\mathrm{opt}}}$, is defined as

$$\delta_{L^{\mathrm{p}}_{\sigma,\mathrm{opt}}} = \frac{\Delta L^{\mathrm{p}}_{\sigma,\mathrm{opt}}}{L^{\mathrm{p}}_{\sigma,\mathrm{opt}}} = \frac{L_{\sigma,\text{non-opt}} - L^{\mathrm{p}}_{\sigma,\mathrm{opt}}}{L^{\mathrm{p}}_{\sigma,\mathrm{opt}}} \tag{5.16}$$

where $L_{\sigma,\text{non-opt}}$ is the non-optimum value of the leakage inductance. Similarly, the deviation in the RMS current, $\delta_{I_{1\phi\mathrm{p,RMS}}}$, is defined as

$$\delta_{I_{1\phi\mathrm{p,RMS}}} = \frac{\left| I_{1\phi\mathrm{p,RMS}}\big|_{L_{\sigma,\text{non-opt}}} - I_{1\phi\mathrm{p,RMS}}\big|_{L^{\mathrm{p}}_{\sigma,\mathrm{opt}}} \right|}{I_{1\phi\mathrm{p,RMS}}\big|_{L^{\mathrm{p}}_{\sigma,\mathrm{opt}}}} \times 100\,\%. \tag{5.17}$$

Figure 5.10 shows the value of $\delta_{I_{1\phi\mathrm{p,RMS}}}$ for the points with the maximum current in the operation domain when $\delta_{L^{\mathrm{p}}_{\sigma,\mathrm{opt}}} = \pm 2.5\,\%$. The maximum current occurs on points p_1 or p_3 for $\delta_{L^{\mathrm{p}}_{\sigma,\mathrm{opt}}} = -2.5\,\%$. For these points, $\delta_{I_{1\phi\mathrm{p,RMS}}}$ is below 2 %, as shown in Figure 5.10a. Similarly, Figure 5.10b shows $\delta_{I_{1\phi\mathrm{p,RMS}}}$ for the point with maximum current when $\delta_{L^{\mathrm{p}}_{\sigma,\mathrm{opt}}} = 2.5\,\%$ (i.e., point p_2). Similar to $\delta_{L^{\mathrm{p}}_{\sigma,\mathrm{opt}}} = -2.5\,\%$ case, the deviation stays below 2 % for most of $(\sigma_{\mathrm{dc,p}}, \sigma_{\mathrm{dc,s}})$ pairs. However, for certain $(\sigma_{\mathrm{dc,p}}, \sigma_{\mathrm{dc,s}})$ pairs, the deviation increases dramatically and even becomes a complex value (where iso-lines disappear). In that region, the phase shift between the primary side and the secondary side bridges is close to 90°. Therefore, the converter will lose the capability to transmit the full power at point p_2 for a small change in L^{p}_{σ}. Additionally, for large values of φ, $\mathrm{d}I_{1\phi\mathrm{p,RMS}}/\mathrm{d}L^{\mathrm{p}}_{\sigma}$ increases quickly [see Figure 5.7]. Therefore, a small deviation in $L^{\mathrm{p}}_{\sigma,\mathrm{opt}}$ will result in a large deviation in the RMS value of the current.

5.5 Simulation and verification

An analytical expression is derived for $L^{\mathrm{p}}_{\sigma,\mathrm{opt}}$, and sensitivity analysis is performed. However, these are done assuming that the ac resistance of the MFT and the harmonics can be neglected. A simulation model is developed to in-

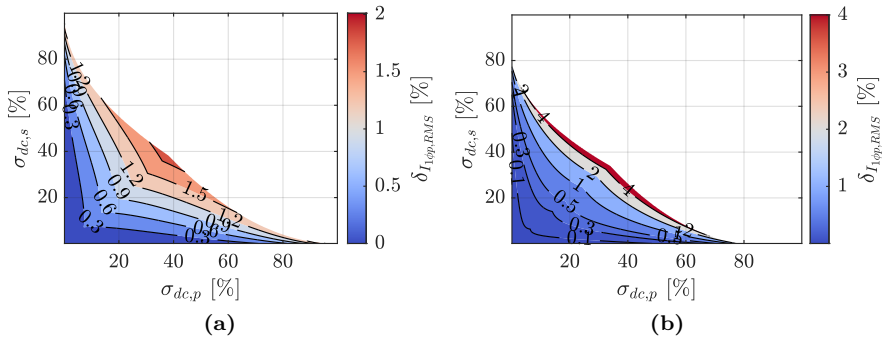

Figure 5.10: $\delta_{I_{1\phi\mathrm{p,RMS}}}$ for different $\sigma_{\mathrm{dc,p}}$ and $\sigma_{\mathrm{dc,s}}$ values. **(a)** For $\delta_{L^{\mathrm{p}}_{\sigma,\mathrm{opt}}} = -2.5\,\%$ on points p_1 or p_3. **(b)** For $\delta_{L^{\mathrm{p}}_{\sigma,\mathrm{opt}}} = 2.5\,\%$ on point p_2.

vestigate the validity of these assumptions and to verify the analytical model.

Case study setup

A MATLAB model, which emulates the behavior of a 3ϕ multilevel DAB dc-dc converter, is developed. The rated power is assumed to be 2 MW, and both dc-link voltages are assumed to be 5 kV. An MMC topology is selected for both bridges. The number of submodules per arm is selected to be five. It is assumed that the converter has a switching frequency of 5 kHz and the dwell-time is 2.5 µs. Table 5.1 summarizes the specifications of the converter.

Table 5.1: The simulated dc-dc converters' specifications

Parameter	Value	Parameter	Value	Parameter	Value
$V^{\mathrm{nom}}_{\mathrm{dc,p}}$	5 kV	N_{sm}	5	$V^{\mathrm{rated}}_{\mathrm{sw}}$	1.7 kV
$V^{\mathrm{nom}}_{\mathrm{dc,s}}$	5 kV	$\sigma_{\mathrm{dc,p}}$	$[2, 35]\,\%$	f_{sw}	5 kHz
$P^{\mathrm{nom}}_{3\phi}$	2 MW	$\sigma_{\mathrm{dc,s}}$	$[2, 35]\,\%$	$\frac{\psi_{\mathrm{p}}}{\omega} = \frac{\psi_{\mathrm{s}}}{\omega}$	2.5 µs

The series ac resistance is neglected for this simulation, and the method explained in Section 5.3 is used to obtain the desired leakage inductance.

Study of simulation results

Figure 5.11 shows the desired leakage inductance of the 3ϕ-YY-DAB and 3ϕ-YΔ-DAB obtained from the simulations. As can be seen, they have similar patterns as Figure 5.8a.

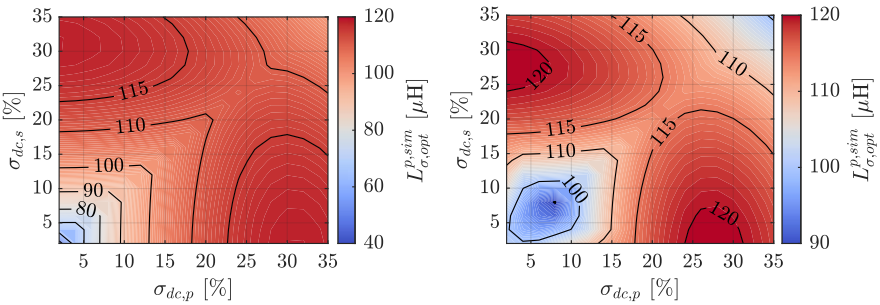

Figure 5.11: Numerical solution for $L^{\mathrm{p}}_{\sigma,\mathrm{opt}}$ with the converter specifications given in Table 5.1. **(a)** For the 3ϕ-YY-DAB. **(b)** For the 3ϕ-YΔ-DAB.

For an MMC with five submodules and dc-links voltages of 5 kV, $U^{\mathrm{nom}}_{\mathrm{p}}$ and $U^{\mathrm{nom}}_{\mathrm{s}}$ are equal to 1 kV. Moreover, $\sigma^{+}_{\mathrm{dc,p}}$ and $\sigma^{-}_{\mathrm{dc,p}}$ are assumed to be equal (similarly, $\sigma^{+}_{\mathrm{dc,s}} = \sigma^{-}_{\mathrm{dc,s}}$). Using (5.2), one can get $\sigma_{\mathrm{dc,p}} = \sigma^{+}_{\mathrm{dc,p}} = \sigma^{-}_{\mathrm{dc,p}}$, $\sigma_{\mathrm{dc,s}} = \sigma^{+}_{\mathrm{dc,s}} = \sigma^{-}_{\mathrm{dc,s}}$, and $U_{\mathrm{pm}} = U^{\mathrm{nom}}_{\mathrm{p}} = U^{\mathrm{nom}}_{\mathrm{s}} = U_{\mathrm{sm}}$. Additionally, $u_{1\mathrm{pm}} = u_{1\mathrm{sm}} = 0.5 + \cos(\psi) + \cos(2\psi)$ kV. Eventually, (5.13) can be used to calculate $L^{\mathrm{p}}_{\sigma,\mathrm{opt}}$. Figure 5.12 shows the percentage of error in the estimation of the leakage inductance from (5.13), which is defined as

$$L^{\mathrm{p,error}}_{\sigma,\mathrm{opt}} = \frac{L^{\mathrm{p,sim}}_{\sigma,\mathrm{opt}} - L^{\mathrm{p,calc}}_{\sigma,\mathrm{opt}}}{L^{\mathrm{p,sim}}_{\sigma,\mathrm{opt}}} \times 100\,\% \tag{5.18}$$

where $L^{\mathrm{p,sim}}_{\sigma,\mathrm{opt}}$ is the value obtained from the simulations (shown in Figure 5.11), and $L^{\mathrm{p,calc}}_{\sigma,\mathrm{opt}}$ is the value obtained from the analytical expressions (5.13).

As can be seen, for most of the region $L^{\mathrm{p,error}}_{\sigma,\mathrm{opt}}$ is below 2.5 % for the 3ϕ-YY-DAB. $L^{\mathrm{p,error}}_{\sigma,\mathrm{opt}}$ increases for the YΔ case when deviations in the dc-links are below 10 %. This is because the lower the deviations in the dc-links, the lower the phase shift obtained from L^{p}_{σ} optimization. The fifth and seventh harmonics are the dominant components of the current for low phase shifts

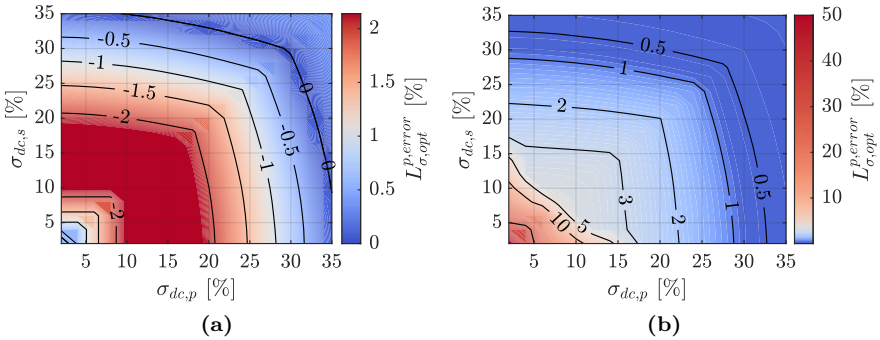

Figure 5.12: $L^{\mathrm{p,error}}_{\sigma,\mathrm{opt}}$ **(a)** For the 3ϕ-YY-DAB. **(b)** For the 3ϕ-YΔ-DAB.

for the ΔY configuration [66]. This makes the first harmonic approximation invalid for the ΔY configuration and low phase shift values. Thus, the solution obtained from the analytical calculations has a higher error in this region.

Figure 5.13 shows $L^{\mathrm{p,error}}_{\sigma,\mathrm{opt}}$ of the YY-3ϕ-DAB for three different percentages of the total transition times per fundamental period ($\tau_{\%} \triangleq \tau f_{\mathrm{sw}} \times 100\,\%$). For $\sigma_{\mathrm{dc,p}} \leq 2\,\%$ or $\sigma_{\mathrm{dc,s}} \leq 2\,\%$, the estimation error increases dramatically. However, for the rest of the region, $L^{\mathrm{p,error}}_{\sigma,\mathrm{opt}}$ is below 3 %. For a given $(\sigma_{\mathrm{dc,p}}, \sigma_{\mathrm{dc,s}})$, an increase in $\tau_{\%}$ reduces the estimation error. This is because the total harmonic distortion (THD) of the phase current reduces with higher transition times, and accordingly, the accuracy of the first harmonic approximation increases.

Figure 5.14 visualizes the deviation in the RMS value of the phase current for a 3ϕ-YY-DAB at the nominal power for different percentages of deviation from the desired leakage inductance obtained from (5.13). When the converter operates with nominal voltages, $\delta_{I_{\mathrm{RMS}}}$ is larger than zero for any $\delta_{L^{\mathrm{p}}_{\sigma,\mathrm{opt}}} > 0$. The maximum value of $\delta_{I_{\mathrm{RMS}}}$ occurs at $\sigma_{\mathrm{dc,p}} = \sigma_{\mathrm{dc,s}} \approx 23\,\%$, which is below 1 % for $\delta_{L^{\mathrm{p}}_{\sigma,\mathrm{opt}}} < 10\,\%$. The larger the $\left|\delta_{L^{\mathrm{p}}_{\sigma,\mathrm{opt}}}\right|$, the higher the $|\delta_{I_{\mathrm{RMS}}}|$. The effect is more pronounced when the converter operates at non-nominal points—specifically at points p_i, $i \in \{1,2,3\}$. For these points, the higher the $\sigma_{\mathrm{dc,p}} = \sigma_{\mathrm{dc,s}}$, the higher the $|\delta_{I_{\mathrm{RMS}}}|$. For example, a 10 % deviation from the desired leakage inductance value can cause 2 % higher RMS currents at points p_1 or p_3 in the converter for $\sigma_{\mathrm{dc,p}} = \sigma_{\mathrm{dc,s}} = 11\,\%$. For large enough $\sigma_{\mathrm{dc,p}} = \sigma_{\mathrm{dc,s}}$, even a 5 % deviation from $L^{\mathrm{p}}_{\sigma,\mathrm{opt}}$ can cause more than 5 %

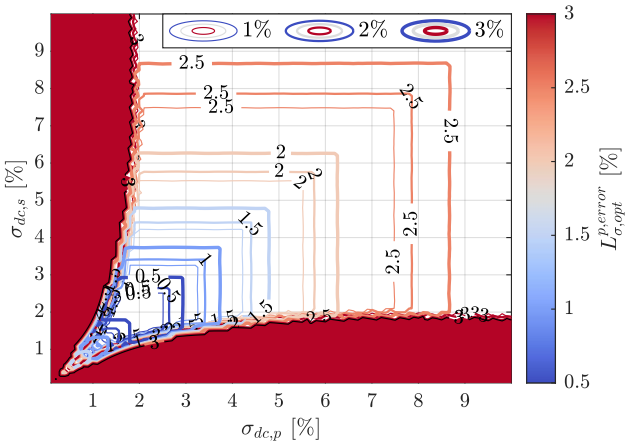

Figure 5.13: $L^{\mathrm{p,error}}_{\sigma,\mathrm{opt}}$ of the YY-connected 3ϕ MFT for different $\tau_{\%}$. In the red-colored region, the error is higher than 3 %.

higher currents in the converter. Therefore, it is important to choose the leakage inductance value as close to the value given by (5.13) as possible to avoid extra losses in the converter.

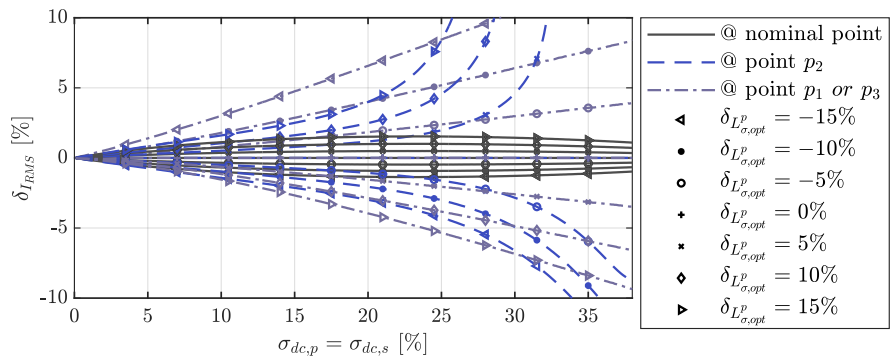

Figure 5.14: The deviation in the RMS value of the phase current for the 3ϕ-YY-DAB at the nominal power for different percentages of deviation from the desired leakage inductance obtained form (5.13).

Sensitivity study on the ac resistance

In this section, only the YY-DAB is analyzed. To include the series ac resistance in the simulation, the first-order differential equation

$$L_{\sigma}^{\mathrm{p}} \frac{\mathrm{d}i_{\mathrm{L}x}^{\mathrm{YY}}(\omega t)(\omega t)}{\mathrm{d}t} + R_{\mathrm{ac}}^{\mathrm{p}} i_{\mathrm{L}x}^{\mathrm{YY}}(\omega t)(\omega t) = v_{x\mathrm{N}}(\omega t) - v_{y\mathrm{n}}^{\mathrm{p}}(\omega t - \varphi) \tag{5.19}$$

should be solved while ensuring that $P_{3\phi} = P_{3\phi}^{\mathrm{nom}}$ holds. The initial condition for the current in (5.19) is unknown. And, L_{σ}^{p} should be selected such that the RMS value of $i_{\mathrm{L}x}^{\mathrm{YY}}(\omega t)$ is minimized for a certain range of variations in the amplitudes of $v_{x\mathrm{N}}(\omega t)$ and $v_{y\mathrm{n}}^{\mathrm{p}}(\omega t - \varphi)$. Overall, the problem becomes time demanding to solve. Therefore, the simulation with the ac resistance is performed only for a single design where $(\sigma_{\mathrm{dc,p}}, \sigma_{\mathrm{dc,s}}) = (0.1, 0.1)$. The converter is assumed to have the same specifications as in Table 5.1. $R_{\mathrm{ac}}^{\mathrm{p}}$ is varied such that the $\omega L_{\sigma}^{\mathrm{p}}/R_{\mathrm{ac}}^{\mathrm{p}}$ ratio is kept close to or higher than the values shown in Figure 5.4 for a fundamental frequency of 5 kHz.

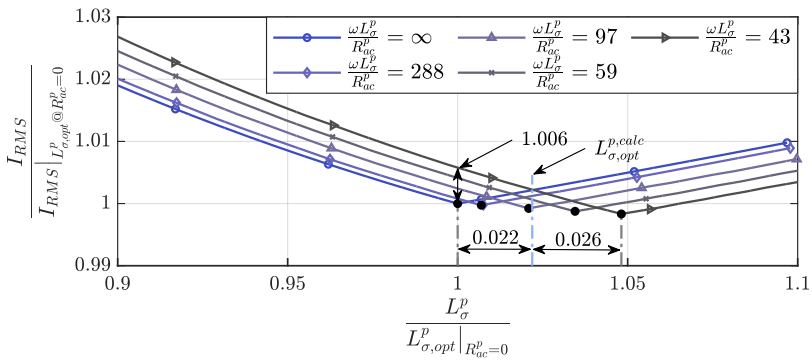

Figure 5.15: The maximum of the currents in the operation domain as a function of the leakage inductance for different $\omega L_{\sigma}^{\mathrm{p}}/R_{\mathrm{ac}}^{\mathrm{p}}$ values obtained from the simulation model for $(\sigma_{\mathrm{dc,p}},\ \sigma_{\mathrm{dc,s}}) = (0.1,\ 0.1)$. The dashed blue line marks the value of $L_{\sigma,\mathrm{opt}}^{\mathrm{p}}$ from the analytical expression $(L_{\sigma,\mathrm{opt}}^{\mathrm{p,calc}})$.

Figure 5.15 depicts the maximum of the currents in the operation domain as a function of leakage inductance for different $\omega L_{\sigma}^{\mathrm{p}}/R_{\mathrm{ac}}^{\mathrm{p}}$ values obtained from the simulation model. $\omega L_{\sigma}^{\mathrm{p}}/R_{\mathrm{ac}}^{\mathrm{p}} = \infty$ means that the ac resistance is neglected in the simulation. The current and the leakage inductance are normalized with respect to the case where $R_{\mathrm{ac}}^{\mathrm{p}} = 0$. When $\omega L_{\sigma}^{\mathrm{p}}/R_{\mathrm{ac}}^{\mathrm{p}}$ reduces, the error in the

$L^{\mathrm{p}}_{\sigma,\mathrm{opt}}$ value increases. For $\omega L^{\mathrm{p}}_{\sigma}/R^{\mathrm{p}}_{\mathrm{ac}} = 43$, the value of $L^{\mathrm{p}}_{\sigma,\mathrm{opt}}$ is 4.8 % higher compared with the case without resistance. As seen, 4.8 % error in $L^{\mathrm{p}}_{\sigma,\mathrm{opt}}$ will cause less than 1 % error in the RMS value of the current. The value of $L^{\mathrm{p}}_{\sigma,\mathrm{opt}}$ from the analytical expression is depicted with a blue dashed line. The error between the $L^{\mathrm{p,calc}}_{\sigma,\mathrm{opt}}$ and $L^{\mathrm{p,sim}}_{\sigma,\mathrm{opt}}|_{R^{\mathrm{p}}_{\mathrm{ac}}=0}$ is 2.2 %, which is the same value as shown in Figure 5.12a for $(\sigma_{\mathrm{dc,p}}, \sigma_{\mathrm{dc,s}}) = (0.1,\ 0.1)$.

5.6 Conclusions and discussion

Analytical expressions are derived to estimate the desired leakage inductance value of the MFT for a DAB dc-dc converter. The estimated leakage inductance minimizes the RMS current for deviations in the dc-links voltages.

The derived equations are validated with MATLAB simulation models. It is shown that, in a broad design range, the error in the estimation of the leakage inductance can be less than 2.5 % for the YY-3ϕ-DAB. It is also highlighted that soft-switching can be ensured for specific converter designs using the presented equations [see Figure 5.8a].

The importance of selecting the leakage inductance correctly for a given voltage span is quantified. As an example, it is shown that for 11 % deviations in the dc-links voltages, a 10 % deviation from the desired leakage inductance value can cause 2 % higher currents in the converter. In addition, the effect of neglecting the MFT's ac resistance on the leakage inductance's optimum value (and also the RMS current) is quantified. It is demonstrated that including an ac resistance close to its actual value in the optimization can cause a 5 % difference in the value of the obtained optimum leakage inductance. Moreover, it is also shown that the estimation error is high for the YΔ connection when deviations less than 10 % in the dc-links are expected. This is attributed to the first harmonic approximation. The main limitation of the proposed method is high estimation errors when a small deviation ($\sigma < 2\,\%$) is expected only in one of the dc-links [see Figure 5.13].

CHAPTER 6

Capacitor Size, Switch Size, and Lifetime Studies

This chapter is based on the following articles

[I] **B. Khanzadeh**, T. Thiringer, "Capacitor and switch size comparisons on high-power medium-voltage dc–dc converters with three-phase medium-frequency transformer," Published in *IEEE Journal of Emerging and Selected Topics in Power Electronics*, vol. 9, no. 3, pp. 3331–3338, 2021.

[II] **B. Khanzadeh**, T. Thiringer, and Y. Okazaki, "Capacitor size comparison on high-power dc-dc converters with different transformer winding configurations on the ac-link," in Proceedings of *22nd European Conference on Power Electronics and Applications (EPE'20 ECCE Europe)*, 2020, P.1– P.7.

[III] **B. Khanzadeh**, C. Tang, and T. Thiringer, "A study on the lifetime of Q2L-MMC-DAB's switches for wind turbine applications," in Proceedings of *fifteenth International Conference on Ecological Vehicles and Renewable Energies (EVER)*, 2020, pp. 1–6.

6.1 Introduction

Passive components like capacitors and inductors are the main contributors to the weight and volume of the converters. Therefore, it is important to evaluate their size when choosing between different converter topologies.

Q2L modulation was introduced for multilevel converters in [22], with the aim of reducing the capacitor requirement and improving the power density. In [23], the cell capacitance design and comparison for multilevel galvanically isolated dc-dc converters with Q2L modulation were presented. However, the dc-link capacitors were not taken into account in the comparison. Moreover, [23] has focused only on quantifying the capacitor requirement for converters with the YY connection of windings. Another feature of the Q2L modulation is the possibility of using small devices for the auxiliary switches [23]. This feature is discussed and investigated for a Q2L-operating MMC-DAB in [22], [24]. However, the thermal stresses on the switches are not quantified.

This chapter aims to quantify the capacitance requirement of selected multilevel DAB dc-dc converters operating with Q2L modulation for a range of switching frequencies and transition times. This study considers not only the submodule capacitors but also the dc-link capacitors, which so far have not been presented in the scientific literature for multilevel DAB dc-dc converters. The share of the dc-link capacitors in the total energy storage requirement of the converters is presented quantitatively. Furthermore, the combinations of the switching frequencies and the transition times, where designing the converters will result in oversized capacitors, are pinpointed. Moreover, the effect of the MFT' winding configurations on the capacitor requirement is quantified.

Another focus of this chapter is on the semiconductor requirements of different DAB converter topologies under Q2L modulation. The total installed apparent power of semiconductor switches is compared for different topologies. Also, insight is provided into the thermal cycles of switching devices with Q2L modulation for wind turbine applications.

6.2 Capacitor and semiconductor sizing

Since the multilevel converters also need capacitors in the submodules, the capacitor size calculation can be divided into the dc-link capacitors' size determination and the submodule capacitor size calculation.

DC-link capacitor sizing

Considering zero current flow to node G, the currents flowing to the nodes dc^+ and dc^- are enough to calculate the dc-link capacitors' currents [see Figure 2.3 and Figure 2.4 for the node and current direction definitions]. The instantaneous current flowing to (from) the converter arms from (to) the dc-link can be calculated from the arm currents as

$$i_{\Sigma}^{\pm}(\omega t) = \sum_{x \in \{A,B,C\}} i_{x}^{\pm}(\omega t) \tag{6.1}$$

where $i_{\Sigma}^{+}(\omega t)$ is the positive pole current flowing from the dc-link to the converter arms; $i_{\Sigma}^{-}(\omega t)$ is the negative pole current flowing from the converter arms to the dc-link; and $i_{x}^{\pm}(\omega t)$, $x \in \{A, B, C\}$ are the respective phase arm currents. In steady-state, a capacitor's average current should be zero. Therefore, the dc-link capacitors currents, $i_{C_{\mathrm{dc}}}^{\pm}$, are given by

$$i_{C_{\mathrm{dc}}}^{\pm}(\omega t) = \frac{1}{2\pi}\int_{0}^{2\pi} i_{\Sigma}^{\pm}(\omega t)\,\mathrm{d}\omega t - i_{\Sigma}^{\pm}(\omega t)\,. \tag{6.2}$$

By knowing the capacitors' currents, the capacitors' instantaneous charge, $Q_{C_{\mathrm{dc}}}^{\pm}(\omega t)$, can be calculated as

$$Q_{C_{\mathrm{dc}}}^{\pm}(\omega t) = \int i_{C_{\mathrm{dc}}}^{\pm}(\omega t)\,\mathrm{d}t\,. \tag{6.3}$$

The dc-link capacitors, $C_{\mathrm{dc}}^{\pm}$, can be designed to limit the voltage oscillations to $\pm\sigma_{\mathrm{dc}}\%$ of the nominal dc-link voltage as

$$C_{\mathrm{dc}}^{\pm} = \max\left(\left|\frac{\max\left(Q_{C_{\mathrm{dc}}}^{\pm}(\omega t) - \overline{Q_{C_{\mathrm{dc}}}^{\pm}}\right)}{\sigma_{\mathrm{dc}} V_{\mathrm{dc}}^{\mathrm{nom}} \times 10^{-2}}\right|, \left|\frac{\min\left(Q_{C_{\mathrm{dc}}}^{\pm}(\omega t) - \overline{Q_{C_{\mathrm{dc}}}^{\pm}}\right)}{\sigma_{\mathrm{dc}} V_{\mathrm{dc}}^{\mathrm{nom}} \times 10^{-2}}\right|\right) \tag{6.4}$$

where $\overline{Q_{C_{\mathrm{dc}}}^{\pm}}$ is the average value of the capacitors' instantaneous charge. Eventually, the energy storage requirement of the dc-link per nominal power of the converter, E_{dc}, can be expressed as

$$E_{\mathrm{dc}} = \frac{\left(C_{\mathrm{dc}}^{+} + C_{\mathrm{dc}}^{-}\right)\left(V_{\mathrm{dc}}^{\mathrm{nom}}\right)^2}{8P_{3\phi}^{\mathrm{nom}}}. \tag{6.5}$$

Chain-links capacitor sizing

The ac terminals of the converter operating with Q2L modulation are clamped to one of the dc-rails for most of the fundamental period. Thus, the chain-links conduct the currents only during the transition intervals. Since the capacitors are inserted or bypassed at different time instants during the transition period, they will charge and discharge to different values depending on the current waveform. To limit all submodule capacitors' voltages to $\pm\sigma_{\mathrm{sm}}\%$ of their nominal value, it is necessary to dimension them using the submodule with the highest voltage oscillation. The kth submodule capacitor's charge variation from the balanced state, $\Delta Q_{C_{\mathrm{sm}k}}(\omega t)$, can be calculated from the respective cell's current, $i_{C_{\mathrm{sm}k}}(\omega t)$, as

$$\Delta Q_{C_{\mathrm{sm}k}}(\omega t) = \int_{t_{\mathrm{balanced}}}^{t} i_{C_{\mathrm{sm}k}}(\omega t')\,\mathrm{d}t' \tag{6.6}$$

where t_{balanced} is the time instant during the transition period, at which all of the capacitors of the chain-link are balanced. The kth submodule capacitance, $C_{\mathrm{sm}k}$, can be calculated using (6.6) as

$$C_{\mathrm{sm}k} = \max\left(\left|\frac{\max\left(\Delta Q_{C_{\mathrm{sm}k}}(\omega t)\right)}{\sigma_{\mathrm{sm}} U^{\mathrm{nom}} \times 10^{-2}}\right|, \left|\frac{\min\left(\Delta Q_{C_{\mathrm{sm}k}}(\omega t)\right)}{\sigma_{\mathrm{sm}} U^{\mathrm{nom}} \times 10^{-2}}\right|\right) \tag{6.7a}$$

$$C_{\mathrm{sm}} = \max\left(C_{\mathrm{sm}1}, C_{\mathrm{sm}2}, ..., C_{\mathrm{sm}N_{\mathrm{sm}}}\right) \tag{6.7b}$$

where C_{sm} is the submodule capacitance. Subsequently, the required energy storage for a chain-link per nominal power of the converter, E_{cl}, is given by

$$E_{\mathrm{cl}} = \frac{N_{\mathrm{sm}} C_{\mathrm{sm}} \left(U^{\mathrm{nom}}\right)^2}{2P_{3\phi}^{\mathrm{nom}}}. \tag{6.8}$$

Eventually, the total capacitive energy storage requirement of the converter, E_{tot}, can be calculated using (6.5) and (6.8) as

$$E_{\mathrm{tot}} = \left(E_{\mathrm{dc,p}} + N_{\mathrm{cl,p}} E_{\mathrm{cl,p}}\right) + \left(E_{\mathrm{dc,s}} + N_{\mathrm{cl,s}} E_{\mathrm{cl,s}}\right) \tag{6.9}$$

where N_{cl} is the number of chain-links per converter—0 for the conventional DAB, 6 for the MTAC and MMC, and 3 for the TAC and CTB.

Note that the method described for the sizing of the capacitors is based on the maximum capacitors' charge variation and design requirements on their

voltage swings. As long as these variations can be identified, the method can be used to size the capacitors. As discussed in Section 2.4, identifying these cycles is straightforward for converters of Figure 2.3 and Figure 2.4 operating with Q2L or SPS modulations.

Semiconductor sizing

Voltage and current ratings of the semiconductor switches should be dimensioned properly for reliable operation. The design should also ensure a long lifetime without compromising the cost of the whole system.

Voltage rating of semiconductors

The switches should be selected to block the applied voltage during the OFF-state without a breakdown. Also, the stray inductance and the voltage transients introduced during switching should be considered. For circuits with high stray inductances, a safety margin of 60 % can be considered [67].

The semiconductors of the 2LC and T-type converters should be able to block the full dc-link voltage. Similarly, the switches of a three-level NPC experience half dc-link voltage during the OFF-state. Thus, with a safety margin of S_f percent, the minimum blocking voltage, $V_\mathrm{sw}^\mathrm{min}$, can be calculated as [67]

$$V_\mathrm{sw,T\text{-}type}^\mathrm{min} \equiv V_\mathrm{sw,2LC}^\mathrm{min} = V_\mathrm{dc}^\mathrm{nom}\left(1 + \frac{S_\mathrm{f}}{100}\right) \tag{6.10a}$$

$$V_\mathrm{sw,NPC}^\mathrm{min} = 0.5 V_\mathrm{dc}^\mathrm{nom}\left(1 + \frac{S_\mathrm{f}}{100}\right) \tag{6.10b}$$

where $V_\mathrm{dc}^\mathrm{nom}$ is the nominal dc-link voltage. Then the switch should be selected such that $V_\mathrm{sw}^\mathrm{rated} \geq V_\mathrm{sw}^\mathrm{min}$; where $V_\mathrm{sw}^\mathrm{rated}$ is the rated blocking voltage.

For multilevel converters, the rating of the switch should be decided based on the number of submodules and the nominal dc-link voltage. Alternatively, the number of submodules can be selected based on the rated blocking voltage of the semiconductors. The latter is used for the studies in this thesis. The chain-links of the MMC and TAC converters should be able to block the full dc-link voltage. On the other hand, only half of the dc-link voltage appears on the chain-links of the CTB and the MTAC converters. The required number of submodules per arm of MMC, TAC, MTAC; and per leg of CTB converters

can be calculated as

$$N_{\mathrm{sm,MMC}} \equiv N_{\mathrm{sm,TAC}} = \left\lceil \frac{V_{\mathrm{dc}}^{\mathrm{nom}}(1+\frac{S_{\mathrm{f}}}{100})}{V_{\mathrm{sw}}^{\mathrm{rated}}} \right\rceil \tag{6.11a}$$

$$N_{\mathrm{sm,CTB}} \equiv N_{\mathrm{sm,MTAC}} = \left\lceil \frac{0.5V_{\mathrm{dc}}^{\mathrm{nom}}(1+\frac{S_{\mathrm{f}}}{100})}{V_{\mathrm{sw}}^{\mathrm{rated}}} \right\rceil . \tag{6.11b}$$

Current rating of semiconductors

The terms main and auxiliary switched are used hereafter. The main switch refers to all the switches in the 2LC converter. For the NPC and T-type converters, the main switch refers to any switch other than the clamping switches. The switches that insert the submodule capacitors in the current path in the MMC, TAC, MTAC, and CTB converter are referred to as auxiliary switches. This is because these switches conduct the current only for a short period of time during the transition period. the rest of the switches in these converters are identified as the main switches.

In this thesis, the RMS current is used for dimensioning the semiconductors. The RMS current of the kth main switch, $I_{\mathrm{sw}k,\mathrm{main}}^{\mathrm{RMS}}$, or auxiliary switch, $I_{\mathrm{sw}k,\mathrm{aux}}^{\mathrm{RMS}}$, can be calculated using the phase currents and duty cycles of the respective switches. Finally, the switches can be dimensioned based on the highest RMS current as

$$I_{\mathrm{sw,main}}^{\mathrm{RMS}} = \max\left(I_{\mathrm{sw1,main}}^{\mathrm{RMS}}, I_{\mathrm{sw2,main}}^{\mathrm{RMS}}, ..., I_{\mathrm{sw}N_{\mathrm{sm}},\mathrm{main}}^{\mathrm{RMS}}\right) \tag{6.12a}$$

$$I_{\mathrm{sw,aux}}^{\mathrm{RMS}} = \max\left(I_{\mathrm{sw1,aux}}^{\mathrm{RMS}}, I_{\mathrm{sw2,aux}}^{\mathrm{RMS}}, ..., I_{\mathrm{sw}N_{\mathrm{sm}},\mathrm{aux}}^{\mathrm{RMS}}\right) . \tag{6.12b}$$

Case study setup

In this section, a case study will be done on a few DAB converters to compare their capacitive energy storage and switch requirements. The 2LC, MMC, TAC, MTAC, and CTB converters are selected for this study [see Figure 2.3 and Figure 2.4]. To avoid permutations of different converter topologies, it is assumed that the primary and secondary bridges have the same topology. Also, the names of the converters are abbreviated to one of the bridges (e.g.,

MMC-MMC-DAB abbreviated to MMC-DAB). For simplicity, it is assumed that the primary and secondary sides have the same nominal dc-link voltage ($V_{\mathrm{dc,p}}^{\mathrm{nom}} = V_{\mathrm{dc,s}}^{\mathrm{nom}} = 5\,\mathrm{kV}$). The blocking voltage of the semiconductors is set to be 1.7 kV, and a safety margin of $S_{\mathrm{f}} = 60\,\%$ is considered in the cell design. The number of submodules for the multilevel converters and the number of series-connected switches for the two-level converter is calculated using (6.10a)-(6.11b). The specifications of the dc-dc converters used for the study are summarized in Table 6.1.

Table 6.1: The simulated dc-dc converters' specifications

Parameter	Value	Parameter	Value	Parameter	Value
$V_{\mathrm{dc,p}}^{\mathrm{nom}}$	5 kV	N_{sm}	3, 5[a]	$V_{\mathrm{sw}}^{\mathrm{rated}}$	1.7 kV
$V_{\mathrm{dc,s}}^{\mathrm{nom}}$	5 kV	$\sigma_{\mathrm{sm,p}} = \sigma_{\mathrm{sm,s}}$	10 %	f_{sw}	$[1, 20]$ kHz
$P_{3\phi}^{\mathrm{nom}}$	2 MW	$\sigma_{\mathrm{dc,p}} = \sigma_{\mathrm{dc,s}}$	10 %	$\frac{\psi_{\mathrm{p}}}{\omega} = \frac{\psi_{\mathrm{s}}}{\omega}$	$[0.3, 4.9]$ µs

[a] 3 for CTB and MTAC chain-links, 5 for TAC and MMC chain-links.

The switching frequency of the converter is swept from 1 kHz up till 20 kHz, to make the comparison for a range of converter designs rather than a single design point. To avoid triangular waveforms on the ac-link, τ should be less than $1/(2f_{\mathrm{sw}})$. Moreover, the minimum value of the dwell time can change by the utilized switch technology and the tolerable $\mathrm{d}v/\mathrm{d}t$ stress. Thus, for the selected switching frequency range and the switch's specifications, the dwell time is selected to be less than 5 µs [65]; and is swept between 0.3 µs and 4.9 µs.

For this analysis, only YY and YΔ winding configurations are considered. The turns ratio, $N_{\mathrm{p}} : N_{\mathrm{s}}$, is selected to be 33 : 33 and 33 : 57 for the YY and YΔ configurations, respectively. The MFT is modeled with a series leakage inductance. It is selected using the method described in Section 5.3 to minimize the RMS phase currents for ±10 % deviation in the dc-links voltages. Figure 6.1 shows considered L_{σ}^{p}, used for different combinations of the switching frequency and the transition time for both winding configurations. It is noteworthy to mention that every point in Figure 6.1 corresponds to a different design of the converter.

Numerical calculations are carried out with MATLAB codes to determine the capacitor requirement of each converter. The switching frequency and the

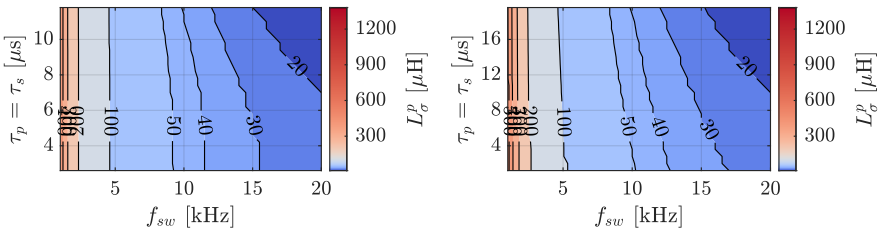

Figure 6.1: Optimum value of L_σ^{p} for different design points. **(a)** For the YY configuration. **(b)** For the YΔ configuration.

dwell time are swept in the aforementioned ranges. For every combination, the submodules and the dc-links capacitors are designed using (6.4)-(6.7) to confine the voltage ripples to $\pm 10\,\%$ of their nominal values.

Comparison of the converters' capacitor requirement

Only YY winding configuration is considered for the study of this section. Figure 6.2a depicts the total energy storage requirement of the Q2L-operating MMC-DAB as a function of the switching frequency and the transition time expressed in $\mathrm{kJ\,MW^{-1}}$. For a given f_{sw} (e.g., 1 kHz), an increase in τ increases E_{tot} of the converter. The higher the transition time, the higher the deviation in the capacitor's charges. Therefore, larger capacitors are required to keep the voltage oscillations in the desired span.

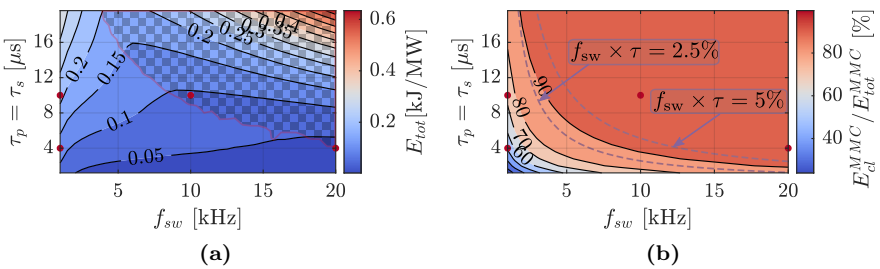

Figure 6.2: The energy storage requirement of the MMC-DAB. **(a)** The total capacitor requirement. **(b)** The chain-links capacitor requirement.

It is expected that an increase in the switching frequency should reduce the

capacitor requirement of the converter. However, for a given τ after a certain point, an increase in the switching frequency enhances E_{tot} (negative slope of the iso-lines). To better visualize this, the area with positive $\mathrm{d}E_{\text{tot}}/\mathrm{d}f_{\text{sw}}$ is illustrated with the checkered pattern. The design of the converter in this area might not be preferable from the footprint and cost points of view. By keeping τ constant and increasing the switching frequency, the percentage of the clamping period to the dc-links reduces, which makes the voltage waveforms more triangular. This changes the ac-link currents waveforms. Consequently, the currents passing through the capacitors and their charge levels are affected. For the MMC-DAB, on the border of the checkered pattern area, $\max(\Delta Q_{C_{\text{sm}k}}(\omega t))$ is equal to $\min(\Delta Q_{C_{\text{sm}k}}(\omega t))$. Moving away from that line results in an increase in either $\max(\Delta Q_{C_{\text{sm}k}}(\omega t))$ or $\min(\Delta Q_{C_{\text{sm}k}}(\omega t))$ and therefore, an increase in the capacitor size.

Figure 6.2b illustrates the percentage of chain-links capacitor requirement of the MMC-DAB. The chain-links capacitors amount to more than 70 % of E_{tot} in most design points. Thus, the pattern seen in Figure 6.2a is mainly a result of the chain-links capacitors. However, by reducing the percentage of the transition times per period—shown by blue-dashed-lines in Figure 6.2b—the size of the dc-link capacitors become comparable with the chain-links capacitors. Therefore, it is essential to include dc-link capacitors in the capacitor size evaluation of multilevel converters.

Figure 6.3 shows E_{tot} of the rest of the converters per-unitized with respect to E_{tot} map of the MMC-DAB which is calculated as

$$E_{\text{tot,pu}}^{\text{conv}}(f_{\text{sw}},\ \tau) = \frac{E_{\text{tot}}^{\text{conv}}(f_{\text{sw}}, \tau^*)}{E_{\text{tot}}^{\text{MMC}}(f_{\text{sw}}, \tau)} \tag{6.13}$$

where conv $\in \{\text{2LC},\ \text{TAC},\ \text{MTAC},\ \text{CTB}\}$. For the conventional DAB, τ^* equals zero, and for the rest of the converters, $\tau^* = \tau$.

Compared to the other converters, the conventional DAB—shown in Figure 6.3a—has the smallest E_{tot} as it does not have any chain-links. Moreover, for a given transition time, $\mathrm{d}E_{\text{tot}}/\mathrm{d}f_{\text{sw}}$ is more pronounced for the conventional DAB compared to the other converters. This is due to the size predominance of the chain-links capacitors in the multilevel converters at higher switching frequencies.

Excluding the checkered patterned areas, the TAC-DAB needs higher E_{tot} than the MMC-DAB as depicted in Figure 6.3b. Because of the complemen-

tary switching the MMC, the ac-link currents are distributed among the upper and the lower arms during the transition time. Thus, deviations in the submodules charges are smaller for the MMC-DAB, requiring a smaller chain-link capacitance than the TAC-DAB. Moreover, the immediate commutation of the currents from the lower arms to the upper arms before the transition from the negative dc rail to the positive rail in the TAC converter results in high current ripples in the dc-link compared to the MMC. Therefore, the TAC-DAB requires up to 4 times higher dc-link capacitance than the MMC-DAB.

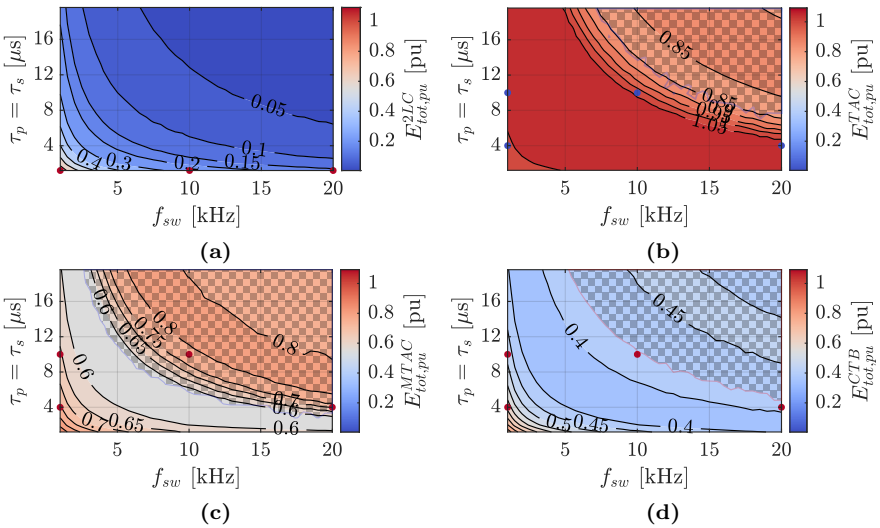

Figure 6.3: E_{tot} of the converters per-unitized by E_{tot} of the MMC-DAB shown in Figure 6.2a. **(a)** For the conventional DAB. **(b)** For the TAC-DAB. **(c)** For the MTAC-DAB. **(d)** For the CTB-DAB.

The MTAC-DAB and the CTB-DAB need smaller E_{tot} than the MMC-DAB as illustrated in Figure 6.3c and Figure 6.3d respectively. The MTAC capacitors are distributed between the arms. Besides, each arm conducts the current only for half of the transition time; therefore, the deviation in the capacitors' charges is smaller. However, due to immediate commutation of the currents between the arms—similar to the TAC—the MTAC needs larger dc-link capacitors than the MMC (and considerably smaller than the TAC). Since the chain-link capacitors are bulkier than the dc-link capacitors, the

resultant overall capacitor demand of the MTAC-DAB is up to 40 % smaller than the MMC-DAB in a wide design range.

The ac-link currents commutate from the converter's arms to the chain-links just before the transition starts in the CTB converter. This results in current notches in the dc-link. Therefore, the CTB-DAB converter needs an up to 3 times larger dc-link capacitors than the MMC-DAB. On the contrary, the CTB has a smaller chain-link capacitor requirement for two reasons. Firstly, the capacitors' charges get balanced twice per cycle (once per transition time), similar to the MTAC. Secondly, each cell is required to provide both positive and negative voltage on its terminals per transition time (due to the full-bridge configuration of the cells). Consequently, each cell is charged and discharged per transition interval for a given current direction. Accordingly, the charge oscillations per capacitor have smaller magnitudes. All in all, the CTB-DAB converter needs up to 60 % less E_{tot} compared to the MMC-DAB converter.

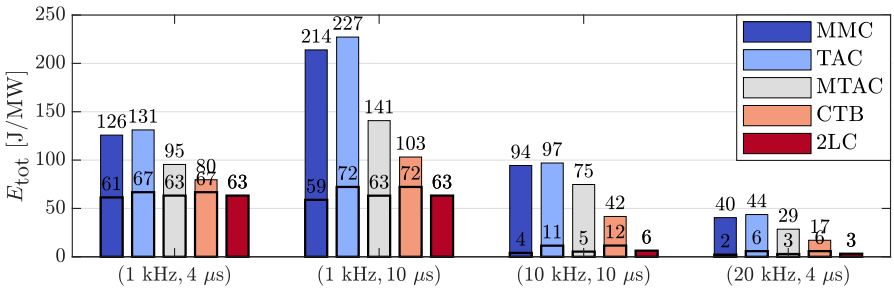

Figure 6.4: The energy storage requirement of the converters provided for (f_{sw}, τ) pairs shown by $(*)$ on Figure 6.2 and Figure 6.3. (the highlighted portions of the bars are the amount of energy required for the dc-links).

To better visualize the comparison, Figure 6.4 depicts E_{tot} of the converters for four (f_{sw}, τ) pairs shown by $(*)$ on Figure 6.2 and Figure 6.3. The lower the $f_{\text{sw}} \times \tau$, the higher the percentage of the dc-link capacitors (e.g., for the CTB-DAB and (1 kHz,4 µs) the dc-link capacitors are 84 % of the total required capacitance). Moreover, the comparison between converters for all of the selected design points shows consistent trends; with the conventional DAB having the minimum capacitor requirement followed by the CTB-DAB, MTAC-DAB, MMC-DAB, and TAC-DAB.

Comparison of the converter's semiconductor requirement

Only YY winding configuration is considered for the study of this section. Figure 6.5 depicts the RMS currents in the main (wide bars) and the auxiliary switches (narrow bars) of the converters. The RMS currents are calculated using (6.12). There are only slight variations in the RMS currents of the main switches, which was expected. However, there is a noticeable variation in the auxiliary switches' currents among the converters. $I^{\mathrm{RMS}}_{\mathrm{sw,aux}}$ for the TAC-DAB is almost two times higher than that of the MMC-DAB. This is due to the complementary switching of the MMC-DAB. Each arm of the MTAC conducts current for only half of the fundamental cycle. Therefore, it has a smaller $I^{\mathrm{RMS}}_{\mathrm{sw,aux}}$ than the TAC. Similarly, each radial switch pair in the full-bridge submodules of the CTB has to carry the current for half of the transition period. Hence, the CTB and the MTAC have equal $I^{\mathrm{RMS}}_{\mathrm{sw,aux}}$.

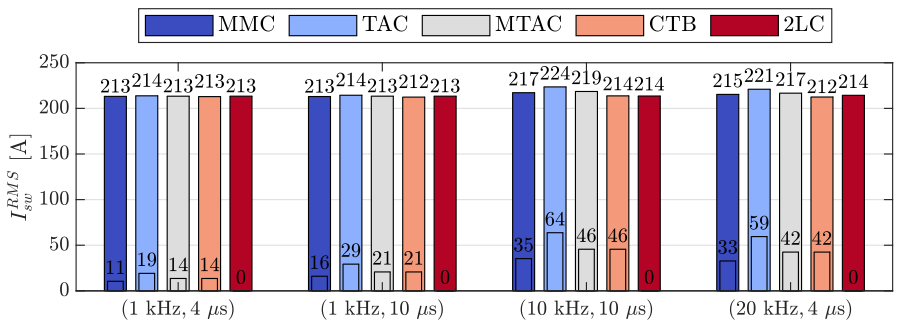

Figure 6.5: The RMS currents of the converters' switches provided for (f_{sw}, τ) pairs shown by $(*)$ on Figure 6.2 and Figure 6.3, (the wide bars and the narrow bars represent the main and the auxiliary switches respectively).

Figure 6.6 shows the semiconductor requirement of the converters in the form of the total installed apparent power of the switches defined as

$$S^{\mathrm{pu}}_{\mathrm{sw,tot}} = \frac{N_{\mathrm{sw,main}} I^{\mathrm{RMS}}_{\mathrm{sw,main}} V^{\mathrm{rated}}_{\mathrm{sw}} + N_{\mathrm{sw,aux}} I^{\mathrm{RMS}}_{\mathrm{sw,aux}} V^{\mathrm{rated}}_{\mathrm{sw}}}{S_{3\phi,\mathrm{conv}}} \tag{6.14}$$

where $N_{\mathrm{sw,main}}$ and $N_{\mathrm{sw,aux}}$ are the total number of the main and the auxiliary switches, respectively; and $S_{3\phi,\mathrm{conv}}$ is the apparent power of the converter. The highlighted portions of the bars represent the contributions of the auxil-

iary switches. As seen, much smaller switches—more than 10 % smaller—can be used for the auxiliary switches compared to the main switches.

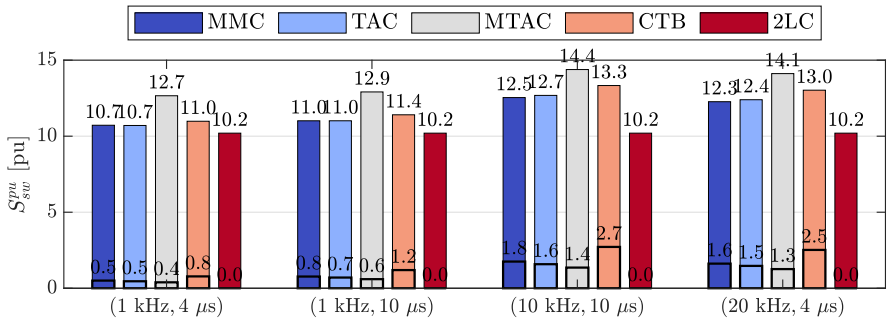

Figure 6.6: $S_{\text{sw,tot}}^{\text{pu}}$ of the converters provided for (f_{sw}, τ) pairs shown by $(*)$ on Figure 6.2 and Figure 6.3, (the highlighted portions of the bars are the installed apparent power for the auxiliary switches).

A comparison between different design points shows that the higher the $f_{\text{sw}} \times \tau$, the larger the RMS currents—especially in the auxiliary switches. Therefore, semiconductors with larger chip areas are required to transmit the same active power. Among the five topologies, the conventional DAB has the minimum $S_{\text{sw,tot}}^{\text{pu}}$ as it does not require any auxiliary switches. TAC-DAB requires almost the same semiconductor area as the MMC-DAB, even though the number of its auxiliary switches is half of the MMC-DAB's. This is due to high RMS currents in the auxiliary switches of the TAC-DAB. The MTAC-DAB and the CTB-DAB need higher $S_{\text{sw,tot}}^{\text{pu}}$ compared to the other converters. For the former, it is due to the extra submodule required to even out the number of submodules between the upper and the lower arms. While for the latter, three full-bridge submodules are required to block half of the dc-link voltages, which increases the required number of auxiliary switches.

Effects of windings configuration

It was shown in the previous section that the CTB-DAB converter has the lowest capacitor requirements among the considered multilevel DAB converters. In this section, the effects of winding configuration on the capacitor requirement of CTB-DAB and MMC-DAB are studied. The latter is an established topology in the industry and is used as a base for comparison in this section.

Figure 6.7 shows E_{tot} of the converters in $\text{kJ}\,\text{MW}^{-1}$ for both winding configurations. The grey-dashed lines show iso-lines of $\tau_{\%} = \tau_{\text{p}\%} = \tau_{\text{s}\%}$ where $\tau_{j\%} \triangleq \tau_j f_{\text{sw}} \times 100\,\%, \quad \forall j \in \{\text{p}, \text{s}\}$. For a given $\tau_{\%}$, increasing the switch-

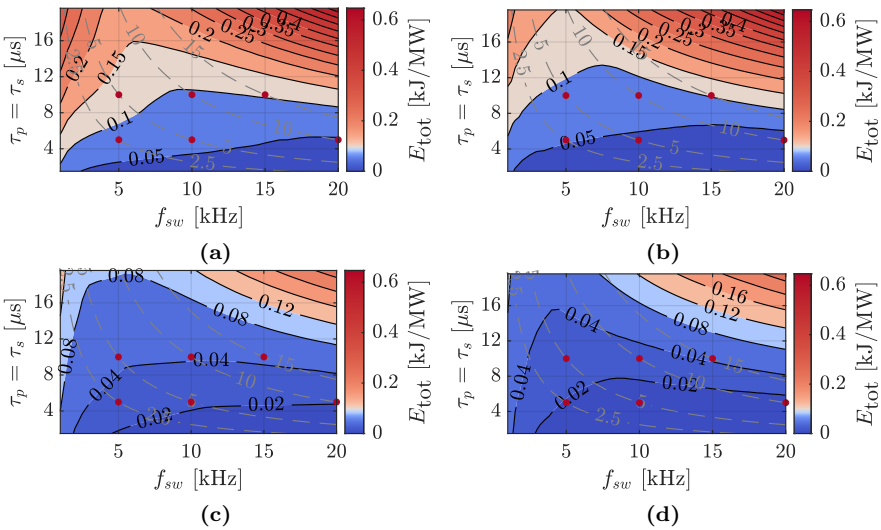

Figure 6.7: E_{tot} of the converters. The grey-dashed lines show iso-lines of $\tau_{\%}$. **(a)** For the YY-MMC-DAB. **(b)** For the YΔ-MMC-DAB. **(c)** For the YY-CTB-DAB. **(d)** For the YΔ-CTB-DAB.

ing frequency decreases E_{tot} for all converters. This is because the current waveform stays unchanged along a given $\tau_{\%}$ iso-line. Therefore, by increasing the switching frequency, the ripple in the capacitors' charges reduce. Thus, smaller capacitors can be used to limit voltage oscillations. For a constant transition time, an increase in the switching frequency results in a reduction of E_{tot} until a certain point (e.g., approximately $\tau_{\%} = 10\,\%$ for the MMC-DAB cases). Any further increase in the switching frequency increases the capacitors' sizes.

Figure 6.8 shows the ratio of $E_{\text{tot}}^{\text{Y}\Delta}$ to $E_{\text{tot}}^{\text{YY}}$ for both MMC-DAB and CTB-DAB converters. The converters with YΔ configurations need less energy storage than the converters with YY configuration, in a wide range up to $\tau_{\%} = 15\,\%$. A maximum reduction of $30\,\%$ in the total capacitor requirement can be attained for the MMC-DAB case using the YΔ configuration instead

of YY. The improvement in the CTB-DAB case is up to 40 %.

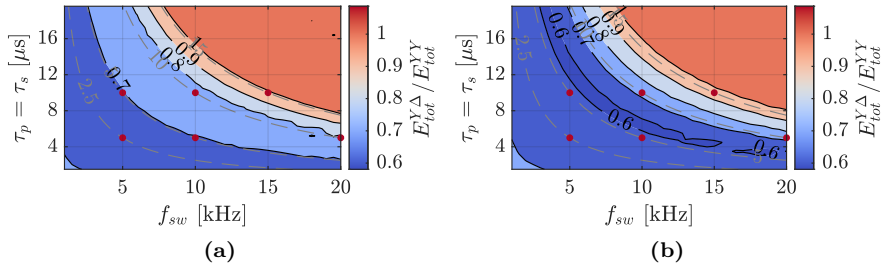

Figure 6.8: The ratio of the total energy storage requirement between the converter with YΔ connection and the converter with YY connection. **(a)** For the MMC-DAB. **(b)** For the CTB-DAB.

As can be seen from Figure 6.8, the ratio of $E_{\text{tot}}^{\text{Y}\Delta}$ to $E_{\text{tot}}^{\text{YY}}$ increases by increasing $\tau_{\%}$ where it approaches unity around $\tau_{\%} = 15\,\%$. To explain this, Figure 6.9 illustrates the phase A winding voltages and line currents of both winding configurations for $\tau_{\%} = 5\,\%$.

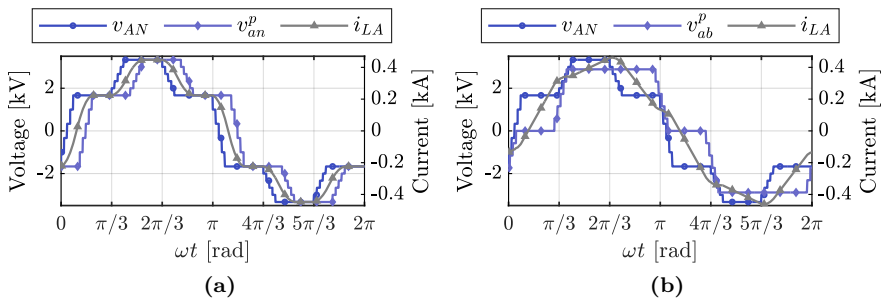

Figure 6.9: The phase A winding voltages and line currents. **(a)** For YY winding configuration. **(b)** For YΔ winding configuration.

One can see from Figure 6.9 that around $\omega t \approx \pi$, the value of $v_{\text{AN}}(\omega t) - v_{ab}^{\text{P}}(\omega t)$ (for the YΔ case) is much larger than the value of $v_{\text{AN}}(\omega t) - v_{an}^{\text{P}}(\omega t)$ (for the YY case). Therefore, the current drops faster for the YΔ case, and the chain-links experience smaller currents when they start to conduct at $\omega t \approx \pi$. Consequently, the charge variations are less, and smaller capacitors are required to limit the voltage oscillations. By increasing the value of $\tau_{\%}$, the

THD of the currents reduce for both YY and YΔ cases, and for $\tau_{\%} \approx 15\,\%$, the currents become almost sinusoidal. Therefore, for $\tau_{\%} \approx 15\,\%$, the converters with YΔ connection have similar capacitor requirements as the YY variants.

Figure 6.10 shows the share of dc-links' capacitors for different converters. For the MMC-DAB and $\tau_{\%} \geq 5\,\%$, more than 90 % of the total energy storage requirement belongs to the chain-links. The share of the dc-links increases by up to 70 % as the value of $\tau_{\%}$ decreases. On the other hand, dc-link capacitors have a considerable share in the total energy storage requirement for the CTB-DAB where E_{dc} account for more than 40 % of E_{tot} of CTB-DAB with both YY and YΔ connections and $\tau_{\%} \leq 5\,\%$.

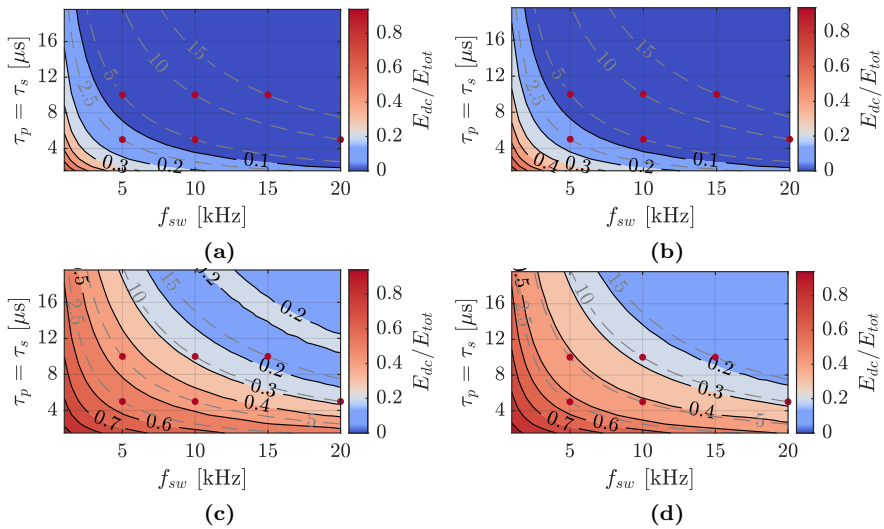

Figure 6.10: The ratio of dc-links' energy storage requirement to the total value. **(a)** For the YY-MMC-DAB. **(b)** For the YΔ-MMC-DAB. **(c)** For the YY-CTB-DAB. **(d)** For the YΔ-CTB-DAB.

To sum up, Figure 6.11 shows the capacitor requirement of the converters on points marked with (∗) in Figure 6.7 and Figure 6.10. The share of the dc-link capacitors is highlighted for each converter. The CTB-DAB needs less capacitor compared to the MMC-DAB in general. Similarly, the converters with the YΔ configuration have a smaller capacitor requirement than the YY variants. Thus, the YΔ-CTB-DAB has the smallest, and the YY-MMC-

DAB has the highest energy storage requirements. For $\tau_{\%} \leq 15\,\%$, the YΔ-connected CTB-DAB can achieve up to 78 % (58 %) less capacitor requirement compared to the YY-connected MMC-DAB in the best case (the worst case). Another observation is that the dc-link capacitors amount to a considerable

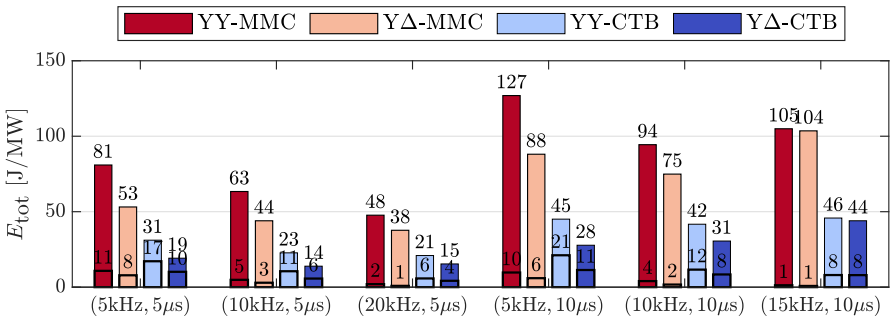

Figure 6.11: Energy storage requirement of the converters for a few selected points marked with (∗) in Figure 6.7 and Figure 6.10 (the highlighted portion of the bars depicts the share of the dc-link capacitors).

share of the total capacitor requirement for the CTB-DAB converter. On the other hand, the chain-links capacitors are considerably larger for the MMC-DAB.

6.3 Lifetime of semiconductors

Reliability and long lifetime are two of the main factor in selecting a semiconductor for converters [68]. The two major failure mechanisms inside power devices are bond wire degradation and solder fatigue. According to the study in [69], the thermal cycling stresses in the range of seconds are mainly responsible for the former failure mechanism, while the slow thermal cycling stresses caused by ambient temperature variations are more related to the latter. Bond wire degradation is considered to be the main failure mechanism in this thesis.

Different lifetime models for silicon-based power devices have been summarized in [70]. The SKiM63 lifetime model proposed in [41] considers bond wire degradation as the main failure mechanism. According to the SKiM63 model, the expected number of cycles to failure N_{f} is calculated as

$$N_{\mathrm{f}} = A\,(\Delta T_{\mathrm{j}})^{\alpha}\,(ar)^{(\beta_1 \Delta T_{\mathrm{j}} + \beta_0)} \left(\frac{C + (t_{\mathrm{on}})^{\gamma}}{C+1}\right) \exp\left(\frac{E_{\mathrm{a}}}{k_{\mathrm{B}} \times T_{\mathrm{jm}}}\right) f_{\mathrm{diode}} \quad (6.15)$$

where A is a scaling factor, ΔT_{j} is the semiconductor junction temperature swing, ar is the wire bond aspect ratio, t_{on} is the load pulse duration in s, E_{a} is the activation energy in eV, T_{jm} is the mean junction temperature in K, K_{B} is the Boltzmann constant in $\mathrm{eV\,K^{-1}}$, and f_{diode} is a factor to consider the lifetime of diode ($f_{\mathrm{diode}} = 0.6204$) or switches ($f_{\mathrm{diode}} = 1$). Table 6.2 summarizes the parameters of SKiM63 model [41].

Table 6.2: The SKiM63 model parameters [41]

Parameter	Value	Parameter	Value
A	3.4368×10^{14}	α	-4.923
E_{a}	$6.606 \times 10^{-2}\,\mathrm{eV}$	β_0	1.942
β_1	$-9.012 \times 10^{-3}\,\mathrm{K^{-1}}$	C	1.434
K_{B}	$8.617 \times 10^{-5}\,\mathrm{eV\,K^{-1}}$	γ	-1.208
f_{diode}	1, 0.6204[a]		

[a] 1 for switches and 0.6204 for diodes.

The accumulated damage D_{sw} of switches under a single run of a given mission profile can be determined by Miner's rule [71] as

$$D_{\mathrm{sw}} = \sum_{j=1}^{n} \frac{N_j}{N_{\mathrm{f}j}} \quad (6.16)$$

where n is the number of distinct cycles in the mission profile, $N_j\ \forall j \in \{1, ..., n\}$ is the number of repetitions of jth cycle in the mission profile, and $N_{\mathrm{f}j}$ is the expected number of cycles to failure for the jth cycle, calculated from (6.15). The parameters n and N_j can be obtained from the mission profile using the rainflow counting algorithms [72]. For a given mission profile, the repetition rate, N_{r} is defined as the inverse of D_{sw}. $N_{\mathrm{r}} = 1$ means that the switch can only withstand a single run of the mission profile.

Case study setup

The temperature swings are affected by the mission profile of the converter. Therefore, a lifetime analysis of the converter's switches considering the mission profile is necessary [73]. In this section, a case study on a Q2L-operating MMC-DAB for wind turbine applications is performed.

Partial load losses are of significant importance for wind turbine applications. SiC metal–oxide–semiconductor field-effect transistors (MOSFETs) have low losses in partial loads compared to insulated-gate bipolar transistors (IGBTs). Also, low switching losses of SiC MOSFETs make them a suitable choice for DAB converters for wind turbine applications. For the SiC MOSFETs, the research on the lifetime models is still ongoing [74]. However, existing methods for silicon-based power devices can still provide a reasonable estimation of the lifetime.

Mission profile of a wind turbine

Wind speed and generated electrical power measurements for 300 days were available for a 2 MW on-shore wind turbine located in Munkagård area, nearby Tvååker community in Sweden [75]. Figure 6.12 shows the measured wind speed and generated electrical power from the turbine for 300 days with the sampling frequency of 1 Hz.

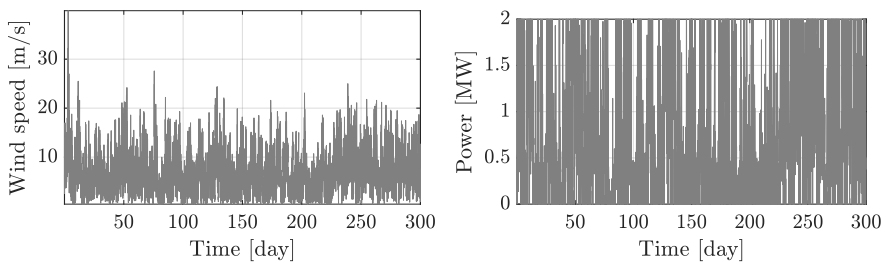

Figure 6.12: 300 days mission profile of a wind turbine with 1 Hz sampling frequency. **(a)** The wind speed. **(b)** The generated electrical power.

Converter modeling

The model of an MMC-DAB is implemented in MATLAB. For simplicity, it is assumed that the primary and secondary sides have the same nominal dc-link voltages ($V_{\mathrm{dc,p}}^{\mathrm{nom}} = V_{\mathrm{dc,s}}^{\mathrm{nom}} = 5\,\mathrm{kV}$). The converter is rated for 2 MW and is switched with 5 kHz. The MFT is modeled with a series leakage inductance. It is selected using the method described in Section 5.3 to minimize the RMS phase currents for $\pm 10\,\%$ deviation in the dc-links voltages. Specifications of the dc-dc converters used for the study are summarized in Table 6.3.

Table 6.3: The simulated dc-dc converters' specifications

Parameter	Value	Parameter	Value	Parameter	Value
$V_{\mathrm{dc,p}}^{\mathrm{nom}}$	5 kV	N_{sm}	5	f_{sw}	5 kHz
$V_{\mathrm{dc,s}}^{\mathrm{nom}}$	5 kV	$V_{\mathrm{sw}}^{\mathrm{rated}}$	1.7 kV	L_{σ}^{p}	92 µH
$P_{3\phi}^{\mathrm{nom}}$	2 MW	$\sigma_{\mathrm{sm},j} = \sigma_{\mathrm{dc,j}}$	10 %[a]	τ_j	10 µs[a]

[a] for $j \in \{\mathrm{p}, \mathrm{s}\}$.

The blocking voltage of the semiconductors is selected to be 1.7 kV. A safety margin of $S_{\mathrm{f}} = 60\,\%$ is considered in the cell design, and the number of submodules is calculated using (6.11a). CAS300M17BM2 SiC MOSFET power modules [76] and C2M0045170P discrete SiC MOSFETs with TO-247-4-plus packaging [77] from CREE are used as the main and auxiliary switches. The switches' thermal behavior is modeled using a fourth-order Foster network representing the junction-to-case thermal impedance.

The measurement data for the temperature inside the nacelle was unavailable. Therefore, the heat sink temperature is set as a fixed value for simplicity. It is assumed that the case temperatures of the switches are constant at 40 °C. Therefore, slow thermal cycling stresses can be neglected, and bond wire degradation becomes the main factor to be considered when conducting the lifetime analysis. The SKiM63 model (6.15) is used to estimate the lifetime of the switches. For thermal cycles longer than 1 s, it is assumed that $t_{\mathrm{on}} = 1\,\mathrm{s}$; while for the thermal cycles shorter than 1 s, t_{on} is selected to be 0.07 s. Also, it is assumed that $ar = 0.31$.

Direct simulation of a converter with 5 kHz switching frequency for 300 days

of mission profile is impossible. Therefore, the study is divided into two parts; the first is to calculate the life consumption for long-term thermal cycles (i.e., longer than one second), and the second is to perform the calculations for short-term thermal cycles (i.e., shorter than one second). The converter is simulated at different load levels, and the steady-state junction temperatures are stored. The average junction temperature profile of the switches is obtained by combining the converter's power profile (shown in Figure 6.12b) and the average junction temperatures of the switches obtained from the simulations. Figure 6.13 shows the low-pass-filtered average junction temperature profile for one of the primary-side submodule's switches.

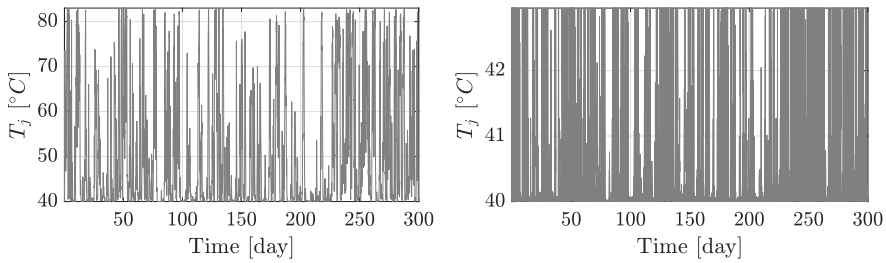

Figure 6.13: T_j profile of the primary-side switches. **(a)** The First submodule's main switch. **(b)** The First submodule's auxiliary switch.

The rainflow counting algorithm is employed to identify the number of thermal cycles in the junction temperature profile. In addition to the cycle numbers, the temperature swings, ΔT_j, and the medium junction temperature of the corresponding cycles, T_jm, are extracted. Figure 6.14 shows the rainflow counting results for one of the main switches of the secondary side. $N_{\mathrm{f}j}$ of each switch is calculated by using ΔT_j and T_jm as inputs to (6.15). Finally, the lifetime of the switches is estimated using (6.16) and the length of the mission profile.

Analysis of simulation results

Table 6.4 summarizes the lifetimes of the switches considering only long-term thermal cycles for one of the inverter's arms. Since complementary switching is used and the intermediate 3ϕ system is assumed to be symmetrical, the

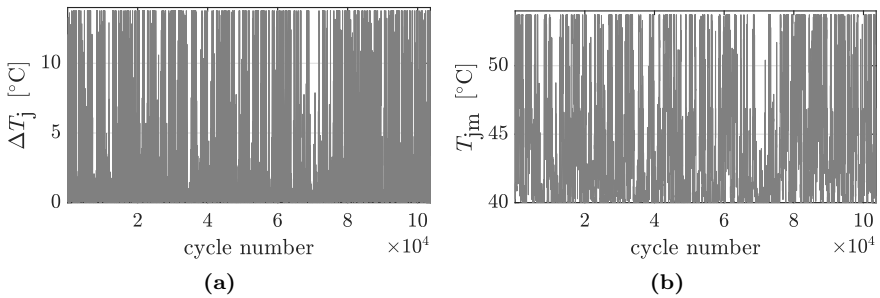

Figure 6.14: The rainflow counting results for one of the secondary-side main switches. **(a)** ΔT_j of distinct cycles. **(b)** T_{jm} of distinct cycles.

same results will be obtained for the rest of the arms.

Table 6.4: Simulation results for the lifetime of switches

Lifetime [years]	**main switches**				
	#1	**#2**	**#3**	**#4**	**#5**
Primary	552	552	552	552	550
Secondary	2.7×10^5	2.5×10^5	2.7×10^5	2.6×10^5	2.5×10^5
Lifetime [years]	**auxiliary switches**				
	#1	**#2**	**#3**	**#4**	**#5**
Primary	1.3×10^8	2.3×10^8	1.4×10^8	2.1×10^8	1.1×10^8
Secondary	5.1×10^4	5.9×10^4	4.9×10^4	4.4×10^4	4.6×10^4

The first observation is the absurdly long lifetime of the switches. This is due to the low ΔT_j and the average temperature of the switches, as shown in Figure 6.14. Nonetheless, there is a variation in the lifetime of the switches in different submodules of the inverter. The reason is the sorting algorithm; the submodules are sorted every half-cycle based on their voltages and the direction of the phase currents—irrespective of the junction temperatures. This causes a slight variation between the junction temperatures of the switches of the submodules and therefore affecting their lifetime.

Figure 6.15 depicts the switch junction temperature profiles of one of the submodules under full-load operation. The main switches conduct the currents for almost half a cycle and have moderate temperature swings of 2.6 °C and 0.8 °C for the primary and the secondary sides, respectively. However, the auxiliary switches conduct short pulses of high currents, which results in severe temperature swings of 2.5 °C and 17 °C for the primary and the secondary side inverters, respectively.

For most of the conduction period, the primary-side main switches and the secondary-side auxiliary switches conduct positive currents and operate in the forward conduction mode. On the other hand, the secondary-side main switches and the primary-side auxiliary switches conduct negative currents. Therefore, these switches operate in the third quadrant. The conduction losses predominate in MOSFETs, and operation in the third-quadrant results in lower conduction losses. Therefore, the primary-side auxiliary switches and the secondary-side main switches are less thermally stressed than their counterparts in the other inverter, as shown in Figure 6.15.

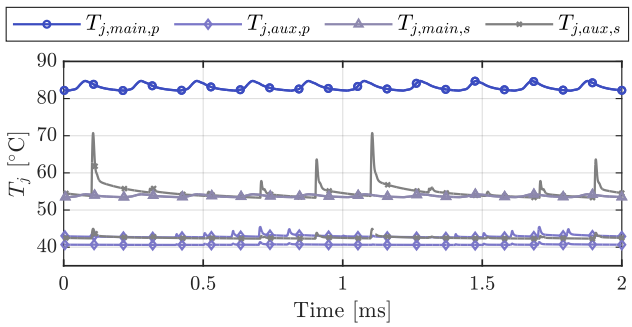

Figure 6.15: The junction temperature of the switches of the first submodule under full-load operation for ten cycles. The dashed lines are the Junction temperatures for the case with two C2M0045170P in parallel.

Figure 6.16 shows one of the submodule's switches junction temperature as a function of the converter power. The solid lines show the average junction temperatures, and the dashed lines depict the maximum and minimum temperatures of the switch. As can be seen, the secondary-side auxiliary MOSFET is the most thermally stressed switch for all power levels. Considering these short-term temperature swings, it is not sufficient to assess the stress on the

switches for the Q2L modulation only with the long-term thermal cycles.

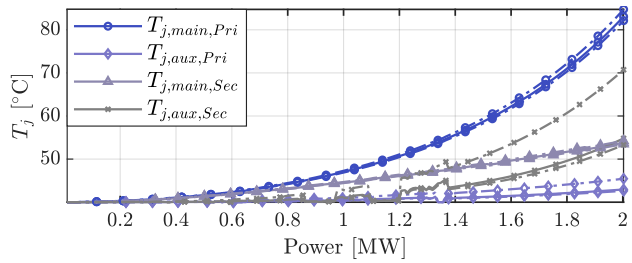

Figure 6.16: The junction temperature of the switches of the first submodule. The solid lines are the average junction temperatures, and the dashed lines are the bounds of the temperature profiles.

To consider these short-term temperature oscillations, the power profile shown in Figure 6.12b is binned into 200 power intervals. Figure 6.17 shows the duration of the power production from the turbine for each power interval. The mean value of the power in each bin is considered to represent that bin, and the temperature profile for the representative power level is used to calculate the life consumption of the switches.

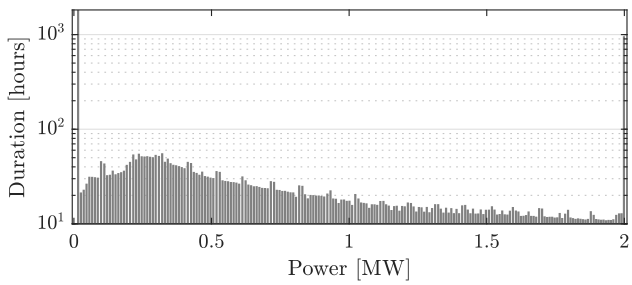

Figure 6.17: The power distribution of the wind profile given in Figure 6.12.

The total life consumption of a switch can be calculated by summing up the life consumption from the long-term and the short-term thermal cycles. Since the same mission profile is used to calculate both life consumptions, the lifetime can be easily calculated by dividing the length of the mission profile by the total life consumption.

Figure 6.18 shows the lifetime of the primary-side and the secondary-side

inverters' first submodule's switches. The thinner bars are the lifetimes considering the short-term temperature cycles, and the thick bars are without them. As can be seen, neglecting the short-term cycles has a negligible effect on the lifetime of the main switches. The reason is that the temperature variations are insignificant for the main switches. However, there is a drastic decrease in the lifetime of the auxiliary switches when the short-term cycles are considered—especially for the secondary side inverter.

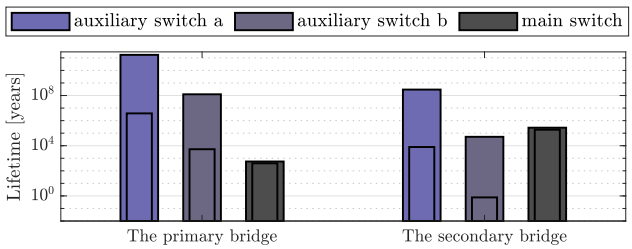

Figure 6.18: Lifetime comparison of the primary-side and the secondary-side inverters' first submodule's switches (The lifetime considering the short-term thermal cycles are illustrated with the thinner bars) where $\{a, b\} \in \{2 \times \text{C2M0045170P},\ \text{C2M0045170P}\}$.

As shown in Figure 6.18, the secondary side submodules will reach the end of their life in less than a year if C2M0045170P is used as the auxiliary switches. Two C2M0045170P in parallel are used instead to solve this issue. In this way, the lifetime of the secondary side auxiliary switches is extended considerably. The lifetime of the primary-side auxiliary switches can be extended with the same approach. However, the main switch will be the weakest link in the lifetime of the primary-side submodules.

6.4 Conclusions and discussion

The capacitor and semiconductor requirements of selected isolated dc-dc converters for high-power and medium-voltage applications are compared in this chapter. A numerical comparison is made for a range of switching frequencies and transition times, considering not only the submodule capacitors of the converters but also the dc-link capacitors. Likewise, a comparison regarding the semiconductor requirement is performed for the converters.

The comparison between the converters revealed that the conventional DAB requires the minimum amount of capacitance. Among the multilevel converters, the TAC-DAB needs the highest capacitance, more than 5 % higher than the MMC-DAB. Furthermore, the MTAC-DAB and the CTB-DAB need a smaller amount of capacitance than the MMC-DAB. It is concluded that by utilizing the MTAC and the CTB instead of MMC, the amount of required energy storage can be reduced by up to 40 % and 60 %, respectively.

Also, the effect of winding configurations on the required energy storage is studied. An MMC-DAB and a CTB-DAB converter are compared for different winding configurations. It is shown that the YΔ connection considerably reduces the capacitor requirements of the converters. In the best case, the capacitor requirement can be reduced for the MMC-DAB and the CTB-DAB by 30 % and 40 %, respectively. A comparison between the converters showed that the YY-MMC-DAB and the YΔ-CTB-DAB have the highest and the lowest energy storage requirements, respectively. Moreover, it is shown that the YΔ-CTB-DAB can achieve up to 78 % (58 %) less energy storage compared to the YY-MMC-DAB in the best case (worst case).

Moreover, it was demonstrated that the size of the dc-link capacitors becomes comparable with the chain-link capacitors when the percentage of the transition time per period is reduced. It was shown that an increase in the switching frequency does not necessarily result in capacitor size reduction. On the contrary, for a given transition time, an increase in the switching frequency after a certain point can result in a capacitor size increase for the studied multilevel topologies with the Q2L modulation. The comparison regarding the semiconductor requirement revealed that the MMC-DAB requires the smallest installed switch power, followed by the TAC-DAB and CTB-DAB among the multilevel converters.

The study of the Q2L-operating MMC-DAB with MOSFETs revealed that the primary-side main and the secondary-side auxiliary switches have higher average junction temperatures than their secondary- and primary-side counterparts, respectively. Moreover, it is shown that the auxiliary switches are more thermally stressed than the main switches due to the impulsive conduction of currents. It is demonstrated that secondary-side auxiliary switches cannot endure a single mission profile, While their primary-side counterparts have an acceptable lifetime. To solve this issue, it is suggested to use two parallel switches on the secondary-side converter for the auxiliary switches.

CHAPTER 7

Soft-Switching Boundaries of M-Level-to-N-Level DAB

This chapter is based on the following article

[I] **B. Khanzadeh**, T. Thiringer, "Closed-Form ZVS boundaries for three-phase M-level-to-N-level DAB converters with different winding configurations," Published in *IEEE Transactions on Power Electronics*, pp. 1–16, 2023, doi: 10.1109/TPEL.2023.3260682.

7.1 Introduction

The soft-switching operation region of a 1ϕ conventional DAB (2LC) with SPS modulation is discussed in [7]. It is shown that the converter switches can turn ON under ZVS under certain conditions. Since then, extensive research has been done on analyzing and improving the ZVS range of the 1ϕ conventional DAB converter [78]–[84]. The ZVS operation of 1ϕ multilevel DAB converters is also studied to a great extent in literature. This includes: NPC based NPC-NPC-DAB converter [37], [85], [86], MMC based MMC-MMC-DAB converter [87], and 2LC-NPC-DAB converter [88].

The ZVS operating range of the conventional 3ϕ DAB (2LC-2LC-DAB) with

YY connection of the MFT windings and SPS modulation is also discussed in [7]. Similar to the 1ϕ conventional DAB, its ZVS operation is limited in partial loads. Different methods are discussed in the literature to widen the 3ϕ-YY-DAB's ZVS range in partial loads. One way is the duty-cycle control and asymmetrical operation of the converter as discussed [89]–[91]. Another solution is to use a winding configuration other than the YY connection [25], [92]. The impact of winding configurations of the MFT on the ZVS range of the 2LC-2LC-DAB with SPS modulation is discussed in [25]. It is shown that the converter with the YΔ connection of the windings has a wider ZVS range compared to the YY and the $\Delta\Delta$ variants at partial loads.

The soft-switching operation of 3ϕ multilevel DAB converters is also studied in the literature [24], [26], [27]. In [26], the performance of a YY-type 3ϕ DAB with three-level phase legs is investigated. It is shown that the extra degrees of freedom provided by the three-level legs can be used to extend the ZVS operation range of the converter. A DAB converter with a combination of two-level and three-level inverters (2LC-NPC-DAB) is studied in [27], where the effect of winding resistance on the performance and the soft-switching operation of the converter is investigated. The ZVS range of a Q2L operating 3ϕ MMC-MMC-DAB with SPS modulation and YY connection of MFT windings is discussed in [24]. This study has focused on specific operating conditions where both bridges have the same transition times, and the phase shift is limited to specific values.

Available literature has focused on combinations of specific converter topologies with certain winding configurations. The effects of having a different number of levels or transition times for the bridges have not been studied in detail. Furthermore, the effects of winding configurations on the ZVS operation of the multilevel converters are not studied. To summarize, missing is a generalized closed-form formulation of ZVS boundaries independent of the primary and the secondary converter topologies. Where also the effects of winding configurations of the MFT, the number of levels in the bridges, transition times of the bridges, and dead times are considered in a combined way. The purpose of this chapter is to fill these gaps by

- providing general closed-form ZVS conditions independent of the topology of the bridges;
- studying and quantifying the effects of the number of levels in the bridges, the transition times, and the dead times of the switches;

- considering the effects of different winding configurations;

The provided closed-form ZVS conditions can be easily implemented in numeric computing platforms for design optimizations. The converter topologies that the derived boundaries can be used for include (but are not limited to): 2LC, T-type converter, NPC converter, MMC, TAC [38], and CTB converter [40]. Eventually, a set of approximated ZVS conditions is provided, which can be a helpful rule of thumb for design engineers.

7.2 Modeling of soft-switching boundaries

In this section, closed-form equations are derived that identify the ZVS boundaries of a 3ϕ-ML-NL-DAB converter. A current-based method is used to derive the turn-ON ZVS boundaries. According to this method, the switch will turn ON with zero voltage if the antiparallel diode conducts the current during the switching event [7].

Converter specific conditions

Let's define $i_A^+ \equiv i_A^+(\omega t)$ as the phase A upper arm current flowing from the positive dc-link to the phase terminal node. Similarly, $i_A^- \equiv i_A^-(\omega t)$ is defined as the phase A lower arm current flowing from the phase terminal node to the negative dc-link. Also, $i_A^0 \equiv i_A^0(\omega t)$ is defined as the phase A clamping leg current flowing from the phase terminal node to the mid-point of the dc-link. i_A^+, i_A^-, and i_A^0 are illustrated in Figure 2.3 and Figure 2.4 for different converter topologies. Using the waveforms of Figure 2.5 as a reference, the ZVS conditions for each converter are denied as follows.

Two-level converter (2LC)

The turn-ON ZVS is achieved when $i_A^+(\omega t = 0) < 0$ and $i_A^-(\omega t = \pi) < 0$ [7].

NPC and T-type converter

The lower and upper arms ZVS is ensured when $i_A^-(\omega t = \pi + \theta_0) < 0$, and $i_A^+(\omega t = \theta_0) < 0$. To achieve ZVS for the clamping arm $i_A^0(\omega t = \pi - \theta_0) < 0$, and $i_A^0(\omega t = 2\pi - \theta_0) > 0$ [26].

Modular multilevel converter (MMC)

To ensure ZVS for the main switches of the upper arm, $i_A^+(\omega t = \theta_k) < 0$ and $i_A^+(\omega t = 2\pi - \theta_k) < 0$ where $k \in \{0, ..., M-1\}$. For the auxiliary switches of the upper arm $i_A^+(\omega t = \pi \pm \theta_k) > 0$ where $k \in \{0, ..., M-1\}$. To turn ON the main switches of the lower arm under ZVS $i_A^-(\omega t = \pi \pm \theta_k) < 0$ where $k \in \{0, ..., M-1\}$. Finally, for the auxiliary switches of the lower arm $i_A^-(\omega t = \theta_k) > 0$, $i_A^-(\omega t = 2\pi - \theta_k) > 0$ where $k \in \{0, ..., M-1\}$.

Transition arm converter (TAC)

To turn ON the main switches of the upper arm with ZVS, $i_A^+(\omega t = \theta_k) < 0$ and $i_A^+(\omega t = 2\pi - \theta_k) < 0$ where $k \in \{0, ..., M-1\}$. For the auxiliary switches of the upper arm $i_A^+(\omega t = \pi \pm \theta_k) > 0$ where $k \in \{0, ..., M-1\}$. Finally, $i_A^-(\omega t = \pi + \theta_{M-1}) < 0$ to ensure ZVS for the lower arm switches.

Controlled transition bridge (CTB)

The lower and upper arms ZVS is ensured when $i_A^-(\omega t = \pi + \theta_{M-1}) < 0$, and $i_A^+(\omega t = \theta_{M-1}) < 0$. To turn ON the switches of chain-links under ZVS $i_A^0(\omega t = \theta_k) > 0$, $i_A^0(\omega t = \pi \pm \theta_k) < 0$, and $i_A^0(\omega t = 2\pi - \theta_k) > 0$.

General conditions

The ZVS conditions of converters are summarized in Table 7.1. A closer examination of Table 7.1 conditions and Figure 2.3 and Figure 2.4 reveals that the ac-link currents can be used instead of the arm currents to derive ZVS boundaries independent of the converter topology. Also, it would be enough to investigate only half of the ac-link currents due to the half-wave symmetry. Considering the directions of the currents shown in Figure 2.3 and Figure 2.4, the relations given in Table 7.1, and the interval $\omega t \in \left[-\frac{\pi}{2}, \frac{\pi}{2}\right]$ as half of the waveform, the ZVS conditions of all of the converters can be summarized as

$$i_{LA}(\omega t = \pm\theta_k) < 0 \qquad \forall k \in \{0, ..., M-1\}. \tag{7.1}$$

The ZVS conditions derived hereafter can be used for any other converter topology than shown in Figure 2.3 and Figure 2.4 if its ZVS conditions can be formulated as (7.1).

Table 7.1: Turn-ON ZVS conditions of the converters

2LC	**NPC**	**T-type**
$i_A^+(\omega t = 0) < 0$	$i_A^+(\omega t = \theta_0) < 0$	$i_A^+(\omega t = \theta_0) < 0$
$i_A^-(\omega t = \pi) < 0$	$i_A^0(\omega t = \pi - \theta_0) < 0$	$i_A^0(\omega t = \pi - \theta_0) < 0$
	$i_A^-(\omega t = \pi + \theta_0) < 0$	$i_A^-(\omega t = \pi + \theta_0) < 0$
	$i_A^0(\omega t = 2\pi - \theta_0) > 0$	$i_A^0(\omega t = 2\pi - \theta_0) > 0$
MMC[a]	**TAC**[a]	**CTB**[a]
$i_A^+(\omega t = \pm\theta_k) < 0$	$i_A^+(\omega t = \pm\theta_k) < 0$	$i_A^0(\omega t = \pm\theta_k) > 0$
$i_A^-(\omega t = \pm\theta_k) > 0$	$i_A^+(\omega t = \pi \pm \theta_k) > 0$	$i_A^+(\omega t = \theta_{M-1}) < 0$
$i_A^+(\omega t = \pi \pm \theta_k) > 0$	$i_A^-(\omega t = \pi + \theta_{M-1}) < 0$	$i_A^0(\omega t = \pi \pm \theta_k) < 0$
$i_A^-(\omega t = \pi \pm \theta_k) < 0$		$i_A^-(\omega t = \pi + \theta_{M-1}) < 0$

[a] for these converters $k \in \{0, ..., M-1\}$.

Identification of soft-switching boundaries

A common approach for deriving the ZVS conditions of the conventional DAB is to use piecewise linear equations of currents [7], [25]. A similar approach is taken in [24] for a Q2L-operating 3ϕ-YY-MMC-MMC-DAB. However, this method can not be easily generalized for M-level-to-N-level DAB converters due to the complexity of the waveforms. An alternate approach is the identification of ZVS from the Fourier-decomposed waveforms. This method is used in [80] for 2LC-2LC-DAB converters. In this method, the sign of current at the switching events is identified in the Fourier domain. Then the final ZVS conditions are back-calculated using inverse Fourier calculations. The reference P2G waveforms used for ZVS calculation of YY and YΔ configurations are shown in Figure 7.1.

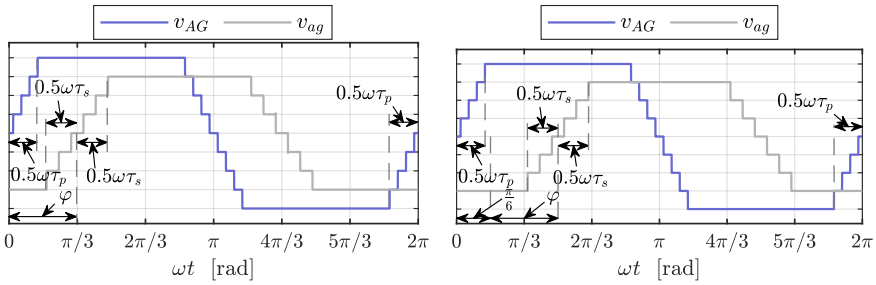

Figure 7.1: Reference P2G waveforms for ZVS calculations. **(a)** For YY-DAB. **(b)** For YΔ-DAB.

YY-connected DAB

Considering the references waveforms of Figure 7.1a, the switching events of the YY-connected converters occur in the interval $-0.5\omega\tau_\mathrm{p} \leq \omega t \leq 0.5\omega\tau_\mathrm{p}$ for the primary bridge and $\varphi - 0.5\omega\tau_\mathrm{s} \leq \omega t \leq \varphi + 0.5\omega\tau_\mathrm{s}$ for the secondary bridge. The phase current of the converter is equivalent to the line current of the MFT. Therefore, the ZVS conditions (7.1) can be reformulated as

$$i_{\mathrm{L}A}^{\mathrm{YY}}\left(\omega t = \pm\theta_{k_\mathrm{p}\mathrm{p}}\right) < 0 \qquad \forall k_\mathrm{p} \in \{0, ..., M_\mathrm{p} - 1\} \tag{7.2a}$$

$$i_{\mathrm{L}a}^{\mathrm{YY}}\left(\omega t = \varphi \pm \theta_{k_\mathrm{s}\mathrm{s}}\right) > 0 \qquad \forall k_\mathrm{s} \in \{0, ..., M_\mathrm{s} - 1\}. \tag{7.2b}$$

YΔ-connected DAB

The YΔ connection of the windings introduces a phase shift on the primary-side-referred waveforms based on the vector group of the winding connection [34]. In this section, the vector group with $+30°$ phase displacement (YΔ11) is used during the derivation process of currents. Regardless, the final results can be used for any vector group as $\varphi \in [0, \pi/2]$. Considering the references waveforms given in Figure 7.1b, the switching events of the YΔ-connected converters occur in the interval $-0.5\omega\tau_\mathrm{p} \leq \omega t \leq 0.5\omega\tau_\mathrm{p}$ for the primary bridge and $\varphi + \pi/6 - 0.5\omega\tau_\mathrm{s} \leq \omega t \leq \varphi + \pi/6 + 0.5\omega\tau_\mathrm{s}$ for the secondary bridge. The phase current of the converter is equivalent to the line current of the MFT.

Therefore, the ZVS conditions (7.1) can be reformulated as

$$i_{\mathrm{L}A}^{\mathrm{Y}\Delta}\left(\omega t=\pm\theta_{k_{\mathrm{p}}\mathrm{p}}\right)<0 \qquad \forall k_{\mathrm{p}}\in\{0,...,M_{\mathrm{p}}-1\} \tag{7.3a}$$

$$i_{\mathrm{L}a}^{\mathrm{Y}\Delta}\left(\omega t=\varphi+\pi/6\pm\theta_{k_{\mathrm{s}}\mathrm{s}}\right)>0 \qquad \forall k_{\mathrm{s}}\in\{0,...,M_{\mathrm{s}}-1\}. \tag{7.3b}$$

Closed-form general soft-switching boundaries

Steps of calculating (7.2) and (7.3) are discussed in Appendix B. Only the final results are presented here.

YY-connected DAB

Expanding the ZVS boundaries of the primary bridge $i_{\mathrm{L}A}^{\mathrm{YY}}\left(\omega t=\pm\vartheta_{\mathrm{p}}\right)<0$ where $\vartheta_{\mathrm{p}}\in\{\theta_{k\mathrm{p}},\ \forall k\in\{0,...,M_{\mathrm{p}}-1\}\}$ results in

$$\frac{N_{\mathrm{s}}U_{\mathrm{p}}}{N_{\mathrm{p}}U_{\mathrm{s}}}>\frac{\sum_{k=0}^{M_{\mathrm{s}}-1}\left(h_1\left(\theta_{k\mathrm{s}}\mp\vartheta_{\mathrm{p}}+\varphi\right)+h_1\left(\theta_{k\mathrm{s}}\pm\vartheta_{\mathrm{p}}-\varphi\right)\right)}{\sum_{k=0}^{M_{\mathrm{p}}-1}\left(h_1\left(\theta_{k\mathrm{p}}-\vartheta_{\mathrm{p}}\right)+h_1\left(\theta_{k\mathrm{p}}+\vartheta_{\mathrm{p}}\right)\right)}. \tag{7.4}$$

Similarly, the ZVS boundaries of the secondary bridge $i_{\mathrm{L}a}^{\mathrm{YY}}\left(\omega t=\varphi\pm\vartheta_{\mathrm{s}}\right)>0$ where $\vartheta_{\mathrm{s}}\in\{\theta_{k\mathrm{s}},\ \forall k\in\{0,...,M_{\mathrm{s}}-1\}\}$ can be expanded as

$$\frac{N_{\mathrm{s}}U_{\mathrm{p}}}{N_{\mathrm{p}}U_{\mathrm{s}}}<\frac{\sum_{k=0}^{M_{\mathrm{s}}-1}\left(h_1\left(\theta_{k\mathrm{s}}-\vartheta_{\mathrm{s}}\right)+h_1\left(\theta_{k\mathrm{s}}+\vartheta_{\mathrm{s}}\right)\right)}{\sum_{k=0}^{M_{\mathrm{p}}-1}\left(h_1\left(\theta_{k\mathrm{p}}\mp\vartheta_{\mathrm{s}}-\varphi\right)+h_1\left(\theta_{k\mathrm{p}}\pm\vartheta_{\mathrm{s}}+\varphi\right)\right)} \tag{7.5}$$

where the piecewise linear periodic function $h_1(\omega t)$ is defined in (A.2).

YΔ-connected DAB

Expanding the ZVS boundaries of the primary bridge $i_{LA}^{\mathrm{Y}\Delta}\left(\omega t=\pm\vartheta_{\mathrm{p}}\right)<0$ where $\vartheta_{\mathrm{p}}\in\{\theta_{k\mathrm{p}},\ \forall k\in\{0,...,M_{\mathrm{p}}-1\}\}$ results in

$$\frac{N_{\mathrm{s}}U_{\mathrm{p}}}{N_{\mathrm{p}}U_{\mathrm{s}}}>\frac{\sum_{k=0}^{M_{\mathrm{s}}-1}\Big(h_1\big(\theta_{k\mathrm{s}}\mp\vartheta_{\mathrm{p}}+\varphi+\frac{\pi}{6}\big)+h_1\big(\theta_{k\mathrm{s}}\pm\vartheta_{\mathrm{p}}-\varphi-\frac{\pi}{6}\big)+h_1\big(\theta_{k\mathrm{s}}\mp\vartheta_{\mathrm{p}}+\varphi-\frac{\pi}{6}\big)+h_1\big(\theta_{k\mathrm{s}}\pm\vartheta_{\mathrm{p}}-\varphi+\frac{\pi}{6}\big)\Big)}{\sum_{k=0}^{M_{\mathrm{p}}-1}\left(h_1\left(\theta_{k\mathrm{p}}-\vartheta_{\mathrm{p}}\right)+h_1\left(\theta_{k\mathrm{p}}+\vartheta_{\mathrm{p}}\right)\right)}. \tag{7.6}$$

Similarly, $i_{La}^{\mathrm{Y}\Delta}\left(\omega t=\varphi+\pi/6\pm\vartheta_{\mathrm{s}}\right)>0$ where $\vartheta_{\mathrm{s}}\in\{\theta_{k\mathrm{s}},\ \forall k\in\{0,...,M_{\mathrm{s}}-1\}\}$ can be expanded as

$$\frac{N_{\mathrm{s}}U_{\mathrm{p}}}{N_{\mathrm{p}}U_{\mathrm{s}}}<\frac{\sum_{k=0}^{M_{\mathrm{s}}-1}\Big(h_1\left(\theta_{k\mathrm{s}}-\vartheta_{\mathrm{s}}-\frac{\pi}{3}\right)+h_1\left(\theta_{k\mathrm{s}}+\vartheta_{\mathrm{s}}+\frac{\pi}{3}\right)+h_1\left(\theta_{k\mathrm{s}}-\vartheta_{\mathrm{s}}+\frac{\pi}{3}\right)+h_1\left(\theta_{k\mathrm{s}}+\vartheta_{\mathrm{s}}-\frac{\pi}{3}\right)+2h_1\left(\theta_{k\mathrm{s}}-\vartheta_{\mathrm{s}}\right)+2h_1\left(\theta_{k\mathrm{s}}+\vartheta_{\mathrm{s}}\right)\Big)}{\sum_{k=0}^{M_{\mathrm{p}}-1}\Big(h_1\big(\theta_{k\mathrm{p}}\pm\vartheta_{\mathrm{s}}+\varphi+\frac{\pi}{6}\big)+h_1\big(\theta_{k\mathrm{p}}\mp\vartheta_{\mathrm{s}}-\varphi-\frac{\pi}{6}\big)+h_1\big(\theta_{k\mathrm{p}}\pm\vartheta_{\mathrm{s}}+\varphi-\frac{\pi}{6}\big)+h_1\big(\theta_{k\mathrm{p}}\mp\vartheta_{\mathrm{s}}-\varphi+\frac{\pi}{6}\big)\Big)}. \tag{7.7}$$

Closed-form Q2L soft-switching boundaries

The general ZVS conditions (7.5)-(7.7) can be simplified if it is assumed that the converters are modulated with the Q2L modulation under conditions given in (2.1). Let's also assume that

$$0\leq\omega\tau_j\leq\frac{\pi}{3}\xrightarrow[(2.1a)]{(2.1b)}0\leq\theta_{k_jj}\leq\frac{\pi}{6}\qquad\forall k_j\in\{0,...,M_j-1\} \tag{7.8}$$

where $j\in\{\mathrm{p},\mathrm{s}\}$. This assumption ensures no overlap between the transitions of any two phases of a given converter. Let's also define D as the ratio of the

primary dc-link voltage, $V_{\mathrm{dc,p}}$, to the secondary dc-link voltage, $V_{\mathrm{dc,s}}$ as

$$D \triangleq \frac{V_{\mathrm{dc,p}}}{V_{\mathrm{dc,s}}} \equiv \frac{M_{\mathrm{p}} U_{\mathrm{p}}}{M_{\mathrm{s}} U_{\mathrm{s}}} \tag{7.9}$$

YY-connected DAB

The soft-switching conditions of a YY-M_{p}-level-M_{s}-level-DAB are given as

$$\begin{aligned} i_{\mathrm{L}A}^{\mathrm{YY}}\left(\omega t = \pm\theta_{k_{\mathrm{p}}\mathrm{p}}\right) <& 0, \qquad \forall k_{\mathrm{p}} \in \{0, ..., M_{\mathrm{p}} - 1\} \\ \Longrightarrow D_{k_{\mathrm{p}}\mathrm{p}}^{\pm} >& \frac{N_{\mathrm{p}} f\left(M_{\mathrm{s}}, M_{\mathrm{p}}, \psi_{\mathrm{s}}, \psi_{\mathrm{p}}, \left|\theta_{k_{\mathrm{p}}\mathrm{p}}\right|, \left|\varphi \mp \theta_{k_{\mathrm{p}}\mathrm{p}}\right|\right)}{N_{\mathrm{s}}} \end{aligned} \tag{7.10a}$$

$$\begin{aligned} i_{\mathrm{L}a}^{\mathrm{YY}}\left(\omega t = \varphi \pm \theta_{k_{\mathrm{s}}\mathrm{s}}\right) >& 0, \qquad \forall k_{\mathrm{s}} \in \{0, ..., M_{\mathrm{s}} - 1\} \\ \Longrightarrow \frac{1}{D_{k_{\mathrm{s}}\mathrm{s}}^{\pm}} >& \frac{N_{\mathrm{s}} f\left(M_{\mathrm{p}}, M_{\mathrm{s}}, \psi_{\mathrm{p}}, \psi_{\mathrm{s}}, \left|\theta_{k_{\mathrm{s}}\mathrm{s}}\right|, \left|\varphi \pm \theta_{k_{\mathrm{s}}\mathrm{s}}\right|\right)}{N_{\mathrm{p}}} \end{aligned} \tag{7.10b}$$

where the piecewise function $f\left(M_1, M_2, \psi_1, \psi_2, \theta, \lambda\right)$ is defined in (A.9).

YΔ-connected DAB

The soft-switching conditions of a YΔ-M_{p}-level-M_{s}-level-DAB are given as

$$\begin{aligned} i_{\mathrm{L}A}^{\mathrm{Y}\Delta}(\omega t = \pm\,\theta_{k_{\mathrm{p}}\mathrm{p}}) < 0, \qquad & \forall k_{\mathrm{p}} \in \{0, ..., M_{\mathrm{p}} - 1\} \\ \Longrightarrow D_{k_{\mathrm{p}}\mathrm{p}}^{\pm} > & \frac{N_{\mathrm{p}} g\left(M_{\mathrm{s}}, M_{\mathrm{p}}, \psi_{\mathrm{s}}, \psi_{\mathrm{p}}, \left|\theta_{k_{\mathrm{p}}\mathrm{p}}\right|, \left|\varphi \mp \theta_{k_{\mathrm{p}}\mathrm{p}}\right|\right)}{N_{\mathrm{s}}} \end{aligned} \tag{7.11a}$$

$$\begin{aligned} i_{\mathrm{L}a}^{\mathrm{Y}\Delta}(\omega t = & \varphi + \pi/6 \pm \theta_{k_{\mathrm{s}}\mathrm{s}}) > 0, \qquad \forall k_{\mathrm{s}} \in \{0, ..., M_{\mathrm{s}} - 1\} \\ \Longrightarrow \frac{1}{D_{k_{\mathrm{s}}\mathrm{s}}^{\pm}} > & \frac{N_{\mathrm{s}} g\left(M_{\mathrm{p}}, M_{\mathrm{s}}, \psi_{\mathrm{p}}, \psi_{\mathrm{s}}, \left|\theta_{k_{\mathrm{s}}\mathrm{s}}\right|, \left|\varphi \pm \theta_{k_{\mathrm{s}}\mathrm{s}}\right|\right)}{3N_{\mathrm{p}}} \end{aligned} \tag{7.11b}$$

where the piecewise function $g\left(M_1, M_2, \psi_1, \psi_2, \theta, \lambda\right)$ is defined in (A.11).

The soft-switching condition of every single switch for any converter given in Figure 2.3 and Figure 2.4 can be calculated using (7.10)-(7.11). The boundaries where at least one of the switches of the primary bridge or the secondary bridge loses ZVS, D_j^{first} where $j \in \{\mathrm{p}, \mathrm{s}\}$, can be calculated as

$$D_{\mathrm{p}}^{\mathrm{first}} \leq \max\left(D_{k_{\mathrm{p}}\mathrm{p}}^{-}, D_{k_{\mathrm{p}}\mathrm{p}}^{+}\right) \qquad \forall k_{\mathrm{p}} \in \{0, ..., M_{\mathrm{p}} - 1\} \tag{7.12a}$$

$$D_{\mathrm{s}}^{\mathrm{first}} \geq \min\left(D_{k_{\mathrm{s}}\mathrm{s}}^{-}, D_{k_{\mathrm{s}}\mathrm{s}}^{+}\right) \qquad \forall k_{\mathrm{s}} \in \{0, ..., M_{\mathrm{s}} - 1\}. \tag{7.12b}$$

Similarly, the boundaries where all of the switches of the primary bridge or the secondary bridge lose ZVS, D_j^{all} where $j \in \{\mathrm{p}, \mathrm{s}\}$, are given as

$$D_{\mathrm{p}}^{\mathrm{all}} \leq \min\left(D_{k_{\mathrm{p}}\mathrm{p}}^{-}, D_{k_{\mathrm{p}}\mathrm{p}}^{+}\right) \qquad \forall k_{\mathrm{p}} \in \{0, ..., M_{\mathrm{p}} - 1\} \tag{7.13a}$$

$$D_{\mathrm{s}}^{\mathrm{all}} \geq \max\left(D_{k_{\mathrm{s}}\mathrm{s}}^{-}, D_{k_{\mathrm{s}}\mathrm{s}}^{+}\right) \qquad \forall k_{\mathrm{s}} \in \{0, ..., M_{\mathrm{s}} - 1\}. \tag{7.13b}$$

Effects of dead time

One of the key assumptions in the calculations was analyzing the ZVS conditions under ideal switching transitions. However, the ZVS boundaries can be compromised due to nonidealities like dead times [93]. Therefore, the obtained ZVS boundaries will provide the minimum requirement for zero voltage switching of the converters. A methodology for considering the effect of dead time is provided in [80].

According to [80], for each half-bridge leg, the effect of dead time can be considered by analyzing the current sign both at the switching instant and the beginning of the dead time, and, accordingly, considering the worst case. However, this method has shortcomings. As will be shown in Section 7.3, multiple current zero crossings can occur during the dead time. This effect can be observed especially in multilevel DAB converters where the transitions of bridges overlap. This simply means that in (7.2) and (7.3), the inequalities should be queried not only at the turn-ON event ($\theta_{k_j j}$ where $j \in \{\mathrm{p}, \mathrm{s}\}$) but also at the beginning and end of the dead time and for all values in between.

YY-connected DAB

The ZVS conditions for the YY case can be updated as follows

$$\begin{aligned} i_{LA}^{\mathrm{YY}}\left(\omega t = \pm\theta_{k_{\mathrm{p}}\mathrm{pd}}\right) &< 0, \qquad \forall k_{\mathrm{p}} \in \{0, ..., M_{\mathrm{p}} - 1\} \\ \implies D_{k_{\mathrm{p}}\mathrm{pd}}^{\pm} &> \frac{N_{\mathrm{p}} f\left(M_{\mathrm{s}}, M_{\mathrm{p}}, \psi_{\mathrm{s}}, \psi_{\mathrm{p}}, \left|\theta_{k_{\mathrm{p}}\mathrm{pd}}\right|, \left|\varphi \mp \theta_{k_{\mathrm{p}}\mathrm{pd}}\right|\right)}{N_{\mathrm{s}}} \end{aligned} \tag{7.14a}$$

$$i_{\mathrm{La}}^{\mathrm{YY}}\left(\omega t=\varphi \pm \theta_{k_{\mathrm{s}}\mathrm{sd}}\right)>0, \qquad \forall k_{\mathrm{s}} \in \{0,...,M_{\mathrm{s}}-1\}$$
$$\Longrightarrow \frac{1}{D_{k_{\mathrm{s}}\mathrm{sd}}^{\pm}}>\frac{N_{\mathrm{s}} f\left(M_{\mathrm{p}}, M_{\mathrm{s}}, \psi_{\mathrm{p}}, \psi_{\mathrm{s}},\left|\theta_{k_{\mathrm{s}}\mathrm{sd}}\right|,\left|\varphi \pm \theta_{k_{\mathrm{s}}\mathrm{sd}}\right|\right)}{N_{\mathrm{p}}} \tag{7.14b}$$

where $D_{k_{\mathrm{p}}\mathrm{pd}}^{\pm}$ and $D_{k_{\mathrm{s}}\mathrm{sd}}^{\pm}$ are the ZVS conditions during the dead time. Also,

$$\theta_{k_{jj}\mathrm{d}} \triangleq \theta_{k_{jj}}+0.5\omega t_{k_{jj}}, \qquad \forall t_{k_{jj}} \in \{t|\ -t_{k_{jj}\mathrm{d}} \leq t \leq t_{k_{jj}\mathrm{d}}\} \tag{7.15}$$

where $\theta_{k_{jj}}+0.5\omega t_{k_{jj}\mathrm{d}}$ is the turn-ON instant of the target switch, $\theta_{k_{jj}}-0.5\omega t_{k_{jj}\mathrm{d}}$ is the turn-OFF instant of the complementary switch, and $t_{k_{jj}\mathrm{d}}$ is the dead time of the switch. Finally, the ZVS condition of every single switch can be calculated using (7.14)-(7.15) as

$$D_{k_{\mathrm{p}}\mathrm{p}}^{\pm} \geq \max(D_{k_{\mathrm{p}}\mathrm{pd}}^{\pm}), \quad \forall \theta_{k_{\mathrm{p}}\mathrm{pd}} \in \{\theta_{k_{\mathrm{p}}\mathrm{p}}+0.5\omega t|\ -t_{k_{\mathrm{p}}\mathrm{pd}} \leq t \leq t_{k_{\mathrm{p}}\mathrm{pd}}\} \tag{7.16a}$$
$$D_{k_{\mathrm{s}}\mathrm{s}}^{\pm} \leq \min(D_{k_{\mathrm{s}}\mathrm{pd}}^{\pm}), \quad \forall \theta_{k_{\mathrm{s}}\mathrm{sd}} \in \{\theta_{k_{\mathrm{s}}\mathrm{s}}+0.5\omega t|\ -t_{k_{\mathrm{s}}\mathrm{sd}} \leq t \leq t_{k_{\mathrm{s}}\mathrm{sd}}\}. \tag{7.16b}$$

Moreover, (7.12) and (7.13) can be used in conjunction with (7.16) to identify boundaries where the first switch or all of the switches lose soft-switching.

YΔ-connected DAB

The ZVS conditions for the YΔ case can be updated as follows

$$i_{\mathrm{L}A}^{\mathrm{Y}\Delta}(\omega t=\pm \theta_{k_{\mathrm{p}}\mathrm{pd}})<0, \qquad \forall k_{\mathrm{p}} \in \{0,...,M_{\mathrm{p}}-1\}$$
$$\Longrightarrow D_{k_{\mathrm{p}}\mathrm{pd}}^{\pm}>\frac{N_{\mathrm{p}} g\left(M_{\mathrm{s}}, M_{\mathrm{p}}, \psi_{\mathrm{s}}, \psi_{\mathrm{p}},\left|\theta_{k_{\mathrm{p}}\mathrm{pd}}\right|,\left|\varphi \mp \theta_{k_{\mathrm{p}}\mathrm{pd}}\right|\right)}{N_{\mathrm{s}}} \tag{7.17a}$$
$$i_{\mathrm{La}}^{\mathrm{Y}\Delta}(\omega t=\varphi+\pi/6 \pm \theta_{k_{\mathrm{s}}\mathrm{sd}})>0, \qquad \forall k_{\mathrm{s}} \in \{0,...,M_{\mathrm{s}}-1\}$$
$$\Longrightarrow \frac{1}{D_{k_{\mathrm{s}}\mathrm{sd}}^{\pm}}>\frac{N_{\mathrm{s}} g\left(M_{\mathrm{p}}, M_{\mathrm{s}}, \psi_{\mathrm{p}}, \psi_{\mathrm{s}},\left|\theta_{k_{\mathrm{s}}\mathrm{sd}}\right|,\left|\varphi \pm \theta_{k_{\mathrm{s}}\mathrm{sd}}\right|\right)}{3N_{\mathrm{p}}} \tag{7.17b}$$

where $D_{k_{\mathrm{p}}\mathrm{pd}}^{\pm}$ and $D_{k_{\mathrm{s}}\mathrm{sd}}^{\pm}$ are the ZVS conditions during the dead time, and $\theta_{k_{jj}\mathrm{d}}$ is defined in (7.15). Similar to the YY case, the ZVS condition of every single switch can be calculated using (7.15)-(7.17).

Approximated soft-switching boundaries

The ZVS models provided in the previous sections are complicated to analyze without computing tools. It is useful to have a rule of thumb for evaluating a performance of a system. Certain assumptions will be made in this section (even though not necessarily correct all the time) to simplify the ZVS models. The introduced errors will be quantified in Chapter 7.

Let's assume that the effect of dead time can be neglected, then it is enough to analyze (7.10) and (7.11). If it is assumed that the value of ψ_j where $j \in \{\mathrm{p},\mathrm{s}\}$ is small, then $\aleph_j$ used in functions $f(M_1, M_2, \psi_1, \psi_2, \theta, \lambda)$ and $g(M_1, M_2, \psi_1, \psi_2, \theta, \lambda)$ can be approximated with M_j [see definitions in (A.9) and (A.11)]. This considerably simplifies functions $f(M_1, M_2, \psi_1, \psi_2, \theta, \lambda)$ and $g(M_1, M_2, \psi_1, \psi_2, \theta, \lambda)$. Consequently, (7.10) for the YY configuration will be simplified to

$$D^{\pm}_{k_\mathrm{p}\mathrm{p}} > \frac{N_\mathrm{p}}{N_\mathrm{s}} \begin{cases} \frac{2\pi-3\left|\varphi\mp\theta_{k_\mathrm{p}\mathrm{p}}\right|}{2\pi-3\theta_{k_\mathrm{p}\mathrm{p}}} & 0 \le \left|\varphi\mp\theta_{k_\mathrm{p}\mathrm{p}}\right| \le \frac{\pi}{3} \\ \frac{3\pi-6\left|\varphi\mp\theta_{k_\mathrm{p}\mathrm{p}}\right|}{2\pi-3\theta_{k_\mathrm{p}\mathrm{p}}} & \frac{\pi}{3} \le \left|\varphi\mp\theta_{k_\mathrm{p}\mathrm{p}}\right| \le \frac{2\pi}{3} \end{cases} \quad \forall k_\mathrm{p} \in \{0, ..., M_\mathrm{p}-1\} \tag{7.18a}$$

$$\frac{1}{D^{\pm}_{k_\mathrm{s}\mathrm{s}}} > \frac{N_\mathrm{s}}{N_\mathrm{p}} \begin{cases} \frac{2\pi-3\left|\varphi\pm\theta_{k_\mathrm{s}\mathrm{s}}\right|}{2\pi-3\theta_{k_\mathrm{s}\mathrm{s}}} & 0 \le \left|\varphi\pm\theta_{k_\mathrm{s}\mathrm{s}}\right| \le \frac{\pi}{3} \\ \frac{3\pi-6\left|\varphi\pm\theta_{k_\mathrm{s}\mathrm{s}}\right|}{2\pi-3\theta_{k_\mathrm{s}\mathrm{s}}} & \frac{\pi}{3} \le \left|\varphi\pm\theta_{k_\mathrm{s}\mathrm{s}}\right| \le \frac{2\pi}{3} \end{cases} \quad \forall k_\mathrm{s} \in \{0, ..., M_\mathrm{s}-1\} \tag{7.18b}$$

Similarly, (7.11) for the YΔ configuration will be simplified to

$$D^{\pm}_{k_\mathrm{p}\mathrm{p}} > \frac{N_\mathrm{p}}{N_\mathrm{s}} \begin{cases} \frac{3\pi}{2\pi-3\theta_{k_\mathrm{p}\mathrm{p}}} & 0 \le \left|\varphi\mp\theta_{k_\mathrm{p}\mathrm{p}}\right| \le \frac{\pi}{6} \\ \frac{9\pi-18\left|\varphi\mp\theta_{k_\mathrm{p}\mathrm{p}}\right|}{4\pi-6\theta_{k_\mathrm{p}\mathrm{p}}} & \frac{\pi}{6} \le \left|\varphi\mp\theta_{k_\mathrm{p}\mathrm{p}}\right| \le \frac{2\pi}{3} \end{cases} \quad \forall k_\mathrm{p} \in \{0, ..., M_\mathrm{p}-1\} \tag{7.19a}$$

$$\frac{1}{D^{\pm}_{k_\mathrm{s}\mathrm{s}}} > \frac{N_\mathrm{s}}{N_\mathrm{p}} \begin{cases} \frac{\pi}{2\pi-3\theta_{k_\mathrm{s}\mathrm{s}}} & 0 \le \left|\varphi\pm\theta_{k_\mathrm{s}\mathrm{s}}\right| \le \frac{\pi}{6} \\ \frac{3\pi-6\left|\varphi\pm\theta_{k_\mathrm{s}\mathrm{s}}\right|}{4\pi-6\theta_{k_\mathrm{s}\mathrm{s}}} & \frac{\pi}{6} \le \left|\varphi\pm\theta_{k_\mathrm{s}\mathrm{s}}\right| \le \frac{2\pi}{3} \end{cases} \quad \forall k_\mathrm{s} \in \{0, ..., M_\mathrm{s}-1\} \tag{7.19b}$$

Approximated ZVS conditions given in (7.18) and (7.19) can further be simplified if we assume $\max\left(D^{-}_{k_\mathrm{p}\mathrm{p}}, D^{+}_{k_\mathrm{p}\mathrm{p}}\right) = D^{+}_{M_\mathrm{p}-1,\mathrm{p}} \triangleq D^{\sim}_\mathrm{p}$, where $D^{\sim}_\mathrm{p}$ is the approximate dc ratio for the primary converter. This simply means that the

first switch to lose ZVS from the primary converter is assumed to be the one responsible for the switching event at the end of the transition ($\omega t = \theta_{M_\mathrm{p}-1,\mathrm{p}}$) and also defining the ZVS boundary of the converter. Similarly, it is assumed that $\min\left(D^-_{k_\mathrm{s}\mathrm{s}}, D^+_{k_\mathrm{s}\mathrm{s}}\right) = D^-_{M_\mathrm{s}-1,\mathrm{s}} \triangleq D^\sim_\mathrm{s}$, where $D^\sim_\mathrm{s}$ is the approximate dc ratio for the secondary converter. This implies that the first switch to lose ZVS from the secondary converter is assumed to be the one responsible for the switching event at the beginning of the transition ($\omega t = \varphi - \theta_{M_\mathrm{s}-1,\mathrm{s}}$ for the YY and $\omega t = \varphi + \pi/6 - \theta_{M_\mathrm{s}-1,\mathrm{s}}$ for the YΔ) and also defining the ZVS boundary of the converter. Considering these, (7.18) and (7.19) can be simplified into

$$D^\sim_\mathrm{p} > \frac{N_\mathrm{p}}{N_\mathrm{s}} \begin{cases} \frac{2\pi - 3|\varphi - 0.5\omega\tau_\mathrm{p}|}{2\pi - 1.5\omega\tau_\mathrm{p}} & 0 \le |\varphi - 0.5\omega\tau_\mathrm{p}| \le \frac{\pi}{3} \\ \frac{3\pi - 6|\varphi - 0.5\omega\tau_\mathrm{p}|}{2\pi - 1.5\omega\tau_\mathrm{p}} & \frac{\pi}{3} \le |\varphi - 0.5\omega\tau_\mathrm{p}| \le \frac{2\pi}{3} \end{cases} \tag{7.20a}$$

$$D^\sim_\mathrm{s} < \frac{N_\mathrm{p}}{N_\mathrm{s}} \begin{cases} \frac{2\pi - 1.5\omega\tau_\mathrm{s}}{2\pi - 3|\varphi - 0.5\omega\tau_\mathrm{s}|} & 0 \le |\varphi - 0.5\omega\tau_\mathrm{s}| \le \frac{\pi}{3} \\ \frac{2\pi - 1.5\omega\tau_\mathrm{s}}{3\pi - 6|\varphi - 0.5\omega\tau_\mathrm{s}|} & \frac{\pi}{3} \le |\varphi - 0.5\omega\tau_\mathrm{s}| \le \frac{2\pi}{3} \end{cases} \tag{7.20b}$$

for the YY configuration and into

$$D^\sim_\mathrm{p} > \frac{N_\mathrm{p}}{N_\mathrm{s}} \begin{cases} \frac{3\pi}{2\pi - 1.5\omega\tau_\mathrm{p}} & 0 \le |\varphi - 0.5\omega\tau_\mathrm{p}| \le \frac{\pi}{6} \\ \frac{9\pi - 18|\varphi - 0.5\omega\tau_\mathrm{p}|}{4\pi - 3\omega\tau_\mathrm{p}} & \frac{\pi}{6} \le |\varphi - 0.5\omega\tau_\mathrm{p}| \le \frac{2\pi}{3} \end{cases} \tag{7.21a}$$

$$D^\sim_\mathrm{s} < \frac{N_\mathrm{p}}{N_\mathrm{s}} \begin{cases} \frac{2\pi - 1.5\omega\tau_\mathrm{s}}{\pi} & 0 \le |\varphi - 0.5\omega\tau_\mathrm{s}| \le \frac{\pi}{6} \\ \frac{4\pi - 3\omega\tau_\mathrm{s}}{3\pi - 6|\varphi - 0.5\omega\tau_\mathrm{s}|} & \frac{\pi}{6} \le |\varphi - 0.5\omega\tau_\mathrm{s}| \le \frac{2\pi}{3} \end{cases} \tag{7.21b}$$

for the YΔ configuration. Substituting $\tau_\mathrm{p} = \tau_\mathrm{s} = 0$ in (7.20) and (7.21) yields the ZVS boundaries for the conventional DAB converter which matches with the boundaries reported in [25]. If it is assumed that $\tau \triangleq \tau_\mathrm{p} = \tau_\mathrm{s} \neq 0$ and $0 \le |\varphi - \tau| \le \pi/3$, then (7.20) simplifies down to the relations reported in [24] for a Q2L operating MMC-MMC-DAB.

Summary of different ZVS conditions

The ZVS conditions of both winding configurations are summarized in Table 7.2. The respective method can be selected based on the modulation technique used and the desired complexity of the model. It should be noted that the approximated boundaries of the Q2L modulation are the conditions where at least one of the switches of the respective bridge loses ZVS. The rest of the

Table 7.2: Summary of the ZVS conditions

Arbitrary modulation		For the k_pth switch of the primary bridge[a]	For the k_sth switch of the secondary bridge[a]
Neglecting dead time	**YY**	(7.4) at $\vartheta_\mathrm{p} \equiv \theta_{k_\mathrm{p}\mathrm{p}}$	(7.5) at $\vartheta_\mathrm{s} \equiv \theta_{k_\mathrm{s}\mathrm{s}}$
	YΔ	(7.6) at $\vartheta_\mathrm{p} \equiv \theta_{k_\mathrm{p}\mathrm{p}}$	(7.7) at $\vartheta_\mathrm{s} \equiv \theta_{k_\mathrm{s}\mathrm{s}}$
Considering dead time[b]	**YY**	(7.4) at $\vartheta_\mathrm{p} \equiv \theta_{k_\mathrm{p}\mathrm{pd}}$	(7.5) at $\vartheta_\mathrm{s} \equiv \theta_{k_\mathrm{s}\mathrm{sd}}$
	YΔ	(7.6) at $\vartheta_\mathrm{p} \equiv \theta_{k_\mathrm{p}\mathrm{pd}}$	(7.7) at $\vartheta_\mathrm{s} \equiv \theta_{k_\mathrm{s}\mathrm{sd}}$
Q2L modulation		For the k_pth switch of the primary bridge[a]	For the k_sth switch of the secondary bridge[a]
Neglecting dead time	**YY**	evaluate (7.10a)	evaluate (7.10b)
	YΔ	evaluate (7.11a)	evaluate (7.11b)
Considering dead time[b]	**YY**	(7.16a) with (7.14a)	(7.16b) with (7.14b)
	YΔ	(7.16a) with (7.17a)	(7.16b) with (7.17b)
Q2L modulation		The first primary switch to loose ZVS	The first secondary switch to loose ZVS
Approximated boundaries	**YY**	(7.20a)	(7.20b)
	YΔ	(7.21a)	(7.21b)

[a] where $k_\mathrm{p} \in \{0, ..., M_\mathrm{p} - 1\}$ and $k_\mathrm{s} \in \{0, ..., M_\mathrm{s} - 1\}$.
[b] where $\theta_{k_j\mathrm{jd}} = \theta_{k_j j} + 0.5\omega t$, and the conditions with $\theta_{k_j\mathrm{jd}}$ should be evaluated for all $-t_{k_j\mathrm{jd}} \leq t \leq t_{k_j\mathrm{jd}}$ and the worst case should be selected.

conditions in Table 7.2 are evaluated for every single switch of the converter. If the boundaries where at least one of the switches (or all of the switches) loses ZVS are of interest, then (7.12) or (7.13) should also be evaluated. A flow chart to obtain the ZVS boundaries is provided in Figure 7.2.

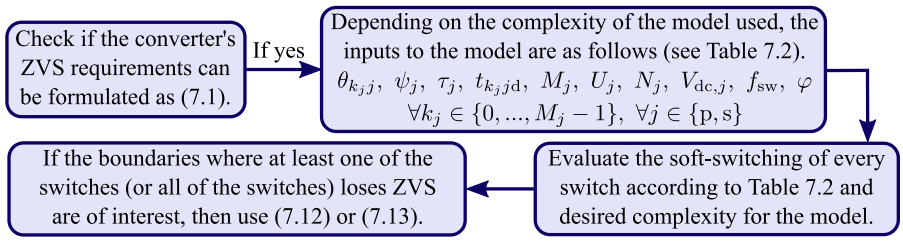

Figure 7.2: The flow chart of evaluating ZVS.

7.3 Analysis of soft-switching boundaries

The ZVS boundaries can be visualized using either D-φ curves (as done in [24], [80]) or D-$P_{3\phi}$ curves (as done in [25], [26], [89], [90]). The former can be directly plotted from (7.10)-(7.11). For the latter, the active power should be calculated from (4.26a) or (4.26b) first, and then (7.10)-(7.11) should be used in conjunction with the active power. Both methods are used here for visualization.

Parameter definitions

To generalize the analysis, D and $P_{3\phi}$ are per-unitized. Also, the transition times are presented as a percentage per fundamental period, $\tau_{j\%}$ as

$$D_{\mathrm{pu}} \triangleq D \times \frac{V_{\mathrm{dc,s}}^{\mathrm{nom}}}{V_{\mathrm{dc,p}}^{\mathrm{nom}}} \tag{7.22a}$$

$$\tau_{j\%} \triangleq \tau_j f_{\mathrm{sw}} \times 100\,\%, \quad \forall j \in \{\mathrm{p}, \mathrm{s}\} \tag{7.22b}$$

where D_{pu} is the per-unitized value of D, and $V_{\mathrm{dc,p}}^{\mathrm{nom}}$ and $V_{\mathrm{dc,s}}^{\mathrm{nom}}$ are the nominal dc-links voltages. The base powers for the converters are defined as the active power transferred using the conventional DAB with respective windings connection, $D = 1$, and $\varphi = \pi/2\,\mathrm{rad}$. In addition, the number of turns of the

windings is selected as

$$\begin{aligned} &\text{for YY connection to be } \frac{N_\mathrm{s}}{N_\mathrm{p}} \approx \frac{V_\mathrm{dc,s}^\mathrm{nom}}{V_\mathrm{dc,p}^\mathrm{nom}} \\ &\text{for Y}\Delta \text{ connection to be } \frac{N_\mathrm{s}}{N_\mathrm{p}} \approx \frac{\sqrt{3}V_\mathrm{dc,s}^\mathrm{nom}}{V_\mathrm{dc,p}^\mathrm{nom}}. \end{aligned} \tag{7.23}$$

Effects of winding connections and converter topology

For the studies of this section, the ZVS boundaries of the conventional DAB are provided with solid black lines as a reference. It is noteworthy that for medium to high-voltage applications, it is impossible to use a single switch in the conventional DAB; instead, several switches must be connected in series, and active balancing circuits are needed during turn-ON and turn-OFF. This will lead to a slower switching transition and a limited ZVS range for the conventional DAB. An alternative would be the input-series output-parallel (ISOP) converter configuration as studied in [94], eliminating the abovementioned issue. Only the case of using a single switch enabling a quick switching transition is studied here.

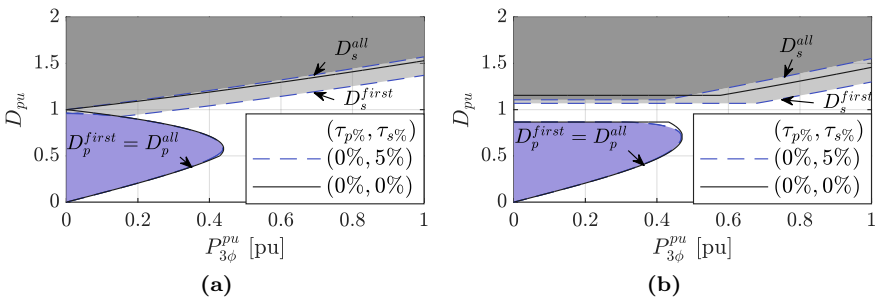

Figure 7.3: Turn-ON ZVS boundaries of a 2LC-CTB-DAB converter. **(a)** For the YY windings configuration. **(b)** For the YΔ windings configuration.

Figure 7.3 shows the ZVS operation range of a multilevel DAB converter with the two winding connections. The primary bridge is a two-level converter, and the secondary bridge is a CTB converter with five submodules (2LC-CTB-DAB). The region where the primary bridge is hard switched is depicted with a purple-colored patch. Similarly, the hard-switching region of the secondary

bridge is depicted with a grey-colored patch. The white-colored area is where the ZVS can be achieved for all of the switches on both of the bridges.

One can see from Figure 7.3a that the ZVS range of the primary bridge of the 2LC-CTB-DAB is slightly wider compared to the conventional DAB at the proximities of $(0.4, 0.5)$ and $(0, 1)$. These two proximities in D-φ domain correspond to phase shifts, $\varphi_1 = [0, 0.5\omega\tau_s]$ and $\varphi_2 = [\pi/3 - 0.5\omega\tau_s, \pi/3 + 0.5\omega\tau_s]$, respectively. For all $\varphi \in \varphi_1$, the transitions of the primary phase A voltage and the secondary phase A voltage overlap. Similarly, for all $\varphi \in \varphi_2$, the transitions of the primary phase A voltage and the secondary phase B voltage overlap. Since the secondary voltage is reduced due to the trapezoidal waveform during the transitions, the ZVS conditions can be satisfied with a further reduced primary voltage compared to the conventional DAB. Therefore, the ZVS range expands slightly for $\varphi \in \{\varphi_1, \varphi_2\}$. On the other hand, the ZVS range for the secondary bridge is smaller for the whole power range due to the introduction of the transition period. Starting from the boundary D_s^{first} and moving toward the boundary D_s^{all} (the area marked with light gray color), the secondary bridge switches lose ZVS one at a time. So, a partial ZVS can be achieved for the secondary bridge in this region. A similar pattern can be seen for the YΔ-connection of the windings in Figure 7.3b. The ZVS range of the primary bridge is marginally wider at the proximity of the point (0.4, 0.8), while the ZVS range of the secondary side is narrower in the whole power range. As for the YY case, operation in the area with light gray color results in partial ZVS of the secondary bridge switches. The expansion of the primary side ZVS range is due to a similar reason as the YY case. However, the region corresponds to $\varphi \in [\pi/6 - 0.5\omega\tau_s, \pi/6 + 0.5\omega\tau_s]$ due to the 30° phase shift introduced by the winding connection.

Figure 7.4 shows the ZVS range of a CTB-2LC-DAB converter, where the CTB has five submodules. Compared to the conventional DAB, the soft-switching range of the secondary bridge is increased in small regions, which correspond to $\varphi \in [\pi/6 - 0.5\omega\tau_p, \pi/6 + 0.5\omega\tau_p]$ for YΔ type and $\varphi \in \{[0, 0.5\omega\tau_p], [\pi/3 - 0.5\omega\tau_p, \pi/3 + 0.5\omega\tau_p]\}$ for YY type—due to similar reasons as before. In contrast, the hard-switching range of the primary bridge has widened considerably for both winding types. The areas with light purple color mark the region where the partial ZVS can be achieved for the primary bridge.

It is shown in [25] that the YΔ connection of the windings can provide

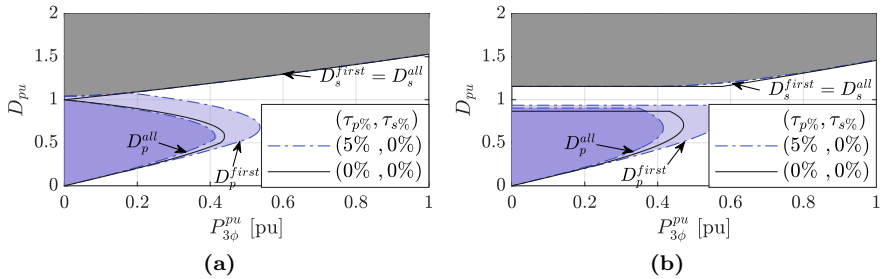

Figure 7.4: Turn-ON ZVS boundaries of a CTB-2LC-DAB converter. **(a)** For the YY windings configuration. **(b)** For the YΔ windings configuration.

a wider ZVS range at low powers for the conventional DAB. This can be seen in Figure 7.3b and Figure 7.4b, where two parallel lines ($D_{pu} = 1.155$ and $D_{pu} = 0.866$) extend to low powers. One can see from Figure 7.3 and Figure 7.4b that the 2LC-CTB-DAB and the CTB-2LC-DAB converters with YΔ type MFT also can achieve ZVS in partial loads and a dc ratio close to unity. However, the ZVS gap is narrower than the conventional DAB. The ZVS gap closes from the side where the transition time is introduced (i.e., from the primary side for the CTB-2LC-DAB and the secondary side for the 2LC-CTB-DAB).

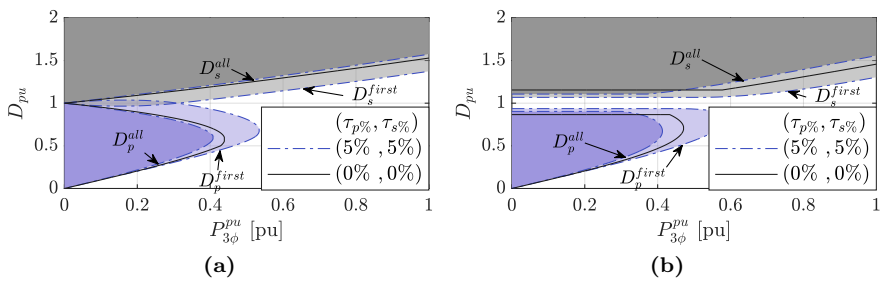

Figure 7.5: Turn-ON ZVS boundaries of a CTB-CTB-DAB converter. **(a)** For the YY windings configuration. **(b)** For the YΔ windings configuration.

Figure 7.5 shows a case where a CTB converter with five submodules is used as both primary and secondary bridges. The CTB-CTB-DAB shows a combined behavior of the converters 2LC-CTB-DAB and CTB-2LC-DAB. The ZVS range of the CTB-CTB-DAB is smaller than the conventional DAB

for both winding types. However, there are regions—shown by light color patches—where partial ZVS can be achieved for either of the bridges. The soft-switching is lost for the powers below 0.3 pu for the YY-connection of the windings, whereas it is retained in a narrow band for the whole power range with the YΔ-connected windings due to the constant flow of reactive currents.

Effects of transition times and number of levels

According to (7.10)-(7.11), the transition times of the bridges affect the ZVS boundaries. Figure 7.6 illustrates the effect of the transition time on the ZVS boundaries of a CTB-CTB-DAB converter with five submodules per arm of the converter. For the simplicity of visualization, the partial ZVS boundaries are not depicted in the figure, and it is assumed that the transition times of the bridges are equal (i.e., $\tau_{\mathrm{p/s}} = \tau_{\mathrm{p}} = \tau_{\mathrm{s}}$). The area confined to the y-axis and $\tau_{\mathrm{p/s}} = 0\,\%$ lines show the hard-switching region for $\tau_{\mathrm{p/s}} = 0\,\%$. If the transition times are increased to 2.5 %, the ZVS will be lost in at least one of the bridges in the areas confined to the lines $\tau_{\mathrm{p/s}} = 0\,\%$ and $\tau_{\mathrm{p/s}} = 2.5\,\%$. As can be seen, the higher the transition time, the larger the hard-switching area for both winding types.

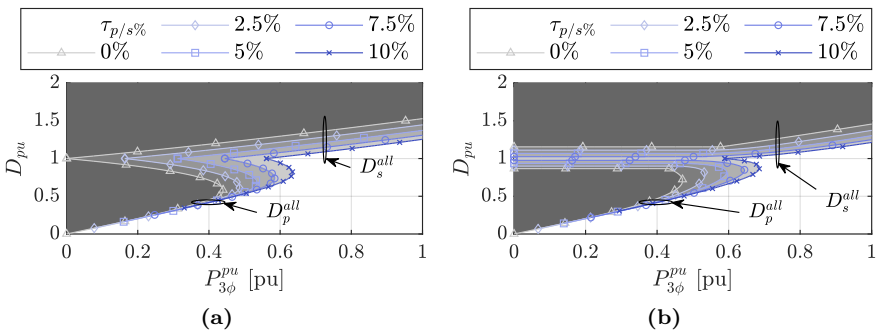

Figure 7.6: Effect the transition times ($\tau_{\mathrm{p/s}} = \tau_{\mathrm{p}} = \tau_{\mathrm{s}}$) on the turn-ON ZVS boundaries of a CTB-CTB-DAB converter with $M_{\mathrm{p/s}} = 5$. **(a)** For the YY windings configuration. **(b)** For the YΔ windings configuration.

Similar to the transition times, the number of levels of the bridges affects the ZVS boundaries. Figure 7.7 shows the effect of the number of levels on the ZVS range of a CTB-CTB-DAB converter. For the sake of simplicity, it

is assumed that the bridges have the same transition times, $\tau_{\mathrm{p/s}} = 10\,\%$, and the same number of levels (i.e., $M_{\mathrm{p/s}} = M_{\mathrm{p}} = M_{\mathrm{s}}$).

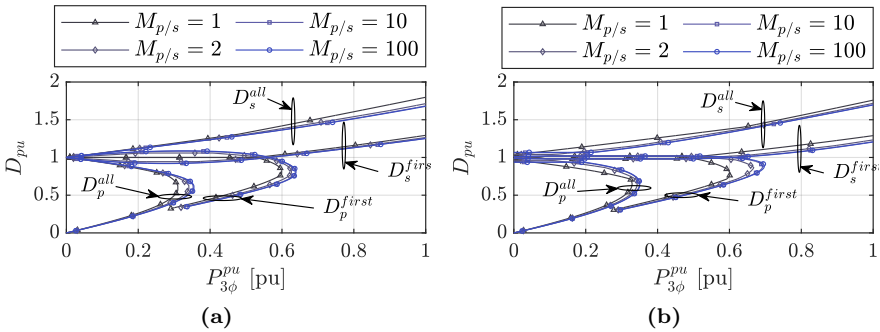

Figure 7.7: Effect of number of levels ($M_{\mathrm{p/s}} = M_{\mathrm{p}} = M_{\mathrm{s}}$) on the turn-ON ZVS boundaries of a CTB-CTB-DAB converter with $\tau_{\mathrm{p/s}} = 10\,\%$. **(a)** For the YY windings configuration. **(b)** For the YΔ configuration.

One can see from Figure 7.7 that the ZVS operation region shrinks slightly as the number of levels increases (e.g., from 1 to 2). Reduced regions corresponds to $\varphi \in \pi/3 + [0.5\omega(\tau_{\mathrm{p}} - \tau_{\mathrm{s}}), 0.5\omega(\tau_{\mathrm{p}} + \tau_{\mathrm{s}})]$ for the primary bridge and $\varphi \in \pi/3 + [0.5\omega(\tau_{\mathrm{s}} - \tau_{\mathrm{p}}), 0.5\omega(\tau_{\mathrm{p}} + \tau_{\mathrm{s}})]$ for the secondary bridge of the YY type. For the YΔ type, these bounds should be shifted by 30°. However, the ZVS boundaries of the converter with $M_{\mathrm{p/s}} = 10$ nearly overlap with the boundaries of the converter with $M_{\mathrm{p/s}} = 100$. The higher number of levels for a given transition time, the lower the dwell time. Therefore, the P2G voltages approach a trapezoid, and the effect of short dwell times can be neglected in the waveform of the current.

Effects of dead time

Two converter topologies are considered to study the effects of dead times. Table 7.3 tabulates the parameters of these converters. Additionally, both winding configurations are studied, resulting in four different cases.

Figure 7.8a and Figure 7.8b show the effects of dead times on the ZVS boundaries of the YY and the YΔ cases, respectively. For simplicity, only the boundaries $D_{\mathrm{p}}^{\mathrm{first}}$ and $D_{\mathrm{s}}^{\mathrm{first}}$ are visualized. The boundaries are depicted for two cases without a dead time and with a dead time of $t_{kjj\mathrm{d}} = 1\,\mu\mathrm{s}$. As

Table 7.3: Specifications of the converters for dead time studies

Converters	τ_p	τ_s	M_p	M_s	$t_{k_j j\mathrm{d}}$ [a]
CTB-2LC	5 %	0 %	5	1	$[0, 1]$ µs
2LC-CTB	0 %	5 %	1	5	$[0, 1]$ µs
Winding type	f_sw	L_σ	$V_\mathrm{dc,p}^\mathrm{nom}$	$V_\mathrm{dc,s}^\mathrm{nom}$	$N_\mathrm{p} : N_\mathrm{s}$
YY	5 kHz	92 µH	5 kV	5 kV	33 : 33
YΔ	5 kHz	92 µH	5 kV	5 kV	33 : 57

[a] where $j \in \{\mathrm{p}, \mathrm{s}\}$.

can be seen, for both the winding configurations and converter topologies, the ZVS operating region of both bridges shrinks by considering the dead time. This is because the current should be negative during the dead time instead of only at the switching instant, which expands the hard switching region. In Figure 7.8c, the low-power regions are magnified. The ZVS operating region shrinks even at low powers (phase shifts) where the transition of bridges overlaps.

In Figure 7.9, the effects of different dead times on the ZVS boundaries at operating points (a)-(d) (shown in Figure 7.8c) are depicted. Points (a) and (b) are plotted for constant D_pu, whereas for points (c) and (d), the power is kept constant. For these points, the inequalities (7.14) and (7.17) are only evaluated at the start and end of dead time instead of for all points between these two boundaries.

As expected, the higher the dead time, the more pronounced the reduction of the ZVS range at points (a) and (b) as shown in Figure 7.9a. However, at point (c) (which shows the secondary bridge boundary), the value of D_pu decreases up to $t_\mathrm{sd} = 0.5\,\mu\mathrm{s}$ and then increases [see Figure 7.9b]. Similarly, at point (d) (which shows the primary bridge boundary), the value of D_pu increases up to $t_\mathrm{pd} = 0.25\,\mu\mathrm{s}$ and then decreases. This means evaluating (7.14) and (7.17) for points (c) and (d) only at the beginning and end of the dead time results in the reduced soft-switching region at first and then

increased soft-switching region after specific dead time.

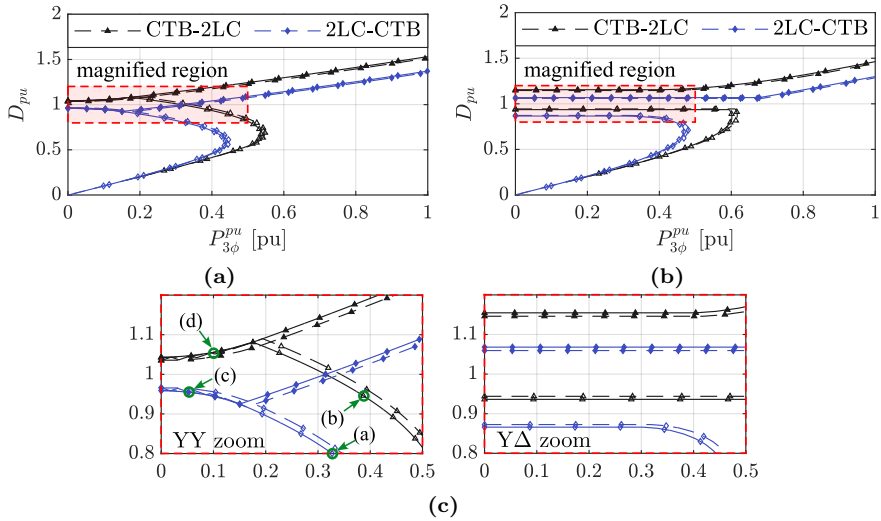

Figure 7.8: Effect of dead time on the turn-ON ZVS boundaries. Thick lines with filled markers illustrate $D_{\mathrm{s}}^{\mathrm{first}}$, and the thin lines with non-filled markers are used for $D_{\mathrm{p}}^{\mathrm{first}}$. The cases with dead time are depicted with dashed lines. **(a)** For the YY-connected MFT windings. **(b)** For the YΔ-connected MFT windings. **(c)** Magnification of low powers for both winding configurations.

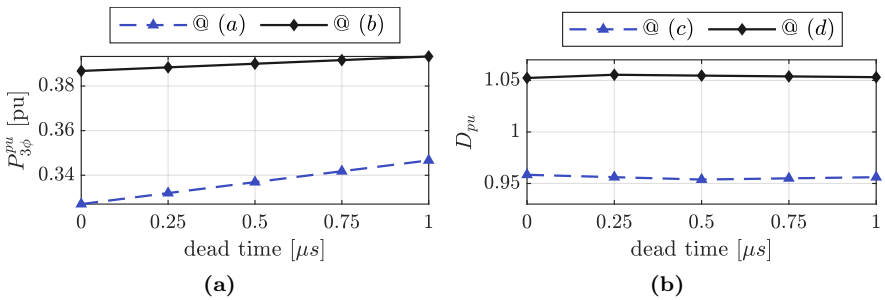

Figure 7.9: Case studies of the effect of dead time on the turn-ON ZVS boundaries of YY type. **(a)** At points (a) and (b) shown in Figure 7.8c. **(b)** At points (c) and (d) shown in Figure 7.8c.

Figure 7.10 shows the ac-link waveforms of the YY type 2LC-CTB-DAB converter operating on point (c) given in Figure 7.8c. As can be seen, the secondary line current has six zero-crossings. Out of these, the ones marked with a green circle happen in a shorter time than 0.5 µs.

Therefore, for a given dead time of $t_{k_jj\mathrm{d}}$, evaluating (7.14) and (7.17) only on at the start and end of dead time is not sufficient to ensure ZVS due to the possibility of multiple zero-crossing of the current. Consequently, for a given dead time of $t_{k_jj\mathrm{d}}$, (7.14) and (7.17) should be evaluated at all $\theta_{k_jj\mathrm{d}} \in \{\theta_{k_jj} + 0.5\omega t_{k_jj} \mid -t_{k_jj\mathrm{d}} \leq t_{k_jj} \leq t_{k_jj\mathrm{d}}\}$ and the worst case should be selected.

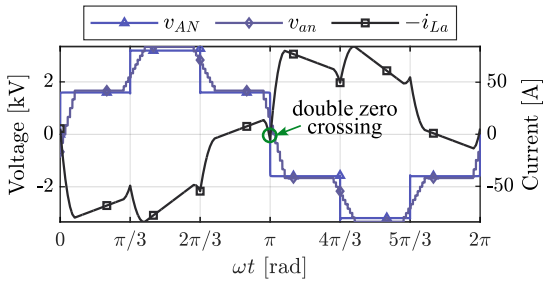

Figure 7.10: The ac-link waveforms of the YY type 2LC-CTB-DAB converter operating on point (c) given in Figure 7.8c.

7.4 Simulation validation

A simulation model of a CTB-CTB-DAB with ideal switches is developed in MATLAB to verify the derived ZVS boundaries. Extracting the ZVS boundaries from a simulation is a time-consuming process. Therefore, three key cases are considered for verification. Table 7.4 summarizes converter parameters for these three cases.

The secondary side dc-link voltage is kept constant at its nominal value of 5 kV, while the primary side dc-link voltage is swept between 0 and two times the nominal value (i.e., 10 kV). The phase shift between the two bridges is swept between 0° and 90°. After identifying the ZVS boundaries, the precision of the parameter sweeping has increased at the proximity of the boundaries. This process has been repeated several times to achieve smooth ZVS boundaries with low simulation times.

Table 7.4: Specifications of the simulated dc-dc converter

Cases	$\tau_{\mathrm{p}\%}$	$\tau_{\mathrm{s}\%}$	M_{p}	M_{s}	f_{sw}
A	5 %	5 %	3	3	5 kHz
B	16.67 %	1 %	3	1	5 kHz
C	1 %	16.67 %	1	3	5 kHz

Closed-form Q2L soft-switching boundaries

Figure 7.11 shows the ZVS boundaries (D-φ curves) obtained from simulations and analytic relations (7.10)-(7.11) for both windings types. The simulation results are depicted with markers. As can be seen, there is a perfect match between the simulation results and the calculations for all three cases and both winding types. This was expected as no simplifying assumptions have been made during the derivation process.

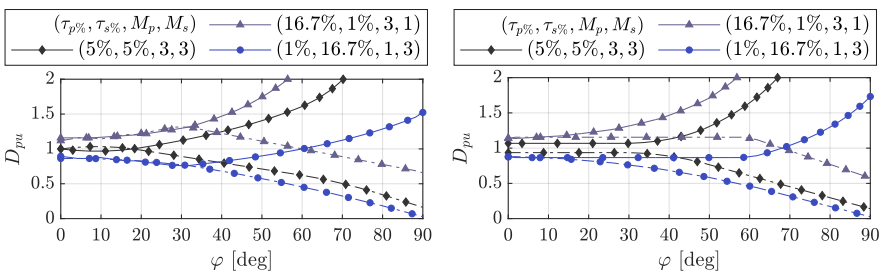

Figure 7.11: Comparison of the turn-ON ZVS boundaries obtained from simulations (shown by markers) and calculation for a CTB-CTB-DAB. **(a)** For the YY windings configuration. **(b)** For the YΔ windings configuration.

Approximated soft-switching boundaries

Figure 7.12 shows a comparison between the approximated (obtained from (7.20) or (7.21)) and accurate (obtained from (7.10) or (7.11)) ZVS boundaries for a CTB-CTB-DAB converter. It is assumed that both bridges have five submodules per leg and the same transition times (i.e., $\tau_{\mathrm{p/s}} = \tau_{\mathrm{p}} = \tau_{\mathrm{s}}$). The boundaries obtained from the simplified relations are depicted with markers. One can see that the approximated boundaries mismatch with the actual boundaries in certain regions. The difference between the actual and approximated boundaries is patched with the respective color. It can be seen that for both winding types, the higher the transition times, the larger the mismatch region. However, the approximate boundaries match well with the accurate ones for most operating points. Additionally, for both winding types, the approximate expressions are conservative in predicting the ZVS range of the converter.

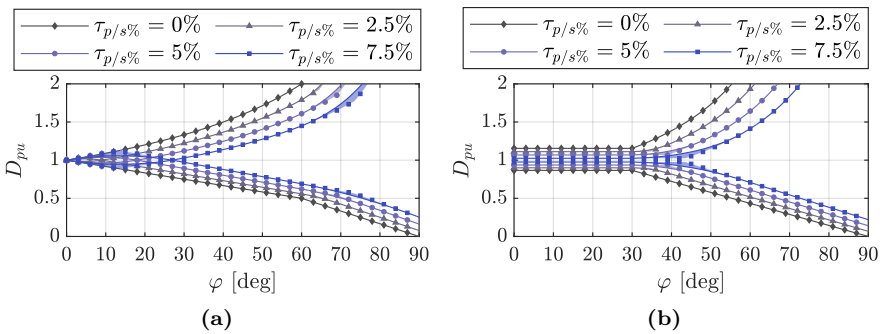

Figure 7.12: Comparison of the turn-ON ZVS boundaries obtained from approximate (shown by markers) and accurate calculations for a CTB-CTB-DAB. **(a)** For the YY configuration. **(b)** For the YΔ configuration.

The approximated boundaries for the YY configuration mismatch with the actual boundaries for only small and large values of φ. If the ZVS range of both bridges is of interest, then the small φ regions will be out of the ZVS range anyway. Therefore, the only introduced error on the whole ZVS range of the DAB converter by the approximated boundaries is in the high φ regions. As shown in Figure 7.12b, the approximation error is concentrated in the knee regions for the YΔ connection of the windings, and there is a perfect match for the other operating points.

The conditions where the ZVS gap of the YΔ-connected DAB converter closes can be calculated with the help of the approximate expressions as

$$\begin{aligned} &D_{\mathrm{p}}^{\sim} \leq D_{\mathrm{s}}^{\sim} \Rightarrow \frac{3\pi}{2\pi - 1.5\omega\tau_{\mathrm{p}}} \leq \frac{2\pi - 1.5\omega\tau_{\mathrm{s}}}{\pi} \\ &(4\pi - 3\omega\tau_{\mathrm{p}})\,(4\pi - 3\omega\tau_{\mathrm{s}}) \geq 12\pi^2 \end{aligned} \tag{7.24}$$

With equal transition times for the bridges, the limit is $\tau_{\mathrm{p/s}\%} = \frac{2-\sqrt{3}}{3} \times 100\,\% = 8.93\,\%$. It can be seen from Figure 7.6b that for $\tau_{\mathrm{p/s}} = 10\,\% > 8.93\,\%$ the gap is already closed and the converter operation is under hard switching.

The accurate ZVS conditions (7.10) or (7.11) are functions of at least eight parameters. Moreover, the soft-switching region of the DAB converter depends on both the primary and secondary converters' conditions. considering all the parameters and comparing them accurately with approximate boundaries is impossible in two dimensions. To overcome this limitation and perform a comparison for different parameter values, root mean squared percentage error (RMSPE) will be used [see the definition of RMSPE for four functions in (A.14)]. As an example, the output of RMSPE($D_{\mathrm{p}}^{\mathrm{first}}, D_{\mathrm{p}}^{\sim}, D_{\mathrm{s}}^{\mathrm{first}}, D_{\mathrm{s}}^{\sim}$) is a single number showing the error between approximate and accurate ZVS models. $D_{\mathrm{p}}^{\mathrm{first}}$ and $D_{\mathrm{p}}^{\sim}$ are compared together. Similarly, $D_{\mathrm{s}}^{\mathrm{first}}$ and $D_{\mathrm{s}}^{\sim}$ are compared and the cumulative error is quantified.

The quantification of the mismatch between the approximated expressions and the accurate ones will be limited to the region where both bridges operate under ZVS (i.e., $D_{\mathrm{p}}^{\mathrm{first}} \leq D_{\mathrm{s}}^{\mathrm{first}}$). Additionally, it is assumed that dc-link voltages have a maximum of 10 % deviation from their nominal values (i.e., $0.82 = \frac{1-0.1}{1+0.1} \leq D \leq \frac{1+0.1}{1-0.1} = 1.22$). These correspond to the phase shifts below 60° and 30° for the YY and the YΔ configurations, respectively.

Figure 7.13 shows RMSPE($D_{\mathrm{p}}^{\mathrm{first}}, D_{\mathrm{p}}^{\sim}, D_{\mathrm{s}}^{\mathrm{first}}, D_{\mathrm{s}}^{\sim}$) of a CTB-CTB-DAB converter for both winding types and three different number of submodules ($M_{\mathrm{p/s}} = M_{\mathrm{p}} = M_{\mathrm{s}}$). For the YY type, the approximation error is the highest when one of the bridges has a high transition time while the other has a small one. In contrast, for the YΔ type, the approximation error is the highest when the transition time of both of the bridges is high. For both winding types, the higher the number of levels, the lower the approximation error. This was expected because the higher the number of levels, the lower the ψ. Therefore, the assumption of small ψ for simplification of ZVS bounds is justified.

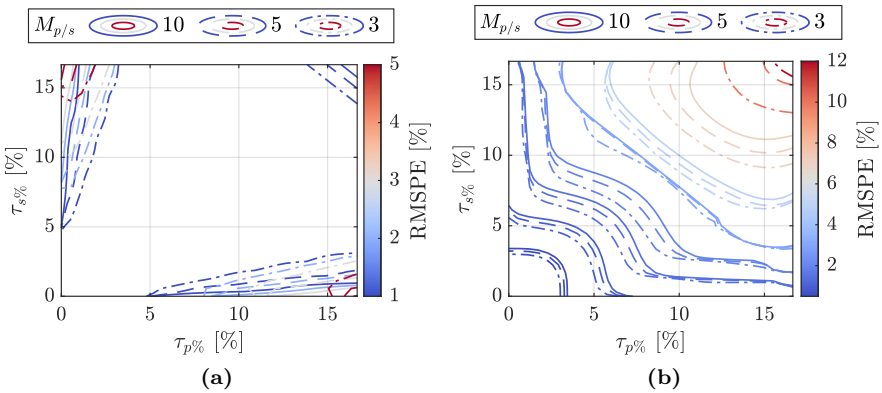

Figure 7.13: The RMSPE of the approximated expressions **(a)** For the YY-connected MFT windings. **(b)** For the YΔ-connected MFT windings.

7.5 Experimental validation

The down-scaled converter prototype shown in Figure 3.2 is used to validate the proposed analytical solutions. See Section 3.5 for more information about the experimental setup. The three different converter configurations used for validations are a 3ϕ-YY-2LC-CTB-DAB, 3ϕ-YY-CTB-2LC-DAB, and 3ϕ-YΔ-CTB-2LC-DAB. Two values (5 % and 10 %) are considered for the transition time of the CTB converter for each configuration, resulting in six different case studies in total. The specifications of these converters are summarized in Table 7.5.

In order to change the dc-link voltage ratio, the CTB-side's dc-link voltage is kept constant at its nominal value, and the 2LC-side's dc-link voltage is varied between 50 % and 150 % of its nominal value in steps of one volt for all case studies. Three 80 µH external inductors are series connected with the 2LC-side of the MFT to avoid extreme current surges in the ac-link due to the large operating span of the 2LC-side dc-link voltage. These inductors are kept in the circuit for all operating points to be consistent in the measurements.

The phase shift between the converters is swept in a large range to identify the ZVS conditions at different operating points. The ac-link currents and voltages are recorded at each operating point for post-processing. The turn-ON switching currents, the currents in the middle of the dead time, and the

Table 7.5: Specifications of the converter prototype

Converters	τ_p	τ_s	M_p	M_s	t_pd	t_sd
CTB-2LC	5 %	0 %	2	1	0.4 µs	0.5 µs
CTB-2LC	10 %	0 %	2	1	0.4 µs	0.5 µs
2LC-CTB	0 %	5 %	1	2	0.5 µs	0.4 µs
2LC-CTB	0 %	10 %	1	2	0.5 µs	0.4 µs
Winding type	f_sw	L_σ^p	$V_\mathrm{dc,p}^\mathrm{nom}$	$V_\mathrm{dc,s}^\mathrm{nom}$	$N_\mathrm{p} : N_\mathrm{s}$	
YY(2LC-CTB)	5 kHz	3.6 µH	100 V	200 V	15 : 30	
YY(CTB-2LC)	5 kHz	14.4 µH	200 V	100 V	30 : 15	
YΔ(CTB-2LC)	5 kHz	14.4 µH	346 V	100 V	30 : 15	

where $t_{j\mathrm{d}}$ ($j \in \{\mathrm{p}, \mathrm{s}\}$) are the dead time of the switches.

current at the turn-OFF instant of the complementary switch are extracted using the phase current and the switching instants at each operating point for each switch of the converters. If these three currents are negative, the soft switching will be maintained for the respective switch.

The measurement results for the six cases are summarized using these criteria in Figure 7.14. The analytical solutions are plotted using dashed or solid lines, and the measurement results are illustrated with markers. Each marker corresponds to one of the switching instants (i.e., one of the switches) and highlights the operating point where the soft-switching is lost for the respective switch. As can be seen, the analytical solutions match the measurement results for all six cases. There is a slight difference, which was expected. Firstly, due to the discrete one-volt steps taken during the measurements. Secondly, due to nonidealities that are not considered in the analytical solution. These include the voltage drop across the switches and the oversimplified model used for the MFT.

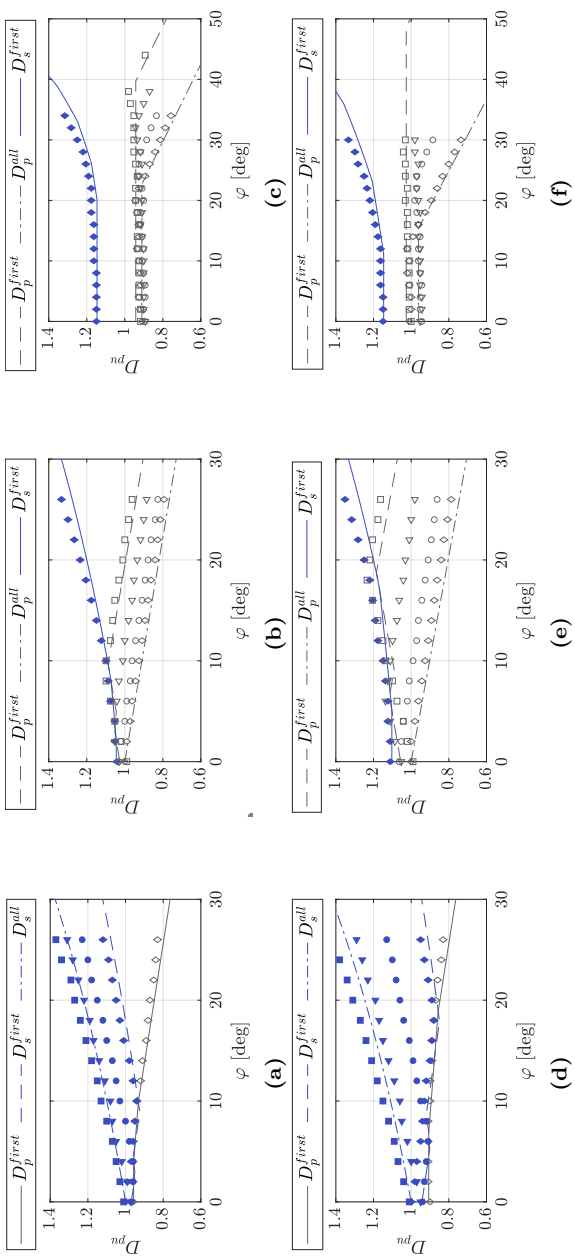

Figure 7.14: Comparison of measurement results with analytical solutions for different (τ_p, τ_s, M_p, M_s) combinations. The solid and dashed lines show the analytical solutions, and the measurement results are illustrated with markers. Gray and blue colors illustrate the ZVS boundaries of the primary and secondary bridges, respectively. **(a)** 3ϕ-YY-2LC-CTB-DAB for $(0\,\%, 5\,\%, 1, 2)$. **(b)** 3ϕ-YY-CTB-2LC-DAB for $(5\,\%, 0\,\%, 2, 1)$. **(c)** 3ϕ-YΔ-CTB-2LC-DAB for $(5\,\%, 0\,\%, 2, 1)$. **(d)** 3ϕ-YY-2LC-CTB-DAB for $(0\,\%, 10\,\%, 1, 2)$. **(e)** 3ϕ-YY-CTB-2LC-DAB for $(10\,\%, 0\,\%, 2, 1)$. **(f)** 3ϕ-YΔ-CTB-2LC-DAB for $(10\,\%, 0\,\%, 2, 1)$.

7.6 Conclusions and discussion

In this chapter, analytical ZVS boundaries for 3ϕ M-level-to-N-level DAB converters are derived, analyzed, and validated with MATLAB simulations and experiments. The region where the converter can achieve partial ZVS is identified. In addition, the effects of having different transition times and the number of levels on the ZVS range of the converter are studied. It is shown that the ZVS operation region shrinks slightly for a given transition time as the number of levels increases. It is also shown that the higher the transition time, the narrower the complete ZVS range and the wider the partial ZVS range of the converter.

The effects of the winding configurations are considered in the analysis. It is demonstrated that, as the transition time of the bridges increases, the converters with the YY connection of the windings lose the ZVS capability at partial loads, and the dc ratios close to unity. However, the converters with the YΔ connection of the windings can retain the ZVS capability at partial loads in a narrow region where the dc ratio is between 0.87 and 1.15. An interesting result is that the ZVS gap starts to close as the transition time increases. A 9 % transition time is a limit where the YΔ connection loses this benefit.

The effect of dead time on the ZVS boundaries of the multilevel DABs is formulated. For a few case studies, it is shown that introducing a dead time results in a reduction of the ZVS operating region of both the primary and secondary bridges, independent of the winding configuration. It is also established that evaluating the sign of the phase current in the whole dead time region is mandatory due to multiple zero-crossing in a short time frame.

Additionally, approximations of the ZVS boundaries are provided that are easy to implement and provide conservative ZVS boundaries. The error introduced by the approximations of the ZVS boundaries is quantified. The effect of the transition times and the number of levels on the approximation error is visualized. It is concluded that the approximated expressions can identify the ZVS boundaries of the YY and YΔ configurations with high accuracy for phase shifts below 60° and 30°, respectively.

CHAPTER 8

Magnetic Flux and Core Loss Modeling

This chapter is based on the following articles

[I] **B. Khanzadeh**, Y. Serdyuk, and T. Thiringer, "Evaluation of core losses in transformers for three-phase multilevel DAB converters," in Proceedings of *24th European Conference on Power Electronics and Applications (EPE'22 ECCE Europe)*, 2022, pp. 1–11.

8.1 Introduction

Improving the power density and evaluating the overall efficiency of the converter is one of the main design steps of DAB converters. In this regard, evaluating the losses of the transformer is crucial in the design process. One of the main components of transformer losses is iron losses. To estimate these losses, different methods can be used [30], [31]. If research focuses on transformer design, FEM can be used for detailed and accurate iron loss analysis. However, for research focusing on the power electronics aspects, FEM analysis is time inefficient. Nonetheless, the impact of power electronics characteristics (e.g., any modulation technique or control strategy) on the core losses

should be considered. A practical solution is empirical methods [95]. One such empirical method is the so-called IGSE [96]. According to IGSE [96], the time-average power loss per unit volume of a magnetic material, $\overline{P_\mathrm{v}}$, can be calculated from

$$\overline{P_\mathrm{v}} = \frac{1}{T}\int_0^T k_i \left|\frac{\mathrm{d}B}{\mathrm{d}t}\right|^\alpha (\Delta B)^{\beta-\alpha}\,\mathrm{d}t\,, \tag{8.1a}$$

$$k_i = \frac{k}{(2\pi)^{\alpha-1}\displaystyle\int_0^{2\pi} |\cos(\theta)|^\alpha\, 2^{\beta-\alpha}\,\mathrm{d}\theta} \tag{8.1b}$$

where α, β, and k are the Steinmetz coefficients of the core material; ΔB is the peak-to-peak magnetic flux density; and T is the fundamental period of the flux waveform. It has been shown that IGSE tends to be a good compromise between the accuracy of the model and the number of parameters required to model the losses [95]. The three required Steinmetz coefficients can be extracted from the material datasheet or experiments, and the flux waveforms can be used to estimate the losses using (8.1).

A few papers have studied different aspects of 3ϕ multilevel DAB converters with Q2L modulation [22], [24], [28], [29]. However, the effects of the modulation strategy on the transformer core losses are not investigated. An option for this study is IGSE. Nonetheless, direct implementation of (8.1) in the power electronics design optimization is time inefficient. In this chapter, closed-form expressions are derived to tackle this issue. The accuracy of these simplified expressions is evaluated and compared with direct calculation from IGSE and flux waveforms. The derived expressions can be applied to core-type 1ϕ transformers connected in 3ϕ configuration or E-core 3ϕ transformers. Also, they can be used to estimate the losses inside limbs of Hexa-core and E-cut core transformers. In addition, a set of equations are derived to estimate the flux waveform inside the transformer core for different winding configurations. The models are verified with simulations and experiments.

8.2 Flux and core loss modeling

The total instantaneous flux linkage in the core is a complex function of voltage waveforms of both windings, leakage fluxes, winding resistances, and the core geometry.

Simplified flux model

Modeling can be simplified if the flux is assumed to be distributed homogeneously across the core cross-section and remain homogeneous along the core. Furthermore, the voltage drop across the resistance of the windings can be neglected if their value is small. With these assumptions, the total instantaneous flux in the limbs, $\Phi_{\mathrm{L}}(\omega t)$, can be calculated as

$$\frac{\mathrm{d}\Phi_{\mathrm{L}}(\omega t)}{\mathrm{d}t} = k_\sigma \frac{v_{\mathrm{p}}(\omega t)}{N_{\mathrm{p}}} + (1-k_\sigma)\frac{v_{\mathrm{s}}(\omega t)}{N_{\mathrm{s}}}, \quad k_\sigma \triangleq \frac{L^{\mathrm{s}}_{\sigma\mathrm{s}}}{L^{\mathrm{s}}_{\sigma\mathrm{p}} + L^{\mathrm{s}}_{\sigma\mathrm{s}}} \tag{8.2}$$

where $v_{\mathrm{p}}(\omega t)$ and $v_{\mathrm{s}}(\omega t)$ are the primary and secondary winding voltages, respectively; $L^{\mathrm{s}}_{\sigma\mathrm{p}}$ is the primary winding's leakage inductance referred to the secondary side, and $L^{\mathrm{s}}_{\sigma\mathrm{s}}$ is the secondary winding's leakage inductance.

YY-connected DAB

The P2N voltages appear on each winding of a YY-connected MFT. Therefore, (8.2) can be rewritten as

$$\dot{\Phi}^{\mathrm{YY}}_{\mathrm{L}x} = k_\sigma \frac{v_{x\mathrm{N}}}{N_{\mathrm{p}}} + (1-k_\sigma)\frac{v_{y\mathrm{n}}}{N_{\mathrm{s}}}, \quad \forall (x,y) \in \{(A,a),(B,b),(C,c)\}. \tag{8.3}$$

Then the flux in the limbs can be calculated by substituting $v_{x\mathrm{N}}$ and $v_{y\mathrm{n}}$ from (4.5) in (8.3) and integrating the result as

$$\begin{aligned}\Phi^{\mathrm{YY}}_{\mathrm{L}x}(\omega t) = &-\frac{k_\sigma}{N_{\mathrm{p}}}\sum_{H=1}^{\infty}\sum_{k=0}^{M_{\mathrm{p}}-1}\left(\frac{4U_{\mathrm{p}}\cos(H\theta_k)}{H^2\pi\omega}\cos(H(\omega t+\alpha))\right)\\ &-\frac{1-k_\sigma}{N_{\mathrm{s}}}\sum_{H=1}^{\infty}\sum_{k=0}^{M_{\mathrm{s}}-1}\left(\frac{4U_{\mathrm{s}}\cos(H\theta_k)}{H^2\pi\omega}\cos(H(\omega t+\alpha-\varphi))\right).\end{aligned} \tag{8.4}$$

YΔ-connected DAB

For a YΔ-connected MFT, the P2N and P2P voltages appear on the Y- and Δ-side windings, respectively. Therefore, (8.2) can be rewritten as

$$\dot{\Phi}^{\mathrm{Y}\Delta}_{\mathrm{L}x} = k_\sigma \frac{v_{x\mathrm{N}}}{N_{\mathrm{p}}} + (1-k_\sigma)\frac{v_{yz}}{N_{\mathrm{s}}}, \quad \forall (x,yz) \in \{(A,ab),(B,bc),(C,ca)\}. \tag{8.5}$$

Then the flux in the limbs can be calculated by substituting $v_{x\mathrm{N}}$ and v_{yz} from (4.5) and (4.8) in (8.5) and integrating the result as

$$\begin{aligned}\Phi_{\mathrm{L}x}^{\mathrm{Y}\Delta}(\omega t) = &\frac{-k_\sigma}{N_\mathrm{p}}\sum_{H=1}^{\infty}\sum_{k=0}^{M_\mathrm{p}-1}\left(\frac{4U_\mathrm{p}\cos(H\theta_k)}{H^2\pi\omega}\cos(H(\omega t+\alpha))\right)\\ &-\frac{1-k_\sigma}{N_\mathrm{s}}\sum_{H=1}^{\infty}\sum_{k=0}^{M_\mathrm{s}-1}\left(\frac{4U_\mathrm{s}\cos(H\theta_k)}{H^2\pi\omega}\cos\Big(H(\omega t+\alpha-\varphi-\frac{\pi}{6})\Big)\right)\\ &+\frac{1-k_\sigma}{N_\mathrm{s}}\sum_{H=1}^{\infty}\sum_{k=0}^{M_\mathrm{s}-1}\left(\frac{4U_\mathrm{s}\cos(H\theta_k)}{H^2\pi\omega}\cos\Big(H(\omega t+\alpha-\varphi-\frac{5\pi}{6})\Big)\right).\end{aligned} \tag{8.6}$$

ΔY-connected DAB

For a ΔY-connected MFT, the P2P and P2N voltages appear on the Δ- and Y-side windings, respectively. Therefore, (8.2) can be rewritten as

$$\dot{\Phi}_{\mathrm{L}x}^{\Delta\mathrm{Y}} = k_\sigma\frac{v_{xy}}{N_\mathrm{p}} + (1-k_\sigma)\frac{v_{z\mathrm{n}}}{N_\mathrm{s}},\quad \forall(xy,z)\in\{(AB,a),(BC,b),(CA,c)\}. \tag{8.7}$$

Then the flux in the limbs can be calculated by substituting v_{xy} and $v_{z\mathrm{n}}$ from (4.8) and (4.5) in (8.7) and integrating the result as

$$\begin{aligned}\Phi_{\mathrm{L}x}^{\Delta\mathrm{Y}}(\omega t) = &-\frac{k_\sigma}{N_\mathrm{p}}\sum_{H=1}^{\infty}\sum_{k=0}^{M_\mathrm{p}-1}\left(\frac{4U_\mathrm{p}\cos(H\theta_k)}{H^2\pi\omega}\cos(H(\omega t+\alpha))\right)\\ &+\frac{k_\sigma}{N_\mathrm{p}}\sum_{H=1}^{\infty}\sum_{k=0}^{M_\mathrm{p}-1}\left(\frac{4U_\mathrm{p}\cos(H\theta_k)}{H^2\pi\omega}\cos\Big(H(\omega t+\alpha-\frac{2\pi}{3})\Big)\right)\\ &-\frac{1-k_\sigma}{N_\mathrm{s}}\sum_{H=1}^{\infty}\sum_{k=0}^{M_\mathrm{s}-1}\left(\frac{4U_\mathrm{s}\cos(H\theta_k)}{H^2\pi\omega}\cos\Big(H(\omega t+\alpha-\varphi+\frac{\pi}{6})\Big)\right)\end{aligned} \tag{8.8}$$

ΔΔ-connected DAB

For a ΔΔ-connected MFT, the P2P voltages appear on both windings. Therefore, (8.2) can be rewritten as

$$\dot{\Phi}_{\mathrm{L}x}^{\Delta\Delta} = k_\sigma \frac{v_{xy}}{N_\mathrm{p}} + (1-k_\sigma)\frac{v_{zw}}{N_\mathrm{s}}, \quad \forall (xy, zw) \in \{(AB, ab), (BC, bc), (CA, cA)\}. \tag{8.9}$$

Then the flux in the limbs can be calculated by substituting v_{xy} and v_{zw} from (4.8) in (8.9) and integrating the result as

$$\begin{aligned}
\Phi_{\mathrm{L}x}^{\Delta\Delta}(\omega t) = &-\frac{k_\sigma}{N_\mathrm{p}} \sum_{H=1}^{\infty} \sum_{k=0}^{M_\mathrm{p}-1} \left(\frac{4U_\mathrm{p}\cos(H\theta_k)}{H^2\pi\omega} \cos(H(\omega t + \alpha)) \right) \\
&+\frac{k_\sigma}{N_\mathrm{p}} \sum_{H=1}^{\infty} \sum_{k=0}^{M_\mathrm{p}-1} \left(\frac{4U_\mathrm{p}\cos(H\theta_k)}{H^2\pi\omega} \cos\left(H(\omega t + \alpha - \frac{2\pi}{3}) \right) \right) \\
&-\frac{1-k_\sigma}{N_\mathrm{s}} \sum_{H=1}^{\infty} \sum_{k=0}^{M_\mathrm{s}-1} \left(\frac{4U_\mathrm{s}\cos(H\theta_k)}{H^2\pi\omega} \cos(H(\omega t + \alpha - \varphi)) \right) \\
&+\frac{1-k_\sigma}{N_\mathrm{s}} \sum_{H=1}^{\infty} \sum_{k=0}^{M_\mathrm{s}-1} \left(\frac{4U_\mathrm{s}\cos(H\theta_k)}{H^2\pi\omega} \cos\left(H(\omega t + \alpha - \varphi - \frac{2\pi}{3}) \right) \right).
\end{aligned} \tag{8.10}$$

Approximated flux model

To further simplify the flux model, one can assume that only one winding is excited (the extreme cases of $k_\sigma \in \{0, 1\}$). Then, the flux linkage of a winding, $\Psi(t)$, can be calculated from the applied voltage on its terminals, $v(t)$, as

$$v(t) = \frac{\mathrm{d}\Psi(t)}{\mathrm{d}t} \Rightarrow \Psi(t) = \Psi(0) + \int_0^t v(t')\,\mathrm{d}t'. \tag{8.11}$$

Y-connected 3ϕ windings

The P2N voltages appear on each coil of Y-connected 3ϕ windings. Thus, the flux linkage of a Y-connected balanced 3ϕ windings exited with the voltages given in Figure 2.5, $\Psi_x^{\mathrm{Y}}(\omega t)$, can be calculated using (4.5) and (8.11) as

$$\Psi_x^{\mathrm{Y}}(\omega t) = \Psi_x^{\mathrm{Y}}(0) + \sum_{H=1}^{\infty} \sum_{k=0}^{M-1} \left(\frac{4U\cos(H\theta_k)}{H^2\pi\omega} (1 - \cos(H(\omega t + \alpha))) \right) \tag{8.12}$$

where $H \in \{2h-1 | h \in \mathbb{N},\ 3 \nmid 2h-1\}$, $(x, \alpha) \in \{(A,0),(B,-2\pi/3),(C,2\pi/3)\}$. Due to the half-wave symmetry of the waveforms $\Psi_x^{\mathrm{Y}}(\pi) = -\Psi_x^{\mathrm{Y}}(0)$. Thus (8.12) can be simplified as

$$\Psi_x^{\mathrm{Y}}(\omega t) = \sum_{H=1}^{\infty} \sum_{k=0}^{M-1} \left(\frac{-4U\cos(H\theta_k)}{H^2 \pi \omega} \cos(H(\omega t + \alpha)) \right). \tag{8.13}$$

The extremum of $\Psi_x^{\mathrm{Y}}(\omega t)$ occurs at $\omega t = n\pi + \alpha$ for $n \in \mathbb{Z}$. Among these points, the maximums are located at $\omega t = n\pi + \alpha$ for $n \in \{2k-1 | k \in \mathbb{Z}\}$. Therefore, the maximum flux linkage, $\Psi_{\max}^{\mathrm{Y}}$ can be calculated as

$$\Psi_{\max}^{\mathrm{Y}} = \Psi_x^{\mathrm{Y}}(n\pi + \alpha) = \sum_{k=0}^{M-1} \frac{4U}{\pi\omega} \sum_{H=1}^{\infty} \frac{\cos(H\theta_k)}{H^2} \overset{(A.2)}{=\!=} \sum_{k=0}^{M-1} \frac{4U}{\pi\omega} h_1(\theta_k) \tag{8.14}$$

which can be expanded using the time-domain definition of $h_1(\omega t)$ from (A.2) and assuming $0 \le \theta_k \le \pi/3$ as

$$\Psi_{\max}^{\mathrm{Y}} = \sum_{k=0}^{M-1} \left(\frac{4U}{\pi\omega} \frac{\pi}{18} (2\pi - 3\theta_k) \right) = \frac{2U}{9\omega} \left(2\pi M - 3 \sum_{k=0}^{M-1} \theta_k \right). \tag{8.15}$$

Equation (8.15) can be used for arbitrary values of θ_k for a general staircase waveform. However, it can be simplified further for a Q2L waveform excitation defined under the conditions mentioned in (2.1) as

$$\Psi_{\max}^{\mathrm{Y}} = \frac{2U}{9\omega} \left(2\pi M - 3 \sum_{k=0}^{M-1} (k + 0.5)\,\psi \right) = \frac{2MU}{9\omega} (2\pi - 1.5\psi M). \tag{8.16}$$

For all converters shown in Figure 2.3 and Figure 2.4 $MU \equiv 0.5 V_{\mathrm{dc}}$ therefore

$$\Psi_{\max}^{\mathrm{Y}} = \frac{V_{\mathrm{dc}}}{9\omega} (2\pi - 1.5\psi M). \tag{8.17}$$

Δ-connected 3ϕ windings

The P2P voltages appear on each coil of Δ-connected 3ϕ windings. Thus, the flux linkage of a Δ-connected balanced 3ϕ windings exited with the voltages

given in Figure 2.5, $\Psi_x^{\Delta}(\omega t)$, can be calculated using (4.8) and (8.11) as

$$\Psi_x^{\Delta}(\omega t) = \tag{8.18}$$
$$\sum_{H=1}^{\infty}\sum_{k=0}^{M-1}\frac{4U\cos(H\theta_k)}{H^2\pi\omega}\left(\cos\left(H(\omega t+\alpha)-\frac{2H\pi}{3}\right)-\cos(H(\omega t+\alpha))\right)$$

where $H\in\{2h-1|h\in\mathbb{N},\ 3\nmid 2h-1\}$, $(x,\alpha)\in\{(A,0),(B,-2\pi/3),(C,2\pi/3)\}$. The extremum of $\Psi_x^{\Delta}(\omega t)$ occurs at $\omega t=n\pi+5\pi/6+\alpha$ for $n\in\mathbb{Z}$. Among these points, the maximums are located at $\omega t=n\pi+5\pi/6+\alpha$ for $n\in\{2k|k\in\mathbb{Z}\}$. Therefore, the maximum flux linkage, $\Psi_{\max}^{\Delta}$ can be calculated as

$$\begin{aligned}\Psi_{\max}^{\Delta} =&\Psi_x^{\Delta}(n\pi+5\pi/6+\alpha) \qquad (8.19)\\ =&\sum_{k=0}^{M-1}\frac{2U}{\pi\omega}\Big(\sum_{H=1}^{\infty}\frac{\cos(H(\theta_k+\pi/6))}{H^2}+\sum_{H=1}^{\infty}\frac{\cos(H(\theta_k-\pi/6))}{H^2}\\ &-\sum_{H=1}^{\infty}\frac{\cos(H(\theta_k+5\pi/6))}{H^2}-\sum_{H=1}^{\infty}\frac{\cos(H(\theta_k-5\pi/6))}{H^2}\Big)\\ \overset{(A.2)}{=\!=}&\sum_{k=0}^{M-1}\frac{2U}{\pi\omega}\Big(h_1(\theta_k+\frac{\pi}{6})+h_1(\theta_k-\frac{\pi}{6})-h_1(\theta_k+\frac{5\pi}{6})-h_1(\theta_k-\frac{5\pi}{6})\Big)\end{aligned}$$

which can be reduced using the time-domain definition of $h_1(\omega t)$ from (A.2) and assuming $0\le\theta_k\le\pi/6$ into

$$\Psi_{\max}^{\Delta}=\frac{2MU\pi}{3\omega}\xrightarrow{MU\equiv 0.5V_{\mathrm{dc}}}\Psi_{\max}^{\Delta}=\frac{V_{\mathrm{dc}}}{6f_{\mathrm{sw}}}. \tag{8.20}$$

Simplified core loss model

Assuming that the flux distribution is homogenous in a core with a cross-section of A, which is excited using a coil with N number of turns, the flux linkage inside the core can be written as $\Psi=N\Phi=NBA$. Therefore, (8.11) can be reformulated as

$$v(t)=\frac{\mathrm{d}\Psi(t)}{\mathrm{d}t}=NA\frac{\mathrm{d}B(t)}{\mathrm{d}t}. \tag{8.21}$$

A fundamental period of the voltage waveforms applied on the transformer windings can be divided into two sections. A monotonically increasing half-cycle and a monotonically decreasing half-cycle. This means, there will be no minor loops in the hysteresis curve of the core. Therefore, K_i and ΔB terms can be moved out of integration in (8.1a). Considering these, (8.1a) can be reformulated as

$$\overline{P_{\mathrm{v}}} = \frac{k_i \left(\Delta B\right)^{\beta-\alpha}}{\left(NA\right)^{\alpha} T} \int_0^T \left|v\left(t\right)\right|^{\alpha} \mathrm{d}t = \frac{k_i \left(2B_{\max}\right)^{\beta-\alpha}}{\left(NA\right)^{\alpha} T} \int_0^T \left|v\left(t\right)\right|^{\alpha} \mathrm{d}t \tag{8.22}$$

where $B_{\max}$ is the maximum flux density.

Y-connected 3ϕ windings

Let's assume a set of Y-connected 3ϕ coils excited with a converter generating P2G voltage waveforms similar to the ones shown in Figure 2.5. Moreover, let's assume that the waveforms are Q2L meeting the conditions mentioned in (2.1). The maximum magnetic flux density inside the limbs of this core can be calculated using (8.16) and (8.21) as

$$B_{\max}^{\mathrm{Y}} = \frac{\Psi_{\max}^{\mathrm{Y}}}{NA} = \frac{2MU}{9NA\omega} \left(2\pi - 1.5\psi M\right). \tag{8.23}$$

Moreover, the magnetic loss density inside the limbs of this core can be calculated from (8.22) as

$$\overline{P_{\mathrm{v}}^{\mathrm{Y}}} = \frac{k_i \left(2B_{\max}^{\mathrm{Y}}\right)^{\beta-\alpha}}{\left(NA\right)^{\alpha} 2\pi} \int_0^{2\pi} \left|v_{AN}(\omega t)\right|^{\alpha} \mathrm{d}\omega t \tag{8.24}$$

which can be further simplified considering the quarter-wave symmetry of (4.7) along $\omega t = 0$, and non-negative values of $v_{AN}(\omega t)$ for $0 \leq \omega t \leq 0.5\pi$ as

$$\overline{P_{\mathrm{v}}^{\mathrm{Y}}} = \frac{k_i \left(2B_{\max}^{\mathrm{Y}}\right)^{\beta-\alpha}}{\left(NA\right)^{\alpha} 0.5\pi} \int_0^{\frac{\pi}{2}} \left(v_{AN}(\omega t)\right)^{\alpha} \mathrm{d}\omega t \tag{8.25}$$

The integration in (8.25) can be divided into intervals where $v_{AN}(\omega t)$ is constant using (4.7) and then evaluated. By doing so, and plugging $B_{\max}^{\mathrm{Y}}$ from

(8.23), and reducing the obtained expression results in

$$\overline{P_{\mathrm{v}}^{\mathrm{Y}}} = 4k \left(B_{\mathrm{max}}^{\mathrm{Y}}\right)^{\beta} f_{\mathrm{sw}}^{\alpha} \chi_{\mathrm{Q2L}}^{\mathrm{Y}} \tag{8.26a}$$

$$\chi_{\mathrm{Q2L}}^{\mathrm{Y}} = \frac{\left(1+2^{\alpha-1}\right)\left(\frac{\pi}{3}-(2M-1)\,\psi\right)+\psi\left(\sum_{k=1}^{M-1}\left(\frac{k}{M}\right)^{\alpha}+\sum_{k=1}^{2M-1}\left(1+\frac{k}{2M}\right)^{\alpha}\right)}{\left(\frac{2\pi}{3}-\frac{M\psi}{2}\right)^{\alpha}\int_{0}^{2\pi}\left|\cos(\theta)\right|^{\alpha}\,\mathrm{d}\theta}. \tag{8.26b}$$

For $\psi = 0$ (8.26) models a core loss of 2LC-DAB simplified as

$$\overline{P_{\mathrm{v}}^{\mathrm{Y}}} = k \left(B_{\mathrm{max}}^{\mathrm{Y}}\right)^{\beta} f_{\mathrm{sw}}^{\alpha} \times \frac{2+2^{\alpha}}{\left(\frac{2\pi}{3}\right)^{\alpha-1}\int_{0}^{2\pi}\left|\cos(\theta)\right|^{\alpha}\,\mathrm{d}\theta}. \tag{8.27}$$

Δ-connected 3ϕ windings

Let's assume a set of Δ-connected 3ϕ coils excited with a converter generating P2G voltage waveforms similar to the ones shown in Figure 2.5. Moreover, let's assume that the waveforms are Q2L meeting the conditions mentioned in (2.1). The maximum magnetic flux density inside the limbs of this core can be calculated using (8.20) and (8.21) as

$$B_{\mathrm{max}}^{\Delta} = \frac{\Psi_{\mathrm{max}}^{\Delta}}{NA} = \frac{2MU\pi}{3NA\omega}. \tag{8.28}$$

Moreover, the magnetic loss density inside the limbs of this core can be calculated from (8.22) as

$$\overline{P_{\mathrm{v}}^{\Delta}} = \frac{k_i \left(2B_{\mathrm{max}}^{\Delta}\right)^{\beta-\alpha}}{(NA)^{\alpha}\,2\pi}\int_{0}^{2\pi}\left|v_{AB}(\omega t)\right|^{\alpha}\,\mathrm{d}\omega t \tag{8.29}$$

which can be further simplified considering the quarter-wave symmetry of (4.10) along $\omega t = -\pi/6$, and non-negative values of $v_{AB}(\omega t)$ for $-\pi/6 \leq \omega t \leq \pi/3$ as

$$\overline{P_{\mathrm{v}}^{\Delta}} = \frac{k_i \left(2B_{\mathrm{max}}^{\Delta}\right)^{\beta-\alpha}}{(NA)^{\alpha}\,0.5\pi}\int_{-\frac{\pi}{6}}^{\frac{\pi}{3}}\left(v_{AB}(\omega t)\right)^{\alpha}\,\mathrm{d}\omega t\,. \tag{8.30}$$

The integration in (8.30) can be divided into intervals where $v_{AB}(\omega t)$ is constant using (4.10) and then evaluated. By doing so, and plugging $B^{\Delta}_{\max}$ from (8.28), and reducing the obtained expression results in

$$\overline{P^{\Delta}_{\mathrm{v}}} = 4k \left(B^{\Delta}_{\max}\right)^{\beta} f^{\alpha}_{\mathrm{sw}} \chi^{\Delta}_{\mathrm{Q2L}} \tag{8.31a}$$

$$\chi^{\Delta}_{\mathrm{Q2L}} = \frac{\frac{\pi}{3} - (M-0.5)\,\psi + \psi \sum_{k=1}^{2M-1} \left(\frac{k}{2M}\right)^{\alpha}}{\left(\frac{\pi}{3}\right)^{\alpha} \int_{0}^{2\pi} |\cos(\theta)|^{\alpha}\, d\theta}. \tag{8.31b}$$

For $\psi = 0$ (8.31) models a core loss of 2LC-DAB simplified as

$$\overline{P^{\Delta}_{\mathrm{v}}} = 4k \left(B^{\Delta}_{\max}\right)^{\beta} f^{\alpha}_{\mathrm{sw}} \times \frac{1}{\left(\frac{\pi}{3}\right)^{\alpha-1} \int_{0}^{2\pi} |\cos(\theta)|^{\alpha}\, d\theta}. \tag{8.32}$$

8.3 Analysis of developed models

Flux waveforms

According to (8.2), the instantaneous flux in the core of an MFT with YY, YΔ, ΔY, and ΔΔ configurations can be calculated using (8.4), (8.6), (8.8), and (8.10), respectively. Figure 8.1 shows the phase voltages and flux waveforms of a 3ϕ multilevel DAB converter for different winding configurations and $\varphi = \pi/6$. The flux inside the core is depicted for different values of k_σ. When $k_\sigma = 0$, there is no leakage flux from the secondary winding, or one can say that only the secondary winding is excited. Thus, the flux waveform inside the core depends just on the secondary phase voltage. Similarly, if $k_\sigma = 1$, there is no leakage flux from the primary winding (or one can say that only the primary winding is excited). In this case, the flux waveform inside the core depends only on the primary phase voltage.

In reality, there will be leakage flux from both windings, and $k_\sigma \in \{0, 1\}$ are two extreme cases. Therefore, the flux waveform will depend on the primary and the secondary voltages and the phase shift between them. As can be seen from Figure 8.1, the higher the k_σ, the closer the flux waveform to the case where only the primary winding is excited. Similarly, the lower the k_σ, the closer the flux waveform to the case where only the secondary winding is

excited.

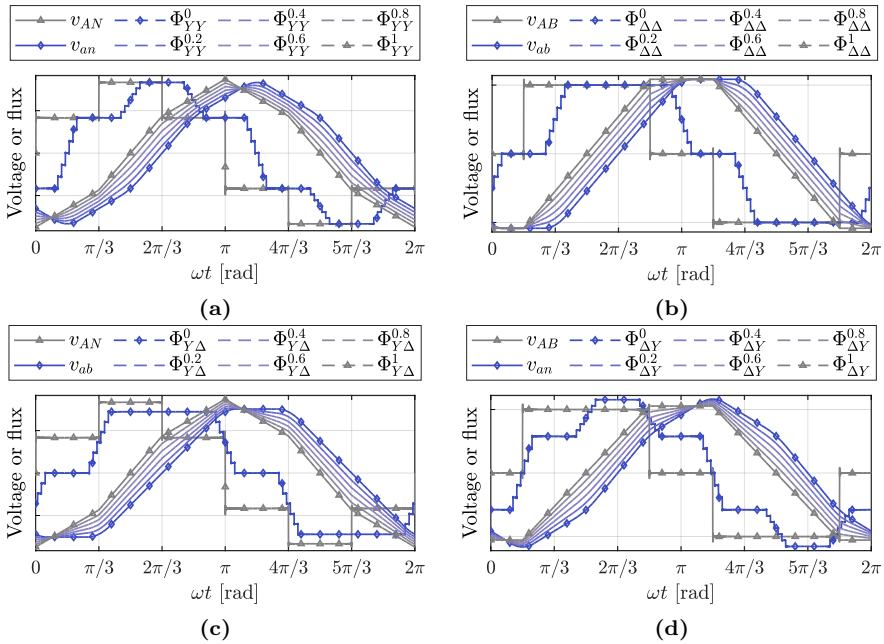

Figure 8.1: Phase voltages and flux waveforms, Φ^{k_σ}, of a multilevel DAB converter at $\varphi = \pi/6$ for different values of k_σ. **(a)** YY configuration. **(b)** $\Delta\Delta$ configuration. **(c)** YΔ configuration. **(d)** ΔY configuration.

Simplified core loss model

One can use the extreme cases of $k_\sigma \in \{0, 1\}$ and assume that only one winding is excited. Then the voltage applied to the energized winding terminals determines the core's flux shape. This is an impactful assumption, and its effects are quantified here. The loss models developed based on this assumption are given in (8.26) and (8.31).

Effect of Q2L modulation

The core loss density modeled by (8.26) and (8.31) depends on the coefficient χ_{Q2L} which is a function of Steinmetz coefficient α, number of levels in the

waveform and the dwell angle. Figure 8.2 visualizes $\chi^{\mathrm{Y}}_{\mathrm{Q2L}}$ and $\chi^{\Delta}_{\mathrm{Q2L}}$ for three values of $\alpha \in \{1.5, 1.75, 2\}$. As seen from Figure 8.2, the value of $\chi^{\mathrm{Y}}_{\mathrm{Q2L}}$ reduces with increasing α for a given M and ψ. On the contrary, larger α results in higher $\chi^{\Delta}_{\mathrm{Q2L}}$. In Figure 8.2c and Figure 8.2f, the iso-lines of $\omega\tau$ are also plotted. The higher the $\omega\tau$, the higher the value of $\chi^{\mathrm{Y}}_{\mathrm{Q2L}}$. Consequently, the loss density in the core increases if $B^{\mathrm{Y}}_{\mathrm{max}}$ is kept constant. However, the increase is marginal because a decrease in the core cross-section compensates for the reduction in $\dot{\Phi}^{\mathrm{Y}}$ to keep $B^{\mathrm{Y}}_{\mathrm{max}}$ constant. On the other hand, $\chi^{\Delta}_{\mathrm{Q2L}}$ reduces considerably by increasing $\omega\tau$ as shown in Figure 8.2f. This is because $N^{\Delta}B^{\Delta}_{\mathrm{max}}A^{\Delta}$ is independent of $\omega\tau$. Therefore, increasing $\omega\tau$ only reduces $\mathrm{d}B^{\Delta}/\mathrm{d}t$, resulting in lower loss density.

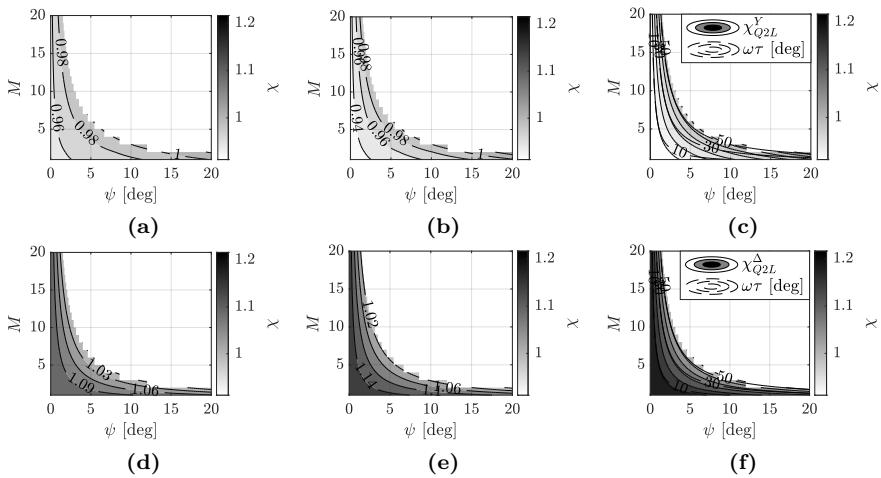

Figure 8.2: $\chi^{\mathrm{Y}}_{\mathrm{Q2L}}$ and $\chi^{\Delta}_{\mathrm{Q2L}}$ as a function of M and ψ. **(a)** $\chi^{\mathrm{Y}}_{\mathrm{Q2L}}$ for $\alpha = 1.5$. **(b)** $\chi^{\mathrm{Y}}_{\mathrm{Q2L}}$ for $\alpha = 1.75$. **(c)** $\chi^{\mathrm{Y}}_{\mathrm{Q2L}}$ for $\alpha = 2$. **(d)** $\chi^{\Delta}_{\mathrm{Q2L}}$ for $\alpha = 1.5$. **(e)** $\chi^{\Delta}_{\mathrm{Q2L}}$ for $\alpha = 1.75$. **(f)** $\chi^{\Delta}_{\mathrm{Q2L}}$ for $\alpha = 2$.

Quantification of the simplification error

In the derivation of (8.26) and (8.31), it is assumed that $k_\sigma \in \{0, 1\}$. However, in practical applications, there is a leakage flux from both sides ($k_\sigma \in [0, 1]$), and the losses depend on the distribution of the leakage inductance. A model of a DAB converter is developed in PLECS to verify the assumptions and

quantify the introduced error.

Simulation case setup

The primary bridge is assumed to be a two-level converter ($M_\mathrm{p} = 1$, $\theta_{0\mathrm{p}} = 0$), and the secondary bridge is an CTB with three submodules per arm ($M_\mathrm{s} = 3$). The primary side switches are modulated with a 50 % duty cycle, and the secondary bridge is modulated with the Q2L modulation technique. The primary and the secondary dc-links nominal voltage are selected to be equal for simplicity ($V_{\mathrm{dc,p}}^{\mathrm{nom}} = V_{\mathrm{dc,s}}^{\mathrm{nom}} = 5\,\mathrm{kV}$). The converter has a nominal power of $P_{3\phi}^{\mathrm{nom}} = 2\,\mathrm{MW}$ and a switching frequency of $f_\mathrm{sw} = 5\,\mathrm{kHz}$. A controller regulates the active power flow by adjusting the phase shift between the two bridges. The specification of the simulated converters is presented in Table 8.1.

It is assumed that the transformer has a 3ϕ E-core structure. The core is modeled in the magnetic domain of PLECS with linear magnetic permeances. Different winding configurations are realized by electrical connections in the electrical domain of PLECS. It is assumed that the primary winding has a resistance value of $R_\mathrm{p} = 10\,\mathrm{m\Omega}$. The primary-side-referred secondary winding resistance is also assumed to be $R_\mathrm{s}^\mathrm{p} = 10\,\mathrm{m\Omega}$.

Table 8.1: Specifications of the simulated dc-dc converter

Converter	f_sw	$P_{3\phi}^{\mathrm{nom}}$	M_p	M_s	$\theta_{0\mathrm{p}}$	ψ_s
2LC-CTB	5 kHz	2 MW	1	3	0	3.6°[a]
Winding type	$V_{\mathrm{dc,p}}^{\mathrm{nom}}$	$V_{\mathrm{dc,s}}^{\mathrm{nom}}$	φ^{nom}	L_σ^p	$R_\mathrm{p} = R_\mathrm{s}^\mathrm{p}$	$N_\mathrm{p} : N_\mathrm{s}$
YY	5 kV	5 kV	20°	84.2 µH	10 mΩ	11 : 11
YΔ	5 kV	5 kV	20°	80.2 µH	10 mΩ	11 : 19
ΔY	5 kV	5 kV	20°	240.6 µH	10 mΩ	19 : 11
ΔΔ	5 kV	5 kV	20°	252.4 µH	10 mΩ	19 : 19

[a] where $\theta_{k_\mathrm{s}\mathrm{s}} = (k_\mathrm{s} + 0.5)\psi_\mathrm{s},\ \forall k_\mathrm{s} \in \{0, ..., (M_\mathrm{s} - 1)\}$.

A nanocrystalline magnetic material, VITROPERM 500 F [46], from Vac-

uumschmelze is selected as the core material for this study. The Steinmetz coefficients of the material are extracted from the typical loss curve provided in the material datasheet as $\alpha \approx 1.8$, $\beta \approx 2.09$, $k \approx 0.0093\,\mathrm{W\,m^{-3}}$. The core cross-section is assumed constant throughout the study and is selected as $A = 100\,\mathrm{cm}^2$.

The value of the leakage inductance for each winding configuration is selected such that the nominal power of the converter is transferred at $\varphi^{\mathrm{nom}} = 20°$. It is important to note that designing the converter with high values of φ is undesirable due to high reactive power flow. The value of total leakage inductance, L_σ, is kept constant while its distribution between the primary and secondary sides is altered to validate the assumptions. This is done by tuning the leakage permeances of the primary and secondary windings. The values of the total leakage inductances and the turn ratios of the windings for different winding configurations are provided in Table 8.1.

The waveforms of the fluxes in different parts of the core are captured in steady-state periods and are saved for post-processing. Eventually, (8.1) is applied to the obtained waveforms from the simulation to calculate the loss density. The loss density is also estimated for two extreme cases of $k_\sigma \in \{0, 1\}$ using (8.26) and (8.31). As mentioned earlier, when $k_\sigma = 0$, there is no flux leakage from the secondary side winding. Therefore, the secondary bridge waveforms should be used to estimate the losses. Similarly, the primary bridge waveforms should be used to estimate the losses when $k_\sigma = 1$. The estimation error, $\Delta\overline{P_{\mathrm{v}j}}$ (where $j \in \{\mathrm{p}, \mathrm{s}\}$), is defined as

$$\Delta\overline{P_{\mathrm{v}j}} = \frac{\overline{P_{\mathrm{v}}^{\mathrm{sim}}} - \overline{P_{\mathrm{v}j}^{\mathrm{calc}}}}{\overline{P_{\mathrm{v}}^{\mathrm{sim}}}} \times 100\,\% \tag{8.33}$$

where $\overline{P_{\mathrm{v}}^{\mathrm{sim}}}$ is the loss density obtained from applying (8.1) on the flux waveforms of PLECS; and $\overline{P_{\mathrm{v}j}^{\mathrm{calc}}}$ (where $j \in \{\mathrm{p}, \mathrm{s}\}$) is the loss density calculated from (8.26) and (8.31). As an example, if the primary winding is Y-connected, then $\overline{P_{\mathrm{vp}}^{\mathrm{calc}}}$ is calculated from (8.26) using the primary bridge parameters.

YY and ΔΔ winding configurations

Figure 8.3 depicts $\Delta\overline{P_{\mathrm{v}j}}$ at different load levels, $P_{3\phi}^{\mathrm{pu}}$, for YY and ΔΔ winding configurations. The primary bridge parameters are used to calculate the losses for Figure 8.3a and Figure 8.3c, whereas for Figure 8.3b and Figure 8.3d, the

parameters of the secondary bridge are used. It can be seen that the estimation error is zero if there is a leakage flux only from one of the windings (i.e., $k_\sigma \in \{0, 1\}$). This is because (8.26) and (8.31) are derived under these assumptions, and they are the most accurate when $k_\sigma \approx \{0, 1\}$. Using the primary bridge parameters for both winding connections and $k_\sigma \lessapprox 0.7$ overestimates the losses. This is because of higher $\frac{\mathrm{d}B}{\mathrm{d}t}$ and (or) higher $B_{\max}$ when $k_\sigma \approx 1$ [see Figure 8.1a and Figure 8.1b].

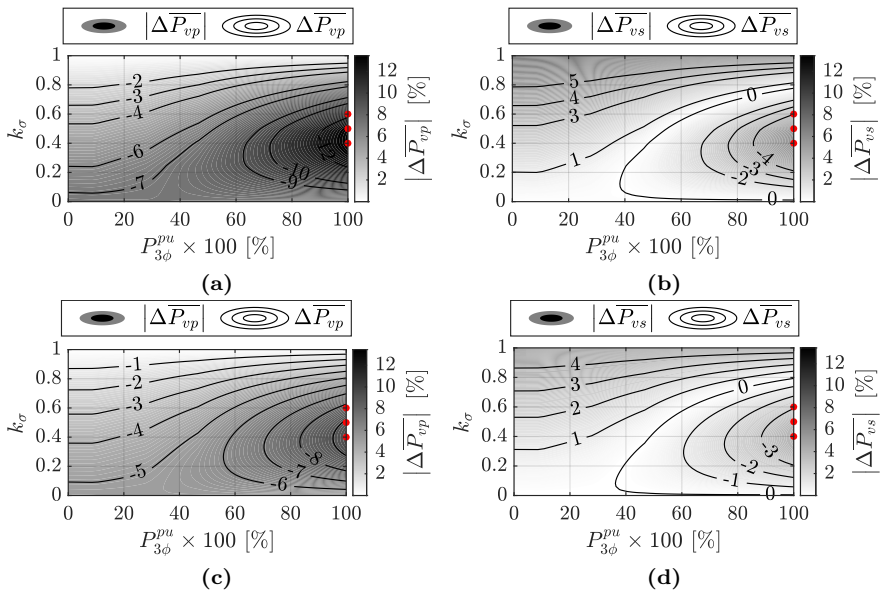

Figure 8.3: The estimation error of core loss density. **(a)** $\Delta\overline{P_{\mathrm{vp}}}$ for YY configuration. **(b)** $\Delta\overline{P_{\mathrm{vs}}}$ for YY configuration. **(c)** $\Delta\overline{P_{\mathrm{vp}}}$ for $\Delta\Delta$ configuration. **(d)** $\Delta\overline{P_{\mathrm{vs}}}$ for $\Delta\Delta$ configuration.

For the YY configuration, increasing load (increasing φ) reduces $B_{\max}$ [see Figure 8.1a]. On the other hand, for the $\Delta\Delta$ configuration, $B_{\max}$ remains constant while $\frac{\mathrm{d}B}{\mathrm{d}t}$ reduces as load increases [see Figure 8.1b]. Therefore, the higher the load (or φ), the higher the estimation error for both winding configurations. This effect is more pronounced when $k_\sigma \approx 0.5$, as shown in Figure 8.3.

The value of $|\Delta\overline{P_{\mathrm{vp}}}|$ is larger than $|\Delta\overline{P_{\mathrm{vs}}}|$ for most of the points in the plots (excluding the cases where k_σ is close to 1). To highlight this further, the

primary bridge is changed to a CTB with three submodules per arm. The dwell angles of both bridges are swept between 0° and 12° for three cases where $(k_\sigma, P_{3\phi}^{\mathrm{pu}}) \in \{(0.4, 1), (0.5, 1), (0.6, 1)\}$.

Figure 8.4 depicts $|\Delta\overline{P_{\mathrm{v}}^{\mathrm{min}}}| \triangleq \min(|\Delta\overline{P_{\mathrm{vp}}}|, |\Delta\overline{P_{\mathrm{vs}}}|)$ for both winding configurations. The points where $|\Delta\overline{P_{\mathrm{vp}}}| < |\Delta\overline{P_{\mathrm{vs}}}|$ are marked with a checkerboard pattern. For both winding configurations and all three conditions, the boundary $|\Delta\overline{P_{\mathrm{vp}}}| = |\Delta\overline{P_{\mathrm{vs}}}|$ is identified as $\omega\tau_{\mathrm{p}} = \omega\tau_{\mathrm{s}}$. The values of the Steinmetz coefficients are altered to see whether they impact the boundary $\omega\tau_{\mathrm{p}} = \omega\tau_{\mathrm{s}}$ or not. Simulation results established that the boundary is independent of Steinmetz coefficients value for the YY and the ΔΔ winding configurations.

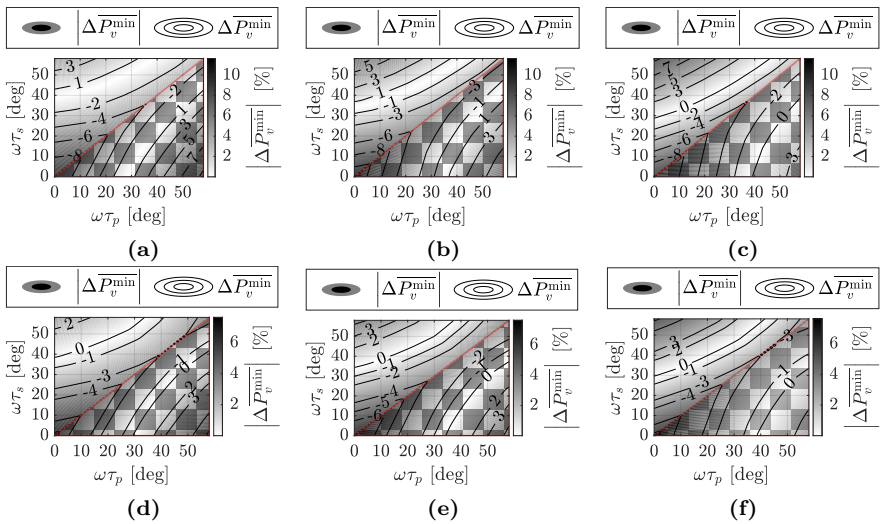

Figure 8.4: The value of $|\Delta\overline{P_{\mathrm{v}}^{\mathrm{min}}}|$ at $P_{3\phi}^{\mathrm{pu}} = 1\,\mathrm{pu}$. **(a)** For YY and $k_\sigma = 0.4$. **(b)** For YY and $k_\sigma = 0.5$. **(c)** For YY and $k_\sigma = 0.6$. **(d)** For ΔΔ and $k_\sigma = 0.4$. **(e)** For ΔΔ and $k_\sigma = 0.5$. **(f)** For ΔΔ and $k_\sigma = 0.6$.

As seen from Figure 8.4, using the primary bridge parameters results in less estimation error when $\omega\tau_{\mathrm{p}} > \omega\tau_{\mathrm{s}}$. Looking at Figure 8.1a and Figure 8.1b, one can see that the flux waveform obtained from the bridge with higher $\omega\tau$ is a smoother and better representative of the actual flux in the core. Therefore, the estimation error is less when the parameters of the bridge with the highest $\omega\tau$ are used for the loss density estimation. As seen from

Figure 8.4, the maximum estimation error is below 7.5 % for most parameter combinations and the ΔΔ winding configuration. This value is 11.5 % for the YY configuration. The higher estimation error of the YY configuration is due to pronounced flux peaks, especially at low $\omega\tau$.

YΔ and ΔY winding configurations

Figure 8.5 shows $|\Delta\overline{P_{\mathrm{v}}}|$ for YΔ and ΔY winding configurations. Similar to the YY and the ΔΔ configurations, the estimation error is lower when the value k_σ is close to 1 or 0, and the waveforms of the winding with the lowest leakage flux are used.

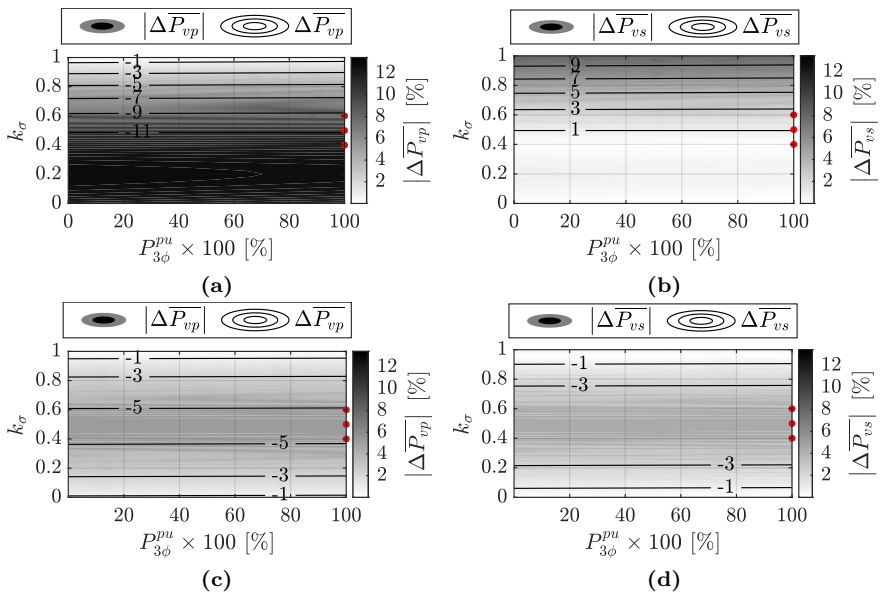

Figure 8.5: The estimation error of core loss density. **(a)** $\Delta\overline{P_{\mathrm{vp}}}$ for YΔ configuration. **(b)** $\Delta\overline{P_{\mathrm{vs}}}$ for YΔ configuration. **(c)** $\Delta\overline{P_{\mathrm{vp}}}$ for ΔY configuration. **(d)** $\Delta\overline{P_{\mathrm{vs}}}$ for ΔY configuration.

For the YΔ winding configuration and the cases where k_σ diverges from 0 or 1, an estimation using the Δ-side waveforms gives a considerably lower error. However, for the ΔY configuration, $|\Delta\overline{P_{\mathrm{vp}}}| \approx |\Delta\overline{P_{\mathrm{vs}}}|$ when k_σ diverges from 0 or 1. To investigate this further, the topology of the primary bridge

is changed to a CTB with three submodules per arm. The dwell angles of both bridges are swept between0° and 12° for three cases where $(k_\sigma, P_{3\phi}^{\mathrm{pu}}) \in \{(0.4, 1), (0.5, 1), (0.6, 1)\}$.

Figure 8.6 shows $\Delta\overline{P_{\mathrm{v}}^{\mathrm{min}}} \triangleq \min(|\Delta\overline{P_{\mathrm{vp}}}|, |\Delta\overline{P_{\mathrm{vs}}}|)$ for YΔ and ΔY winding configurations for the three cases. The domain where $|\Delta\overline{P_{\mathrm{vp}}}| < |\Delta\overline{P_{\mathrm{vs}}}|$ is marked with a checkerboard pattern. The boundary where $|\Delta\overline{P_{\mathrm{vp}}}| = |\Delta\overline{P_{\mathrm{vs}}}|$ is identified as $\omega\tau_\Delta \approx 1.4\omega\tau_{\mathrm{Y}} - 22.4°$. This boundary remains unchanged for phase shifts below 20°. Using the waveforms of the Δ-side results in lower estimation error for both winding configurations and $\omega\tau_\Delta \geq 1.4\omega\tau_{\mathrm{Y}} - 22.4°$. Moreover, the maximum estimation error is below 8.5 % for both winding configurations. For these two winding configurations, the boundary where $|\Delta\overline{P_{\mathrm{vp}}}| = |\Delta\overline{P_{\mathrm{vs}}}|$ is dependent on the values of the Steinmetz coefficients. The larger the α, the smaller the domain where $|\Delta\overline{P_{\mathrm{v}\Delta}}| < |\Delta\overline{P_{\mathrm{vY}}}|$. This domain also reduces with a decrease in β. Nonetheless, using the waveforms of the Δ-side still results in lower estimation error for most of the points shown in Figure 8.6.

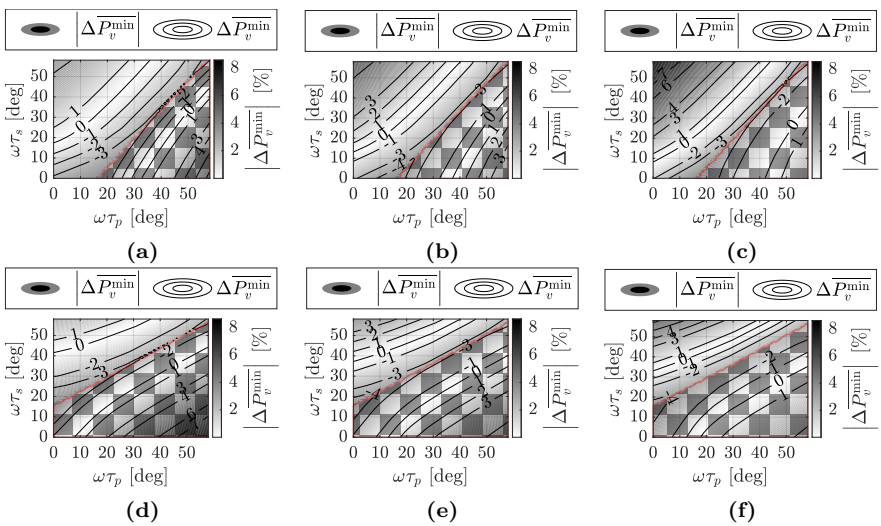

Figure 8.6: The value of $|\Delta\overline{P_{\mathrm{v}}^{\mathrm{min}}}|$ at $P_{3\phi}^{\mathrm{pu}} = 1\,\mathrm{pu}$. **(a)** For YΔ and $k_\sigma = 0.4$. **(b)** For YΔ and $k_\sigma = 0.5$. **(c)** For YΔ and $k_\sigma = 0.6$. **(d)** For ΔY and $k_\sigma = 0.4$. **(e)** For ΔY and $k_\sigma = 0.5$. **(f)** For ΔY and $k_\sigma = 0.6$.

8.4 Experimental verification

An experimental setup is prepared to measure the flux waveforms and validate (8.4)-(8.10). The measurements are done on a Hexa-core 3ϕ transformer. Figure 8.7 shows the measuring setup. The primary and the secondary windings have 57 and 33 turns, respectively. The transformer is connected to the converter shown in Figure 3.1, and the windings are excited with 3ϕ-DAB waveforms. A set of test winding is wound on different parts of the core to measure the induced voltage.

Figure 8.7: The experimental setup for measuring flux waveforms.

Two cases are considered for measurements. A YY-connected CTB-2LC-DAB and a ΔY-connected 2LC-CTB-DAB. For both cases, the CTB has two submodules and is Q2L modulated with 5 % transition time. For both cases, the nominal operating point is considered at 20°. Moreover, the power flow is from the 2LC side to the CTB side, and the converter is switched with 2 kHz. Table 8.2 summarized the converter parameters.

Models (8.4)-(8.10) are used to calculate flux waveforms. The number of winding turns and k_σ are the only required transformer parameters in these models. The primary and secondary leakage inductances are measured using a GW Instek 8110G LCR meter. Afterwards, k_σ is calculated using (8.2). Figure 8.8 shows the measurement setup and the value of k_σ for different phases. As can be seen, there is a small difference between the phases. This

Table 8.2: Specifications of the converter prototype

Converters	τ_p	τ_s	M_p	M_s	φ^nom
YY-CTB-2LC	5 %	0 %	2	1	−20°
ΔY-2LC-CTB	0 %	5 %	1	2	20°
Winding type	f_sw	L_σ^p	$V_\mathrm{dc,p}^\mathrm{nom}$	$V_\mathrm{dc,s}^\mathrm{nom}$	$N_\mathrm{p} : N_\mathrm{s}$
YY-CTB-2LC	2 kHz	185 µH	173 V	100 V	57 : 33
ΔY-2LC-CTB	2 kHz	185 µH	100 V	100 V	57 : 33

is because the leakage inductances are not perfectly balanced between the phases. Nonetheless, the value of k_σ is between 0.95 and 1 at 2 kHz—only a small variance in the parameter.

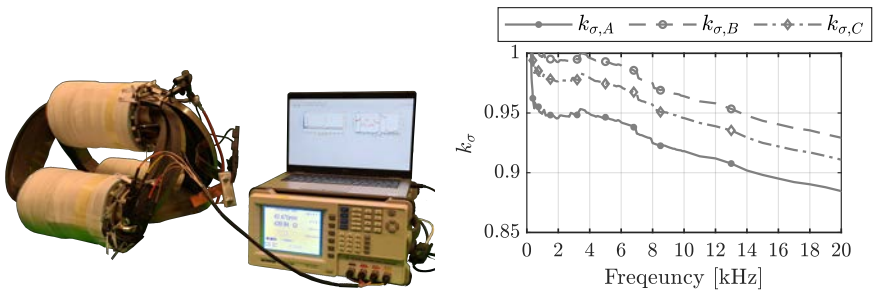

(a) **(b)**

Figure 8.8: Measuring the flux model parameters. **(a)** Impedance measurement setup. **(b)** Value of k_σ for different phases.

Figures 8.9 and 8.10 show the measurement results of the YY-CTB-2LC-DAB and ΔY-2LC-CTB-DAB converters respectively. The P2G voltages are similar, with the only difference being the phase shift between the bridges.

Figure 8.9b shows the measured induced voltages in the test loops on the limbs of YY-CTB-2LC-DAB. These waveforms are similar to the P2N voltages of the CTB side. Since k_σ is larger than 0.95, the leakage inductance of the

secondary bridge constitutes more than 95 % of the total leakage inductance. This means that the flux generated from the primary winding determines the flux waveform inside the core.

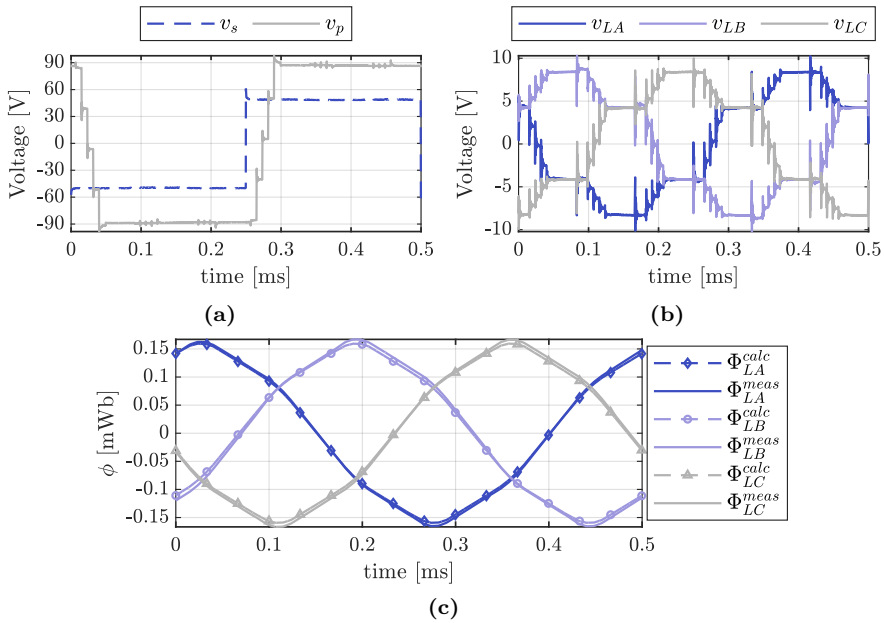

Figure 8.9: Measurement results on YY-CTB-2LC-DAB converter. **(a)** The phase A P2G voltages of the converters. **(b)** Measured induced voltages in the test loops on the limbs. **(c)** Measured and calculated limb fluxes.

The flux in the limbs of the setup, $\phi_{\mathrm{L}x}^{\mathrm{meas}}$ where $x \in \{A, B, C\}$, is calculated by integrating the induced voltages. Figure 8.9c shows the measured fluxes and the calculated flux waveforms from (8.4). There is nearly a perfect match between the measured and calculated values. The slight difference in the amplitudes is due to neglecting the winding resistances, and the unbalances between the phases.

The measured induced voltages in the test loops on the limbs of ΔY-2LC-CTB-DAB are shown in Figure 8.9b. Since the primary winding is excited with the 2LC converter, the induced voltages have the same shape as the P2P voltages of a 2LC converter. The flux in the limbs is calculated by integrating these voltages. As shown in Figure 8.10 there is a perfect match between the

measurements and calculations.

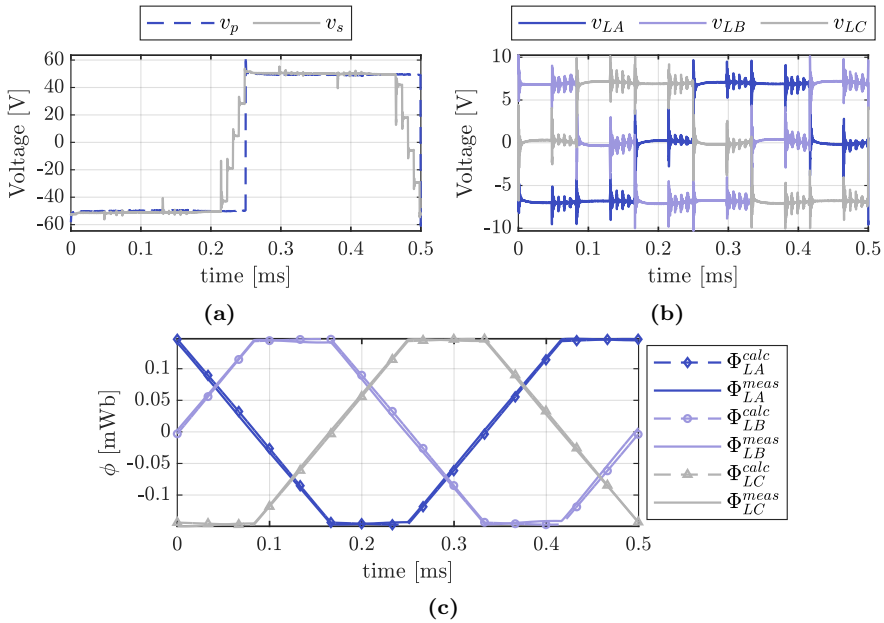

Figure 8.10: Measurement results on ΔY-2LC-CTB-DAB converter. **(a)** The phase A P2G voltages of the converters. **(b)** Measured induced voltages in the test loops on the limbs. **(c)** Measured and calculated limb fluxes.

Since $k_\sigma \approx 1$, then estimating losses using the waveforms of the primary should give the lowest error for these cases. Using Figure 8.3a, the estimation error of core losses for the YY-CTB-2LC-DAB, $k_\sigma \approx 0.95$ and $\varphi = 20°$ is 1.7 %. For the ΔY-2LC-CTB-DAB, using Figure 8.5a the core loss estimation error is less than 1 %. To conclude, if there is a possibility of measuring the distribution of leakage inductance; and if the $k_\sigma \approx 1$ or $k_\sigma \approx 0$ then using the parameters of the winding with the lowest leakage inductance gives highly accurate core loss estimation. Otherwise, the guidelines provided in the previous section can be used to get low estimation errors.

8.5 Conclusions and discussion

Models are developed to estimate the flux waveform inside the core of a 3ϕ DAB converter with arbitrary waveform excitation of windings. The windings can have YY, YΔ, ΔY, and $\Delta\Delta$ configurations. The developed models are verified by simulations and experiments.

Additionally, core loss models are developed for a Q2L-operating 3ϕ DAB converter with different winding configurations. The models are the most accurate when the distribution of the leakage inductance is highly concentrated on one of the windings—$k_\sigma \approx 1$ or $k_\sigma \approx 0$. For the cases where k_σ deviates from 0 or one, guidelines are provided to achieve the highest accuracy using the provided expressions. The effect of the transition times of the bridges on the estimation error of the simplified core loss model is studied. It is shown that using the parameters of the bridge with the longest transition time for the YY and $\Delta\Delta$ configurations results in lower estimation error. Following this guideline for the phase shifts below 20°, estimation errors lower than 7.5 % and 11.5 % can be attained for the $\Delta\Delta$ and the YY configurations, respectively. It is demonstrated that using the parameters of the Δ side results in less estimation error for the YΔ and the ΔY configurations and most of the studied designs. The maximum estimation error for these two winding configurations is below 8.5 %.

CHAPTER 9

Harmonics and Partial Load Performance Studies

This chapter is based on the following articles

[I] **B. Khanzadeh**, T. Thiringer, Y.V. Serdyuk, "Loss reduction at partial loads of multilevel DAB converters using adjusted switching patterns," Submitted to *IEEE transaction*, 2023, (under review).

[II] **B. Khanzadeh**, T. Thiringer, and Y. Serdyuk, "Analysis and improvement of harmonic content in multilevel three-phase DAB converters with different transformer windings connections," in Proceedings of *International Power Electronics Conference (IPEC-Himeji 2022- ECCE Asia)*, 2022, pp. 2653–2658.

9.1 Introduction

Chapter 6 showed that the ΔY configuration could reduce the required capacitor of the converter by 40 % compared to the YY connection of the windings [29]. Also, it was shown in Chapter 7 that the converters with the YY configuration lose the ZVS capability at partial loads, and the dc ratios close to unity. However, the converters with the YΔ configuration could retain the ZVS ca-

pability at partial loads in a narrow region where the dc ratio is between 0.87 and 1.15. Besides the size of the dc-links capacitors, the performance of the 3ϕ-DAB converter is also greatly affected by the windings connections of the MFT [25], [32], [97], [98]. It has been shown in [25], [32] that the 3ϕ-ΔY-DAB has poor efficiency and low transformer utilization in partial loads. This makes the 3ϕ-ΔY-DAB unattractive for applications with recurrent operation at these points unless the partial load performance could be improved. On the other hand, the small capacitor requirement of the 3ϕ-ΔY-DAB converter and its wide ZVS range is advantageous for high power density applications. This provides an incentive to improve its partial load performance.

The performance of a conventional 1ϕ-DAB can easily be improved and optimized for different load conditions. Numerous papers discuss double-phase-shift modulation or triple-phase-shift modulation to minimize reactive power or reduce switching losses [99]–[104]. However, it is impossible to employ the same strategies directly for a conventional 3ϕ-DAB. This is because zero-voltage levels can not be applied to the terminals of the MFT by a three-phase two-level converter. Different methods are proposed in the literature to solve this issue [32], [33], [35], [89], [91], [105]–[109].

In [35], it is proposed to operate the conventional YY-3ϕ-DAB as a 1ϕ-DAB at partial loads. The 1ϕ operation is achieved by giving identical gate signals to two phases [35]. In this way, the former strategies can be used to improve the performance of 3ϕ-DAB in partial loads. Even though this method is effective, the switches are loaded differently, and the operation is not symmetrical anymore.

A burst-mode operation of 3ϕ-DAB is investigated in [32], [109]. In this mode of operation, the power is delivered in discontinuous intervals to ensure the soft-switching of the bridges. This method focuses mainly on the switching losses rather than the conduction losses. Furthermore, it is shown in [32] that the 3ϕ-ΔY-DAB suffers from poor efficiency despite using the burst-mode operation at partial loads.

Asymmetrical duty-cycle control of a 3ϕ-YY-DAB is introduced in [89] to extend the soft-switching range of the converter at partial loads. Further studies using this method are done in [91], [105], [106] to optimize the converter operation at partial loads. It is shown that a considerable reduction in partial load losses can be achieved by this method. However, this strategy requires extra efforts to balance the thermal stress of the switches [91].

The studies performed in [89], [91], [105], [106] have focused only on the YY connection of the winding, and the 3ϕ-ΔY-DAB is not considered in these studies. In [33], [107], [108], T-type active bridges are used instead of two-level converters to increase the soft-switching range of 3ϕ-YΔ-DAB and 3ϕ-YY-DAB converters. In [33], the authors have tried to minimize the RMS current of a 3ϕ-YΔ-DAB by utilizing the duty cycles of the primary and the secondary bridges while ensuring soft-switching operation for wide input and output voltage ranges. However, the proposed control method results in complicated switching patterns, have low accuracy in the partial loads, and has a large no-load current flow in the ac-link, resulting in poor efficiencies.

Missing in the available literature is a proposal for utilizing the benefits of the 3ϕ-ΔY-DAB, while also tackling the problem with high reactive current at low loads. Accordingly, the contribution of this chapter is the investigation of partial load performance of 3ϕ-ΔY-DAB. Moreover, the proposal and study of a control strategy for a 3ϕ-ΔY-DAB which minimizes the partial load currents and reduces the no-load current to zero.

9.2 Harmonic contents of voltages and currents

The transformer of the DAB converter is usually designed to operate with the fundamental frequency ranging from a few kHz to hundreds of kHz, depending on the application of the converter [53], [110], [111]. Since the ac-link waveforms are non-sinusoidal, the transformer is subjected to harmonics of the fundamental frequency. The higher the harmonic content of the voltages and the currents, the higher the losses in the transformer. Thus, it is crucial to study the harmonic performance of the converter.

Studies considering the effects of the transformer winding connections on the harmonic performance of multilevel DAB converters are scarce. One such study is done in [24], where the focus has been on the harmonic content of the phase voltages of a multilevel 3ϕ-YY-DAB. However, neither the ΔY connection of the windings nor the harmonic content of the phase currents is considered in the study.

In this section, mathematical models developed in Chapter 4 will be used to analyze the harmonic content of the waveforms. A case study on a DAB for wind turbine application is done to provide a comprehensible analysis of the mathematical models. The DAB converter is intended to boost the output dc

voltage of a wind turbine from $V_{\mathrm{dc,p}}^{\mathrm{nom}} = 5\,\mathrm{kV}$ to $V_{\mathrm{dc,s}}^{\mathrm{nom}} = 50\,\mathrm{kV}$. The converter is assumed to have a rated active power of $P_{3\phi}^{\mathrm{nom}} = 10\,\mathrm{MW}$. Figure 9.1 shows the topology of the considered DAB converter. The primary converter is assumed to be a 2LC, whereas the secondary side is an CTB with eight submodules per converter's leg.

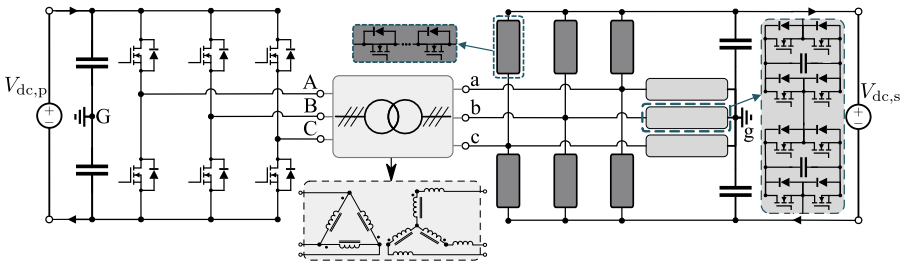

Figure 9.1: The topology of a 3ϕ-ΔY-2LC-CTB-DAB.

The specifications of the converter are summarized in Table 9.1. The leakage inductance of the transformer is selected using the method described in Section 5.3 to ensure minimum reactive power flow in the nominal operating point [65].

Table 9.1: Specifications of the dc-dc converter

Converter	f_{sw}	$P_{3\phi}^{\mathrm{nom}}$	$V_{\mathrm{dc,p}}^{\mathrm{nom}}$	$V_{\mathrm{dc,s}}^{\mathrm{nom}}$	M_{p}	M_{s}
2LC-CTB	5 kHz	10 MW	5 kV	50 kV	1	8
Winding type	$\theta_{0\mathrm{p}}$	ψ_{s}	L_{σ}^{s}	φ^{nom}	N_{p}	N_{s}
YY	0	6.28 mrad[a]	730 µH	8.21°	20	200
ΔY	0	6.28 mrad[a]	2416.7 µH	30.19°	20	115

[a]where $\theta_{k_{\mathrm{s}}\mathrm{s}} = (k_{\mathrm{s}} + 0.5)\psi_{\mathrm{s}},\ \forall k_{\mathrm{s}} \in \{0, ..., (M_{\mathrm{s}} - 1)\}$.

The voltage and current models developed in Chapter 4 are used to evaluate the harmonic performance of the converters. The maximum harmonic order for calculation is limited to 1000. A converter model is also developed in

PLECS to strengthen the study and validate the mathematical models. Since the thermal dynamics of the switches are not the focus of this study, the semiconductors are modeled with ideal switches. The MFT is implemented in the magnetic domain of the PLECS, where the desired leakage inductance value is achieved by properly selecting the leakage permeances. A controller is designed to regulate the power flow and balance the submodule capacitors of the multilevel converter.

Comparison of YY and ΔY

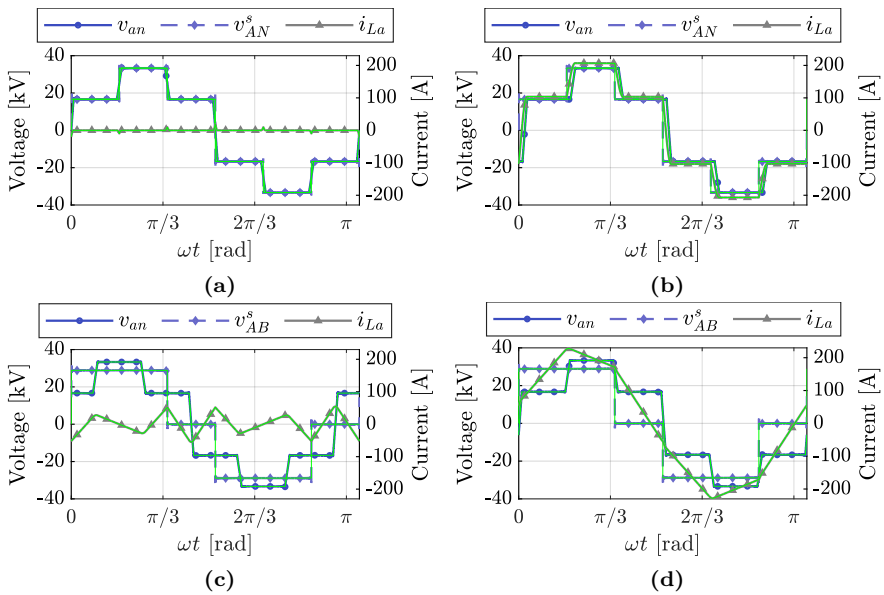

Figure 9.2: The phase A waveforms of a 3ϕ-DAB. The simulation results from PLECS are overlaid with green color. **(a)**YY connection at no-load. **(b)**YY connection at full-load. **(c)**ΔY connection at no-load. **(d)**ΔY connection at full-load.

Figure 9.2 shows the phase voltages and secondary side phase current of the MFT for both winding configurations. The primary phase voltage is referred to the secondary side for ease of visualization. The waveforms are shown only for the extreme cases of no-load and full-load for briefness. The simulation

waveforms obtained from PLECS are overlaid with green colors. As can be seen, there is a perfect match between the simulations and the calculations.

The full-load currents of both windings have the same order of magnitude, as shown in Figure 9.2b and Figure 9.2d. This is due to the selection of the leakage inductances, as discussed earlier, which ensures minimum current at full load. However, the situation is different at no-load. Since there is no active power flow between the bridges, the current is expected to be zero. As seen from Figure 9.2a, the current is almost zero, with small spikes during the transition times for the YY configuration. On the other hand, for the ΔY configuration (as shown in Figure 9.2c), there is a flow of large no-load currents. Since the current waveform has more than two zero crossings per fundamental cycle, it is suspected that low-order harmonics are responsible for these currents.

The harmonic content of the secondary side phase current for both windings configurations is depicted for a few selected operating points in Figure 9.3. The operating point is denoted on the x-axis as the percentage of the nominal power, $P_{3\phi}^{\text{pu}} \triangleq P_{3\phi}^{\text{load}}/P_{3\phi}^{\text{nom}}$. The y-axis shows $I_{H\phi\text{s,RMS}}/I_{\phi\text{s,RMS}}$, where $I_{\phi\text{s,RMS}}$ is the RMS value of the current waveform and $I_{H\phi\text{s,RMS}}$ is the RMS value of the Hth component of the current. In low loads, the share of harmonics increases marginally for the YY configuration. Nonetheless, the fundamental has the highest share for all loads, and the percentage of harmonics remains unchanged.

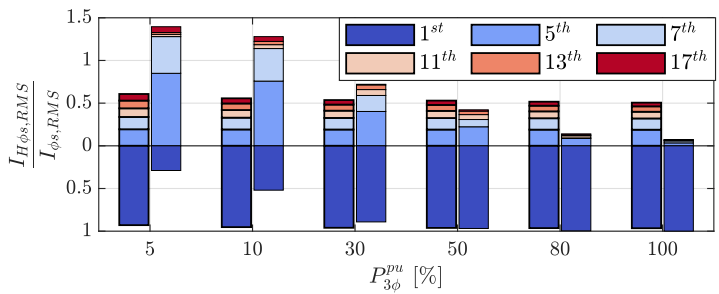

Figure 9.3: Harmonic content of the phase current at different load levels. The YY and ΔY are illustrated with bold and solid bars, respectively.

As shown in Figure 9.3, the trend is completely different for the ΔY configuration. At high loads, the share of harmonics is insignificant and is much

less compared to the YY configuration. However, the share of fundamental component reduces while the percentage of harmonics increases as the load decrease. The RMS value of the harmonics becomes comparable to the fundamental component for loads below 50 %. At loads below 30 %, the dominant harmonics are the 5^{th} and the 7^{th}, respectively. In conclusion, the ΔY configuration has better current harmonic performance than the YY configuration at high loads, whereas it is the contrary in partial loads.

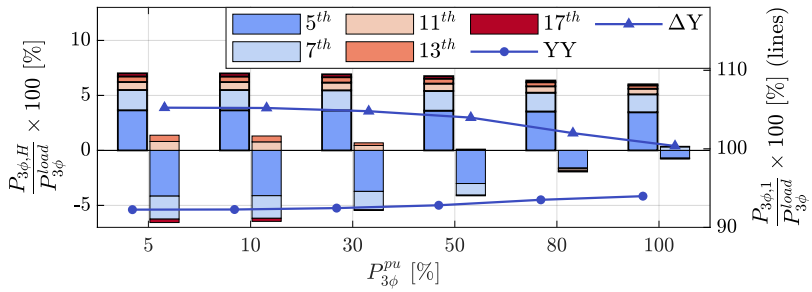

Figure 9.4: The active power transferred by each harmonic. The YY and ΔY are illustrated with bold and solid bars, respectively.

The active power transferred by each harmonic, $P_{3\phi,H}$, is illustrated in Figure 9.4 to highlight the issue with the ΔY configuration in partial loads. It is presented as the percentage of transferred active power, $P_{3\phi}^{\text{load}}$ (e.g., 4 % $P_{3\phi,5}$ at 10 % load level corresponds to $0.04 \times 0.1 \times P_{3\phi}^{\text{nom}} = 40\,\text{kW}$ for the 5^{th} harmonic). The main component transferring the active power is the fundamental component for both windings configurations and all loads. The power flow of harmonics or the YY configuration is from the primary to the secondary, in the same direction as the fundamental. On the contrary, the active power flow direction of the harmonic components (especially the 5^{th} and the 7^{th}) is the opposite of the fundamental for the ΔY configuration. This deteriorates the low load performance of the ΔY configuration as higher fundamental power is required to both meet the load demand and to counteract the harmonics ($P_{3\phi,1} > P_{3\phi}^{\text{pu}}$ as shown in Figure 9.4).

Improving harmonic content of ΔY

As shown in the previous section, the ΔY-DAB has a better harmonic performance in high loads. Moreover, it is shown in [29] that the ΔY connection of the windings can reduce the capacitor size requirement of the converter. Therefore, a remedy for the poor harmonic performance of the ΔY configuration at low loads is highly desired. For wind turbine applications, the switching losses of the output rectifier after the generator can be reduced if the dc-link voltage is lowered [112]. The reduction of the dc-link voltage alongside the extra degrees of freedom provided by the multilevel converter can be used to improve the performance of the ΔY-DAB.

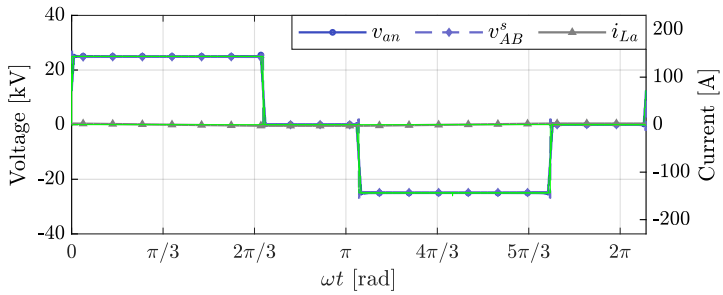

Figure 9.5: The secondary side phase A waveforms of a ΔY type 3ϕ-DAB at no-load with the proposed control method.

The zero level of the output voltage of the multilevel converter (the secondary side) can be increased by controlling the insertion time of the respective submodules (by increasing θ_0 [see Figure 2.5]). By combining this degree of freedom with the reduction of the primary dc-link voltage, the current harmonics of the ΔY-DAB at low loads can be suppressed. Figure 9.5 shows the ac-link waveforms of the ΔY-DAB utilizing the proposed technique. The secondary dc-link voltage is reduced to 86.6 % of its nominal value, and θ_0 is increased by 0.5 rad. As can be seen, the no-load current is reduced to near zero with this method. A similar approach can be taken for partial loads to reduce the harmonic content of the waveforms.

Figure 9.6 shows the harmonic content of the phase voltages at different load levels for both winding types. The YY, ΔY, and ΔY with the proposed control are illustrated with bold solid bars, solid bars, and dashed bars, respectively. Each color represents the ratio of the RMS value of the respective harmonic

to the total RMS value of the waveform.

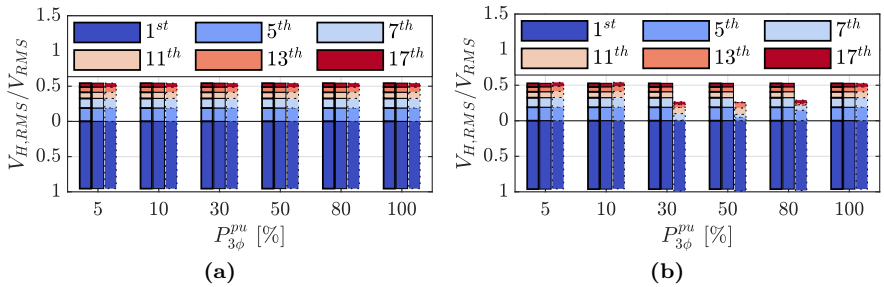

Figure 9.6: Harmonic content of the waveforms at different load levels. The YY, ΔY, and ΔY with the proposed control are illustrated with bold solid bars, solid bars, and dashed bars, respectively. **(a)**Primary phase voltage. **(b)**Secondary phase voltage.

For the primary side voltages (Figure 9.6b), the harmonic content is identical for all three cases. The fundamental is the dominant component, followed by the 5$^{\text{th}}$, the 7$^{\text{th}}$, and the 11$^{\text{th}}$ harmonics. The harmonic content of the secondary side phase voltage (Figure 9.6a) is also identical without any action. However, the 5$^{\text{th}}$ and the 7$^{\text{th}}$ components of ΔY with the proposed control method reduce for the loads between 20 % and 100 % of the nominal power.

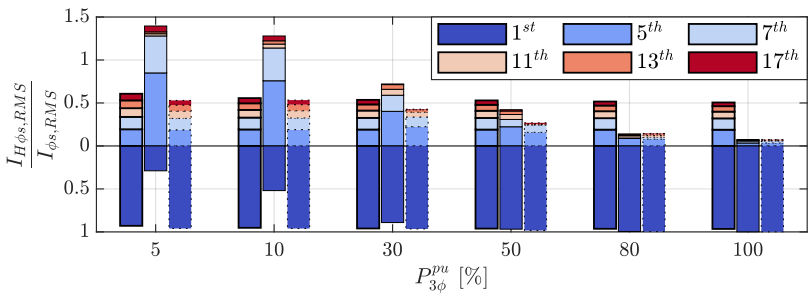

Figure 9.7: Harmonic content of secondary phase currents. The YY, ΔY, and ΔY with the proposed control are illustrated with bold solid bars, solid bars, and dashed bars, respectively.

The harmonic content of the secondary side phase current, shown in Figure 9.7, is the most divergent. It is independent of the load level for the YY

configuration. The 5^{th}, the 7^{th}, and the 11^{th} harmonics are the dominant ones after the fundamental for all loads. As the load reduces below 5 %, the share of these harmonics increases, and they dominate the fundamentals.

As discussed earlier, the 5^{th} and 7^{th} harmonics dominate the fundamental component as the load level reduces for the ΔY configuration. The lower the load, the higher their share in the current waveform. At the no-load, these two components are the dominant ones. Their effect can be seen clearly in Figure 9.2c, where a high no-load current flows in the ac-link. Considerable improvement is achieved with the proposed control method. The percentage of the 5^{th} and the 7^{th} harmonics reduce drastically, and they do not dominate the fundamental anymore. Using the proposed method at a 5 % load level, the amplitudes of the 5^{th} and the 7^{th} harmonics reduce by 78 % and 70 %, respectively. Comparing the three cases for all loads, one can see that the ΔY configuration with the proposed control method has the lowest harmonic content of the secondary phase currents.

The active power transferred by each harmonic is compared for the three cases in Figure 9.8. The harmonics contribute positively to the active power transfer for the YY configuration. The cumulative contribution sums up to 6 % of the demand at full load, which increases to 7 % at a 5 % load level. For the ΔY configuration, the fundamental component has to increase higher than 1 pu to counteract the effect of negative power flow from the low-order harmonics. The lower the load level, the higher the fundamental power increase. At 0.05 pu load ($P_{3\phi}^{\text{load}} = 500\,\text{kW}$), 5.2 % higher power from the fundamental component (total of $0.05 \times 0.052 \times P_{3\phi}^{\text{nom}} = 26\,\text{kW}$) is required to nullify the effect of the harmonics.

The amount of negative power flow from the harmonics reduces with the proposed control method for the load levels below 0.9 pu. The net flow of harmonic power reverses as the load reduces below 0.5 pu. Therefore, the harmonics contribute positively to the active power flow of the ΔY configuration for the loads below 0.5 pu with the proposed control method. The contribution is more than 5 % at loads below 0.1 pu.

9.3 Partial load performance improvement of ΔY

A key problem with the 3ϕ-ΔY-DAB is its low efficiency in partial loads due to the high reactive power flow in the converter [25]. As shown in the

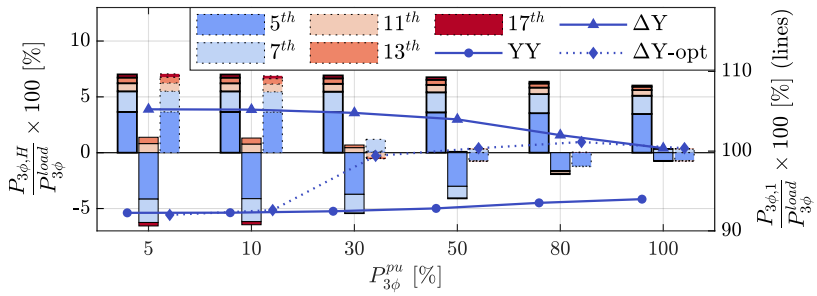

Figure 9.8: The active power transferred by each harmonic. The YY, ΔY, and ΔY with the proposed control are illustrated with bold solid bars, solid bars, and dashed bars, respectively.

previous section, the flow of low-order harmonics in the opposite direction of the fundamental component results in high currents at low loads. A method is described in the same section to reduce the harmonic content of the waveforms. The same method can be used to minimize the RMS current for a given active power and therefore minimize the reactive power.

In this section, the extra degrees of freedom provided by multilevel converters are used to tackle the low efficiency of the 3ϕ-ΔY-DAB at partial load. For the proposed strategies, the Δ-side bridge can be either a multilevel or two-level converter. The Y-side, on the other hand, must be a multilevel topology with at least three levels (e.g., NPC or T-type converters).

For simplicity, it is assumed that the Δ-side bridge is a two-level converter. A CTB converter is selected as the Y-side bridge. The considered DAB converter is shown in Figure 9.1. Despite the secondary bridge topology, the modulation strategy discussed in this section can be applied to any multilevel converter capable of introducing a zero voltage level on its terminals, this includes NPC, T-type, MMC, TAC, and MTAC converters.

Modulation strategies for minimization of RMS currents

The reactive power can be reduced if the RMS current is minimized for a given active power. The phase shift between the bridges is the main degree of freedom to control the active power flow. To improve the converter's performance, the duration of the zero-level voltage of the Y-side, θ_{0s}, is selected as the second degree of freedom. The dwell angles, $\psi_s = \theta_{k_s s} - \theta_{(k_s-1)s}$, are kept

constant for all $k_s \in \{1, ..., M_s\}$ to avoid complicated modulation strategies. By doing so, the resultant modulation can also be used for any multilevel topology other than CTB.

In some applications, reducing the dc-link voltage in partial loads is beneficial. One such application is dc grid-connected wind turbines, as shown in Figure 9.9. In this application, the losses of the turbine-side inverter can be reduced by reducing the LVDC voltage [5], [112]. In addition, the generator losses are lowered, which makes it a double gain at low powers. The DAB controls the power flow in this application, while the turbine-side inverter controls the LVDC voltage—or vice versa. For a given power level, the dc-link voltage can be controlled such that the losses in the DAB converter are minimized. Thus, the LVDC voltage can be used as the third degree of freedom for performance improvement.

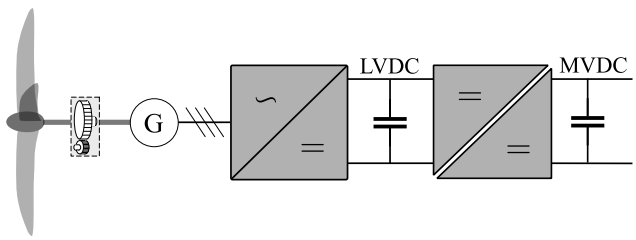

Figure 9.9: Schematic of a dc wind turbine.

In this study, the Δ side is connected to the LVDC link. Therefore, to simplify the study, the third degree of freedom is defined as the ratio of the Δ-side dc-link voltage to its nominal value (i.e., $V_{\mathrm{dc,p}}^{\mathrm{pu}} \triangleq V_{\mathrm{dc,p}}/V_{\mathrm{dc,p}}^{\mathrm{nom}}$). Different modulation strategies can be formulated by combining the three degrees of freedom (i.e., φ, $\theta_{0\mathrm{s}}$, $V_{\mathrm{dc,p}}^{\mathrm{pu}}$). Three modulation strategies are considered, with φ as the main degree of freedom, along with $\theta_{0\mathrm{s}}$, and $V_{\mathrm{dc,p}}^{\mathrm{pu}}$ as the two extra degrees of freedom for the performance improvement.

An optimization problem is formulated for each modulation strategy as $\arg\min\left(I_{\phi\mathrm{s,RMS}}^{\Delta\mathrm{Y}}\right)$ to achieve the best performance; where $I_{\phi\mathrm{s,RMS}}^{\Delta\mathrm{Y}}$ is given by (4.21c). In all optimizations, $P_{3\phi}^{\Delta\mathrm{Y}} = P_{3\phi}^{\mathrm{pu}} P_{3\phi}^{\mathrm{nom}}$ is used as the main constraint; where $P_{3\phi}^{\mathrm{nom}}$ is the nominal power of the converter; $P_{3\phi}^{\mathrm{pu}}$ is a multiplier between 0 and 1, dictating the load level of the converter; and $P_{3\phi}^{\Delta\mathrm{Y}}$ is given by (4.26c). This constraint means that the desired load power should be delivered

irrespective of the modulation strategy.

Control strategy I (S1)

In this strategy, $V_{\mathrm{dc,p}}^{\mathrm{pu}}$ is used for performance improvement, and $\theta_{0\mathrm{s}}$ is kept constant at ψ_{s}. Two sets of inequality constraints are used as $0 \leq \varphi \leq 0.5\pi$, and $V_{\mathrm{dc,p}}^{\mathrm{pu,min}} \leq V_{\mathrm{dc,p}}^{\mathrm{pu}} \leq V_{\mathrm{dc,p}}^{\mathrm{pu,max}}$; where $V_{\mathrm{dc,p}}^{\mathrm{pu,min}}$, and $V_{\mathrm{dc,p}}^{\mathrm{pu,max}}$ are the minimum and maximum values. The optimization should be solved for all values of $P_{3\phi}^{\mathrm{pu}}$ to ensure optimum operation in all load levels (i.e., $\forall P_{3\phi}^{\mathrm{pu}} \in [0,1]$). Thus, the optimization can be formulated as

$$\begin{aligned} &\underset{\varphi, V_{\mathrm{dc,p}}^{\mathrm{pu}}}{\arg\min} \left(I_{\phi\mathrm{s,RMS}}^{\Delta\mathrm{Y}}\right) \\ \text{subject to: } & P_{3\phi}^{\Delta\mathrm{Y}} = P_{3\phi}^{\mathrm{pu}} P_{3\phi}^{\mathrm{nom}}, \\ & V_{\mathrm{dc,p}}^{\mathrm{pu,min}} \leq V_{\mathrm{dc,p}}^{\mathrm{pu}} \leq V_{\mathrm{dc,p}}^{\mathrm{pu,max}}, \\ & 0 \leq \varphi \leq 0.5\pi. \end{aligned} \tag{9.1}$$

Control strategy II (S2)

In this strategy, $V_{\mathrm{dc,p}}$ is kept constant at its nominal value, and only $\theta_{0\mathrm{s}}$ is used to improve the performance. Therefore, φ and $\theta_{0\mathrm{s}}$ are used as decision variables in the optimization problem. Two sets of inequality constraints are used as $0 \leq \varphi \leq 0.5\pi$, and $\theta_{0\mathrm{s}}^{\mathrm{min}} \leq \theta_{0\mathrm{s}} \leq \theta_{0\mathrm{s}}^{\mathrm{max}}$; where $\theta_{0\mathrm{s}}^{\mathrm{min}}$, and $\theta_{0\mathrm{s}}^{\mathrm{max}}$ are the minimum and maximum values. The optimization should be solved for all values of $P_{3\phi}^{\mathrm{pu}}$ to ensure optimum operation in all load levels (i.e., $\forall P_{3\phi}^{\mathrm{pu}} \in [0,1]$). Thus, the optimization can be formulated as

$$\begin{aligned} &\underset{\varphi, \theta_{0\mathrm{s}}}{\arg\min} \left(I_{\phi\mathrm{s,RMS}}^{\Delta\mathrm{Y}}\right) \\ \text{subject to: } & P_{3\phi}^{\Delta\mathrm{Y}} = P_{3\phi}^{\mathrm{pu}} P_{3\phi}^{\mathrm{nom}}, \\ & \theta_{0\mathrm{s}}^{\mathrm{min}} \leq \theta_{0\mathrm{s}} \leq \theta_{0\mathrm{s}}^{\mathrm{max}}, \\ & 0 \leq \varphi \leq 0.5\pi. \end{aligned} \tag{9.2}$$

Control strategy III (S3)

Both $V_{\mathrm{dc,p}}^{\mathrm{pu}}$ and $\theta_{0\mathrm{s}}$ are used to improve the converter performance in this strategy. Also, three sets of inequality constraints are used as: $0 \leq \varphi \leq 0.5\pi$,

$V_{\mathrm{dc,p}}^{\mathrm{pu,min}} \leq V_{\mathrm{dc,p}}^{\mathrm{pu}} \leq V_{\mathrm{dc,p}}^{\mathrm{pu,max}}$, and $\theta_{0\mathrm{s}}^{\mathrm{min}} \leq \theta_{0\mathrm{s}} \leq \theta_{0\mathrm{s}}^{\mathrm{max}}$, to keep the decision variables within predefined limits. The optimization should be solved for all values of $P_{3\phi}^{\mathrm{pu}}$ to ensure optimum operation in all load levels (i.e., $\forall P_{3\phi}^{\mathrm{pu}} \in [0,1]$). Thus, the optimization can be formulated as

$$\begin{aligned} &\underset{\varphi, V_{\mathrm{dc,p}}^{\mathrm{pu}}, \theta_{0\mathrm{s}}}{\arg\min} \left(I_{\phi\mathrm{s,RMS}}^{\Delta\mathrm{Y}}\right) \\ \text{subject to: } &P_{3\phi}^{\Delta\mathrm{Y}} = P_{3\phi}^{\mathrm{pu}} P_{3\phi}^{\mathrm{nom}}, \\ &V_{\mathrm{dc,p}}^{\mathrm{pu,min}} \leq V_{\mathrm{dc,p}}^{\mathrm{pu}} \leq V_{\mathrm{dc,p}}^{\mathrm{pu,max}}, \\ &\theta_{0\mathrm{s}}^{\mathrm{min}} \leq \theta_{0\mathrm{s}} \leq \theta_{0\mathrm{s}}^{\mathrm{max}}, \\ &0 \leq \varphi \leq 0.5\pi. \end{aligned} \tag{9.3}$$

Case study of proposed modulation strategies

A simulation model of the converter is developed in MATLAB to validate the proposed modulation schemes and investigate the improvement in the performance of the converter. It is assumed that the converter has a nominal power of 2 MW, and the switching frequency is 5 kHz. The nominal voltage of the Δ-side 1 kV. The power is fed to an MVDC link from the Y-side with a fixed dc-link voltage of 5 kV. Semiconductor devices with 1.7 kV rated voltage are used in the simulations. Therefore, three submodules per leg of the CTB converter are required to block the half dc-link voltage with a 60 % safety margin as discussed in Section 6.2.

The dwell angle is considered fixed at 0.36°. The leakage inductance of the transformer is selected using the method described in Section 5.3 to ensure minimum reactive power flow in the nominal operating point [65]. This results in a secondary-side referred inductance value of 125 µH. The minimum and maximum values of $V_{\mathrm{dc,p}}^{\mathrm{pu}}$ are selected such that they are not binding constraints in the optimizations. The minimum value of $\theta_{0\mathrm{s}}$ is calculated as $\theta_{0\mathrm{s}}^{\mathrm{min}} = 0.5\psi_{\mathrm{s}}$, and its maximum value is selected to be 35°. Table 9.2 summarizes the specifications of the converter used for the optimizations.

Solving the optimization problems

The optimizations (9.1)-(9.3) are solved using MATLAB for the converter specifications given in Table 9.2. Figure 9.10 illustrates the solutions to the optimization problems. Using strategy I, the decision variable $V_{\mathrm{dc,p}}^{\mathrm{pu}}$ remains

Table 9.2: Specifications of the simulated dc-dc converter

Parameter	Value	Parameter	Value	Parameter	Value
$V_{\mathrm{dc,p}}^{\mathrm{nom}}$	1 kV	M_{s}	3	$\theta_{0\mathrm{s}}^{\mathrm{min}}$	0.18°
$V_{\mathrm{dc,s}}^{\mathrm{nom}}$	5 kV	ψ_{s}	0.36°	$\theta_{0\mathrm{s}}^{\mathrm{max}}$	35°
f_{sw}	5 kHz	$N_{\mathrm{p}} : N_{\mathrm{s}}$	6 : 17	$V_{\mathrm{dc,p}}^{\mathrm{pu,min}}$	0.8
$P_{3\phi}^{\mathrm{nom}}$	2 MW	L_{σ}^{s}	125 µH	$V_{\mathrm{dc,p}}^{\mathrm{pu,max}}$	1

constant at its maximum value with only a minor change in powers below 20 %. This means that by only reducing the Δ-side dc-link voltage, the value of $I_{\phi\mathrm{s,RMS}}^{\Delta\mathrm{Y}}$ will not improve noticeably. Therefore, this strategy will be dropped hereafter. The decision variables change between their respective bounds for strategies II and III, which means that the converter's performance can be improved using these strategies.

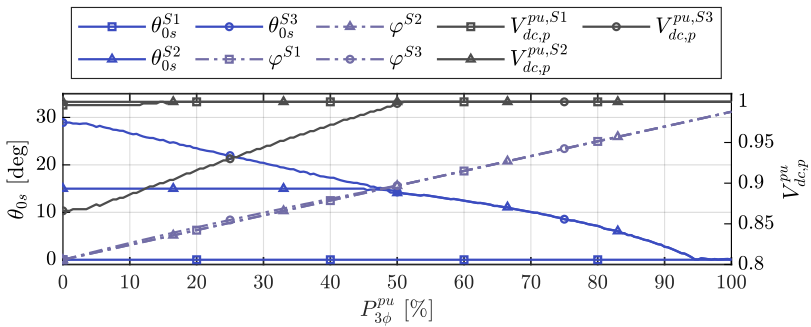

Figure 9.10: Solutions of optimizations (9.1)-(9.3). Strategies I, II, and III are marked with squares, triangles, and circles, respectively.

With strategy III, the optimum solution is obtained at the nominal Δ-side dc-link voltage for load levels between 50 % and 100 %. Since with strategy II, the Δ-side dc-link voltage is kept constant, strategies II and III will have identical performance for load levels between 50 % and the nominal value. The optimization results suggest that $\theta_{0\mathrm{s}}$ should be kept constant at 15° using strategy II for load levels below 50 %. The dc-link voltage for the same power range should be reduced linearly to 86.6 % of its nominal value at no load

using strategy III. Also, θ_{0s} should be increased for the same strategy as the load level is reduced to minimize the current.

Simulation of the converter

The converter shown in Figure 9.1 is modeled in PLECS to investigate its performance improvement using the discussed strategies. The optimization result of Figure 9.10 is incorporated in the controller of the converter using look-up tables. In addition, the values of θ_{0s} and $V_{dc,p}^{pu}$ are controlled based on the active power level of the converter. A capacitor balancing algorithm is also implemented to regulate the capacitors' voltages of the CTB converter. The converter's performance is evaluated based on the RMS currents, the turn-ON current ($i_{sw,on}$), the turn-OFF current ($i_{sw,off}$), and the losses in the semiconductors and the transformer.

The semiconductor devices considered for the loss analysis are 1.7 kV SiC MOSFETs from CREE. CAB500M17HM3 MOSFETs are selected for the primary bridge. Five series-connected CAS300M17BM2 MOSFETs are used as the main switches of the secondary bridges. For the full-bridge chain-links of the secondary bridge, two parallel-connected C2M0045170P MOSFETs are utilized to ensure the same lifetime as the main switches [113]. The semiconductors are modeled based on the manufacturer's datasheets, [76], [77], [114], assuming a fourth-order Foster network connected to a heatsink. For simplicity, the heatsink temperature is kept constant at room temperature.

An optimized design is considered for the 3ϕ transformer. The primary and the secondary windings have 6 and 17 turns, respectively. In addition, the mean length turns of the primary and the secondary windings are 58.5 cm and 88 cm, respectively. The transformer is assumed to have an E-cut core geometry with a core cross-section of 90 cm^2 and a window area of 174 cm^2. The windings are assumed to be copper with a current density of 3 $A\,mm^{-2}$ at the nominal power. Vitroperm 500F, a noncrystalline material from Vacuumschmelze [115], is selected as the core material due to low losses.

The MFT is implemented in the magnetic domain of PLECS with linear permeances. The magnetic fluxes in different core parts are extracted from PLECS for each operating point. Then the core loss density, $\overline{P_v}$, is calculated using the improved generalized Steinmetz equation given by (8.1) [96]. The Steinmetz coefficients are extracted from the material datasheet as $\alpha = 1.8$, $\beta = 2.0961$, and $k = 0.0093\,W\,m^{-3}$. Eventually, the core loss, P_{core}^{MFT}, is

calculated as

$$P_{\text{core}}^{\text{MFT}} = \sum_{k} \overline{P_{\text{v}k}} V_k \tag{9.4}$$

where $\overline{P_{\text{v}k}}$ is the loss density in the kth section of the core and V_k is the volume of the kth section.

Figure 9.11 depicts the absolute value of $I_{\phi\text{s,RMS}}^{\Delta\text{Y}}$ for different strategies and power levels. In addition, the relative change $\Delta I_{\phi\text{s,RMS}}^{\Delta\text{Y}}$ is visualized, which is defined as

$$\Delta I_{\phi\text{s,RMS}}^{\Delta\text{Y}} \triangleq \frac{I_{\phi\text{s,RMS}}^{\Delta\text{Y}}\Big|_{\text{no action}} - I_{\phi\text{s,RMS}}^{\Delta\text{Y}}\Big|_{\text{with action}}}{I_{\phi\text{s,RMS}}^{\Delta\text{Y}}\Big|_{\text{no action}}} \times 100\%. \tag{9.5}$$

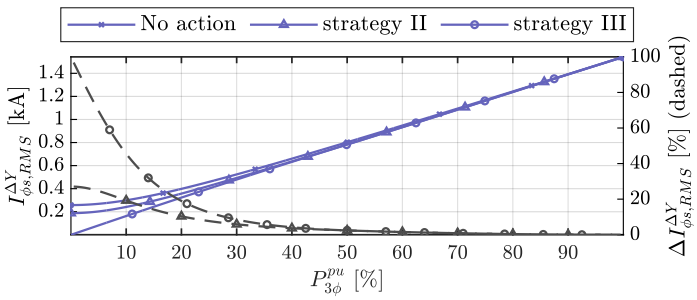

Figure 9.11: $I_{\phi\text{s,RMS}}^{\Delta\text{Y}}$ and its percentage of reduction for different strategies.

As seen by comparing the results for strategies II and III, both approaches result in 2.4 % improvement in $I_{\phi\text{s,RMS}}^{\Delta\text{Y}}$ at a 50 % load level. Strategy III starts to outperform strategy II as the load level reduces. The improvement in $I_{\phi\text{s,RMS}}^{\Delta\text{Y}}$ at 20 % load is 10 % and 19 % with strategies II and III, respectively. Note that the value of $I_{\phi\text{s,RMS}}^{\Delta\text{Y}}$ is 258 A at no-load without any action, and with strategy II, it decreases by 27 % to 188 A; and with strategy III, it reduces to near-zero. Consequently, the conduction losses in the semiconductor devices and the copper losses in the MFT should be reduced.

In Figure 9.12, the switching currents of the semiconductors are visualized. Without any action, the switching currents remain almost constant for loads below 90 %. This will result in high switching losses at partial loads, especially in high-frequency applications. It is noteworthy that all switches can achieve

turn-ON ZVS due to negative currents in the whole power range without any action. Both proposed strategies reduce the switching currents of the Y-side bridge. As expected, the performance of these strategies is identical for load levels between 50 % and the nominal value. Strategy II results in lower currents compared to strategy III below $P_{3\phi}^{\mathrm{pu}} \approx 42\,\%$. However, some switches lose turn-ON ZVS, and others gain turn-OFF zero current switching (ZCS).

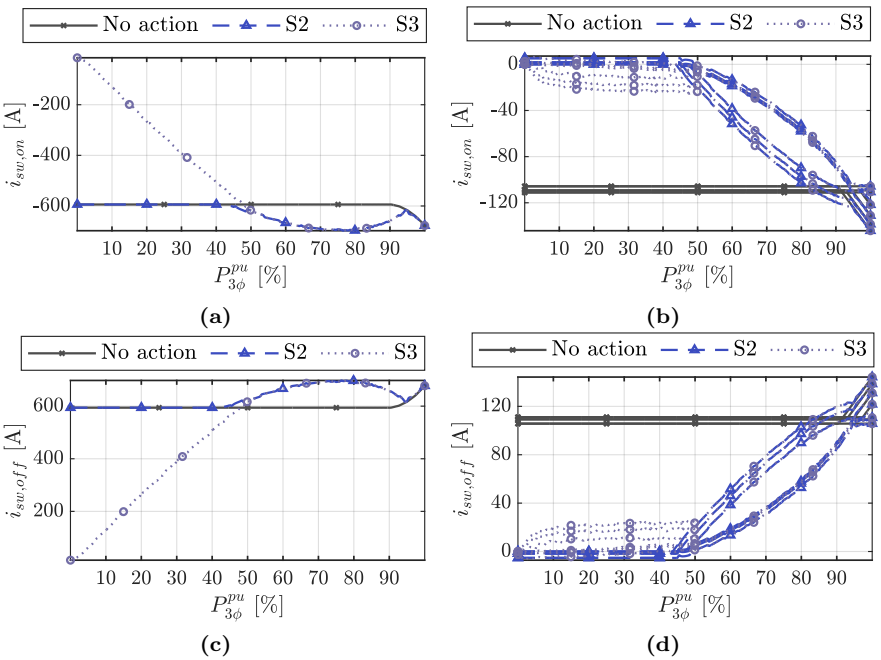

Figure 9.12: The switching currents of the semiconductors for different strategies. **(a)** $i_{\mathrm{sw,on}}$ of the Δ-side bridge. **(b)** $i_{\mathrm{sw,on}}$ of the Y-side bridge. **(c)** $i_{\mathrm{sw,off}}$ of the Δ-side bridge. **(d)** $i_{\mathrm{sw,off}}$ of the Y-side bridge.

The switching currents of the Δ-side bridge are increased by a maximum of 16.5 % for load levels between $P_{3\phi}^{\mathrm{pu}} \approx 50\,\%$ to $P_{3\phi}^{\mathrm{pu}} \approx 95\,\%$ for both strategies compared to the case without action. This will result in higher switching losses in the Δ-side bridge in this operation region. For loads below $P_{3\phi}^{\mathrm{pu}} \approx 40\,\%$, the switching currents of the Δ-side bridge with strategy II remain the same as the case without action. In conclusion, strategy II deteriorates the switching currents of the Δ-side bridge. On the contrary, strategy III

reduces the switching currents of the Δ-side bridge for the load levels below $P_{3\phi}^{\text{pu}} \approx 50\,\%$. To summarize, strategy III outperforms strategy II and the case with no action by lower Δ-side turn-OFF currents for all load levels below $P_{3\phi}^{\text{pu}} \approx 50\,\%$.

Figure 9.13 visualizes the loss breakdown of the converter for different load levels and strategies. The losses are presented as a percentage of the respective load level (e.g., $P_{\text{loss}} = 1\,\%$ at $P_{3\phi}^{\text{pu}} = 50\,\% \equiv 1\,\text{MW}$ is equivalent to $0.01 \times 1\,\text{MW} = 10\,\text{kW}$ losses.). Three sets of bars are presented per load level. The first set of bars with solid edges corresponds to the case with no action; The second set with dashed edges represents strategy II; and strategy III is illustrated with the third set of bars with dashed edges.

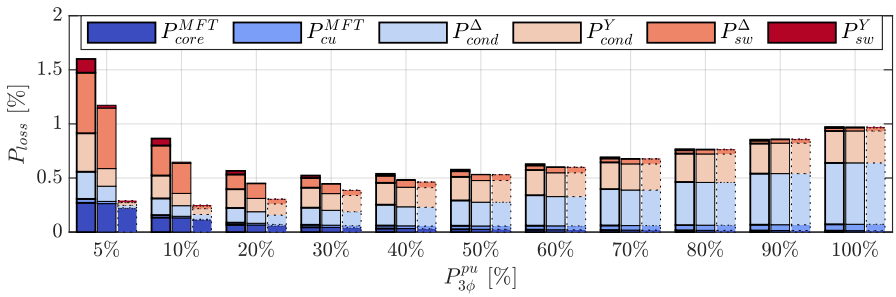

Figure 9.13: Comparison of components of losses with and without proposed strategies. The bars with bold solid, solid, and dashed edges illustrate cases with no action, strategy II and strategy III, respectively. P_x^y, $x \in \{\text{cond}, \text{sw}\}$ $y \in \{\Delta, \text{Y}\}$ is the total semiconductor conduction (cond) and switching (sw) loss of the respective bridge. P_x^{MFT}, $x \in \{\text{core}, \text{cu}\}$ is the total core and copper loss of the MFT.

As follows from the results, the total loss percentage reduces without action as the load level decreases from the nominal value to $P_{3\phi}^{\text{pu}} \approx 30\,\%$. However, P_{loss} increases by reducing the load below $P_{3\phi}^{\text{pu}} \approx 30\,\%$ due to high switching and conduction losses. This is also affected by the core losses of the transformer, $P_{\text{core}}^{\text{MFT}}$. The absolute value of core losses is almost independent of the load level. Therefore, in lower loads, the percentage of $P_{\text{core}}^{\text{MFT}}$ is higher.

For load levels between 50 % and 90 %, the reduction in the cumulative conduction losses and the switching losses of the Y-side bridge dominates and overcomes the increased switching losses of the Δ-side bridge. However, the improvement is marginal with both proposed strategies in the mentioned

load range due to the low switching frequency used in the simulation. The improvement with the proposed strategies is expected to be more significant for higher switching frequencies as the turn-OFF currents of the Y-side bridge trend toward zero.

The improvement is noticeable for load levels below 50 % with both proposed strategies. Moreover, strategy III outperforms strategy II for all load levels. The main reason for the better performance of strategy III compared to strategy II is the reduction of conduction losses and the Δ-side switching losses. Comparing the case with no action with strategy II regarding the switching losses of the Δ-side bridge for the load levels below 40 %, one can see that P_{sw}^{Δ} remains unchanged. This was expected as the switching currents of the Δ-side bridge remain unchanged for these load levels.

To sum up, the total losses at $P_{3\phi}^{\mathrm{pu}} = 5\,\%$ have decreased by 0.4 % unit, from 1.6 % with no action to 1.2 % with strategy II. Comparing strategy III with the case with no action, the total losses have decreased by 1.3 % and 0.6 % unit at $P_{3\phi}^{\mathrm{pu}} = 5\,\%$ and $P_{3\phi}^{\mathrm{pu}} = 10\,\%$, respectively. The semiconductor losses are the main contributor to the improvement. Using strategy III, the improvement in the total semiconductor losses is 94 % and 81 % unit at 5 % and 10 % of the nominal power, respectively.

Experimental validation

The experimental setup shown in Figure 3.2 is used to validate the proposed methods. A set of 30 µH external inductors is connected in series with the primary ac-link to increase the phase shift range of the converter without exceeding the current rating of the submodules. The prototype specifications are summarized in Table 9.3.

Table 9.3: The prototype specifications

Parameter	Value	Parameter	Value	Parameter	Value
$V_{\mathrm{dc,p}}^{\mathrm{nom}}$	100 V	f_{sw}	5 kHz	L_{σ}^{p}	3.6 µH
$V_{\mathrm{dc,s}}^{\mathrm{nom}}$	346 V	M_{s}	2	$N_{\mathrm{p}} : N_{\mathrm{s}}$	15 : 30
$P_{3\phi}^{\mathrm{nom}}$	2.5 kW	ψ_{s}	6°		

A set of optimizations are performed with the converter specifications given

in Table 9.3 to identify $V_{\mathrm{dc,p}}^{\mathrm{pu}}$ and $\theta_{0\mathrm{s}}$ values for strategies II and III. The optimization results are implemented as lookup tables for the converter control. Using the lookup tables based on the phase shift between bridges, the controller changes the gate signals to obtain desired $\theta_{0\mathrm{s}}$. It also sends control commands to the primary side dc power supply to alter the dc-link voltage. The primary and secondary currents are measured at several operating points for each strategy.

Figure 9.14 shows the measured value of $I_{\phi\mathrm{s,RMS}}^{\Delta\mathrm{Y}}$ for different cases. Markers are used to highlight each measurement point. $\Delta I_{\phi\mathrm{s,RMS}}^{\Delta\mathrm{Y}}$ is calculated similarly to (9.5) by interpolating the measurement points. As expected, a marginal improvement is achieved using strategy II compared to the case with no action. However, an RMS current reduction of more than 90 % is observed in no-load when strategy III is deployed. The simulation model is updated with the experimental setup parameters to compare the simulation with the experiments. The results obtained from the simulation are overlaid in Figure 9.14 with the gray solid and dashed lines. As can be seen, the experimental findings perfectly agree with the simulation results.

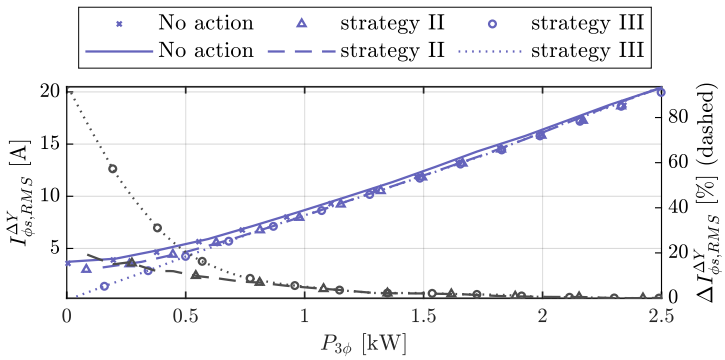

Figure 9.14: Measured (depicted with markers) and simulated (depicted with lines) $I_{\phi\mathrm{s,RMS}}^{\Delta\mathrm{Y}}$ and its percentage of reduction for different strategies.

The switching currents of each semiconductor are identified using the phase currents and switching instants. The turn-OFF switching currents are summarized in Figure 9.15. The measurement results are illustrated with markers, while the simulation results are depicted with lines. As can be seen, the primary side turn-OFF currents are reduced by a factor of nine at no load using

strategy III. The switching currents have also reduced on the secondary side. Moreover, some secondary switches achieve turn-OFF ZVS at partial loads. The measurement results also agree with the simulations. The slight mismatch is due to non-idealities in the measurements, which are not modeled in the simulations.

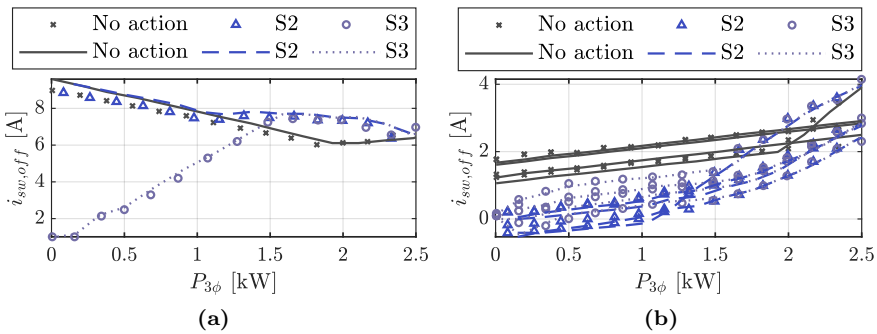

Figure 9.15: Measured (depicted with markers) and simulated (depicted with lines) switching currents. **(a)** $i_{\text{sw,off}}$ of the Δ-side bridge. **(b)** $i_{\text{sw,off}}$ of the Y-side bridge.

9.4 Conclusions and discussion

In this chapter, the harmonic content of the phase voltages and currents of a 3ϕ multilevel DAB converter is studied in detail for different power levels and two winding configurations. Also, control methods are proposed to improve the harmonic performance and efficiency of the ΔY-DAB.

It is established that the current harmonics are dramatically affected by the windings connection. The share of harmonics in the phase current is independent of the power level for the YY configuration. It is shown that the converter with the ΔY winding configuration has higher current harmonics in partial loads than the YY configuration—with the 5^{th} and the 7^{th} being the dominant harmonics. It is also shown that these harmonics contribute positively to the power flow of the YY configuration. On the contrary, the active power flow direction of the harmonics is the opposite of the fundamental for the ΔY configuration. This results in the poor harmonic performance of the ΔY configuration at low loads and potentially can result in increased

losses.

A control method is proposed to improve the harmonic performance of the ΔY-DAB. It is demonstrated that the amplitude of the 5^{th} and 7^{th} harmonics of the secondary phase voltages is reduced using the proposed control method. Moreover, it is shown that the proposed control method reduces the percentage of the low-order current harmonics, especially in partial loads. The amplitudes of the 5^{th} and the 7^{th} harmonics reduces by 78 % and 70 %, respectively, at a 5 % load level with the proposed method. In addition, it is shown that the direction of the active power flow of the harmonics is reversed to match the power transfer direction of the converter with the proposed method. Finally, it is concluded that the ΔY configuration of the windings with the proposed control method has the best harmonic performance.

Approaches for improving the efficiency of multilevel ΔY-DAB converters have been analyzed. Two control strategies have been proposed to minimize the RMS current and improve the partial load performance of the 3ϕ-ΔY converter. The performance improvement is achieved by introducing a zero-level voltage on the Y-side of the converter and (or) reducing the Δ-side dc-link voltage. Both simulations and measurements validate the proposed strategies.

It is shown that the RMS current can be reduced by 27 % at no-load only by increasing the duration of the zero-level voltage of the Y-side. In addition, the turn-ON and turn-OFF currents of the Y-side can be decreased drastically for power levels below 42 % of the nominal power with the same strategy. The study revealed the possibility for considerable improvements in the performance by combining Δ-side dc-link voltage reduction with the Y-side duty cycle variation that leads to the reduction of the RMS current by almost 100 % to near-zero at no-load. This is also validated by measurements where more than 90 % reduction in the RMS current is observed at no-load. Moreover, a dramatic reduction in the switching currents of both bridges is achieved. Measurements highlighted a factor of nine reductions in no-load turn-OFF currents of the primary bridge. At the same time, a loss split calculation showed that the semiconductor losses decreased by 94 % and 81 % at 5 % and 10 % of the nominal power, respectively.

CHAPTER 10

Conclusions and Future Work

10.1 Conclusions

This work studied the 3ϕ DAB converters based on multilevel converter topologies for offshore wind turbine applications. Seven different converter topologies were selected as the candidates for the bridges. These include 2LC, NPC, T-type, MMC, TAC, MTAC, and CTB converters. Also, four winding configurations, namely, YY, YΔ, ΔY, and $\Delta\Delta$ were studied.

Analytical expressions were derived to estimate the desired leakage inductance value of the MFT for a DAB dc-dc converter. The estimated leakage inductance minimized the RMS current for deviations in the dc-links voltages. This was to ensure minimum conduction losses under nominal power operation. The derived expressions were validated with simulations.

The Q2L modulation was considered for the multilevel topologies. The study of the Q2L-operating MMC-DAB with MOSFETs revealed that the primary side's main and the secondary side's auxiliary switches had higher average junction temperatures than the other switches. Moreover, it was shown that the auxiliary switches were more thermally stressed than the main switches due to the impulsive conduction of currents.

The multilevel converters were compared together from the total capacitive energy storage requirement and installed switch power aspects. It was concluded that the CTB converter had the lowest energy storage requirement among the multilevel converters, followed by the MTAC converter. It was shown that the total energy storage requirement of these converters was up to 60 % and 40 % less than for an MMC converter. The CTB had lower installed semiconductors power than the MTAC and was selected for further studies.

The effect of winding configurations on the required energy storage was also studied. An MMC-DAB and CTB-DAB converters were compared for different winding configurations. It was shown that the YΔ connection considerably reduced the capacitor requirements. In the best case, the capacitor requirement of the MMC-DAB and the CTB-DAB was reduced by 30 % and 40 % using the YΔ configuration instead of YY.

General analytical closed-form ZVS boundaries for 3ϕ M-level-to-N-level DAB converters were derived and analyzed. The effects of having different transition times and the number of levels on the ZVS range of the converter were studied. The effects of the winding configurations were also considered in the analysis. It was demonstrated that, unlike the YY connection of the windings, the YΔ connection of the windings could retain the ZVS capability at partial loads in a narrow region where the dc ratio was close to unity. The study was validated with simulations and measurements.

The harmonic content of the phase voltages and currents of a 3ϕ multilevel DAB converter was studied in detail for different power levels and two winding configurations. It was shown that the ΔY-DAB suffers from high harmonic content and low efficiency in low power levels. Control methods were proposed to improve the harmonic performance and efficiency of the ΔY-DAB. The study revealed the possibility for considerable improvements in the performance by combining Δ-side dc-link voltage reduction with the Y-side duty cycle variation that led to the reduction of the RMS current by almost 100 % to near-zero at no-load. This was also validated by measurements where more than 90 % reduction in the RMS current was observed at no-load. Moreover, a dramatic reduction in the switching currents of both bridges was achieved. Measurements highlighted a factor of nine reductions in no-load turn-OFF currents of the primary bridge. At the same time, a loss split calculation showed that the semiconductor losses decreased by 94 % and 81 % at 5 % and 10 % of the nominal power, respectively.

Mathematical expressions were provided to couple the maximum flux density and the required core cross-section with the specifications of 3ϕ multilevel DAB converters. In addition, simple closed-form expressions were derived using IGSE to link the core losses to the modulation parameters. Finally, closed-form expressions were derived to estimate the flux waveforms inside different parts of a 3ϕ transformer core with YY, YΔ, ΔY, and $\Delta\Delta$ winding configurations. The expressions could be used for E-core, E-cut-core, and Hexa-core transformers with arbitrary excitations from different windings. The experimental results showed a perfect match with the developed theory.

10.2 Future work

The studies in the document have focused only on the Y and Δ winding connections. Studying and quantifying the effect of other winding configurations (e.g., zigzag) can be an interesting research topic.

Calculations regarding the desired leakage inductance were done with the first harmonic approximation. It was shown that this assumption results in large errors for YΔ configurations high share of low-order harmonics. A valuable contribution can be solving the optimization using more harmonics.

The studies on the capacitor requirements have assumed that faults were handled with external components on the dc-link. It would be interesting to evaluate the capacitor requirements considering the fault-handling capability of the converter. Moreover, only numerical studies were performed. Deriving closed-form equations can be a valuable contribution.

The output capacitance of the switches was neglected in the soft-switching studies of this document. Including these capacitances in the generalized expressions and evaluating the converter's performance would be interesting.

The MFT's core loss modeling was done using analytical flux waveforms. The flux waveform models were verified both with simulations and experiments. However, the developed loss models were only verified by simulations. It will be a valuable contribution if they are verified by electric or calorimetric measurements.

A simple method was proposed to improve the performance of ΔY-DAB in partial loads. Also, the optimization of leakage inductance focused only on the conduction losses. These can be further improved by including extra constraints like minimum switching loss or MFT losses in the optimizations.

CHAPTER 11

Summary of included papers

This chapter provides a summary of the included papers. In all the papers, the author has contributed to the; conceptualization; methodology; software; validation; formal analysis; investigation; data curation; visualization; and writing.

11.1 Paper I

Babak Khanzadeh, Torbjörn Thiringer
Closed-Form ZVS Boundaries for Three-Phase M-level-to-N-level DAB Converters with Different Winding Configurations
Published in *IEEE Transactions on Power Electronics*, pp. 1–16, 2023 , doi: 10.1109/TPEL.2023.3260682 .

One of the essential characteristics of a three-phase DAB dc-dc converter is its inherent ZVS capability during the turn-ON of the switches. This paper provides closed-form equations that identify the ZVS boundaries for an M-level-to-N-level DAB converter, where M and N can be any natural numbers. It is shown that the derived ZVS boundaries can be used for different con-

verter topologies, including but not limited to 2LC, three-level NPC converter, T-type converter, TAC, MMC, and CTB converter. The effect of different winding configurations of the MFT—YY, YΔ, and $\Delta\Delta$—is also considered in the study. Additionally, easy-to-implement simplified ZVS boundaries are provided and the effects of a different number of levels, transition times, and dead times on the ZVS operation are quantified. An important result shown is that the converters with the YY and the $\Delta\Delta$ windings lose ZVS at partial loads as soon as the transition time increases from zero, whereas the ones with the YΔ configuration retain ZVS at partial loads and dc ratios close to unity, without any advanced modulation techniques. The derived analytical models are validated with MATLAB simulations and experiments.

11.2 Paper II

Babak Khanzadeh, Torbjörn Thiringer, Yuriy V. Serdyuk
Loss Reduction at Partial Loads of Multi-Level DAB Converters Using Adjusted Switching Patterns
Submitted to *IEEE Transactions*, 2023, (under review) .

A three-phase (3ϕ) DAB dc-dc converter built with a medium frequency transformer with ΔY-connected windings has low efficiency and low transformer utilization in partial loads. This makes the 3ϕ-ΔY-DAB less attractive for applications where the performance at partial loads is crucial. This paper presents control strategies utilizing extra degrees of freedom provided by multilevel converters to minimize the RMS current and improve the partial load operation of the 3ϕ-ΔY-DAB converter. The duration of the zero-level voltage of the Y-side is adjusted with the help of multilevel converters, and the Δ-side dc-link voltage is controlled externally. It is shown that the RMS current can be reduced by 27 % at no-load by increasing the duration of the zero-level voltage of the Y-side. In addition, the turn-ON and turn-OFF currents of the switches of the Y-side can be decreased drastically for power levels below 42 % of the nominal power. By combining Δ-side dc-link reduction with the Y-side duty cycle variation, considerable performance improvements can be accomplished. The RMS current at no-load can be reduced by 100 % to zero. This is also validated by measurements where more than 90 % reduction in the RMS current is observed at no-load. Moreover, a dramatic reduction in the turn-ON and turn-OFF currents of the switches of both bridges is achieved.

Measurements highlighted a factor of nine reduction in no-load turn-OFF currents of the primary bridge. Moreover, a loss split calculation shows that the semiconductor losses can be decreased by 94 % and 81 % at 5 % and 10 % of nominal power, respectively.

11.3 Paper III

Babak Khanzadeh, Torbjörn Thiringer, Mohammad Kharezy
Multilevel Dual Active Bridge Leakage Inductance Selection for Various DC-link Voltage Spans
Published in *Energies*, vol. 16, no. 2, 2023, issn: 1996-1073 .

The leakage inductance of the transformer in a DAB dc-dc converter directly impacts the ac current waveforms and the power factor; thus, it can be considered a design requirement for the transformer. In the existing literature, a choice is made to either ensure soft switching in nominal power or to minimize the RMS current of the transformer. The inductance is typically obtained using optimization procedures. Implementing these optimizations is time-consuming, which can be avoided if a closed-form equation is derived for the optimum leakage inductance. In this paper, analytical expressions are derived to estimate the desired leakage inductance such that the highest RMS value of the current in the operation domain of a DAB is kept to its minimum value. The accuracy and sensitivity of the analytical solutions are evaluated. It is shown that in a large design domain, the solution for the YY-connected MFT has less than 3 % error compared to the results obtained from an optimization engine. As an example of the importance of selecting the leakage inductance correctly, it is shown that for 11 % deviations in the dc-links voltages, a 10 % deviation from the desired leakage inductance value can cause 2 % higher RMS currents in the converter.

11.4 Paper IV

Babak Khanzadeh, Yuhei Okazaki, Torbjörn Thiringer
Capacitor and Switch Size Comparisons on High-Power Medium-Voltage dc–dc Converters With Three-Phase Medium-Frequency Transformer
Published in *IEEE Journal of Emerging and Selected Topics in Power*

Electronics, vol. 9, no. 3, pp. 3331-3338, June 2021 .

This paper compares the capacitor requirement of selected isolated dc-dc converters for high-power and medium-voltage applications. A numerical comparison is made for a range of switching frequencies and transition times, considering not only the submodule capacitors of the converters but also the dc-link capacitors. Likewise, a comparison regarding the semiconductor requirement is performed for the converters. Selected inverter topologies to form the DAB dc-dc converter include the 2LC, the MMC, the TAC, the MTAC, and the CTB. The results show that the conventional DAB requires the minimum capacitor size among the converters. Moreover, in the appropriate operation region, the MTAC-DAB and the CTB-DAB provide the possibility of up to 40 % and 60 % reduction in the amount of required energy storage compared to the MMC-DAB, respectively. It is also shown that the size of the dc-link capacitors becomes comparable with the chain-links' capacitors when the percentage of the transition times per period is reduced to be below 5 %. The comparison regarding the semiconductor requirement revealed that the MMC-DAB requires the smallest installed switch power among the multilevel converters.

11.5 Paper V

Babak Khanzadeh, Torbjörn Thiringer, Yuriy Serdyuk
Analysis and Improvement of Harmonic Content in Multi-level Three-phase DAB Converters with Different Transformer Windings Connections
in Proceedings of International Power Electronics Conference (IPEC-Himeji 2022- ECCE Asia), 2022, pp. 2653-2658 .

The transformer of a DAB converter is usually designed to operate with fundamental frequency ranging from a few kHz to hundreds of kHz, depending on the application of the converter. Since the waveforms of the ac-link are non-sinusoidal, the transformer is subjected to harmonics of the fundamental frequency. The higher the harmonic content, the higher the losses in the transformer. This paper studies the harmonic content of the phase voltages and currents for a three-phase multilevel DAB converter. The effect of the windings connection of the transformer—ΔY, and YY—on the harmonic con-

tent is studied in detail. It is shown that the share of harmonics in the phase currents is independent of the power level for the YY type. However, for the ΔY type, the lower the load level, the higher the share of harmonics in the waveform. This results in high no-load currents in the transformer. A control strategy is proposed to reduce the harmonic content of the phase currents of the ΔY type in partial loads. It is shown that the proposed control method effectively reduces the low-order harmonics. As an example, the amplitudes of the 5^{th} and the 7^{th} harmonics reduce by 78 % and 70 %, respectively, at a 5 % load level.

11.6 Paper VI

Babak Khanzadeh, Yuriy Serdyuk, Torbjörn Thiringer
Evaluation of Core Losses in Transformers for Three-phase Multi-level DAB Converters
in Proceedings of 24th European Conference on Power Electronics and Applications (EPE'22 ECCE Europe), 2022, pp. 1-11. .

This paper provides closed-form expressions for estimating the core losses of three-phase transformers excited with multilevel converters for DAB applications. The expressions are derived by applying the improved generalized Steinmetz equation with approximated flux waveforms generated from one of the windings. The effect of different winding configurations on the estimated losses is studied. The results are validated with MATLAB simulations, and their applicability for three-phase multilevel DAB converters is investigated. It is shown that for the YY and the $\Delta\Delta$ configurations, an estimation error of less than 7.5 % and 11.5 %, respectively, can be achieved for most phase shifts between 0° and 20°. It is highest when the distribution of the leakage inductance is more uniform between the primary and the secondary sides. Moreover, the effect of the transition times of the bridges on the estimation error is also studied. It is established that estimating the losses from the winding, whose transition time is the largest, results in a lower estimation error. It is demonstrated that using the parameters of the Δ side results in less estimation error for the YΔ and the ΔY configurations and most of the studied designs. The maximum estimation error for these two winding configurations is below 8.5 % for phase shifts below 20°.

11.7 Paper VII

Babak Khanzadeh, Torbjörn Thiringer, Yuhei Okazaki
Capacitor Size Comparison on High-Power dc-dc Converters with Different Transformer Winding Configurations on the ac-link
in Proceedings of 22nd European Conference on Power Electronics and Applications (EPE'20 ECCE Europe), 2020, pp. P.1-P.7 .

This paper compares the capacitor requirement of the MMC-based DAB and the CTB-based DAB dc-dc converters. Three winding configurations, namely YY, $\Delta\Delta$, and YΔ, are considered for the ac-link's MFT. It is shown that for a specific inverter topology (i.e., MMC or CTB), the YY and $\Delta\Delta$ connections of the MFT result in identical energy storage requirements for the converters. Moreover, it is demonstrated that the YΔ connection considerably reduces the capacitor requirements of the converters. In the best case, the capacitor requirement can be reduced for the MMC-DAB and the CTB-DAB by 30 % and 40 %, respectively. A comparison between the converters showed that the YY-connected MMC-DAB (the YΔ-connected CTB-DAB) has the highest (the lowest) energy storage requirement. Additionally, it is shown that the YΔ-connected CTB-DAB can achieve up to 78 % (58 %) less energy storage compared to the YY-connected MMC-DAB in the best case (worst case).

11.8 Paper VIII

Babak Khanzadeh, Chengjun Tang, Torbjörn Thiringer
A Study on the Lifetime of Q2L-MMC-DAB's Switches for Wind Turbine Applications
in Proceedings of fifteenth International Conference on Ecological Vehicles and Renewable Energies (EVER), 2020, pp. 1-6 .

This paper studies the lifetime of semiconductor switches of a DAB dc-dc converter for wind turbine applications. Q2L operating MMC are used as the building blocks of the DAB converter. One of the established lifetime models is used for the lifetime estimation of the switches. Measurement data of an on-shore wind turbine for three hundred days is used as the mission profile. It is shown that the short-term thermal cycles (cycles with frequency in the

range of switching frequency) are detrimental to the lifetime estimation of the auxiliary switches of the MMCs' submodules. Thus, neglecting the short-term thermal cycles will overestimate the lifetime of the auxiliary switches by several orders of magnitude. On the other hand, these cycles will not affect the lifetime of the bypass switches considerably. It is also shown that the thermal stress on the secondary-side auxiliary switches is more severe than the primary-side ones. It is suggested that two parallel devices should be used for the secondary-side auxiliary switches; consequently, a reasonable lifetime is achieved for the secondary-side auxiliary switches.

11.9 Paper IX

Babak Khanzadeh, Torbjörn Thiringer, Mohammad Kharezy
Optimum Leakage Inductance Determination for a Q2L-Operating MMC-DAB with Different Transformer Winding Configurations
in Proceedings of 20th International Symposium on Power Electronics (Ee), 2019, pp. 1-6 .

This paper discusses the procedure for the determination of the optimum leakage inductance of a MFT for a Q2L operating three-phase modular multilevel converter dual-active bridge (MMC-DAB) considering the effects of the MFT winding configuration. Three different winding configurations——namely, YY, $\Delta\Delta$, and YΔ——are considered for the connection of the MFT windings. The optimum leakage inductance requirement of the MFT, the current THD, and the transformer utilization factor (TUF) are compared for the three winding configurations. It is found that the YY and the $\Delta\Delta$ configurations have similar optimum leakage inductance patterns, which are different from the YΔ configuration. Furthermore, it is established that an optimized leakage inductance value for a conventional DAB, can be utilized for the Q2L-operating MMC-DAB for a wide range of transition time with the YY and the $\Delta\Delta$ winding configurations if less than a 5 % error could be tolerated in its value. A comparison with respect to the TUF and the currents THD revealed that the YY and the $\Delta\Delta$ configurations result in a higher TUF compared to the YΔ configuration; However, the YΔ configuration has approximately two times lower currents THD compared to the other two configurations.

APPENDIX A

Mathematics Terms and Definitions

Kronecker delta function

Kronecker delta function, δ_j, is defined as [116]

$$\delta_j \triangleq \begin{cases} 1 & \text{if } j = 0 \\ 0 & \text{otherwise.} \end{cases} \tag{A.1}$$

Function $h_1(\omega t)$

The piecewise linear periodic function $h_1(\omega t)$ with a period of 2π is defined as

$$h_1(\omega t) \triangleq \sum_{H=1}^{\infty} \frac{\cos(H\omega t)}{H^2} = \frac{\pi}{18} \begin{cases} \pi + 3\omega t & -\pi \leq \omega t \leq -\frac{2\pi}{3} \\ 3\pi + 6\omega t & -\frac{2\pi}{3} \leq \omega t \leq -\frac{\pi}{3} \\ 2\pi + 3\omega t & -\frac{\pi}{3} \leq \omega t \leq 0 \\ 2\pi - 3\omega t & 0 \leq \omega t \leq \frac{\pi}{3} \\ 3\pi - 6\omega t & \frac{\pi}{3} \leq \omega t \leq \frac{2\pi}{3} \\ \pi - 3\omega t & \frac{2\pi}{3} \leq \omega t \leq \pi \end{cases} \tag{A.2}$$

where $H \in \{2h-1 | h \in \mathbb{N}, 3 \nmid 2h-1\}$.

Function $h_1(\omega t - \varsigma) + h_1(\omega t + \varsigma)$

$h_1(\omega t \pm \varsigma)$ can be calculated as

$$h_1(\omega t \pm \varsigma) = \frac{\pi}{18} \begin{cases} \pi + 3\omega t \pm 3\varsigma & -\pi \mp \varsigma \leq \omega t \leq \mp\varsigma - \frac{2\pi}{3} \quad \text{(A.3a)} \\ 3\pi + 6\omega t \pm 6\varsigma & -\frac{2\pi}{3} \mp \varsigma \leq \omega t \leq \mp\varsigma - \frac{\pi}{3} \quad \text{(A.3b)} \\ 2\pi + 3\omega t \pm 3\varsigma & -\frac{\pi}{3} \mp \varsigma \leq \omega t \leq \mp\varsigma \quad \text{(A.3c)} \\ 2\pi - 3\omega t \mp 3\varsigma & \mp\varsigma \leq \omega t \leq \mp\varsigma + \frac{\pi}{3} \quad \text{(A.3d)} \\ 3\pi - 6\omega t \mp 6\varsigma & \frac{\pi}{3} \mp \varsigma \leq \omega t \leq \mp\varsigma + \frac{2\pi}{3} \quad \text{(A.3e)} \\ \pi - 3\omega t \mp 3\varsigma & \frac{2\pi}{3} \mp \varsigma \leq \omega t \leq \mp\varsigma + \pi \quad \text{(A.3f)} \end{cases}$$

where $H \in \{2h-1 | h \in \mathbb{N}, 3 \nmid 2h-1\}$. Let's say we want to calculate $h_1(\omega t - \varsigma) + h_1(\omega t + \varsigma)$ for $0 \leq \omega t \leq \pi/6$. This can be done for different values of ς by breaking ς into intervals of $\pi/6$. If $-5\pi/6 \leq \varsigma \leq -2\pi/3$, then one can write

$$\begin{cases} \begin{cases} h_1(\omega t + \varsigma) \\ \text{from } (A.3a) \end{cases} \Longrightarrow \begin{cases} \text{if } \varsigma = -\frac{5\pi}{6} \Rightarrow -\frac{\pi}{6} \leq \omega t \leq \frac{\pi}{6} & \checkmark \\ \text{if } \varsigma = -\frac{2\pi}{3} \Rightarrow -\frac{\pi}{3} \leq \omega t \leq 0 & \times \end{cases} \\ \begin{cases} h_1(\omega t + \varsigma) \\ \text{from } (A.3b) \end{cases} \Longrightarrow \begin{cases} \text{if } \varsigma = -\frac{5\pi}{6} \Rightarrow \frac{\pi}{6} \leq \omega t \leq \frac{\pi}{2} & \times \\ \text{if } \varsigma = -\frac{2\pi}{3} \Rightarrow 0 \leq \omega t \leq \frac{\pi}{3} & \checkmark \end{cases} \\ \begin{cases} h_1(\omega t - \varsigma) \\ \text{from } (A.3f) \end{cases} \Longrightarrow \begin{cases} \text{if } \varsigma = -\frac{5\pi}{6} \Rightarrow -\frac{\pi}{6} \leq \omega t \leq \frac{\pi}{6} & \checkmark \\ \text{if } \varsigma = -\frac{2\pi}{3} \Rightarrow 0 \leq \omega t \leq \frac{\pi}{3} & \checkmark \end{cases} \end{cases} \quad \text{(A.4)}$$

Therefore, if $0 \leq \omega t \leq \pi/6$ and $-5\pi/6 \leq \varsigma \leq -2\pi/3$ then from (A.4)

$$h_1(\omega t + \varsigma) \overset{(A.3b)}{\underset{(A.3a)}{=\!=}} \frac{\pi}{18} \begin{cases} \pi + 3\omega t + 3\varsigma & 0 \leq \omega t \leq -\varsigma - \frac{2\pi}{3} \\ 3\pi + 6\omega t + 6\varsigma & -\varsigma - \frac{2\pi}{3} \leq \omega t \leq \frac{\pi}{6} \end{cases} \quad \text{(A.5a)}$$

$$h_1(\omega t - \varsigma) \overset{(A.3f)}{=\!=} \frac{\pi}{18}(\pi - 3\omega t + 3\varsigma) \qquad 0 \leq \omega t \leq \frac{\pi}{6} \quad \text{(A.5b)}$$

Therefore, if $0 \leq \omega t \leq \pi/6$ and $-5\pi/6 \leq \varsigma \leq -2\pi/3$ then

$$h_1(\omega t - \varsigma) + h_1(\omega t + \varsigma) = \frac{\pi}{18} \begin{cases} 2\pi + 6\varsigma & 0 \leq \omega t \leq -\varsigma - \frac{2\pi}{3} \\ 4\pi + 3\omega t + 9\varsigma & -\varsigma - \frac{2\pi}{3} \leq \omega t \leq \frac{\pi}{6} \end{cases} \quad \text{(A.6)}$$

Finally, $h_1(\omega t-\varsigma)+h_1(\omega t+\varsigma)$ for $0\leq\omega t\leq\pi/6$ can be calculated following similar steps as (A.4)-(A.6) as

$$h_1(\omega t-\varsigma)+h_1(\omega t+\varsigma)=$$

$$\frac{\pi}{18}\begin{cases}\begin{cases}2\pi+6\varsigma & 0\leq\omega t\leq-\frac{2\pi}{3}-\varsigma\\ 4\pi+9\varsigma+3\omega t & -\frac{2\pi}{3}-\varsigma\leq\omega t\leq\frac{\pi}{6}\end{cases} & \text{when } -\frac{5\pi}{6}\leq\varsigma\leq-\frac{2\pi}{3} \quad \text{(A.7a)}\\ \begin{cases}6\pi+12\varsigma & 0\leq\omega t\leq\frac{2\pi}{3}+\varsigma\\ 4\pi+9\varsigma+3\omega t & \frac{2\pi}{3}+\varsigma\leq\omega t\leq\frac{\pi}{6}\end{cases} & \text{when } -\frac{2\pi}{3}\leq\varsigma\leq-\frac{\pi}{2} \quad \text{(A.7b)}\\ \begin{cases}6\pi+12\varsigma & 0\leq\omega t\leq-\frac{\pi}{3}-\varsigma\\ 5\pi+9\varsigma-3\omega t & -\frac{\pi}{3}-\varsigma\leq\omega t\leq\frac{\pi}{6}\end{cases} & \text{when } -\frac{\pi}{2}\leq\varsigma\leq-\frac{\pi}{3} \quad \text{(A.7c)}\\ \begin{cases}4\pi+6\varsigma & 0\leq\omega t\leq\frac{\pi}{3}+\varsigma\\ 5\pi+9\varsigma-3\omega t & \frac{\pi}{3}+\varsigma\leq\omega t\leq\frac{\pi}{6}\end{cases} & \text{when } -\frac{\pi}{3}\leq\varsigma\leq-\frac{\pi}{6} \quad \text{(A.7d)}\\ \begin{cases}4\pi+6\varsigma & 0\leq\omega t\leq-\varsigma\\ 4\pi-6\omega t & -\varsigma\leq\omega t\leq\frac{\pi}{6}\end{cases} & \text{when } -\frac{\pi}{6}\leq\varsigma\leq0 \quad \text{(A.7e)}\\ \begin{cases}4\pi-6\varsigma & 0\leq\omega t\leq\varsigma\\ 4\pi-6\omega t & \varsigma\leq\omega t\leq\frac{\pi}{6}\end{cases} & \text{when } 0\leq\varsigma\leq\frac{\pi}{6} \quad \text{(A.7f)}\\ \begin{cases}4\pi-6\varsigma & 0\leq\omega t\leq\frac{\pi}{3}-\varsigma\\ 5\pi-9\varsigma-3\omega t & \frac{\pi}{3}-\varsigma\leq\omega t\leq\frac{\pi}{6}\end{cases} & \text{when } \frac{\pi}{6}\leq\varsigma\leq\frac{\pi}{3} \quad \text{(A.7g)}\\ \begin{cases}6\pi-12\varsigma & 0\leq\omega t\leq-\frac{\pi}{3}+\varsigma\\ 5\pi-9\varsigma-3\omega t & -\frac{\pi}{3}+\varsigma\leq\omega t\leq\frac{\pi}{6}\end{cases} & \text{when } \frac{\pi}{3}\leq\varsigma\leq\frac{\pi}{2} \quad \text{(A.7h)}\\ \begin{cases}6\pi-12\varsigma & 0\leq\omega t\leq\frac{2\pi}{3}-\varsigma\\ 4\pi-9\varsigma+3\omega t & \frac{2\pi}{3}-\varsigma\leq\omega t\leq\frac{\pi}{6}\end{cases} & \text{when } \frac{\pi}{2}\leq\varsigma\leq\frac{2\pi}{3} \quad \text{(A.7i)}\\ \begin{cases}2\pi-6\varsigma & 0\leq\omega t\leq-\frac{2\pi}{3}+\varsigma\\ 4\pi-9\varsigma+3\omega t & -\frac{2\pi}{3}+\varsigma\leq\omega t\leq\frac{\pi}{6}\end{cases} & \text{when } \frac{2\pi}{3}\leq\varsigma\leq\frac{5\pi}{6} \quad \text{(A.7j)}\end{cases}$$

Function $h_2(\omega t)$

The piecewise linear periodic function $h_2(\omega t)$ with a period of 2π is defined as

$$h_2(\omega t) \triangleq \sum_{H=1}^{\infty} \frac{\sin(H\omega t)}{H} = \frac{\pi}{6} \begin{cases} -1 & -\pi \le \omega t \le -\frac{2\pi}{3} \\ -2 & -\frac{2\pi}{3} \le \omega t \le -\frac{\pi}{3} \\ -1 & -\frac{\pi}{3} \le \omega t \le 0 \\ 1 & 0 \le \omega t \le \frac{\pi}{3} \\ 2 & \frac{\pi}{3} \le \omega t \le \frac{2\pi}{3} \\ 1 & \frac{2\pi}{3} \le \omega t \le \pi \end{cases} \tag{A.8}$$

where $H \in \{2h-1 | h \in \mathbb{N}, 3 \nmid 2h-1\}$.

Function $f(M_1, M_2, \psi_1, \psi_2, \theta, \lambda)$

The piecewise function $f(M_1, M_2, \psi_1, \psi_2, \theta, \lambda)$ is defined as

$$f\big(M_1, M_2, \psi_1, \psi_2, \theta, \lambda\big) \triangleq \frac{M_2}{M_1} \times \begin{cases} f_1\big(M_1, M_2, \left\lfloor \frac{1}{2} + \frac{\lambda}{\psi_1} \right\rfloor, \lfloor \frac{1}{2} + \frac{\theta}{\psi_2} \rfloor, \psi_1, \psi_2, \theta, \lambda\big) & 0 \le \lambda \le \frac{\pi}{6} \\ f_2\big(M_1, M_2, -\left\lfloor \frac{1}{2} + \frac{\pi/3-\lambda}{\psi_1} \right\rfloor, \lfloor \frac{1}{2} + \frac{\theta}{\psi_2} \rfloor, \psi_1, \psi_2, \theta, \lambda\big) & \frac{\pi}{6} \le \lambda \le \frac{\pi}{3} \\ f_2\big(M_1, M_2, \left\lfloor \frac{1}{2} + \frac{-\pi/3+\lambda}{\psi_1} \right\rfloor, \lfloor \frac{1}{2} + \frac{\theta}{\psi_2} \rfloor, \psi_1, \psi_2, \theta, \lambda\big) & \frac{\pi}{3} \le \lambda \le \frac{\pi}{2} \\ f_3\big(M_1, M_2, \left\lfloor \frac{1}{2} + \frac{2\pi/3-\lambda}{\psi_1} \right\rfloor, \lfloor \frac{1}{2} + \frac{\theta}{\psi_2} \rfloor, \psi_1, \psi_2, \theta, \lambda\big) & \frac{\pi}{2} \le \lambda \le \frac{2\pi}{3} \end{cases} \tag{A.9}$$

where functions $f_k(M_1, M_2, \aleph_1, \aleph_2, \psi_1, \psi_2, \theta, \lambda)$, $k \in \{1,2,3\}$ are defined as

$$f_1(M_1, M_2, \aleph_1, \aleph_2, \psi_1, \psi_2, \theta, \lambda) = \frac{4\pi M_1 - 6\lambda\aleph_1 - 3\psi_1\left(M_1^2 - \aleph_1^2\right)}{4\pi M_2 - 6\theta\aleph_2 - 3\psi_2\left(M_2^2 - \aleph_2^2\right)} \tag{A.10a}$$

$$f_2(M_1, M_2, \aleph_1, \aleph_2, \psi_1, \psi_2, \theta, \lambda) = \frac{\pi(5M_1 + \aleph_1) - \lambda(9M_1 + 3\aleph_1) - 1.5\psi_1\left(M_1^2 - \aleph_1^2\right)}{4\pi M_2 - 6\theta\aleph_2 - 3\psi_2\left(M_2^2 - \aleph_2^2\right)} \tag{A.10b}$$

$$f_3(M_1, M_2, \aleph_1, \aleph_2, \psi_1, \psi_2, \theta, \lambda) = \frac{\pi(4M_1 + 2\aleph_1) - \lambda(9M_1 + 3\aleph_1) + 1.5\psi_1\left(M_1^2 - \aleph_1^2\right)}{4\pi M_2 - 6\theta\aleph_2 - 3\psi_2\left(M_2^2 - \aleph_2^2\right)} \tag{A.10c}$$

where $\lfloor ... \rfloor$ is the floor function. Moreover, $0 \leq |\aleph_1| \leq M_1$, $0 \leq \aleph_2 \leq M_2$ and $\aleph_1$ and $\aleph_2$ are integer numbers.

Function $g\left(M_1, M_2, \psi_1, \psi_2, \theta, \lambda\right)$

The piecewise function $g\left(M_1, M_2, \psi_1, \psi_2, \theta, \lambda\right)$ is defined as

$$g\big(M_1, M_2, \psi_1, \psi_2, \theta, \lambda\big) \triangleq \frac{M_2}{M_1} \times \begin{cases} g_1\big(M_1, M_2, \left\lfloor \frac{1}{2} + \frac{\pi/6-\lambda}{\psi_1} \right\rfloor, \lfloor \frac{1}{2} + \frac{\theta}{\psi_2} \rfloor, \psi_1, \psi_2, \theta, \lambda\big) & 0 \leq \lambda \leq \frac{\pi}{6} \\ g_1\big(M_1, M_2, -\left\lfloor \frac{1}{2} + \frac{-\pi/6+\lambda}{\psi_1} \right\rfloor, \lfloor \frac{1}{2} + \frac{\theta}{\psi_2} \rfloor, \psi_1, \psi_2, \theta, \lambda\big) & \frac{\pi}{6} \leq \lambda \leq \frac{\pi}{3} \\ g_2\big(M_1, M_2, \lfloor \frac{1}{2} + \frac{\theta}{\psi_2} \rfloor, \psi_2, \theta, \lambda\big) & \frac{\pi}{3} \leq \lambda \leq \frac{2\pi}{3} \end{cases} \tag{A.11}$$

where functions g_1 and g_2 are defined as

$$g_1(M_1, M_2, N_1, N_2, \psi_1, \psi_2, \theta, \lambda) = \frac{\pi\left(7.5M_1 - 1.5N_1\right) - 9\lambda\left(M_1 - N_1\right) - 4.5\psi_1\left(M_1^2 - N_1^2\right)}{4\pi M_2 - 6\theta N_2 - 3\psi_2\left(M_2^2 - N_2^2\right)} \tag{A.12a}$$

$$g_2(M_1, M_2, N_2, \psi_2, \theta, \lambda) = \frac{\left(9\pi - 18\lambda\right) M_1}{4\pi M_2 - 6\theta N_2 - 3\psi_2\left(M_2^2 - N_2^2\right)} \tag{A.12b}$$

where $\lfloor ... \rfloor$ is the floor function. Moreover, $0 \leq |\aleph_1| \leq M_1$, $0 \leq \aleph_2 \leq M_2$ and $\aleph_1$ and $\aleph_2$ are integer numbers.

RMSPE

The RMSPE can quantify the mismatch between two sets of values or functions. The RMSPE of two functions X and T is defined as

$$\mathrm{RMSPE}(X, T) = \sqrt{\frac{\sum_{i=1}^{m} \left(\frac{X_i - T_i}{X_i}\right)^2}{m}} \times 100\% \tag{A.13}$$

where functions X and T have m number of samples; X_i and T_i are the i^{th} sample of respective functions; and X is used as the base function. The

RMSPE can be extended for two sets of two functions as

$$\text{RMSPE}(X,T,Y,S) = \sqrt{\frac{\sum_{i=1}^{m}\left(\frac{X_i-T_i}{X_i}\right)^2 + \sum_{j=1}^{n}\left(\frac{Y_j-S_j}{Y_j}\right)^2}{m+n}} \times 100\% \tag{A.14}$$

where functions X and T have m number of samples with function X as the base and are compared together. Similarly, functions Y and S have n number of samples with the function Y as the base and are compared together.

APPENDIX B

Soft-Switching Boundaries Derivations

It is shown in Section 7.2 that the ac-link currents can be used instead of the converter's arm currents to derive ZVS boundaries independent of the converter topology. Also, it is shown that the ZVS conditions are given as

$$i_{\mathrm{L}}\left(\omega t = \pm\beta_{k_j j}\right) < 0 \qquad \forall k_j \in \{0, ..., M_j - 1\}, \qquad \forall j \in \{\mathrm{p}, \mathrm{s}\}\,. \tag{B.1}$$

where $\pm\beta_{k_j j}$, $\forall k_j \in \{0, ..., M_j - 1\}$ and $\forall j \in \{\mathrm{p}, \mathrm{s}\}$ are the switching events of the respective converter. In this chapter, the derivation of ZVS conditions is discussed. It is assumed that the converter operates under balanced conditions. Therefore, it is enough only to investigate phase A currents.

B.1 YY-connected MFT

Considering the references waveforms given in Figure 7.1a, the switching events of the YY-connected topologies happen in the interval $-0.5\omega\tau_{\mathrm{p}} \leq \omega t \leq 0.5\omega\tau_{\mathrm{p}}$ for the primary bridge and $\varphi - 0.5\omega\tau_{\mathrm{s}} \leq \omega t \leq \varphi + 0.5\omega\tau_{\mathrm{s}}$ for the secondary bridge. The phase current of the converter is equivalent to the line

current of the MFT. Therefore, (7.1) can be reformulated as

$$i_{\mathrm{L}A}^{\mathrm{YY}}\left(\omega t=\pm\theta_{k_{\mathrm{p}}\mathrm{p}}\right)<0 \qquad \forall k_{\mathrm{p}}\in\{0,...,M_{\mathrm{p}}-1\} \tag{B.2a}$$

$$i_{\mathrm{L}a}^{\mathrm{YY}}\left(\omega t=\varphi\pm\theta_{k_{\mathrm{s}}\mathrm{s}}\right)>0 \qquad \forall k_{\mathrm{s}}\in\{0,...,M_{\mathrm{s}}-1\}. \tag{B.2b}$$

$i_{\mathrm{L}A}^{\mathrm{YY}}$ given by (4.12) can be rearranged using trigonometry rules for the product of two cosine functions as

$$\begin{aligned} i_{\mathrm{L}A}^{\mathrm{YY}}\left(\omega t\right)=&\frac{2}{\pi\omega L_{\sigma}^{\mathrm{p}}}\Bigg(-U_{\mathrm{p}}\sum_{k=0}^{M_{\mathrm{p}}-1}\sum_{H=1}^{\infty}\left(\frac{\cos\left(H\left(\theta_{k\mathrm{p}}-\omega t\right)\right)+\cos\left(H\left(\theta_{k\mathrm{p}}+\omega t\right)\right)}{H^2}\right)\\ &+\frac{N_{\mathrm{p}}U_{\mathrm{s}}}{N_{\mathrm{s}}}\sum_{k=0}^{M_{\mathrm{s}}-1}\sum_{H=1}^{\infty}\left(\frac{\cos\left(H\left(\theta_{k\mathrm{s}}-\omega t+\varphi\right)\right)+\cos\left(H\left(\theta_{k\mathrm{s}}+\omega t-\varphi\right)\right)}{H^2}\right)\Bigg). \end{aligned} \tag{B.3}$$

where $H\in\{2h-1|h\in\mathbb{N},\ 3\nmid 2h-1\}$. Equation (B.3) can be rewritten as a piecewise linear function using $h_1(\omega t)$ given by (A.2) as

$$\begin{aligned} i_{\mathrm{L}A}^{\mathrm{YY}}\left(\omega t\right)=\frac{2}{\pi\omega L_{\sigma}^{\mathrm{p}}}\Bigg(&\frac{N_{\mathrm{p}}U_{\mathrm{s}}}{N_{\mathrm{s}}}\sum_{k=0}^{M_{\mathrm{s}}-1}\left(h_1\left(\theta_{k\mathrm{s}}-\omega t+\varphi\right)+h_1\left(\theta_{k\mathrm{s}}+\omega t-\varphi\right)\right)\\ &-U_{\mathrm{p}}\sum_{k=0}^{M_{\mathrm{p}}-1}\left(h_1\left(\theta_{k\mathrm{p}}-\omega t\right)+h_1\left(\theta_{k\mathrm{p}}+\omega t\right)\right)\Bigg). \end{aligned} \tag{B.4}$$

Moreover, $i_{\mathrm{L}a}^{\mathrm{YY}}(\omega t)$ can be calculated using (4.11b) and (B.4) as

$$\begin{aligned} i_{\mathrm{L}a}^{\mathrm{YY}}\left(\omega t\right)=\frac{2}{\pi\omega L_{\sigma}^{\mathrm{p}}}\Bigg(&\frac{N_{\mathrm{p}}^2U_{\mathrm{s}}}{N_{\mathrm{s}}^2}\sum_{k=0}^{M_{\mathrm{s}}-1}\left(h_1\left(\theta_{k\mathrm{s}}-\omega t+\varphi\right)+h_1\left(\theta_{k\mathrm{s}}+\omega t-\varphi\right)\right)\\ &-\frac{N_{\mathrm{p}}U_{\mathrm{p}}}{N_{\mathrm{s}}}\sum_{k=0}^{M_{\mathrm{p}}-1}\left(h_1\left(\theta_{k\mathrm{p}}-\omega t\right)+h_1\left(\theta_{k\mathrm{p}}+\omega t\right)\right)\Bigg). \end{aligned} \tag{B.5}$$

Closed-form general ZVS boundaries

The ZVS boundaries of the primary bridge of a YY-connected DAB can be calculated using (B.2a) and (B.4) as

$$i_{\mathrm{L}A}^{\mathrm{YY}}\left(\omega t=\pm\vartheta_{\mathrm{p}}\right)<0\Rightarrow \\ \frac{N_{\mathrm{s}}U_{\mathrm{p}}}{N_{\mathrm{p}}U_{\mathrm{s}}}>\frac{\sum_{k=0}^{M_{\mathrm{s}}-1}\left(h_1\left(\theta_{k\mathrm{s}}\mp\vartheta_{\mathrm{p}}+\varphi\right)+h_1\left(\theta_{k\mathrm{s}}\pm\vartheta_{\mathrm{p}}-\varphi\right)\right)}{\sum_{k=0}^{M_{\mathrm{p}}-1}\left(h_1\left(\theta_{k\mathrm{p}}-\vartheta_{\mathrm{p}}\right)+h_1\left(\theta_{k\mathrm{p}}+\vartheta_{\mathrm{p}}\right)\right)} \tag{B.6}$$

where $\vartheta_{\mathrm{p}}\in\{\theta_{k\mathrm{p}},\ \forall k\in\{0,...,M_{\mathrm{p}}-1\}\}$. Similarly, the ZVS boundaries of the secondary bridge can be calculated using (B.2b) and (B.5) as

$$i_{\mathrm{L}a}^{\mathrm{YY}}\left(\omega t=\varphi\pm\vartheta_{\mathrm{s}}\right)>0\Rightarrow \\ \frac{N_{\mathrm{s}}U_{\mathrm{p}}}{N_{\mathrm{p}}U_{\mathrm{s}}}<\frac{\sum_{k=0}^{M_{\mathrm{s}}-1}\left(h_1\left(\theta_{k\mathrm{s}}-\vartheta_{\mathrm{s}}\right)+h_1\left(\theta_{k\mathrm{s}}+\vartheta_{\mathrm{s}}\right)\right)}{\sum_{k=0}^{M_{\mathrm{p}}-1}\left(h_1\left(\theta_{k\mathrm{p}}\mp\vartheta_{\mathrm{s}}-\varphi\right)+h_1\left(\theta_{k\mathrm{p}}\pm\vartheta_{\mathrm{s}}+\varphi\right)\right)} \tag{B.7}$$

where $\vartheta_{\mathrm{s}}\in\{\theta_{k\mathrm{s}},\ \forall k\in\{0,...,M_{\mathrm{s}}-1\}\}$.

Closed-form Q2L ZVS boundaries

The Q2L definitions given by (2.1) are used here to derive ZVS conditions of a Q2L operating DAB. Moreover, it is assumed that

$$0\leq\omega\tau_j\leq\frac{\pi}{3}\xRightarrow[(2.1a)]{(2.1b)}0\leq\theta_{k_jj}\leq\frac{\pi}{6}\qquad\forall k_j\in\{0,...,M_j-1\} \tag{B.8}$$

where $j\in\{\mathrm{p},\mathrm{s}\}$. This assumption ensures no overlap between the transitions of any two phases of a given bridge. Both (B.6) and (B.7) has terms as

$$\mathcal{F}\left(M_j,\theta_j,\vartheta_j\right)\triangleq\sum_{k_j=0}^{M_j-1}\left(h_1\left(\theta_{k_jj}-\vartheta_j\right)+h_1\left(\theta_{k_jj}+\vartheta_j\right)\right). \tag{B.9}$$

If we put $h_1\left(\theta_{k_j j}-\vartheta_j\right)+h_1\left(\theta_{k_j j}+\vartheta_j\right)$ from (B.9) equivalent with $h_1(\omega t-\varsigma)+h_1(\omega t+\varsigma)$ from A.7, then $\omega t \equiv \theta_{k_j j}$ and $\varsigma \equiv \vartheta_j$. We know that

$$\left.\begin{array}{l}\text{from (B.8): } 0 \leq \theta_{k_j j} \leq \frac{\pi}{6} \overset{\omega t \equiv \theta_{k_j j}}{\Longrightarrow} 0 \leq \omega t \leq \frac{\pi}{6} \\ \text{Also: } \vartheta_j \in \left\{\theta_{k_j j},\ \forall k_j \in \{0,...,M_j-1\}\right\} \text{ where } j \in \{\mathrm{p},\mathrm{s}\}\end{array}\right\} \Rightarrow$$
$$0 \leq \vartheta_j \leq \frac{\pi}{6} \overset{\varsigma \equiv \vartheta_j}{\Longrightarrow} 0 \leq \varsigma \leq \frac{\pi}{6}. \tag{B.10}$$

Since $0 \leq \varsigma \leq \pi/6$ then (A.7f) should be used to expand (B.9) as

$$\mathcal{F}\left(M_j,\theta_j,\vartheta_j\right) \overset{(A.7f)}{=\!=} \frac{\pi}{18}\sum_{k_j=0}^{M_j-1}\begin{cases}4\pi-6\vartheta_j & 0 \leq \theta_{k_j j} \leq \vartheta_j \\ 4\pi-6\theta_{k_j j} & \vartheta_j \leq \theta_{k_j j} \leq \frac{\pi}{6}.\end{cases} \tag{B.11}$$

Expanding (B.11) without introducing new parameters is impossible due to dependency of $\theta_{k_j j}$ bounds on ϑ_j. Let's modify (B.11) as follows

$$\begin{array}{l}\mathcal{F}\left(M_j,\theta_j,\vartheta_j\right) = \\ \quad\frac{\pi}{18}\sum_{k_j=0}^{M_j-1}\begin{cases}4\pi-6\vartheta_j & 0 \leq \theta_{k_j j} \leq \vartheta_j, \quad \forall k_j \in \{0,...,\aleph_j-1\} \\ 4\pi-6\theta_{k_j j} & \vartheta_j \leq \theta_{k_j j} \leq \frac{\pi}{6}, \quad \forall k_j \in \{\aleph_j,...,M_j-1\}.\end{cases}\end{array} \tag{B.12}$$

where $\aleph_j$ is an integer between 0 and M_j, which can be calculated as

$$\begin{array}{l}\theta_{k_j j} \leq \vartheta_j \overset{(B.12)}{\Longrightarrow} \theta_{(\aleph_j-1)j} \leq \vartheta_j \overset{(2.1b)}{\Longrightarrow} \left((\aleph_j-1)+0.5\right)\psi_j \leq \vartheta_j \Rightarrow \\ \aleph_j \leq \frac{\vartheta_j}{\psi_j}+\frac{1}{2} \Longrightarrow \aleph_j = \lfloor\frac{\vartheta_j}{\psi_j}+\frac{1}{2}\rfloor,\ \min(\aleph_j)=0,\ \max(\aleph_j)=M_j.\end{array} \tag{B.13}$$

Finally, (B.12) can be expanded as

$$\mathcal{F}\left(M_j,\theta_j,\vartheta_j\right) = \frac{\pi}{18}\left(4\pi M_j - 6\vartheta_j\aleph_j - 3(M_j-\aleph_j)(M_j+\aleph_j)\psi_j\right) \tag{B.14}$$

where M_j, ψ_j are known parameters from the Q2L modulation, ϑ_j is the query point for ZVS, and $\aleph_j$ is calculated from (B.13). Expanding the rest of the terms in (B.6) and (B.7) can be done similarly. Firstly, ς should be divided into intervals of length $\pi/6$ and for every interval steps taken in (B.9)-(B.14) should be repeated. This is a cumbersome task, and therefore, only the final

results will be presented hereafter.

Let's define D as the ratio of the primary side dc-link voltage, $V_{\mathrm{dc,p}}$, to the secondary side dc-link voltage, $V_{\mathrm{dc,s}}$ as

$$D \triangleq \frac{V_{\mathrm{dc,p}}}{V_{\mathrm{dc,s}}} \equiv \frac{M_{\mathrm{p}} U_{\mathrm{p}}}{M_{\mathrm{s}} U_{\mathrm{s}}} \tag{B.15}$$

If $\lambda_{\mathrm{p}} \triangleq \vartheta_{\mathrm{p}} + \varphi$, cases $i_{LA}^{\mathrm{YY}}(\omega t = -\vartheta_{\mathrm{p}}) < 0$ from (B.6) can be summarized as

$$\begin{aligned}
&\text{if } 0 \le \lambda_{\mathrm{p}} \le \frac{\pi}{6},\ \aleph_{\mathrm{p}} = \lfloor \frac{\vartheta_{\mathrm{p}}}{\psi_{\mathrm{p}}} + \frac{1}{2} \rfloor,\ \aleph_{\mathrm{s}} = \lfloor \frac{\lambda_{\mathrm{p}}}{\psi_{\mathrm{s}}} + \frac{1}{2} \rfloor \\
&\frac{D M_{\mathrm{s}} N_{\mathrm{s}}}{M_{\mathrm{p}} N_{\mathrm{P}}} > \frac{4\pi M_{\mathrm{s}} - 6\lambda_{\mathrm{p}}\aleph_{\mathrm{s}} - 3\psi_{\mathrm{s}}\left(M_{\mathrm{s}}^2 - \aleph_{\mathrm{s}}^2\right)}{4\pi M_{\mathrm{p}} - 6\vartheta_{\mathrm{p}}\aleph_{\mathrm{p}} - 3\psi_{\mathrm{p}}\left(M_{\mathrm{p}}^2 - \aleph_{\mathrm{p}}^2\right)}.
\end{aligned} \tag{B.16a}$$

$$\begin{aligned}
&\text{if } \frac{\pi}{6} \le \lambda_{\mathrm{p}} \le \frac{\pi}{3},\ \aleph_{\mathrm{p}} = \lfloor \frac{\vartheta_{\mathrm{p}}}{\psi_{\mathrm{p}}} + \frac{1}{2} \rfloor,\ \aleph_{\mathrm{s}} = \lfloor \frac{\frac{\pi}{3} - \lambda_{\mathrm{p}}}{\psi_{\mathrm{s}}} + \frac{1}{2} \rfloor \\
&\frac{D M_{\mathrm{s}} N_{\mathrm{s}}}{M_{\mathrm{p}} N_{\mathrm{P}}} > \frac{\pi\left(5M_{\mathrm{s}} - \aleph_{\mathrm{s}}\right) - \lambda_{\mathrm{p}}\left(9M_{\mathrm{s}} - 3\aleph_{\mathrm{s}}\right) - 1.5\psi_{\mathrm{s}}\left(M_{\mathrm{s}}^2 - \aleph_{\mathrm{s}}^2\right)}{4\pi M_{\mathrm{p}} - 6\vartheta_{\mathrm{p}}\aleph_{\mathrm{p}} - 3\psi_{\mathrm{p}}\left(M_{\mathrm{p}}^2 - \aleph_{\mathrm{p}}^2\right)}.
\end{aligned} \tag{B.16b}$$

$$\begin{aligned}
&\text{if } \frac{\pi}{3} \le \lambda_{\mathrm{p}} \le \frac{\pi}{2},\ \aleph_{\mathrm{p}} = \lfloor \frac{\vartheta_{\mathrm{p}}}{\psi_{\mathrm{p}}} + \frac{1}{2} \rfloor,\ \aleph_{\mathrm{s}} = \lfloor \frac{\lambda_{\mathrm{p}} - \frac{\pi}{3}}{\psi_{\mathrm{s}}} + \frac{1}{2} \rfloor \\
&\frac{D M_{\mathrm{s}} N_{\mathrm{s}}}{M_{\mathrm{p}} N_{\mathrm{P}}} > \frac{\pi\left(5M_{\mathrm{s}} + \aleph_{\mathrm{s}}\right) - \lambda_{\mathrm{p}}\left(9M_{\mathrm{s}} + 3\aleph_{\mathrm{s}}\right) - 1.5\psi_{\mathrm{s}}\left(M_{\mathrm{s}}^2 - \aleph_{\mathrm{s}}^2\right)}{4\pi M_{\mathrm{p}} - 6\vartheta_{\mathrm{p}}\aleph_{\mathrm{p}} - 3\psi_{\mathrm{p}}\left(M_{\mathrm{p}}^2 - \aleph_{\mathrm{p}}^2\right)}.
\end{aligned} \tag{B.16c}$$

$$\begin{aligned}
&\text{if } \frac{\pi}{2} \le \lambda_{\mathrm{p}} \le \frac{2\pi}{3},\ \aleph_{\mathrm{p}} = \lfloor \frac{\vartheta_{\mathrm{p}}}{\psi_{\mathrm{p}}} + \frac{1}{2} \rfloor,\ \aleph_{\mathrm{s}} = \lfloor \frac{\frac{2\pi}{3} - \lambda_{\mathrm{p}}}{\psi_{\mathrm{s}}} + \frac{1}{2} \rfloor \\
&\frac{D M_{\mathrm{s}} N_{\mathrm{s}}}{M_{\mathrm{p}} N_{\mathrm{P}}} > \frac{\pi\left(4M_{\mathrm{s}} + 2\aleph_{\mathrm{s}}\right) - \lambda_{\mathrm{p}}\left(9M_{\mathrm{s}} + 3\aleph_{\mathrm{s}}\right) + 1.5\psi_{\mathrm{s}}\left(M_{\mathrm{s}}^2 - \aleph_{\mathrm{s}}^2\right)}{4\pi M_{\mathrm{p}} - 6\vartheta_{\mathrm{p}}\aleph_{\mathrm{p}} - 3\psi_{\mathrm{p}}\left(M_{\mathrm{p}}^2 - \aleph_{\mathrm{p}}^2\right)}.
\end{aligned} \tag{B.16d}$$

If $\lambda_{\mathrm{p}} \triangleq |\varphi - \vartheta_{\mathrm{p}}|$, cases $i_{LA}^{\mathrm{YY}}(\omega t = \vartheta_{\mathrm{p}}) < 0$ from (B.6) can be summarized as

$$\begin{aligned}
&\text{if } 0 \le \lambda_{\mathrm{p}} \le \frac{\pi}{6},\ \aleph_{\mathrm{p}} = \lfloor \frac{\vartheta_{\mathrm{p}}}{\psi_{\mathrm{p}}} + \frac{1}{2} \rfloor,\ \aleph_{\mathrm{s}} = \lfloor \frac{\lambda_{\mathrm{p}}}{\psi_{\mathrm{s}}} + \frac{1}{2} \rfloor \\
&\frac{D M_{\mathrm{s}} N_{\mathrm{s}}}{M_{\mathrm{p}} N_{\mathrm{P}}} > \frac{4\pi M_{\mathrm{s}} - 6\lambda_{\mathrm{p}}\aleph_{\mathrm{s}} - 3\psi_{\mathrm{s}}\left(M_{\mathrm{s}}^2 - \aleph_{\mathrm{s}}^2\right)}{4\pi M_{\mathrm{p}} - 6\vartheta_{\mathrm{p}}\aleph_{\mathrm{p}} - 3\psi_{\mathrm{p}}\left(M_{\mathrm{p}}^2 - \aleph_{\mathrm{p}}^2\right)}.
\end{aligned} \tag{B.17a}$$

$$\text{if } \frac{\pi}{6} \le \lambda_{\mathrm{p}} \le \frac{\pi}{3},\ \aleph_{\mathrm{p}} = \lfloor \frac{\vartheta_{\mathrm{p}}}{\psi_{\mathrm{p}}} + \frac{1}{2} \rfloor,\ \aleph_{\mathrm{s}} = \lfloor \frac{\frac{\pi}{3} - \lambda_{\mathrm{p}}}{\psi_{\mathrm{s}}} + \frac{1}{2} \rfloor$$

$$\frac{DM_sN_s}{M_pN_P} > \frac{\pi\left(5M_s - \aleph_s\right) - \lambda_p\left(9M_s - 3\aleph_s\right) - 1.5\psi_s\left(M_s^2 - \aleph_s^2\right)}{4\pi M_p - 6\vartheta_p\aleph_p - 3\psi_p\left(M_p^2 - \aleph_p^2\right)}. \tag{B.17b}$$

$$\text{if } \frac{\pi}{3} \le \lambda_p \le \frac{\pi}{2},\ \aleph_p = \lfloor\frac{\vartheta_p}{\psi_p} + \frac{1}{2}\rfloor,\ \aleph_s = \lfloor\frac{\lambda_p - \frac{\pi}{3}}{\psi_s} + \frac{1}{2}\rfloor$$

$$\frac{DM_sN_s}{M_pN_P} > \frac{\pi\left(5M_s + \aleph_s\right) - \lambda_p\left(9M_s + 3\aleph_s\right) - 1.5\psi_s\left(M_s^2 - \aleph_s^2\right)}{4\pi M_p - 6\vartheta_p\aleph_p - 3\psi_p\left(M_p^2 - \aleph_p^2\right)}. \tag{B.17c}$$

$$\text{if } \frac{\pi}{2} \le \lambda_p \le \frac{2\pi}{3},\ \aleph_p = \lfloor\frac{\vartheta_p}{\psi_p} + \frac{1}{2}\rfloor,\ \aleph_s = \lfloor\frac{\frac{2\pi}{3} - \lambda_p}{\psi_s} + \frac{1}{2}\rfloor$$

$$\frac{DM_sN_s}{M_pN_P} > \frac{\pi\left(4M_s + 2\aleph_s\right) - \lambda_p\left(9M_s + 3\aleph_s\right) + 1.5\psi_s\left(M_s^2 - \aleph_s^2\right)}{4\pi M_p - 6\vartheta_p\aleph_p - 3\psi_p\left(M_p^2 - \aleph_p^2\right)}. \tag{B.17d}$$

If $\lambda_s = |\varphi - \vartheta_s|$, cases $i_{La}^{YY}\left(\omega t = \varphi - \vartheta_s\right) > 0$ from (B.7) are summarized as

$$\text{if } 0 \le \lambda_s \le \frac{\pi}{6},\ \aleph_s = \lfloor\frac{\vartheta_s}{\psi_s} + \frac{1}{2}\rfloor,\ \aleph_p = \lfloor\frac{\lambda_s}{\psi_p} + \frac{1}{2}\rfloor$$

$$\frac{M_pN_p}{DM_sN_s} > \frac{4\pi M_p - 6\lambda_s\aleph_p - 3\psi_p\left(M_p^2 - \aleph_p^2\right)}{4\pi M_s - 6\vartheta_s\aleph_s - 3\psi_s\left(M_s^2 - \aleph_s^2\right)}. \tag{B.18a}$$

$$\text{if } \frac{\pi}{6} \le \lambda_s \le \frac{\pi}{3},\ \aleph_s = \lfloor\frac{\vartheta_s}{\psi_s} + \frac{1}{2}\rfloor,\ \aleph_p = \lfloor\frac{\frac{\pi}{3} - \lambda_s}{\psi_p} + \frac{1}{2}\rfloor$$

$$\frac{M_pN_p}{DM_sN_s} > \frac{\pi\left(5M_p - \aleph_p\right) - \lambda_s\left(9M_p - 3\aleph_p\right) - 1.5\psi_p\left(M_p^2 - \aleph_p^2\right)}{4\pi M_s - 6\vartheta_s\aleph_s - 3\psi_s\left(M_s^2 - \aleph_s^2\right)}. \tag{B.18b}$$

$$\text{if } \frac{\pi}{3} \le \lambda_s \le \frac{\pi}{2},\ \aleph_s = \lfloor\frac{\vartheta_s}{\psi_s} + \frac{1}{2}\rfloor,\ \aleph_p = \lfloor\frac{\lambda_s - \frac{\pi}{3}}{\psi_p} + \frac{1}{2}\rfloor$$

$$\frac{M_pN_p}{DM_sN_s} > \frac{\pi\left(5M_p + \aleph_p\right) - \lambda_s\left(9M_p + 3\aleph_p\right) - 1.5\psi_p\left(M_p^2 - \aleph_p^2\right)}{4\pi M_s - 6\vartheta_s\aleph_s - 3\psi_s\left(M_s^2 - \aleph_s^2\right)}. \tag{B.18c}$$

$$\text{if } \frac{\pi}{2} \le \lambda_s \le \frac{2\pi}{3},\ \aleph_s = \lfloor\frac{\vartheta_s}{\psi_s} + \frac{1}{2}\rfloor,\ \aleph_p = \lfloor\frac{\frac{2\pi}{3} - \lambda_s}{\psi_p} + \frac{1}{2}\rfloor$$

$$\frac{M_pN_p}{DM_sN_s} > \frac{\pi\left(4M_p + 2\aleph_p\right) - \lambda_s\left(9M_p + 3\aleph_p\right) + 1.5\psi_p\left(M_p^2 - \aleph_p^2\right)}{4\pi M_s - 6\vartheta_s\aleph_s - 3\psi_s\left(M_s^2 - \aleph_s^2\right)}. \tag{B.18d}$$

If $\lambda_s = \vartheta_s + \varphi$, cases $i_{La}^{YY}\left(\omega t = \varphi + \vartheta_s\right) > 0$ from (B.7) are summarized as

$$\text{if } 0 \le \lambda_s \le \frac{\pi}{6},\ \aleph_s = \lfloor\frac{\vartheta_s}{\psi_s} + \frac{1}{2}\rfloor,\ \aleph_p = \lfloor\frac{\lambda_s}{\psi_p} + \frac{1}{2}\rfloor$$

$$\frac{M_\mathrm{p}N_\mathrm{p}}{DM_\mathrm{s}N_\mathrm{s}} > \frac{4\pi M_\mathrm{p} - 6\lambda_\mathrm{s}\aleph_\mathrm{p} - 3\psi_\mathrm{p}\left(M_\mathrm{p}^2 - \aleph_\mathrm{p}^2\right)}{4\pi M_\mathrm{s} - 6\vartheta_\mathrm{s}\aleph_\mathrm{s} - 3\psi_\mathrm{s}\left(M_\mathrm{s}^2 - \aleph_\mathrm{s}^2\right)}. \tag{B.19a}$$

$$\text{if } \frac{\pi}{6} \leq \lambda_\mathrm{s} \leq \frac{\pi}{3},\ \aleph_\mathrm{s} = \lfloor \frac{\vartheta_\mathrm{s}}{\psi_\mathrm{s}} + \frac{1}{2} \rfloor,\ \aleph_\mathrm{p} = \lfloor \frac{\frac{\pi}{3} - \lambda_\mathrm{s}}{\psi_\mathrm{p}} + \frac{1}{2} \rfloor$$

$$\frac{M_\mathrm{p}N_\mathrm{p}}{DM_\mathrm{s}N_\mathrm{s}} > \frac{\pi\left(5M_\mathrm{p} - \aleph_\mathrm{p}\right) - \lambda_\mathrm{s}\left(9M_\mathrm{p} - 3\aleph_\mathrm{p}\right) - 1.5\psi_\mathrm{p}\left(M_\mathrm{p}^2 - \aleph_\mathrm{p}^2\right)}{4\pi M_\mathrm{s} - 6\vartheta_\mathrm{s}\aleph_\mathrm{s} - 3\psi_\mathrm{s}\left(M_\mathrm{s}^2 - \aleph_\mathrm{s}^2\right)}. \tag{B.19b}$$

$$\text{if } \frac{\pi}{3} \leq \lambda_\mathrm{s} \leq \frac{\pi}{2},\ \aleph_\mathrm{s} = \lfloor \frac{\vartheta_\mathrm{s}}{\psi_\mathrm{s}} + \frac{1}{2} \rfloor,\ \aleph_\mathrm{p} = \lfloor \frac{\lambda_\mathrm{s} - \frac{\pi}{3}}{\psi_\mathrm{p}} + \frac{1}{2} \rfloor$$

$$\frac{M_\mathrm{p}N_\mathrm{p}}{DM_\mathrm{s}N_\mathrm{s}} > \frac{\pi\left(5M_\mathrm{p} + \aleph_\mathrm{p}\right) - \lambda_\mathrm{s}\left(9M_\mathrm{p} + 3\aleph_\mathrm{p}\right) - 1.5\psi_\mathrm{p}\left(M_\mathrm{p}^2 - \aleph_\mathrm{p}^2\right)}{4\pi M_\mathrm{s} - 6\vartheta_\mathrm{s}\aleph_\mathrm{s} - 3\psi_\mathrm{s}\left(M_\mathrm{s}^2 - \aleph_\mathrm{s}^2\right)}. \tag{B.19c}$$

$$\text{if } \frac{\pi}{2} \leq \lambda_\mathrm{s} \leq \frac{2\pi}{3},\ \aleph_\mathrm{s} = \lfloor \frac{\vartheta_\mathrm{s}}{\psi_\mathrm{s}} + \frac{1}{2} \rfloor,\ \aleph_\mathrm{p} = \lfloor \frac{\frac{2\pi}{3} - \lambda_\mathrm{s}}{\psi_\mathrm{p}} + \frac{1}{2} \rfloor$$

$$\frac{M_\mathrm{p}N_\mathrm{p}}{DM_\mathrm{s}N_\mathrm{s}} > \frac{\pi\left(4M_\mathrm{p} + 2\aleph_\mathrm{p}\right) - \lambda_\mathrm{s}\left(9M_\mathrm{p} + 3\aleph_\mathrm{p}\right) + 1.5\psi_\mathrm{p}\left(M_\mathrm{p}^2 - \aleph_\mathrm{p}^2\right)}{4\pi M_\mathrm{s} - 6\vartheta_\mathrm{s}\aleph_\mathrm{s} - 3\psi_\mathrm{s}\left(M_\mathrm{s}^2 - \aleph_\mathrm{s}^2\right)}. \tag{B.19d}$$

Finally, the ZVS conditions given by (B.16)-(B.19) can be summarized as

$$\begin{aligned} i_{LA}^{\mathrm{YY}}\left(\omega t = \pm\theta_{k_\mathrm{p}\mathrm{p}}\right) <& 0, \qquad \forall k_\mathrm{p} \in \{0, ..., M_\mathrm{p} - 1\} \\ \Longrightarrow D_{k_\mathrm{p}\mathrm{p}}^{\pm} >& \frac{N_\mathrm{p} f\left(M_\mathrm{s}, M_\mathrm{p}, \psi_\mathrm{s}, \psi_\mathrm{p}, \left|\theta_{k_\mathrm{p}\mathrm{p}}\right|, \left|\varphi \mp \theta_{k_\mathrm{p}\mathrm{p}}\right|\right)}{N_\mathrm{s}} \end{aligned} \tag{B.20a}$$

$$\begin{aligned} i_{La}^{\mathrm{YY}}\left(\omega t = \varphi \pm \theta_{k_\mathrm{s}\mathrm{s}}\right) >& 0, \qquad \forall k_\mathrm{s} \in \{0, ..., M_\mathrm{s} - 1\} \\ \Longrightarrow \frac{1}{D_{k_\mathrm{s}\mathrm{s}}^{\pm}} >& \frac{N_\mathrm{s} f\left(M_\mathrm{p}, M_\mathrm{s}, \psi_\mathrm{p}, \psi_\mathrm{s}, \left|\theta_{k_\mathrm{s}\mathrm{s}}\right|, \left|\varphi \pm \theta_{k_\mathrm{s}\mathrm{s}}\right|\right)}{N_\mathrm{p}}. \end{aligned} \tag{B.20b}$$

where the piecewise function $f\left(M_1, M_2, \psi_1, \psi_2, \theta, \lambda\right)$ is defined in (A.9).

B.2 YΔ-connected MFT

The YΔ connection of the windings introduces a phase shift on the primary-side-referred waveforms based on the vector group of the winding connection [34]. In this document, the vector group with $+30°$ phase displacement (YΔ11) is used during the derivation process of currents. Regardless, the final results can be used for any vector group as $\varphi \in [0, \pi/2]$. Considering the references waveforms given in Figure 2.5, the switching events of the YΔ-connected topologies happen in the interval $-0.5\omega\tau_\mathrm{p} \leq \omega t \leq 0.5\omega\tau_\mathrm{p}$ for the

primary bridge and $\varphi+\pi/6-0.5\omega\tau_\mathrm{s} \leq \omega t \leq \varphi+\pi/6+0.5\omega\tau_\mathrm{s}$ for the secondary bridge. The phase current of the converter is equivalent to the line current of the MFT. Therefore, the ZVS conditions (B.1) can be reformulated as

$$i_{\mathrm{L}A}^{\mathrm{Y}\Delta}\left(\omega t = \pm\theta_{k_\mathrm{p}\mathrm{p}}\right) < 0 \qquad \forall k_\mathrm{p} \in \{0, ..., M_\mathrm{p}-1\} \tag{B.21a}$$

$$i_{\mathrm{L}a}^{\mathrm{Y}\Delta}\left(\omega t = \varphi + \pi/6 \pm \theta_{k_\mathrm{s}\mathrm{s}}\right) > 0 \qquad \forall k_\mathrm{s} \in \{0, ..., M_\mathrm{s}-1\}. \tag{B.21b}$$

$i_{\mathrm{L}A}^{\mathrm{Y}\Delta}$ given by (4.14) can be rearranged using trigonometry rules for the product of two cosine functions as

$$\begin{aligned} i_{\mathrm{L}A}^{\mathrm{Y}\Delta}(\omega t) = \frac{2}{\pi\omega L_\sigma^\mathrm{p}} \times \Bigg(& \frac{N_\mathrm{p}U_\mathrm{s}}{N_\mathrm{s}} \sum_{k=0}^{M_\mathrm{s}-1}\sum_{H=1}^{\infty}\left(\frac{\cos\left(H\left(\omega t-\varphi-\frac{\pi}{6}-\theta_{k\mathrm{s}}\right)\right)}{H^2}\right) \\ & + \frac{N_\mathrm{p}U_\mathrm{s}}{N_\mathrm{s}} \sum_{k=0}^{M_\mathrm{s}-1}\sum_{H=1}^{\infty}\left(\frac{\cos\left(H\left(\omega t-\varphi-\frac{\pi}{6}+\theta_{k\mathrm{s}}\right)\right)}{H^2}\right) \\ & + \frac{N_\mathrm{p}U_\mathrm{s}}{N_\mathrm{s}} \sum_{k=0}^{M_\mathrm{s}-1}\sum_{H=1}^{\infty}\left(\frac{\cos\left(H\left(\omega t-\varphi+\frac{\pi}{6}-\theta_{k\mathrm{s}}\right)\right)}{H^2}\right) \\ & + \frac{N_\mathrm{p}U_\mathrm{s}}{N_\mathrm{s}} \sum_{k=0}^{M_\mathrm{s}-1}\sum_{H=1}^{\infty}\left(\frac{\cos\left(H\left(\omega t-\varphi+\frac{\pi}{6}+\theta_{k\mathrm{s}}\right)\right)}{H^2}\right) \\ & - U_\mathrm{p} \sum_{k=0}^{M_\mathrm{p}-1}\sum_{H=1}^{\infty}\left(\frac{\cos\left(H\left(\omega t-\theta_{k\mathrm{p}}\right)\right)+\cos\left(H\left(\omega t+\theta_{k\mathrm{p}}\right)\right)}{H^2}\right)\Bigg) \end{aligned} \tag{B.22}$$

where $H \in \{2h-1 | h \in \mathbb{N},\ 3 \nmid 2h-1\}$. Similarly, the secondary line current can be rearranged using (4.15) derived as

$$\begin{aligned} i_{\mathrm{L}a}^{\mathrm{Y}\Delta}(\omega t) = \frac{2}{\pi\omega L_\sigma^\mathrm{s}} \times \Bigg(& \\ 2U_\mathrm{s} \sum_{k=0}^{M_\mathrm{s}-1}\sum_{H=1}^{\infty}\left(\frac{\cos\left(H\left(\omega t-\varphi-\frac{\pi}{6}-\theta_{k\mathrm{s}}\right)\right)+\cos\left(H\left(\omega t-\varphi-\frac{\pi}{6}+\theta_{k\mathrm{s}}\right)\right)}{H^2}\right) & \\ - U_\mathrm{s} \sum_{k=0}^{M_\mathrm{s}-1}\sum_{H=1}^{\infty}\left(\frac{\cos\left(H\left(\omega t-\varphi+\frac{\pi}{2}-\theta_{k\mathrm{s}}\right)\right)+\cos\left(H\left(\omega t-\varphi+\frac{\pi}{2}+\theta_{k\mathrm{s}}\right)\right)}{H^2}\right) & \end{aligned}$$

$$
\begin{aligned}
&+U_{\mathrm{s}} \sum_{k=0}^{M_{\mathrm{s}}-1} \sum_{H=1}^{\infty} \left(\frac{\cos\left(H\left(\omega t-\varphi+\frac{\pi}{6}-\theta_{k\mathrm{s}}\right)\right)+\cos\left(H\left(\omega t-\varphi+\frac{\pi}{6}+\theta_{k\mathrm{s}}\right)\right)}{H^2} \right) \\
&-\frac{N_{\mathrm{s}}U_{\mathrm{p}}}{N_{\mathrm{p}}} \sum_{k=0}^{M_{\mathrm{p}}-1} \sum_{H=1}^{\infty} \left(\frac{\cos\left(H\left(\omega t-\frac{\pi}{3}-\theta_{k\mathrm{p}}\right)\right)+\cos\left(H\left(\omega t-\frac{\pi}{3}+\theta_{k\mathrm{p}}\right)\right)}{H^2} \right) \\
&-\frac{N_{\mathrm{s}}U_{\mathrm{p}}}{N_{\mathrm{p}}} \sum_{k=0}^{M_{\mathrm{p}}-1} \sum_{H=1}^{\infty} \left(\frac{\cos\left(H\left(\omega t-\theta_{k\mathrm{p}}\right)\right)+\cos\left(H\left(\omega t+\theta_{k\mathrm{p}}\right)\right)}{H^2} \right) \Bigg) \qquad \text{(B.23)}
\end{aligned}
$$

where $H \in \{2h-1 | h \in \mathbb{N},\ 3 \nmid 2h-1\}$. (B.22) can be rewritten as a piecewise linear function using $h_1(\omega t)$ given by (A.2) as

$$
\begin{aligned}
i_{\mathrm{L}A}^{\mathrm{Y}\Delta}(\omega t) = \frac{2}{\pi\omega L_{\sigma}^{\mathrm{p}}} \Bigg(&\frac{N_{\mathrm{p}}U_{\mathrm{s}}}{N_{\mathrm{s}}} \sum_{k=0}^{M_{\mathrm{s}}-1} \left(h_1\left(\theta_{k\mathrm{s}}-\omega t+\varphi+\frac{\pi}{6}\right)+h_1\left(\theta_{k\mathrm{s}}+\omega t-\varphi-\frac{\pi}{6}\right)\right) \\
&+\frac{N_{\mathrm{p}}U_{\mathrm{s}}}{N_{\mathrm{s}}} \sum_{k=0}^{M_{\mathrm{s}}-1} \left(h_1\left(\theta_{k\mathrm{s}}-\omega t+\varphi-\frac{\pi}{6}\right)+h_1\left(\theta_{k\mathrm{s}}+\omega t-\varphi+\frac{\pi}{6}\right)\right) \\
&-U_{\mathrm{p}} \sum_{k=0}^{M_{\mathrm{p}}-1} \left(h_1\left(\theta_{k\mathrm{p}}-\omega t\right)+h_1\left(\theta_{k\mathrm{p}}+\omega t\right)\right) \Bigg). \qquad \text{(B.24)}
\end{aligned}
$$

Moreover, $i_{\mathrm{L}a}^{\mathrm{Y}\Delta}(\omega t)$ can be reformulated using (A.2) as

$$
\begin{aligned}
i_{\mathrm{L}a}^{\mathrm{Y}\Delta}(\omega t) = \frac{2}{\pi\omega L_{\sigma}^{\mathrm{s}}} \Bigg(&2U_{\mathrm{s}} \sum_{k=0}^{M_{\mathrm{s}}-1} \left(h_1\left(\theta_{k\mathrm{s}}-\omega t+\varphi+\frac{\pi}{6}\right)+h_1\left(\theta_{k\mathrm{s}}+\omega t-\varphi-\frac{\pi}{6}\right)\right) \\
&-U_{\mathrm{s}} \sum_{k=0}^{M_{\mathrm{s}}-1} \left(h_1\left(\theta_{k\mathrm{s}}-\omega t+\varphi-\frac{\pi}{2}\right)+h_1\left(\theta_{k\mathrm{s}}+\omega t-\varphi+\frac{\pi}{2}\right)\right) \\
&+U_{\mathrm{s}} \sum_{k=0}^{M_{\mathrm{s}}-1} \left(h_1\left(\theta_{k\mathrm{s}}-\omega t+\varphi-\frac{\pi}{6}\right)+h_1\left(\theta_{k\mathrm{s}}+\omega t-\varphi+\frac{\pi}{6}\right)\right) \\
&-\frac{N_{\mathrm{s}}U_{\mathrm{p}}}{N_{\mathrm{p}}} \sum_{k=0}^{M_{\mathrm{p}}-1} \left(h_1\left(\theta_{k\mathrm{p}}-\omega t+\frac{\pi}{3}\right)+h_1\left(\theta_{k\mathrm{p}}+\omega t-\frac{\pi}{3}\right)\right) \\
&-\frac{N_{\mathrm{s}}U_{\mathrm{p}}}{N_{\mathrm{p}}} \sum_{k=0}^{M_{\mathrm{p}}-1} \left(h_1\left(\theta_{k\mathrm{p}}-\omega t\right)+h_1\left(\theta_{k\mathrm{p}}+\omega t\right)\right) \Bigg). \qquad \text{(B.25)}
\end{aligned}
$$

Closed-form general ZVS boundaries

The ZVS boundaries of the primary bridge of a YΔ-DAB can be calculated using (B.21a) and (B.24) as

$$\begin{aligned} &i_{\mathrm{L}A}^{\mathrm{Y}\Delta}(\omega t = \pm\,\vartheta_\mathrm{p}) < 0 \Rightarrow \\ &\frac{N_\mathrm{s}U_\mathrm{p}}{N_\mathrm{p}U_\mathrm{s}} > \frac{\sum_{k=0}^{M_\mathrm{s}-1}\Big(h_1\big(\theta_{k\mathrm{s}} \mp \vartheta_\mathrm{p} + \varphi + \frac{\pi}{6}\big) + h_1\big(\theta_{k\mathrm{s}} \pm \vartheta_\mathrm{p} - \varphi - \frac{\pi}{6}\big) + h_1\big(\theta_{k\mathrm{s}} \mp \vartheta_\mathrm{p} + \varphi - \frac{\pi}{6}\big) + h_1\big(\theta_{k\mathrm{s}} \pm \vartheta_\mathrm{p} - \varphi + \frac{\pi}{6}\big)\Big)}{\sum_{k=0}^{M_\mathrm{p}-1}\big(h_1\left(\theta_{k\mathrm{p}} - \vartheta_\mathrm{p}\right) + h_1\left(\theta_{k\mathrm{p}} + \vartheta_\mathrm{p}\right)\big)}. \end{aligned} \tag{B.26}$$

where $\vartheta_\mathrm{p} \in \{\theta_{k\mathrm{p}},\ \forall k \in \{0, ..., M_\mathrm{p} - 1\}\}$. Similarly, the ZVS boundaries of the secondary bridge can be calculated using (B.21b) and (B.25) as

$$\begin{aligned} &i_{\mathrm{L}a}^{\mathrm{Y}\Delta}\left(\omega t = \varphi + \pi/6 \pm \vartheta_\mathrm{s}\right) > 0 \Rightarrow \\ &\frac{N_\mathrm{s}U_\mathrm{p}}{N_\mathrm{p}U_\mathrm{s}} < \frac{\sum_{k=0}^{M_\mathrm{s}-1}\Big(h_1\left(\theta_{k\mathrm{s}} - \vartheta_\mathrm{s} - \frac{\pi}{3}\right) + h_1\left(\theta_{k\mathrm{s}} + \vartheta_\mathrm{s} + \frac{\pi}{3}\right) + h_1\left(\theta_{k\mathrm{s}} - \vartheta_\mathrm{s} + \frac{\pi}{3}\right) + h_1\left(\theta_{k\mathrm{s}} + \vartheta_\mathrm{s} - \frac{\pi}{3}\right) + 2h_1\left(\theta_{k\mathrm{s}} - \vartheta_\mathrm{s}\right) + 2h_1\left(\theta_{k\mathrm{s}} + \vartheta_\mathrm{s}\right)\Big)}{\sum_{k=0}^{M_\mathrm{p}-1}\Big(h_1\big(\theta_{k\mathrm{p}} \pm \vartheta_\mathrm{s} + \varphi + \frac{\pi}{6}\big) + h_1\big(\theta_{k\mathrm{p}} \mp \vartheta_\mathrm{s} - \varphi - \frac{\pi}{6}\big) + h_1\big(\theta_{k\mathrm{p}} \pm \vartheta_\mathrm{s} + \varphi - \frac{\pi}{6}\big) + h_1\big(\theta_{k\mathrm{p}} \mp \vartheta_\mathrm{s} - \varphi + \frac{\pi}{6}\big)\Big)}. \end{aligned} \tag{B.27}$$

where $\vartheta_\mathrm{s} \in \{\theta_{k\mathrm{s}},\ \forall k \in \{0, ..., M_\mathrm{s} - 1\}\}$.

Closed-form Q2L ZVS boundaries

Similar to the YY connection following assumptions and definitions are used

$$0 \le \omega\tau_j \le \frac{\pi}{3} \overset{\text{(2.1b)}}{\underset{\text{(2.1a)}}{\Longrightarrow}} 0 \le \theta_{k_j j} \le \frac{\pi}{6} \quad \forall k_j \in \{0, ..., M_j - 1\} \tag{B.28a}$$

$$D \triangleq \frac{V_{\mathrm{dc,p}}}{V_{\mathrm{dc,s}}} \equiv \frac{M_{\mathrm{p}} U_{\mathrm{p}}}{M_{\mathrm{s}} U_{\mathrm{s}}}. \tag{B.28b}$$

By following a similar procedure as described for the YY-DAB, the ZVS conditions given by (B.26)-(B.27) can also be expanded. If $\lambda_{\mathrm{p}} \triangleq \vartheta_{\mathrm{p}} + \varphi$, cases $i_{LA}^{\mathrm{Y}\Delta}(\omega t = -\vartheta_{\mathrm{p}}) < 0$ from (B.26) can be summarized as

$$\begin{aligned}
&\text{if } 0 \le \lambda_{\mathrm{p}} \le \frac{\pi}{6},\ \aleph_{\mathrm{p}} = \lfloor \frac{\vartheta_{\mathrm{p}}}{\psi_{\mathrm{p}}} + \frac{1}{2} \rfloor,\ \aleph_{\mathrm{s}} = \lfloor \frac{\frac{\pi}{6} - \lambda_{\mathrm{p}}}{\psi_{\mathrm{s}}} + \frac{1}{2} \rfloor \\
&\frac{D M_{\mathrm{s}} N_{\mathrm{s}}}{M_{\mathrm{p}} N_{\mathrm{P}}} > \frac{\pi\left(7.5 M_{\mathrm{s}} - 1.5 \aleph_{\mathrm{s}}\right) - 9\lambda_{\mathrm{p}}\left(M_{\mathrm{s}} - \aleph_{\mathrm{s}}\right) - 4.5\psi_{\mathrm{s}}\left(M_{\mathrm{s}}^2 - \aleph_{\mathrm{s}}^2\right)}{4\pi M_{\mathrm{p}} - 6\vartheta_{\mathrm{p}}\aleph_{\mathrm{p}} - 3\psi_{\mathrm{p}}\left(M_{\mathrm{p}}^2 - \aleph_{\mathrm{p}}^2\right)}.
\end{aligned} \tag{B.29a}$$

$$\begin{aligned}
&\text{if } \frac{\pi}{6} \le \lambda_{\mathrm{p}} \le \frac{\pi}{3},\ \aleph_{\mathrm{p}} = \lfloor \frac{\vartheta_{\mathrm{p}}}{\psi_{\mathrm{p}}} + \frac{1}{2} \rfloor,\ \aleph_{\mathrm{s}} = \lfloor \frac{\lambda_{\mathrm{p}} - \frac{\pi}{6}}{\psi_{\mathrm{s}}} + \frac{1}{2} \rfloor \\
&\frac{D M_{\mathrm{s}} N_{\mathrm{s}}}{M_{\mathrm{p}} N_{\mathrm{P}}} > \frac{\pi\left(7.5 M_{\mathrm{s}} + 1.5 \aleph_{\mathrm{s}}\right) - 9\lambda_{\mathrm{p}}\left(M_{\mathrm{s}} + \aleph_{\mathrm{s}}\right) - 4.5\psi_{\mathrm{s}}\left(M_{\mathrm{s}}^2 - \aleph_{\mathrm{s}}^2\right)}{4\pi M_{\mathrm{p}} - 6\vartheta_{\mathrm{p}}\aleph_{\mathrm{p}} - 3\psi_{\mathrm{p}}\left(M_{\mathrm{p}}^2 - \aleph_{\mathrm{p}}^2\right)}.
\end{aligned} \tag{B.29b}$$

$$\begin{aligned}
&\text{if } \frac{\pi}{3} \le \lambda_{\mathrm{p}} \le \frac{\pi}{2},\ \aleph_{\mathrm{p}} = \lfloor \frac{\vartheta_{\mathrm{p}}}{\psi_{\mathrm{p}}} + \frac{1}{2} \rfloor,\ \aleph_{\mathrm{s}} = \lfloor \frac{\frac{\pi}{2} - \lambda_{\mathrm{p}}}{\psi_{\mathrm{s}}} + \frac{1}{2} \rfloor \\
&\frac{D M_{\mathrm{s}} N_{\mathrm{s}}}{M_{\mathrm{p}} N_{\mathrm{P}}} > \frac{\left(9\pi - 18\lambda_{\mathrm{p}}\right) M_{\mathrm{s}}}{4\pi M_{\mathrm{p}} - 6\vartheta_{\mathrm{p}}\aleph_{\mathrm{p}} - 3\psi_{\mathrm{p}}\left(M_{\mathrm{p}}^2 - \aleph_{\mathrm{p}}^2\right)}.
\end{aligned} \tag{B.29c}$$

$$\begin{aligned}
&\text{if } \frac{\pi}{2} \le \lambda_{\mathrm{p}} \le \frac{2\pi}{3},\ \aleph_{\mathrm{p}} = \lfloor \frac{\vartheta_{\mathrm{p}}}{\psi_{\mathrm{p}}} + \frac{1}{2} \rfloor,\ \aleph_{\mathrm{s}} = \lfloor \frac{\lambda_{\mathrm{p}} - \frac{\pi}{2}}{\psi_{\mathrm{s}}} + \frac{1}{2} \rfloor \\
&\frac{D M_{\mathrm{s}} N_{\mathrm{s}}}{M_{\mathrm{p}} N_{\mathrm{P}}} > \frac{\left(9\pi - 18\lambda_{\mathrm{p}}\right) M_{\mathrm{s}}}{4\pi M_{\mathrm{p}} - 6\vartheta_{\mathrm{p}}\aleph_{\mathrm{p}} - 3\psi_{\mathrm{p}}\left(M_{\mathrm{p}}^2 - \aleph_{\mathrm{p}}^2\right)}.
\end{aligned} \tag{B.29d}$$

If $\lambda_{\mathrm{p}} \triangleq |\varphi - \vartheta_{\mathrm{p}}|$, cases $i_{LA}^{\mathrm{Y}\Delta}(\omega t = \vartheta_{\mathrm{p}}) < 0$ from (B.26) can be summarized as

$$\begin{aligned}
&\text{if } 0 \le \lambda_{\mathrm{p}} \le \frac{\pi}{6},\ \aleph_{\mathrm{p}} = \lfloor \frac{\vartheta_{\mathrm{p}}}{\psi_{\mathrm{p}}} + \frac{1}{2} \rfloor,\ \aleph_{\mathrm{s}} = \lfloor \frac{\frac{\pi}{6} - \lambda_{\mathrm{p}}}{\psi_{\mathrm{s}}} + \frac{1}{2} \rfloor \\
&\frac{D M_{\mathrm{s}} N_{\mathrm{s}}}{M_{\mathrm{p}} N_{\mathrm{P}}} > \frac{\pi\left(7.5 M_{\mathrm{s}} - 1.5 \aleph_{\mathrm{s}}\right) - 9\lambda_{\mathrm{p}}\left(M_{\mathrm{s}} - \aleph_{\mathrm{s}}\right) - 4.5\psi_{\mathrm{s}}\left(M_{\mathrm{s}}^2 - \aleph_{\mathrm{s}}^2\right)}{4\pi M_{\mathrm{p}} - 6\vartheta_{\mathrm{p}}\aleph_{\mathrm{p}} - 3\psi_{\mathrm{p}}\left(M_{\mathrm{p}}^2 - \aleph_{\mathrm{p}}^2\right)}.
\end{aligned} \tag{B.30a}$$

$$\begin{aligned}
&\text{if } \frac{\pi}{6} \le \lambda_{\mathrm{p}} \le \frac{\pi}{3},\ \aleph_{\mathrm{p}} = \lfloor \frac{\vartheta_{\mathrm{p}}}{\psi_{\mathrm{p}}} + \frac{1}{2} \rfloor,\ \aleph_{\mathrm{s}} = \lfloor \frac{\lambda_{\mathrm{p}} - \frac{\pi}{6}}{\psi_{\mathrm{s}}} + \frac{1}{2} \rfloor \\
&\frac{D M_{\mathrm{s}} N_{\mathrm{s}}}{M_{\mathrm{p}} N_{\mathrm{P}}} > \frac{\pi\left(7.5 M_{\mathrm{s}} + 1.5 \aleph_{\mathrm{s}}\right) - 9\lambda_{\mathrm{p}}\left(M_{\mathrm{s}} + \aleph_{\mathrm{s}}\right) - 4.5\psi_{\mathrm{s}}\left(M_{\mathrm{s}}^2 - \aleph_{\mathrm{s}}^2\right)}{4\pi M_{\mathrm{p}} - 6\vartheta_{\mathrm{p}}\aleph_{\mathrm{p}} - 3\psi_{\mathrm{p}}\left(M_{\mathrm{p}}^2 - \aleph_{\mathrm{p}}^2\right)}.
\end{aligned} \tag{B.30b}$$

$$\text{if } \frac{\pi}{3} \le \lambda_{\mathrm{p}} \le \frac{\pi}{2},\ \aleph_{\mathrm{p}} = \lfloor \frac{\vartheta_{\mathrm{p}}}{\psi_{\mathrm{p}}} + \frac{1}{2} \rfloor,\ \aleph_{\mathrm{s}} = \lfloor \frac{\frac{\pi}{2} - \lambda_{\mathrm{p}}}{\psi_{\mathrm{s}}} + \frac{1}{2} \rfloor$$
$$\frac{DM_{\mathrm{s}}N_{\mathrm{s}}}{M_{\mathrm{p}}N_{\mathrm{P}}} > \frac{(9\pi - 18\lambda_{\mathrm{p}})\, M_{\mathrm{s}}}{4\pi M_{\mathrm{p}} - 6\vartheta_{\mathrm{p}}\aleph_{\mathrm{p}} - 3\psi_{\mathrm{p}}\left(M_{\mathrm{p}}^2 - \aleph_{\mathrm{p}}^2\right)}. \tag{B.30c}$$
$$\text{if } \frac{\pi}{2} \le \lambda_{\mathrm{p}} \le \frac{2\pi}{3},\ \aleph_{\mathrm{p}} = \lfloor \frac{\vartheta_{\mathrm{p}}}{\psi_{\mathrm{p}}} + \frac{1}{2} \rfloor,\ \aleph_{\mathrm{s}} = \lfloor \frac{\lambda_{\mathrm{p}} - \frac{\pi}{2}}{\psi_{\mathrm{s}}} + \frac{1}{2} \rfloor$$
$$\frac{DM_{\mathrm{s}}N_{\mathrm{s}}}{M_{\mathrm{p}}N_{\mathrm{P}}} > \frac{(9\pi - 18\lambda_{\mathrm{p}})\, M_{\mathrm{s}}}{4\pi M_{\mathrm{p}} - 6\vartheta_{\mathrm{p}}\aleph_{\mathrm{p}} - 3\psi_{\mathrm{p}}\left(M_{\mathrm{p}}^2 - \aleph_{\mathrm{p}}^2\right)}. \tag{B.30d}$$

If $\lambda_{\mathrm{s}} = |\varphi - \vartheta_{\mathrm{s}}|$, cases $i_{La}^{\mathrm{Y}\Delta}\left(\omega t = \varphi + \pi/6 - \vartheta_{\mathrm{s}}\right) > 0$ from (B.27) expand to

$$\text{if } 0 \le \lambda_{\mathrm{s}} \le \frac{\pi}{6},\ \aleph_{\mathrm{s}} = \lfloor \frac{\vartheta_{\mathrm{s}}}{\psi_{\mathrm{s}}} + \frac{1}{2} \rfloor,\ \aleph_{\mathrm{p}} = \lfloor \frac{\frac{\pi}{6} - \lambda_{\mathrm{s}}}{\psi_{\mathrm{p}}} + \frac{1}{2} \rfloor$$
$$\frac{M_{\mathrm{p}}N_{\mathrm{p}}}{DM_{\mathrm{s}}N_{\mathrm{s}}} > \frac{\pi\left(7.5M_{\mathrm{p}} - 1.5\aleph_{\mathrm{p}}\right) - 9\lambda_{\mathrm{s}}\left(M_{\mathrm{p}} - \aleph_{\mathrm{p}}\right) - 4.5\psi_{\mathrm{p}}\left(M_{\mathrm{p}}^2 - \aleph_{\mathrm{p}}^2\right)}{12\pi M_{\mathrm{s}} - 18\vartheta_{\mathrm{s}}\aleph_{\mathrm{s}} - 9\psi_{\mathrm{s}}\left(M_{\mathrm{s}}^2 - \aleph_{\mathrm{s}}^2\right)}. \tag{B.31a}$$
$$\text{if } \frac{\pi}{6} \le \lambda_{\mathrm{s}} \le \frac{\pi}{3},\ \aleph_{\mathrm{s}} = \lfloor \frac{\vartheta_{\mathrm{s}}}{\psi_{\mathrm{s}}} + \frac{1}{2} \rfloor,\ \aleph_{\mathrm{p}} = \lfloor \frac{\lambda_{\mathrm{s}} - \frac{\pi}{6}}{\psi_{\mathrm{p}}} + \frac{1}{2} \rfloor$$
$$\frac{M_{\mathrm{p}}N_{\mathrm{p}}}{DM_{\mathrm{s}}N_{\mathrm{s}}} > \frac{\pi\left(7.5M_{\mathrm{p}} + 1.5\aleph_{\mathrm{p}}\right) - 9\lambda_{\mathrm{s}}\left(M_{\mathrm{p}} + \aleph_{\mathrm{p}}\right) - 4.5\psi_{\mathrm{p}}\left(M_{\mathrm{p}}^2 - \aleph_{\mathrm{p}}^2\right)}{12\pi M_{\mathrm{s}} - 18\vartheta_{\mathrm{s}}\aleph_{\mathrm{s}} - 9\psi_{\mathrm{s}}\left(M_{\mathrm{s}}^2 - \aleph_{\mathrm{s}}^2\right)}. \tag{B.31b}$$
$$\text{if } \frac{\pi}{3} \le \lambda_{\mathrm{s}} \le \frac{\pi}{2},\ \aleph_{\mathrm{s}} = \lfloor \frac{\vartheta_{\mathrm{s}}}{\psi_{\mathrm{s}}} + \frac{1}{2} \rfloor,\ \aleph_{\mathrm{p}} = \lfloor \frac{\frac{\pi}{2} - \lambda_{\mathrm{s}}}{\psi_{\mathrm{p}}} + \frac{1}{2} \rfloor$$
$$\frac{M_{\mathrm{p}}N_{\mathrm{p}}}{DM_{\mathrm{s}}N_{\mathrm{s}}} > \frac{(9\pi - 18\lambda_{\mathrm{s}})\, M_{\mathrm{p}}}{12\pi M_{\mathrm{s}} - 18\vartheta_{\mathrm{s}}\aleph_{\mathrm{s}} - 9\psi_{\mathrm{s}}\left(M_{\mathrm{s}}^2 - \aleph_{\mathrm{s}}^2\right)}. \tag{B.31c}$$
$$\text{if } \frac{\pi}{2} \le \lambda_{\mathrm{s}} \le \frac{2\pi}{3},\ \aleph_{\mathrm{s}} = \lfloor \frac{\vartheta_{\mathrm{s}}}{\psi_{\mathrm{s}}} + \frac{1}{2} \rfloor,\ \aleph_{\mathrm{p}} = \lfloor \frac{\lambda_{\mathrm{s}} - \frac{\pi}{2}}{\psi_{\mathrm{p}}} + \frac{1}{2} \rfloor$$
$$\frac{M_{\mathrm{p}}N_{\mathrm{p}}}{DM_{\mathrm{s}}N_{\mathrm{s}}} > \frac{(9\pi - 18\lambda_{\mathrm{s}})\, M_{\mathrm{p}}}{12\pi M_{\mathrm{s}} - 18\vartheta_{\mathrm{s}}\aleph_{\mathrm{s}} - 9\psi_{\mathrm{s}}\left(M_{\mathrm{s}}^2 - \aleph_{\mathrm{s}}^2\right)}. \tag{B.31d}$$

If $\lambda_{\mathrm{s}} = \vartheta_{\mathrm{s}} + \varphi$, cases $i_{La}^{\mathrm{Y}\Delta}\left(\omega t = \varphi + \pi/6 + \vartheta_{\mathrm{s}}\right) > 0$ from (B.27) expand to

$$\text{if } 0 \le \lambda_{\mathrm{s}} \le \frac{\pi}{6},\ \aleph_{\mathrm{s}} = \lfloor \frac{\vartheta_{\mathrm{s}}}{\psi_{\mathrm{s}}} + \frac{1}{2} \rfloor,\ \aleph_{\mathrm{p}} = \lfloor \frac{\frac{\pi}{6} - \lambda_{\mathrm{s}}}{\psi_{\mathrm{p}}} + \frac{1}{2} \rfloor$$
$$\frac{M_{\mathrm{p}}N_{\mathrm{p}}}{DM_{\mathrm{s}}N_{\mathrm{s}}} > \frac{\pi\left(7.5M_{\mathrm{p}} - 1.5\aleph_{\mathrm{p}}\right) - 9\lambda_{\mathrm{s}}\left(M_{\mathrm{p}} - \aleph_{\mathrm{p}}\right) - 4.5\psi_{\mathrm{p}}\left(M_{\mathrm{p}}^2 - \aleph_{\mathrm{p}}^2\right)}{12\pi M_{\mathrm{s}} - 18\vartheta_{\mathrm{s}}\aleph_{\mathrm{s}} - 9\psi_{\mathrm{s}}\left(M_{\mathrm{s}}^2 - \aleph_{\mathrm{s}}^2\right)}. \tag{B.32a}$$

$$\text{if } \frac{\pi}{6} \le \lambda_{\rm s} \le \frac{\pi}{3},\ \aleph_{\rm s} = \lfloor \frac{\vartheta_{\rm s}}{\psi_{\rm s}} + \frac{1}{2} \rfloor,\ \aleph_{\rm p} = \lfloor \frac{\lambda_{\rm s} - \frac{\pi}{6}}{\psi_{\rm p}} + \frac{1}{2} \rfloor$$

$$\frac{M_{\rm p} N_{\rm p}}{D M_{\rm s} N_{\rm s}} > \frac{\pi\left(7.5 M_{\rm p} + 1.5\aleph_{\rm p}\right) - 9\lambda_{\rm s}\left(M_{\rm p} + \aleph_{\rm p}\right) - 4.5\psi_{\rm p}\left(M_{\rm p}^2 - \aleph_{\rm p}^2\right)}{12\pi M_{\rm s} - 18\vartheta_{\rm s}\aleph_{\rm s} - 9\psi_{\rm s}\left(M_{\rm s}^2 - \aleph_{\rm s}^2\right)}. \tag{B.32b}$$

$$\text{if } \frac{\pi}{3} \le \lambda_{\rm s} \le \frac{\pi}{2},\ \aleph_{\rm s} = \lfloor \frac{\vartheta_{\rm s}}{\psi_{\rm s}} + \frac{1}{2} \rfloor,\ \aleph_{\rm p} = \lfloor \frac{\frac{\pi}{2} - \lambda_{\rm s}}{\psi_{\rm p}} + \frac{1}{2} \rfloor$$

$$\frac{M_{\rm p} N_{\rm p}}{D M_{\rm s} N_{\rm s}} > \frac{\left(9\pi - 18\lambda_{\rm s}\right) M_{\rm p}}{12\pi M_{\rm s} - 18\vartheta_{\rm s}\aleph_{\rm s} - 9\psi_{\rm s}\left(M_{\rm s}^2 - \aleph_{\rm s}^2\right)}. \tag{B.32c}$$

$$\text{if } \frac{\pi}{2} \le \lambda_{\rm s} \le \frac{2\pi}{3},\ \aleph_{\rm s} = \lfloor \frac{\vartheta_{\rm s}}{\psi_{\rm s}} + \frac{1}{2} \rfloor,\ \aleph_{\rm p} = \lfloor \frac{\lambda_{\rm s} - \frac{\pi}{2}}{\psi_{\rm p}} + \frac{1}{2} \rfloor$$

$$\frac{M_{\rm p} N_{\rm p}}{D M_{\rm s} N_{\rm s}} > \frac{\left(9\pi - 18\lambda_{\rm s}\right) M_{\rm p}}{12\pi M_{\rm s} - 18\vartheta_{\rm s}\aleph_{\rm s} - 9\psi_{\rm s}\left(M_{\rm s}^2 - \aleph_{\rm s}^2\right)}. \tag{B.32d}$$

The soft-switching conditions given by (B.29)-(B.32) can be summarized as

$$\begin{aligned} & i_{LA}^{\rm Y\Delta}(\omega t = \pm\,\theta_{k_{\rm p}{\rm p}}) < 0, \qquad \forall k_{\rm p} \in \{0, ..., M_{\rm p} - 1\} \\ & \qquad \Longrightarrow D_{k_{\rm p}{\rm p}}^{\pm} > \frac{N_{\rm p} g\left(M_{\rm s}, M_{\rm p}, \psi_{\rm s}, \psi_{\rm p}, \left|\theta_{k_{\rm p}{\rm p}}\right|, \left|\varphi \mp \theta_{k_{\rm p}{\rm p}}\right|\right)}{N_{\rm s}} \end{aligned} \tag{B.33a}$$

$$\begin{aligned} & i_{La}^{\rm Y\Delta}(\omega t = \varphi + \pi/6 \pm \theta_{k_{\rm s}{\rm s}}) > 0, \qquad \forall k_{\rm s} \in \{0, ..., M_{\rm s} - 1\} \\ & \qquad \Longrightarrow \frac{1}{D_{k_{\rm s}{\rm s}}^{\pm}} > \frac{N_{\rm s} g\left(M_{\rm p}, M_{\rm s}, \psi_{\rm p}, \psi_{\rm s}, \left|\theta_{k_{\rm s}{\rm s}}\right|, \left|\varphi \pm \theta_{k_{\rm s}{\rm s}}\right|\right)}{3N_{\rm p}} \end{aligned} \tag{B.33b}$$

where the piecewise function $g\left(M_1, M_2, \psi_1, \psi_2, \theta, \lambda\right)$ is defined in (A.11).

References

[1] *The wind power, wind energy market intelligence*, https://www.thewindpower.net, Accessed: 2023-01-20.

[2] *The wind power, wind energy market intelligence*, https://www.thewindpower.net, Accessed: 2019-08-30.

[3] K. Musasa, N. I. Nwulu, M. N. Gitau, and R. C. Bansal, "Review on dc collection grids for offshore wind farms with high-voltage dc transmission system," *IET Power Electronics*, vol. 10, no. 15, pp. 2104–2115, 2017.

[4] S. M. Alagab, S. Tennakoon, and C. Gould, "Review of wind farm power collection schemes," in *2015 50th International Universities Power Engineering Conference (UPEC)*, 2015, pp. 1–5.

[5] J. Robinson, D. Jovcic, and G. Joos, "Analysis and design of an offshore wind farm using a MV DC grid," *IEEE Transactions on Power Delivery*, vol. 25, no. 4, pp. 2164–2173, 2010.

[6] J. D. Páez, D. Frey, J. Maneiro, S. Bacha, and P. Dworakowski, "Overview of dc–dc converters dedicated to HVDC grids," *IEEE Transactions on Power Delivery*, vol. 34, no. 1, pp. 119–128, 2019.

[7] R. De Doncker, D. Divan, and M. Kheraluwala, "A three-phase soft-switched high-power-density dc/dc converter for high-power applications," *IEEE Transactions on Industry Applications*, vol. 27, no. 1, pp. 63–73, 1991.

[8] A. Bahmani, *Design and optimization considerations of medium-frequency power transformers in high-power DC-DC applications*. Chalmers Tekniska Hogskola (Sweden), 2016.

[9] J. W. Kolar and G. Ortiz, "Solid-state-transformers: Key components of future traction and smart grid systems," in *Proceedings of the International Power Electronics Conference-ECCE Asia (IPEC 2014)*, IEEE, 2014, pp. 18–21.

[10] T. Jimichi, M. Kaymak, and R. W. De Doncker, "Comparison of single-phase and three-phase dual-active bridge dc-dc converters with various semiconductor devices for offshore wind turbines," in *2017 IEEE 3rd International Future Energy Electronics Conference and ECCE Asia (IFEEC 2017 - ECCE Asia)*, 2017, pp. 591–596.

[11] H. van Hoek, M. Neubert, A. Kroeber, and R. W. De Doncker, "Comparison of a single-phase and a three-phase dual active bridge with low-voltage, high-current output," in *2012 International Conference on Renewable Energy Research and Applications (ICRERA)*, 2012, pp. 1–6.

[12] M. Stieneker, B. J. Mortimer, N. R. Averous, H. Stagge, and R. W. De Doncker, "Optimum design of medium-voltage dc collector grids depending on the offshore-wind-park power," in *2014 IEEE Symposium on Power Electronics and Machines for Wind and Water Applications*, 2014, pp. 1–8.

[13] H. J. Bahirat, B. A. Mork, and H. K. Høidalen, "Comparison of wind farm topologies for offshore applications," in *2012 IEEE Power and Energy Society General Meeting*, 2012, pp. 1–8.

[14] F. Deng and Z. Chen, "An offshore wind farm with dc grid connection and its performance under power system transients," in *2011 IEEE Power and Energy Society General Meeting*, 2011, pp. 1–8.

[15] T. Jimichi, M. Kaymak, and R. W. De Doncker, "Design and loss analysis of a medium-voltage dc-dc converter intended for offshore wind farms," in *2016 IEEE International Conference on Renewable Energy Research and Applications (ICRERA)*, 2016, pp. 137–142.

[16] T. Lagier, P. Ladoux, and P. Dworakowski, "Potential of silicon carbide mosfets in the dc/dc converters for future hvdc offshore wind farms," *High Voltage*, vol. 2, no. 4, pp. 233–243, 2017.

[17] M. A. Bahmani, T. Thiringer, A. Rabiei, and T. Abdulahovic, "Comparative study of a multi-MW high-power density dc transformer with an optimized high-frequency magnetics in all-dc offshore wind farm," *IEEE Transactions on Power Delivery*, vol. 31, no. 2, pp. 857–866, 2016.

[18] G. P. Adam, I. A. Gowaid, S. J. Finney, D. Holliday, and B. W. Williams, "Review of dc–dc converters for multi-terminal HVDC transmission networks," *IET Power Electronics*, vol. 9, no. 2, pp. 281–296, 2016.

[19] F. Yazdani and M. Zolghadri, "Design of dual active bridge isolated bi-directional dc converter based on current stress optimization," in *2017 8th Power Electronics, Drive Systems & Technologies Conference (PEDSTC)*, 2017, pp. 247–252.

[20] M. D'Antonio, S. Chakraborty, and A. Khaligh, "Design optimization for weighted conduction loss minimization in a dual-active-bridge-based pv microinverter," in *2020 IEEE Energy Conversion Congress and Exposition (ECCE)*, 2020, pp. 6008–6015.

[21] R. U. Lenke, *A contribution to the design of isolated dc-dc converters for utility applications*. E. ON Energy Research Center, RWTH Aachen, Univ., 2012.

[22] I. A. Gowaid, G. P. Adam, A. M. Massoud, S. Ahmed, D. Holliday, and B. W. Williams, "Quasi two-level operation of modular multilevel converter for use in a high-power dc transformer with dc fault isolation capability," *IEEE Transactions on Power Electronics*, vol. 30, no. 1, pp. 108–123, 2015.

[23] I. A. Gowaid, G. P. Adam, A. M. Massoud, S. Ahmed, and B. W. Williams, "Hybrid and modular multilevel converter designs for isolated HVDC–DC converters," *IEEE Journal of Emerging and Selected Topics in Power Electronics*, vol. 6, no. 1, pp. 188–202, 2018.

[24] I. A. Gowaid, G. P. Adam, S. Ahmed, D. Holliday, and B. W. Williams, "Analysis and design of a modular multilevel converter with trapezoidal modulation for medium and high voltage dc-dc transformers," *IEEE Transactions on Power Electronics*, vol. 30, no. 10, pp. 5439–5457, 2015.

[25] N. H. Baars, J. Everts, C. G. E. Wijnands, and E. A. Lomonova, "Performance evaluation of a three-phase dual active bridge dc-dc converter with different transformer winding configurations," *IEEE Transactions on Power Electronics*, vol. 31, no. 10, pp. 6814–6823, 2016.

[26] N. H. Baars, J. Everts, C. G. E. Wijnands, and E. A. Lomonova, "Evaluation of a high-power three-phase dual active bridge dc-dc converter with three-level phase-legs," in *2016 18th European Conference on Power Electronics and Applications (EPE'16 ECCE Europe)*, 2016, pp. 1–10.

[27] H. A. B. Siddique, A. Monti, and R. W. de Doncker, "The three-phase dual-active bridge converter family: Modeling, analysis, optimization and comparison of two-level and three-level converter variants," Institut für Stromrichtertechnik und Elektrische Antriebe, Tech. Rep., 2020.

[28] B. Khanzadeh, Y. Okazaki, and T. Thiringer, "Capacitor and switch size comparisons on high-power medium-voltage dc–dc converters with three-phase medium-frequency transformer," *IEEE Journal of Emerging and Selected Topics in Power Electronics*, vol. 9, no. 3, pp. 3331–3338, 2021.

[29] B. Khanzadeh, T. Thiringer, and Y. Okazaki, "Capacitor size comparison on high-power dc-dc converters with different transformer winding configurations on the ac-link," in *2020 22nd European Conference on Power Electronics and Applications (EPE'20 ECCE Europe)*, 2020, P.1–P.7.

[30] M. A. Bahmani, E. Agheb, T. Thiringer, H. K. Høidalen, and Y. Serdyuk, "Core loss behavior in high frequency high power transformers—I: Effect of core topology," *Journal of Renewable and Sustainable Energy*, vol. 4, no. 3, p. 033 112, 2012.

[31] E. Agheb, M. A. Bahmani, H. K. Høidalen, and T. Thiringer, "Core loss behavior in high frequency high power transformers—II: Arbitrary excitation," *Journal of Renewable and Sustainable Energy*, vol. 4, no. 3, p. 033 113, 2012.

[32] N. S. Mohd Sharifuddin, N. M. L. Tan, and H. Akagi, "Evaluation of a three-phase bidirectional isolated dc-dc converter with varying transformer configurations using phase-shift modulation and burst-mode switching," *Energies*, vol. 13, no. 11, 2020, ISSN: 1996-1073.

[33] N. H. Baars, J. Everts, C. G. E. Wijnands, and E. A. Lomonova, "Modulation strategy for wide-range ZVS operation of a three-level three-phase dual active bridge dc-dc converter," in *2017 IEEE Applied Power Electronics Conference and Exposition (APEC)*, 2017, pp. 3357–3364.

[34] S. V. Kulkarni and S. A. Khaparde, *Transformer engineering: design, technology, and diagnostics*. CRC press, 2017.

[35] H. van Hoek, M. Neubert, and R. W. De Doncker, "Enhanced modulation strategy for a three-phase dual active bridge—boosting efficiency of an electric vehicle converter," *IEEE Transactions on Power Electronics*, vol. 28, no. 12, pp. 5499–5507, 2013.

[36] A. Filba-Martinez, S. Busquets-Monge, and J. Bordonau, "Modulation and capacitor voltage balancing control of multilevel NPC dual active bridge dc–dc converters," *IEEE Transactions on Industrial Electronics*, vol. 67, no. 4, pp. 2499–2510, 2020.

[37] A. Filba-Martinez, S. Busquets-Monge, J. Nicolas-Apruzzese, and J. Bordonau, "Operating principle and performance optimization of a three-level NPC dual-active-bridge dc–dc converter," *IEEE Transactions on Industrial Electronics*, vol. 63, no. 2, pp. 678–690, 2016.

[38] I. A. Gowaid, G. P. Adam, B. W. Williams, A. M. Massoud, and S. Ahmed, "The transition arm multilevel converter — a concept for medium and high voltage dc-dc transformers," in *2015 IEEE International Conference on Industrial Technology (ICIT)*, 2015, pp. 3099–3104.

[39] C. Oates, K. Dyke, and D. Trainer, "The use of trapezoid waveforms within converters for HVDC," in *2014 16th European Conference on Power Electronics and Applications*, 2014, pp. 1–10.

[40] C. Oates and K. Dyke, "The controlled transition bridge," in *2015 17th European Conference on Power Electronics and Applications (EPE'15 ECCE-Europe)*, 2015, pp. 1–10.

[41] U. Scheuermann, R. Schmidt, and P. Newman, "Power cycling testing with different load pulse durations," in *7th IET International Conference on Power Electronics, Machines and Drives (PEMD 2014)*, 2014, pp. 1–6.

[42] *SM15K series, 15 kW bi-directional dc power supplies*, https://delta-elektronika.nl/products/sm15k-series, Accessed: 2023-01-20.

[43] *Half bridge module PEB8038, silicon carbide power module*, https://imperix.com/products/power/half-bridge-module/, Accessed: 2023-01-20.

[44] *Full bridge module PEH2015, igbt-based power module*, https://imperix.com/products/power/full-bridge-module/, Accessed: 2023-01-20.

[45] *Sic power module PEB8024, silicon carbide phase-leg power module*, https://imperix.com/products/power/sic-power-module/, Accessed: 2023-01-20.

[46] *VITROPERM 500 F: Iron-based nanocrystalline material with soft-magnetic properties*, https://vacuumschmelze.com/Nanocrystalline-Material.

[47] *Rapid prototyping controller B-BOX RCP*, https://imperix.com/products/control/rapid-prototyping-controller/, Accessed: 2023-01-20.

[48] *AP015 current probe*, https://teledynelecroy.com/probes/current-probes/resources/product-manuals, Accessed: 2023-01-20.

[49] *AP031 700 V, 25 MHz high-voltage differential probe (÷10, ÷100)*, https://teledynelecroy.com/probes/high-voltage-differential-probes/ap031, Accessed: 2023-01-20.

[50] *100 MHz 700 V differential oscilloscope probe 10:1/100:1*, https://www.picotech.com/accessories/active-differential-high-voltage/100-mhz-700-v-differential-probe, Accessed: 2023-01-20.

[51] *Instruction manual TT-SI 9101 100 MHz active differential probe*, https://www.testec.de/en/assets/pdf/TT-SI/, Accessed: 2023-01-20.

[52] H. Akagi, E. H. Watanabe, and M. Aredes, *Instantaneous power theory and applications to power conditioning*. John Wiley & Sons, 2017.

[53] R. M. Burkart and J. W. Kolar, "Comparative η– ρ– σ pareto optimization of Si and SiC multilevel dual-active-bridge topologies with wide input voltage range," *IEEE Transactions on Power Electronics*, vol. 32, no. 7, pp. 5258–5270, 2017.

[54] M. A. Bahmani and T. Thiringer, "Accurate evaluation of leakage inductance in high-frequency transformers using an improved frequency-dependent expression," *IEEE Transactions on Power Electronics*, vol. 30, no. 10, pp. 5738–5745, 2015.

[55] M. A. Bahmani, T. Thiringer, and M. Kharezy, "Design methodology and optimization of a medium-frequency transformer for high-power dc–dc applications," *IEEE Transactions on Industry Applications*, vol. 52, no. 5, pp. 4225–4233, 2016.

[56] M. A. Bahmani, T. Thiringer, and M. Kharezy, "Design methodology and optimization of a medium frequency transformer for high power dc-dc applications," in *2015 IEEE Applied Power Electronics Conference and Exposition (APEC)*, 2015, pp. 2532–2539.

[57] M. Eslamian, M. Kharezy, and T. Thiringer, "Calculation of the leakage inductance of medium frequency transformers with rectangular-shaped windings using an accurate analytical method," in *2019 21st European Conference on Power Electronics and Applications (EPE '19 ECCE Europe)*, 2019, P.1–P.10.

[58] C. Bin, "Design optimisation of an inductor-integrated mf transformer for a high-power isolated dual-active-bridge dc–dc converter," *IET Power Electronics*, vol. 12, no. 11, pp. 2912–2922, 2019.

[59] B. Chen, X. Liang, and N. Wan, "Design methodology for inductor-integrated litz-wired high-power medium-frequency transformer with the nanocrystalline core material for isolated dc-link stage of solid-state transformer," *IEEE Transactions on Power Electronics*, vol. 35, no. 11, pp. 11 557–11 573, 2020.

[60] A. Garcia-Bediaga, I. Villar, A. Rujas, L. Mir, and A. Rufer, "Multi-objective optimization of medium-frequency transformers for isolated soft-switching converters using a genetic algorithm," *IEEE Transactions on Power Electronics*, vol. 32, no. 4, pp. 2995–3006, 2017.

[61] X. Zhang, F. Xiao, R. Wang, W. Kang, and B. Yang, "Modeling and design of high-power enhanced leakage-inductance-integrated medium-frequency transformers for DAB converters," *Energies*, vol. 15, no. 4, p. 1361, 2022.

[62] K. Siebke, M. Giacomazzo, and R. Mallwitz, "Design of a dual active bridge converter for on-board vehicle chargers using gan and into transformer integrated series inductance," in *2020 22nd European Conference on Power Electronics and Applications (EPE'20 ECCE Europe)*, 2020, pp. 1–8.

[63] H. V. Nguyen, D.-D. To, and D.-C. Lee, "Onboard battery chargers for plug-in electric vehicles with dual functional circuit for low-voltage battery charging and active power decoupling," *iEEE Access*, vol. 6, pp. 70 212–70 222, 2018.

[64] K. D. Hoang and J. Wang, "Design optimization of high frequency transformer for dual active bridge dc-dc converter," in *2012 XXth International Conference on Electrical Machines*, 2012, pp. 2311–2317.

[65] B. Khanzadeh, T. Thiringer, and M. Kharezy, "Optimum leakage inductance determination for a Q2L-operating MMC-DAB with different transformer winding configurations," in *2019 20th International Symposium on Power Electronics (Ee)*, 2019, pp. 1–6.

[66] B. Khanzadeh, T. Thiringer, and Y. Serdyuk, "Analysis and improvement of harmonic content in multi-level three-phase DAB converters with different transformer windings connections," in *2022 International Power Electronics Conference (IPEC-Himeji 2022- ECCE Asia)*, 2022, pp. 2653–2658.

[67] B. Backlund, M. Rahimo, S. Klaka, and J. Siefken, "Topologies, voltage ratings and state of the art high power semiconductor devices for medium voltage wind energy conversion," in *2009 IEEE Power Electronics and Machines in Wind Applications*, 2009, pp. 1–6.

[68] M. H. Rashid, *Power electronics handbook*. Butterworth-heinemann, 2017.

[69] P. D. Reigosa, H. Wang, Y. Yang, and F. Blaabjerg, "Prediction of bond wire fatigue of IGBTs in a PV inverter under a long-term operation," *IEEE Transactions on Power Electronics*, vol. 31, no. 10, pp. 7171–7182, 2016.

[70] J. Lutz, H. Schlangenotto, U. Scheuermann, and R. De Doncker, "Semiconductor power devices," *Physics, characteristics, reliability*, vol. 2, 2011.

[71] M. A. Miner, "Cumulative damage in fatigue," 1945.

[72] S. D. Downing and D. Socie, "Simple rainflow counting algorithms," *International journal of fatigue*, vol. 4, no. 1, pp. 31–40, 1982.

[73] K. Ma, M. Liserre, and F. Blaabjerg, "Lifetime estimation for the power semiconductors considering mission profiles in wind power converter," in *2013 IEEE Energy Conversion Congress and Exposition*, 2013, pp. 2962–2971.

[74] B. Hu, J. Ortiz Gonzalez, L. Ran, *et al.*, "Failure and reliability analysis of a SiC power module based on stress comparison to a Si device," *IEEE Transactions on Device and Materials Reliability*, vol. 17, no. 4, pp. 727–737, 2017.

[75] T. Thiringer, J. Paixao, and M. Bongiorno, "Monitoring of the ride-through ability of a 2MW wind turbine in tvaaker, halland," 2009.

[76] *CAS300M17BM2: 1700 v, 8.0-mΩ, silicon carbide, half-bridge module*, https://www.wolfspeed.com/power/products/sic-power-modules/cas300m17bm2.

[77] *C2M0045170P: Silicon carbide power MOSFET C2M planar MOSFET technology N-channel enhancement mode*, https://www.wolfspeed.com/power/products/sic-mosfets/c2m0045170p.

[78] J. Everts, F. Krismer, J. Van den Keybus, J. Driesen, and J. W. Kolar, "Optimal ZVS modulation of single-phase single-stage bidirectional DAB ac–dc converters," *IEEE Transactions on Power Electronics*, vol. 29, no. 8, pp. 3954–3970, 2014.

[79] J. Everts, "Closed-form solution for efficient ZVS modulation of DAB converters," *IEEE Transactions on Power Electronics*, vol. 32, no. 10, pp. 7561–7576, 2017.

[80] J. Riedel, D. G. Holmes, B. P. McGrath, and C. Teixeira, "ZVS soft switching boundaries for dual active bridge dc–dc converters using frequency domain analysis," *IEEE Transactions on Power Electronics*, vol. 32, no. 4, pp. 3166–3179, 2017.

[81] P. Liu and S. Duan, "A zvs range enhancement strategy for the DAB converter by using blocking capacitors," *IEEE Journal of Emerging and Selected Topics in Power Electronics*, vol. 9, no. 2, pp. 1389–1398, 2021.

[82] T. Uchida, Y. Ishizuka, D. Yamashita, T. Hirose, and K. Ura, "A control method of dual active bridge dc-dc converters maintaining soft-switching at different voltage ratio," in *2020 IEEE Applied Power Electronics Conference and Exposition (APEC)*, 2020, pp. 3364–3370.

[83] M. Mahdavifard, N. Mazloum, F. Zahin, A. KhakparvarYazdi, A. Abasian, and S. A. Khajehoddin, "An asymmetrical dab converter modulation and control systems to extend the zvs range and improve efficiency," *IEEE Transactions on Power Electronics*, vol. 37, no. 10, pp. 12 774–12 792, 2022.

[84] E. L. Carvalho, C. A. Felipe, L. V. Bellinaso, C. M. d. O. Stein, R. Cardoso, and L. Michels, "Asymmetrical-pwm dab converter with extended zvs/zcs range and reduced circulating current for ess applications," *IEEE Transactions on Power Electronics*, vol. 36, no. 11, pp. 12 990–13 001, 2021.

[85] P. Liu, C. Chen, S. Duan, and W. Zhu, "Dual phase-shifted modulation strategy for the three-level dual active bridge dc–dc converter," *IEEE Transactions on Industrial Electronics*, vol. 64, no. 10, pp. 7819–7830, 2017.

[86] L. Jin, B. Liu, and S. Duan, "ZVS soft switching operation range analysis of three-level dual-active bridge dc–dc converter under phase shift control strategy," *IEEE Transactions on Industry Applications*, vol. 55, no. 2, pp. 1963–1972, 2019.

[87] Z. Xing, X. Ruan, H. You, X. Yang, D. Yao, and C. Yuan, "Soft-switching operation of isolated modular dc/dc converters for application in HVDC grids," *IEEE Transactions on Power Electronics*, vol. 31, no. 4, pp. 2753–2766, 2016.

[88] M. A. Moonem, C. L. Pechacek, R. Hernandez, and H. Krishnaswami, "Analysis of a multilevel dual active bridge (ml-dab) dc-dc converter using symmetric modulation," *Electronics*, vol. 4, no. 2, pp. 239–260, 2015, ISSN: 2079-9292.

[89] J. Hu, N. Soltau, and R. W. De Doncker, "Asymmetrical duty-cycle control of three-phase dual-active bridge converter for soft-switching range extension," in *2016 IEEE Energy Conversion Congress and Exposition (ECCE)*, 2016, pp. 1–8.

[90] J. Huang, Y. Wang, Z. Li, Y. Jiang, and W. Lei, "Simultaneous PWM control to operate the three-phase dual active bridge converter under soft switching in the whole load range," in *2015 IEEE Applied Power Electronics Conference and Exposition (APEC)*, 2015, pp. 2885–2891.

[91] J. Hu, Z. Yang, S. Cui, and R. W. De Doncker, "Closed-form asymmetrical duty-cycle control to extend the soft-switching range of three-phase dual-active-bridge converters," *IEEE Transactions on Power Electronics*, vol. 36, no. 8, pp. 9609–9622, 2021.

[92] L. M. Cúnico and A. L. Kirsten, "Improved zvs range for three-phase dual-active-bridge converter with wye-extended-delta transformer," *IEEE Transactions on Industrial Electronics*, vol. 69, no. 8, pp. 7984–7993, 2022.

[93] Z. Wang, C. Li, J. Liu, and Z. Zheng, "Influence of junction-capacitance and dead-time on dual-active-bridge actual soft-switching-range: Analytic analysis and solution," *IEEE Transactions on Power Electronics*, vol. 38, no. 5, pp. 6157–6168, 2023.

[94] S. P. Engel, M. Stieneker, N. Soltau, S. Rabiee, H. Stagge, and R. W. De Doncker, "Comparison of the modular multilevel dc converter and the dual-active bridge converter for power conversion in HVDC and MVDC grids," *IEEE Transactions on Power Electronics*, vol. 30, no. 1, pp. 124–137, 2015.

[95] A. Krings and J. Soulard, "Overview and comparison of iron loss models for electrical machines," *Journal of Electrical Engineering*, vol. 10, no. 3, pp. 8–8, 2010.

[96] K. Venkatachalam, C. Sullivan, T. Abdallah, and H. Tacca, "Accurate prediction of ferrite core loss with nonsinusoidal waveforms using only steinmetz parameters," in *2002 IEEE Workshop on Computers in Power Electronics, 2002. Proceedings.*, 2002, pp. 36–41.

[97] R. Núñez, G. Oggier, F. Botterón, and G. García, "A comparative study of three–phase dual active bridge converters for renewable energy applications," *Sustainable Energy Technologies and Assessments*, vol. 23, pp. 1–10, 2017, ISSN: 2213-1388.

[98] N. Baars, J. Everts, K. Wijnands, and E. Lomonova, "Impact of different transformer-winding configurations on the performance of a three-phase dual active bridge dc-dc converter," in *2015 IEEE Energy Conversion Congress and Exposition (ECCE)*, 2015, pp. 637–644.

[99] B. Zhao, Q. Yu, and W. Sun, "Extended-phase-shift control of isolated bidirectional dc–dc converter for power distribution in microgrid," *IEEE Transactions on Power Electronics*, vol. 27, no. 11, pp. 4667–4680, 2012.

[100] F. Krismer and J. W. Kolar, "Accurate small-signal model for the digital control of an automotive bidirectional dual active bridge," *IEEE Transactions on Power Electronics*, vol. 24, no. 12, pp. 2756–2768, 2009.

[101] F. Krismer and J. W. Kolar, "Closed form solution for minimum conduction loss modulation of DAB converters," *IEEE Transactions on Power Electronics*, vol. 27, no. 1, pp. 174–188, 2012.

[102] H. Shi, H. Wen, J. Chen, Y. Hu, L. Jiang, and G. Chen, "Minimum-reactive-power scheme of dual-active-bridge dc–dc converter with three-level modulated phase-shift control," *IEEE Transactions on Industry Applications*, vol. 53, no. 6, pp. 5573–5586, 2017.

[103] G. G. Oggier, G. O. GarcÍa, and A. R. Oliva, "Switching control strategy to minimize dual active bridge converter losses," *IEEE Transactions on Power Electronics*, vol. 24, no. 7, pp. 1826–1838, 2009.

[104] A. Tong, L. Hang, G. Li, X. Jiang, and S. Gao, "Modeling and analysis of a dual-active-bridge-isolated bidirectional dc/dc converter to minimize RMS current with whole operating range," *IEEE Transactions on Power Electronics*, vol. 33, no. 6, pp. 5302–5316, 2018.

[105] J. Sun, L. Qiu, X. Liu, J. Zhang, J. Ma, and Y. Fang, "Optimal simultaneous PWM control for three-phase dual-active-bridge converters to minimize current stress in the whole load range," *IEEE Journal of Emerging and Selected Topics in Power Electronics*, vol. 9, no. 5, pp. 5822–5837, 2021.

[106] J. Huang, Z. Li, L. Shi, Y. Wang, and J. Zhu, "Optimized modulation and dynamic control of a three-phase dual active bridge converter with variable duty cycles," *IEEE Transactions on Power Electronics*, vol. 34, no. 3, pp. 2856–2873, 2019.

[107] N. H. Baars, C. G. E. Wijnands, and J. Everts, "ZVS modulation strategy for a three-phase dual active bridge dc-dc converter with three-level phase-legs," in *2016 18th European Conference on Power Electronics and Applications (EPE'16 ECCE Europe)*, 2016, pp. 1–10.

[108] N. H. Baars, C. G. E. Wijnands, and J. Everts, "A three-level three-phase dual active bridge dc-dc converter with a star-delta connected transformer," in *2016 IEEE Vehicle Power and Propulsion Conference (VPPC)*, 2016, pp. 1–6.

[109] N. H. Baars, J. Everts, H. Huisman, J. L. Duarte, and E. A. Lomonova, "A 80-kw isolated dc–dc converter for railway applications," *IEEE Transactions on Power Electronics*, vol. 30, no. 12, pp. 6639–6647, 2015.

[110] X. She, A. Q. Huang, and R. Burgos, "Review of solid-state transformer technologies and their application in power distribution systems," *IEEE Journal of Emerging and Selected Topics in Power Electronics*, vol. 1, no. 3, pp. 186–198, 2013.

[111] X. She, R. Burgos, G. Wang, F. Wang, and A. Q. Huang, "Review of solid state transformer in the distribution system: From components to field application," in *2012 IEEE Energy Conversion Congress and Exposition (ECCE)*, 2012, pp. 4077–4084.

[112] M. Stieneker, N. R. Averous, N. Soltau, H. Stagge, and R. W. De Doncker, "Analysis of wind turbines connected to medium-voltage dc grids," in *2014 16th European Conference on Power Electronics and Applications*, 2014, pp. 1–10.

[113] B. Khanzadeh, C. Tang, and T. Thiringer, "A study on the lifetime of Q2L-MMC-DAB's switches for wind turbine applications," in *2020 Fifteenth International Conference on Ecological Vehicles and Renewable Energies (EVER)*, 2020, pp. 1–6.

[114] *CAB500M17HM3: 1700 v, 500 a, silicon carbide, half-bridge module*, https://www.wolfspeed.com/power/products/sic-power-modules/CAB500M17HM3.

[115] *Nanocrystalline VITROPERM: State-of-the-art soft magnetic ribbon*, https://vacuumschmelze.com/Nanocrystalline-Material.

[116] D. Lovelock and H. Rund, *Tensors, differential forms, and variational principles*. Courier Corporation, 1989.